TECHNISCHE UNIVERSITÄT MÜNCHEN

Lehrstuhl E23 für Technische Physik

Walther-Meißner-Institut für Tieftemperaturforschung
der Bayerischen Akademie der Wissenschaften

Electric-field control of magnetization in multifunctional hybrid devices

Andreas Brandlmaier

Vollständiger Abdruck der von der Fakultät für Physik der Technischen Universität München zur Erlangung des akademischen Grades eines

Doktors der Naturwissenschaften

genehmigten Dissertation.

Vorsitzender:	Univ.-Prof. Dr. Ralf Metzler
Prüfer der Dissertation:	1. Univ.-Prof. Dr. Rudolf Gross
	2. apl. Prof. Dr. Martin S. Brandt

Die Dissertation wurde am 20.07.2011 bei der Technischen Universität München eingereicht und durch die Fakultät für Physik am 05.09.2011 angenommen.

Abstract

Multifunctional material systems unite different material properties in a single functional unit. This makes them interesting for both device applications and basic research. One prominent example of multifunctional systems are the so-called magnetoelectric multiferroic materials, which simultaneously exhibit coupled ferroelectric and ferromagnetic properties. Thus, an in-situ electric-field control of magnetization is enabled—a long-standing experimental challenge offering entirely novel device paradigms. A promising approach to magnetoelectric materials are composite-type multifunctional structures made from ferromagnetic and ferroelectric constituents, which are referred to as ferromagnetic/ferroelectric hybrid systems. Such artificial compounds enable an elastic strain-mediated, indirect magnetoelectric coupling across the interface of the constituents by exploiting piezoelectricity in one phase and magnetostriction in the other.

Within the framework of this thesis, we study the spin-mechanics approach. This novel concept is based on the strain-mediated electric-field control of magnetization in ferromagnetic thin film/piezoelectric actuator hybrid systems. More precisely, we investigate magnetization manipulation concepts for both polycrystalline and single-crystalline ferromagnetic thin films. We particularly focus on a control of the magnetization orientation, i.e., we study the feasibility and limitations of a piezovoltage generated manipulation of the macrospin magnetization. We address the reversibility and nonvolatility of all-electric-field controlled magnetization reorientation processes in polycrystalline nickel, single-crystalline dilute magnetic semiconductor (Ga,Mn)As, and single-crystalline magnetite ferromagnetic thin films. The magnetic anisotropy of these multifunctional hybrids is quantified as a function of the voltage V_p applied to the piezoelectric actuator both using ferromagnetic resonance spectroscopy and anisotropic magnetoresistance techniques. The evolution of the magnetization orientation as a function of V_p is determined via superconducting quantum interference device magnetometry and magneto-optical Kerr effect spectroscopy. In short, we show that the magnetization orientation can be rotated continuously and reversibly within up to 90° at zero external magnetic field at room temperature solely by changing V_p. We also demonstrate irreversible and nonvolatile voltage-controlled magnetization reorientations of up to 180° upon an appropriate magnetic field preparation of the magnetization. We furthermore realize a proof-of-principle multifunctional memory device based on a nonvolatile and reversible all-electric-field control of remanent magnetization orientation. All data can be quantitatively understood within a single-domain (macrospin) Stoner-Wohlfarth type of approach. Furthermore, we investigate different concepts towards a nonvolatile, all-voltage-controlled magnetization switching in single-crystalline ferromagnets at room temperature.

Kurzfassung

Multifunktionale Materialsysteme vereinigen unterschiedliche Materialeigenschaften in einer Funktionseinheit. Sie sind daher sowohl für Bauelement-Anwendungen als auch für die Grundlagenforschung von großem Interesse. Ein wichtiges Beispiel für multifunktionale Systeme sind die sogenannten magnetoelektrischen multiferroischen Materialien, die gleichzeitig ferroelektrische und ferromagnetische Eigenschaften aufweisen. Dies erlaubt eine elektrische Kontrolle der Magnetisierung – eine langjährige experimentelle Herausforderung, die völlig neue Bauelement-Konzepte ermöglicht. Eine vielversprechende Herangehensweise an magnetoelektrische Materialien sind verbundartige multifunktionale Strukturen aus ferromagnetischen und ferroelektrischen Komponenten, die als ferromagnetisch/ferroelektrische Hybridstrukturen bezeichnet werden. Derartige künstliche Schichtstrukturen ermöglichen eine über elastische Verspannung vermittelte, indirekte magnetoelektrische Kopplung über die Grenzfläche der Komponenten, indem Piezoelektrizität in einer Phase und Magnetostriktion in der anderen verwendet werden.

Im Rahmen dieser Arbeit haben wir das Spinmechanik-Konzept untersucht. Dieses basiert auf der durch elastische Verspannung vermittelten elektrischen Kontrolle der Magnetisierung in ferromagnetischen Dünnfilm/piezoelektrischer Aktor-Hybridsystemen. Dabei untersuchen und vergleichen wir die Magnetisierungsmanipulation sowohl in polykristallinen als auch in einkristallinen ferromagnetischen dünnen Filmen. Ein zentraler Fokus liegt hierbei insbesondere auf der Kontrolle der Magnetisierungsrichtung, d.h., wir untersuchen die Realisierbarkeit und Grenzen einer durch Piezo-Spannung erzeugten Manipulation der Makrospin-Magnetisierung. Wir behandeln die Reversibilität und Nichtflüchtigkeit von rein elektrisch kontrollierten Umorientierungsprozessen der Magnetisierung in polykristallinen Nickel-Dünnfilmen, einkristallinen Dünnfilmen des magnetischen Halbleiters (Ga,Mn)As und einkristallinen Magnetit-Dünnfilmen. Die magnetische Anisotropie dieser multifunktionalen Hybride wird als Funktion der an den piezoelektrischen Aktor angelegten Spannung V_p quantifiziert, und zwar sowohl mittels ferromagnetischer Resonanz-Spektroskopie als auch durch die Messung des anisotropen Magnetwiderstands. Die Evolution der Magnetisierungsorientierung als Funktion von V_p wird mittels SQUID-Magnetometrie und magnetooptischer Kerr-Effekt-Spektroskopie bestimmt. Zusammenfassend zeigen wir, dass bei Raumtemperatur und in Abwesenheit von externen Magnetfeldern die Magnetisierungsrichtung rein durch Veränderung von V_p kontinuierlich und reversibel um bis zu 90° gedreht werden kann. Wir demonstrieren irreversible und nichtflüchtige, spannungskontrollierte Drehungen der Magnetisierung um bis zu 180° bei einer entsprechenden Magnetfeld-Präparation der Magnetisierung. Weiterhin stellen wir einen Demonstrator eines multifunktionalen Speicherbauelements her, der auf einer nichtflüchtigen und reversiblen elektrischen Kontrolle der remanenten Magnetisierungsrichtung beruht. Alle experimentellen Ergebnisse können quantitativ innerhalb eines eindomänigen (Makrospin) Stoner-Wohlfarth Ansatzes verstanden werden. Des Weiteren untersuchen wir verschiedene Konzepte in Richtung eines nichtflüchtigen, rein spannungskontrollierten Schaltens der Magnetisierung in einkristallinen Ferromagneten bei Raumtemperatur.

Contents

Chapter 1

Introduction: Multifunctional systems

1.1 Multifunctional materials

The discovery of the giant magnetoresistance (GMR) effect by Peter Grünberg and Albert Fert in 1988 [1, 2] has fathered a new field of research called magnetoelectronics or spinelectronics [3–8], which—besides the conventionally used electric charge—additionally utilizes the spin degree of freedom. The GMR effect is a quantum mechanical effect and is observed in layered magnetic thin-film devices, which are composed of alternate ferromagnetic and nonmagnetic layers. Since it is based on spin-dependent scattering, the resistance substantially depends on the relative alignment of the magnetic moments of the ferromagnetic layers, which can be manipulated by external magnetic fields. Hence, magnetoresistive effects like the GMR and the tunneling magnetoresistance (TMR) [9] employed in, e.g., spin valve [10] and magnetic tunnel junction (MTJ) [11] devices, has resulted in both novel fundamental physics discoveries and the development of technologically relevant applications [12–14] within the last two decades. Particularly GMR sensors based on spin valves employed in the read heads of hard disk drives since 1997 gained a major economic impact, since such a sensitive and scalable read technique has lead to a sharp increase in the growth rate for storage areal density. A further application with high economic potential is nonvolatile data storage (random access memory). To this end, there has been considerable effort for developing a magnetic random access memory (MRAM) [15–17], which is mostly based on MTJs as memory elements, to compete with semiconductor-based RAMs in terms of speed and density, combined with key advantages such as nonvolatility and infinite endurance. In the original MRAM design, electrical current-generated magnetic fields are used to switch the magnetization direction and thus the information state of an addressed cell [14, 16]. However, this approach reaches its limits in modern, highly integrated magnetic microstructures due to two major obstacles. First, the write current (and thus the power consumption) for conventional magnetic-field writing is not scalable [15]. Second, stray fields from the write current hamper the addressing of individual magnetic bits [14]. It is though worth to mention that modified concepts circumvent such cross-talk effects by incorporating, e.g., spin-torque transfer and heat-assisted writing [14, 16]. Overall, spintronics devices offer novel functionalities not feasible

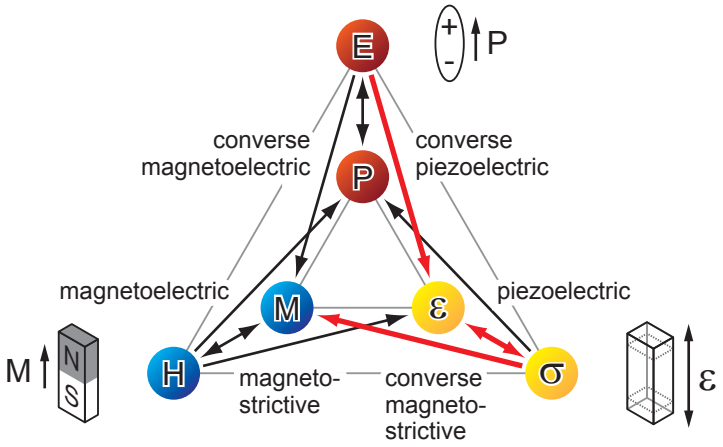

Figure 1.1: Phase control and interactions in multiferroics [18]. The ferroic order parameters (magnetization **M**, electric polarization **P**, or strain ϵ) can be switched by their respective conjugate field (magnetic field **H**, electric field **E**, or stress σ). We here particularly focus on an elastic strain-mediated electric-field control of magnetism, as indicated by the red arrows.

or ineffective with conventional electronics by utilizing both the spin *and* charge. In this sense, spintronic devices can be considered *multifunctional*.

A further class of multifunctional materials are *multiferroics* [18–21]. Ferroic materials exhibit a spontaneous ordering with an order parameter (e.g., magnetization **M**, electric polarization **P**, or strain ϵ), which can be switched by application of the respective conjugate field (magnetic field **H**, electric field **E**, or stress σ), as illustrated in Fig. 1.1 [18]. Intrinsic multiferroics simultaneously unite at least two ferroic properties within one material (single-phase multiferroics) [22]. This can offer entirely new device paradigms, since such a coexistence leads to additional interactions (Fig. 1.1), and thus cross-coupling allows the ferroic orderings to also be controlled by fields other than their conjugates [18, 23]. Magnetoelectric multiferroics, i.e., ferromagnetic-ferroelectric multiferroics with substantial magnetoelectric coupling, are particularly appealing and have triggered a vigorous revival of activity within the last decade, since such material systems open the possibility of controlling the polarization **P** (**H**) by a magnetic field and, conversely, the magnetization **M** (**E**) by an electric field [19, 24–33]. Therefore, magnetoelectric coupling enables novel design concepts, such as an all-electric field control—i.e., a pure voltage control—of magnetism rather than by directly applied or electrical current-induced magnetic fields, opening an avenue towards smaller and more energy-efficient devices. More precisely, it offers the opportunity of magnetic data storage written and read electrically and thus potentially combines the respective advantages of ferroelectric random access memory (FeRAM) [34, 35] and MRAM. To this end, the magnetoelectric random access memory (MERAM) [36–38] permits fast, low-power and nonvolatile electrical write operation and nondestructive magnetic read operation, while avoiding the problems associated with reading FeRAM and high writing energy characteristic of MRAM.

It was shown that the linear magnetoelectric response in single-phase systems is

limited by the relation $\alpha_{ij}^2 \leq \varepsilon_0\mu_0\varepsilon_{ii}\mu_{jj}$ [39], where ε_{ii} (ε_0) and μ_{jj} (μ_0) are the relative permittivity (permittivity of free space) and the relative permeability (permeability of free space), respectively. Hence, the magnetoelectric effect can only be large in materials both ferroelectric and ferromagnetic [24]. However, single-phase magnetoelectric multiferroics are scarce, resulting from a contraindication between the conventional mechanism for cation off-centering in ferroelectrics (i.e., the polarization arises when nonmagnetic cations shift away from their center position) and the formation of magnetic moments (usually due to partially filled d orbitals, which reduce the tendency for off-center ferroelectric distortion) [40]. Thus, most materials have small values of ε_{ii} and/or μ_{jj}, so that the linear magnetoelectric effect is also small [19].

An alternative, vigorously investigated approach are composite material systems of ferromagnetic and ferroelectric constituents [24, 28, 41, 42]. We refer to these multifunctional multi-phase systems as *ferromagnetic/ferroelectric hybrids*. In such artificial compounds, an indirect magnetoelectric coupling is mediated by strain at the interface of the intimately coupled constituents. In contrast to single-phase materials, the coupling strength is not restricted by the above given expression and thus can exceed the response of single-phase systems by orders of magnitude [43, 44]. The hybrid concept offers versatile engineering potential, since it allows to employ and individually optimize the best available materials for each phase to suit the desired application. Strain-mediated magnetoelectric coupling in such hybrid systems can be realized via exploiting piezoelectricity in one phase and magnetostriction in the other (see Fig. 1.1). In particular, an *electric-field control of magnetism* is illustrated in Fig. 1.1 by the red arrows: an applied electric field induces elastic strain in the ferroelectric phase via the converse piezoelectric effect. This strain is then transferred into the ferromagnetic phase due to the intimate elastic coupling and there modifies the magnetic anisotropy via converse magnetostriction, which in turn can result in a magnetization manipulation.

Magnetoelectric, strain-mediated composite-type systems can be roughly classified as (i) particulate composites, (ii) laminated bulk composites, (iii) vertical heterostructures, and (iv) horizontal thin film heterostructures [24, 28, 42, 43]. Particulate composites denote one-phase particles embedded in another phase [28, 45]. Laminated bulk composites are produced in their simplest form by bonding the constituents (e.g., by using epoxy), which provides high flexibility in the choice of materials and enhanced control over, e.g., the materials interfaces and mechanical coupling [43, 45, 46]. Vertical heterostructures are epitaxial columnar nanostructures of nanopillar arrays of the ferromagnetic component embedded in a ferroelectric matrix [47–49]. Vertical heterostructures exhibit strong magnetoelectric coupling, since they have a large interfacial surface area and reduce substrate-imposed mechanical clamping [20]. Horizontal thin film heterostructures show stronger clamping effects due to strong in-plane elastic coupling to the substrate and thus weaker magnetoelectric coupling, but are easier to be fabricated than vertical ones [28, 43]. They furthermore have the advantages of better control of the crystal structure and also a very good elastic coupling between the ferroic phases [28]. Besides magnetic memories, magnetoelectric composites offer great potential and opportunities for device

applications, as comprehensively presented in Refs. [42, 43, 46]. Promising applications include sensors (magnetic-field sensors for ac and dc fields, current sensors), energy harvester and conversion devices, and microwave devices (e.g., transducers, filters, oscillators, and phase shifters).

In the context of thin film heterostructures, such ferromagnetic/ferroelectric hybrids are vigorously investigated, mostly reported in film-on-substrate heterostructures fabricated by growing ferromagnetic thin films on ferroelectric substrates using various materials. The magnetic films are either metallic (e.g., Fe, Ni, Co, and alloys) or oxide-based [e.g., Fe_3O_4, CFO ($CoFe_2O_4$), NFO ($NiFe_2O_4$), and LSMO ($La_{1-x}Sr_xMnO_3$)], and the ferroelectric substrates commonly used are BTO ($BaTiO_3$), PZT [$Pb(Zr, Ti)O_3$], PMN-PT [$Pb\,(Mg, Nb)\,O_3 - PbTiO_3$], and PZN-PT [$Pb\,(Zn, Nb)\,O_3 - PbTiO_3$] single crystals or ceramics [42]. A strain-mediated magnetization control has been realized following two basic strategies. Either the phase transitions of the ferroelectric BTO as a function of temperature associated with changes in strain are exploited [41, 50–56], or the converse piezoelectric effect of the ferroelectric is used to manipulate the strain state [41, 51, 53, 57–68]. Hence, the latter approach allows for an electric-field control of magnetization.

We here use a slightly modified concept to realize a voltage control of magnetization. More precisely, we study ferromagnetic thin film/piezoelectric actuator hybrid systems, where the ferromagnetic film is affixed to the actuator by either directly depositing polycrystalline thin films or by cementing substrate/single-crystalline ferromagnetic thin film structures using a two-component epoxy [69, 70].

1.2 Magnetization control schemes

To appreciate the advantages and drawbacks of a voltage control of magnetization (spin mechanics), we now briefly review magnetization control schemes.

One such scheme utilizes the exchange bias effect [71], which results from an exchange coupling between the uncompensated interfacial spins of an antiferromagnetically ordered multiferroic or magnetoelectric with the spins of an adjacent ferromagnetic film. The exchange coupling leads to a unidirectional magnetic anisotropy in the ferromagnetic layer, which gives raise to a shift of the $M\,(H)$ loop along the magnetic field axis by the so-called exchange bias field. The application of an electric field modifies the antiferromagnetic order and thus consequently controls the magnetic properties of the ferromagnetic component [72–77].

A further approach takes advantage of the charge sensitivity of the magnetic state to electric fields in complex oxides [78] and dilute magnetic semiconductors [79–81]. Hence, hybrid structures of such carrier-mediated magnets and ferroelectrics give raise to a charge-driven magnetoelectric effect, and thus allow for a direct electric-field control of magnetization [82–84]. More precisely, an electric field results in a charge-density modulation in the ferromagnetic layer at the ferromagnetic/ferroelectric interface. However, the sizeable carrier densities in these ferromagnets result in very small screening lengths. Hence, observation of the charge-mediated magnetoelectric effect requires ultrathin ferromagnetic films with thick-

nesses of at most a few nm.

An interesting realization of a magnetization control by utilizing spin-polarized currents was proposed in 1996 [85, 86]. Spin-polarized currents can transfer angular momentum to a ferromagnet and thus alter its magnetization orientation. This so-called spin-transfer torque has been extensively studied [87–90], and may switch the magnetization orientation upon a sufficiently high current density. A major obstacle for applications, however, is the comparatively high switching current density around $10^6 - 10^7\,\mathrm{A/cm^2}$ [8, 15], and an important technological challenge is the reduction of this current density.

A local modification of magnetic properties in magnetic thin films has been demonstrated by means of ion irradiation or ion implantation. In particular, these techniques have been shown to locally alter magnetic properties like the magnetic anisotropy, the exchange coupling, the saturation magnetization, and the magnetic damping behavior [91–93]. All these modifications originate from structural modifications of, e.g., the interface structure, the atomic short range order, the crystalline phase, or the composition of the material [92].

Finally, we conclude this short summary with reports on local magnetic-anisotropy control via anisotropic strain relaxation in dilute magnetic semiconductors controlled by lithographic patterning [94–96]. The deformation of the crystal structure during the uniaxial relaxation leads to a uniaxial magnetic anisotropy due to the strong spin-orbit coupling, which thus allows for a local anisotropy engineering.

1.3 The spin-mechanics concept

In the following, we introduce the concept used in this thesis to realize a voltage control of magnetization in ferromagnetic thin film/piezoelectric actuator hybrids. We here qualitatively anticipate the terminology of the phenomena magnetic anisotropy, free energy, and elasticity, which will be more thoroughly introduced and discussed in Chapters 2 and 3.

Figures 1.2(a), (b), and (c) illustrate the conventional concept employed to control the magnetization via an externally applied magnetic field. Figure 1.2(a) shows a typical hysteretic $M\,(H)$ loop of a ferromagnet normalized to the saturation magnetization M_s, calculated using a single-domain (macrospin) Stoner-Wohlfarth (SW) model [97]. The points A and B depict two magnetic fields of equal magnitude but opposing magnetic field direction. Figures 1.2(b) and (c) show a ferromagnetic thin film with the external magnetic field applied within the film plane. Since the ferromagnet is magnetically saturated at $H = H_\mathrm{A} > 0$ [cf. Fig. 1.2(a)], $\mathbf{M}$ aligns along $\mathbf{H}_\mathrm{A}$. A magnetic-field sweep to $H = H_\mathrm{B} < 0$ induces a switching of $\mathbf{M}$ by 180° into a direction parallel to $\mathbf{H}_\mathrm{B}$.

A mechanical deformation of the ferromagnet in the absence of an external magnetic field can also result in a magnetization manipulation. The application of a stress $\sigma > 0$ along $\mathbf{y}$ induces the tensile and compressive strains $\epsilon_y > 0$ and $\epsilon_x < 0$, respectively, due to the Poisson effect [Fig. 1.2(d)]. Given a finite magnetostrictive coupling, strain affects the ferromagnet's free energy density F via magnetoelastic

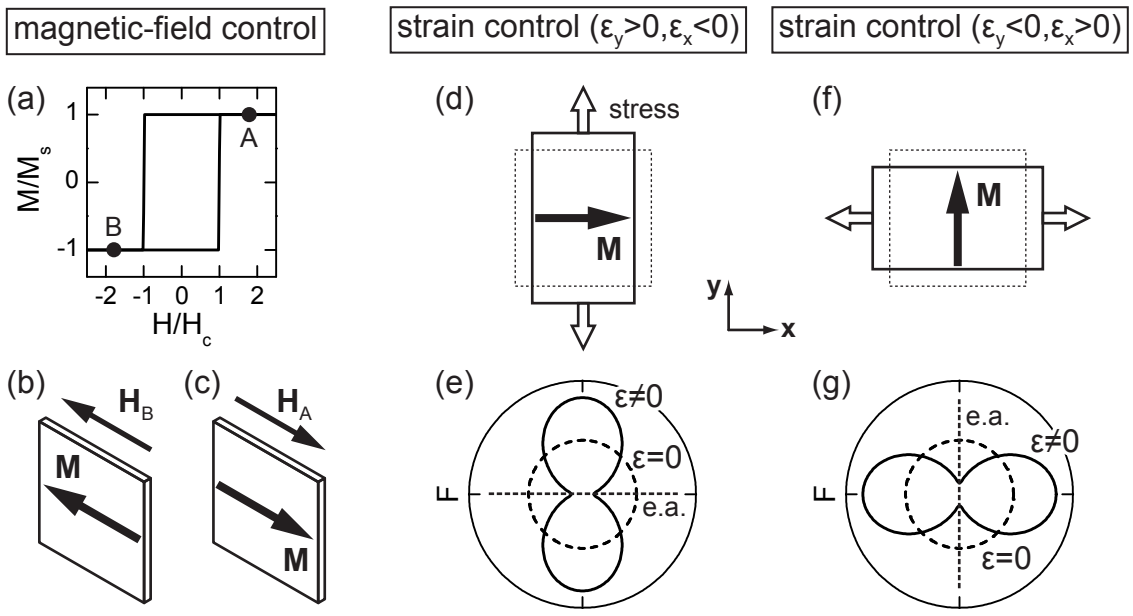

Figure 1.2: (a)–(c) Illustration of a magnetic-field control of magnetization. (a) Typical $M\,(H)$ loop of a ferromagnet. The application of a sufficiently high magnetic field (points A, B) results in a parallel alignment of $\mathbf{M}$ and $\mathbf{H}$. Inverting the orientation of $\mathbf{H}$ leads to a switching of $\mathbf{M}$ [(b), (c)]. (d)–(g) Strain control of magnetization. Given a finite magnetostrictive coupling, mechanical deformation of a ferromagnetic thin film affects its free energy density, as shown by the corresponding contours in the film plane in (e), (g). An inversion of the induced strain results in a switching of the magnetic easy axes (e.a.) by 90°. The unstrained film is indicated by the dotted contours in (d)–(g).

anisotropies. The free energy density contour corresponding to the situation depicted in Fig. 1.2(d) is shown in Fig. 1.2(e). Here, the free energy density is given by the distance from the origin to the contour for a given magnetization direction in the film plane. F is calculated assuming elastic stiffness constants $c_{11} > c_{12}$ and a magnetostriction $\lambda < 0$, as this is the case for, e.g., nickel, and furthermore assuming vanishing crystalline magnetic anisotropy. The magnetization favors orientations corresponding to minima of F, which are referred to as magnetic easy axes (e.a.). Hence, $\mathbf{M}$ aligns along $\mathbf{x}$ as shown in Fig. 1.2(d). Likewise, a stress $\sigma > 0$ along $\mathbf{x}$ induces the strains $\epsilon_y < 0$ and $\epsilon_x > 0$, which result in a magnetic easy axis along $\mathbf{y}$ [Fig. 1.2(g)] and thus a corresponding change of the magnetization orientation [Fig. 1.2(f)]. Overall, Figs. 1.2(d) to (g) demonstrate that a magnetization reorientation by 90° upon an inversion of the induced strain should be possible.

We now turn to the spin-mechanics concept, i.e., the strain-mediated electric-field control of magnetization $\mathbf{M}\,(\mathbf{E})$ in ferromagnetic/ferroelectric hybrids. The spin-mechanics concept allows for a continuous, *in-situ* tuning of the ferromagnet's elastic strain state solely via the application of a voltage V_p to the piezoelectric actuator. Since the elastic strain also affects $\mathbf{M}$, the usual terminology for $\mathbf{M}$ reorientation processes has to be reconsidered. In particular, $\mathbf{M}\,(\mathbf{E})$ and $\mathbf{M}\,(\mathbf{H})$ processes must now be distinguished. In equilibrium, $\mathbf{M}$ always resides in a (local or global) minimum of the free energy density F. The evolution of $\mathbf{M}$ as a function of $\mathbf{E}$

remanent state	distinct **M** orientation retained at $H = 0$
nonvolatile state	distinct **M** orientation retained at $E = 0$
coherent reorientation	reorientation of a single homogeneous magnetic domain
noncoherent reorientation	magnetization reorientation via magnetic domain-wall effects
continuous reorientation	**M** resides in a minimum of F, which undergoes a gradual shift of its position
discontinuous reorientation	**M** abruptly reorients from one to another minimum of F
reversible reorientation	after a **M** reorientation process due to E [H], the initial **M** state can be restored upon inverting E [H]
irreversible reorientation	after a **M** reorientation process due to E [H], the initial **M** state can only be restored upon an additional change of H [E]

Table 1.1: Terminology to classify magnetization orientation states and magnetization reorientation/switching processes.

or **H** can thus be modeled by tracing the minimum of F. Generally speaking, the application of **E** or **H** modifies F and can thus lead to a gradual shift of a given minimum and/or a change of its depth. The corresponding magnetization reorientation can proceed by either a *coherent rotation* (of the minimum "moves") or *switching* (from one minimum to the next) [98]. While the former refers to a simple rotation of the magnetization vector and thus is well described by a single-domain SW model, the latter can occur via magnetic domain-wall nucleation and/or unpinning. The terminology used in this thesis to classify magnetization orientation states and magnetization reorientation/switching processes is summarized in Table 1.1.

The spin-mechanics concept is illustrated in Fig. 1.3. The application of a voltage $V_\mathrm{p} > 0\,\mathrm{V}$ [Fig. 1.3(a)] ($V_\mathrm{p} < 0\,\mathrm{V}$ [Fig. 1.3(b)]) to the actuator results in an elongation with a related uniaxial strain $\epsilon_y > 0$ (contraction with $\epsilon_y < 0$) along the dominant elongation direction **y**. To visualize the terminology presented in Table. 1.1 and to give an introductive overview, Figs. 1.3(c), (d), and (e) demonstrate different magnetization switching concepts, which will be discussed more thoroughly in the experimental Chapters 5, 6, and 7. The panels in Fig. 1.3 depict free energy density contours in the film plane $F(\Theta)$ as a function of **M** orientation Θ at zero external magnetic field, calculated using a single-domain SW model. The different contours in each panel correspond to different voltages V_p applied to the piezoelectric actuator and thus to different elastic strain states, and the full black circles depict the respective equilibrium magnetization orientations. A magnetization switching process can occur either via (i) a *discontinuous reorientation* or (ii) a *continuous reorientation*, shown for ferromagnetic thin films with a magnetically isotropic film plane [Fig. 1.3(c)] and with a cubic magnetic anisotropy [Figs. 1.3(d), (e)]. Hereby, Fig. 1.3(c) illustrates a discontinuous, coherent, and volatile magnetization switch-

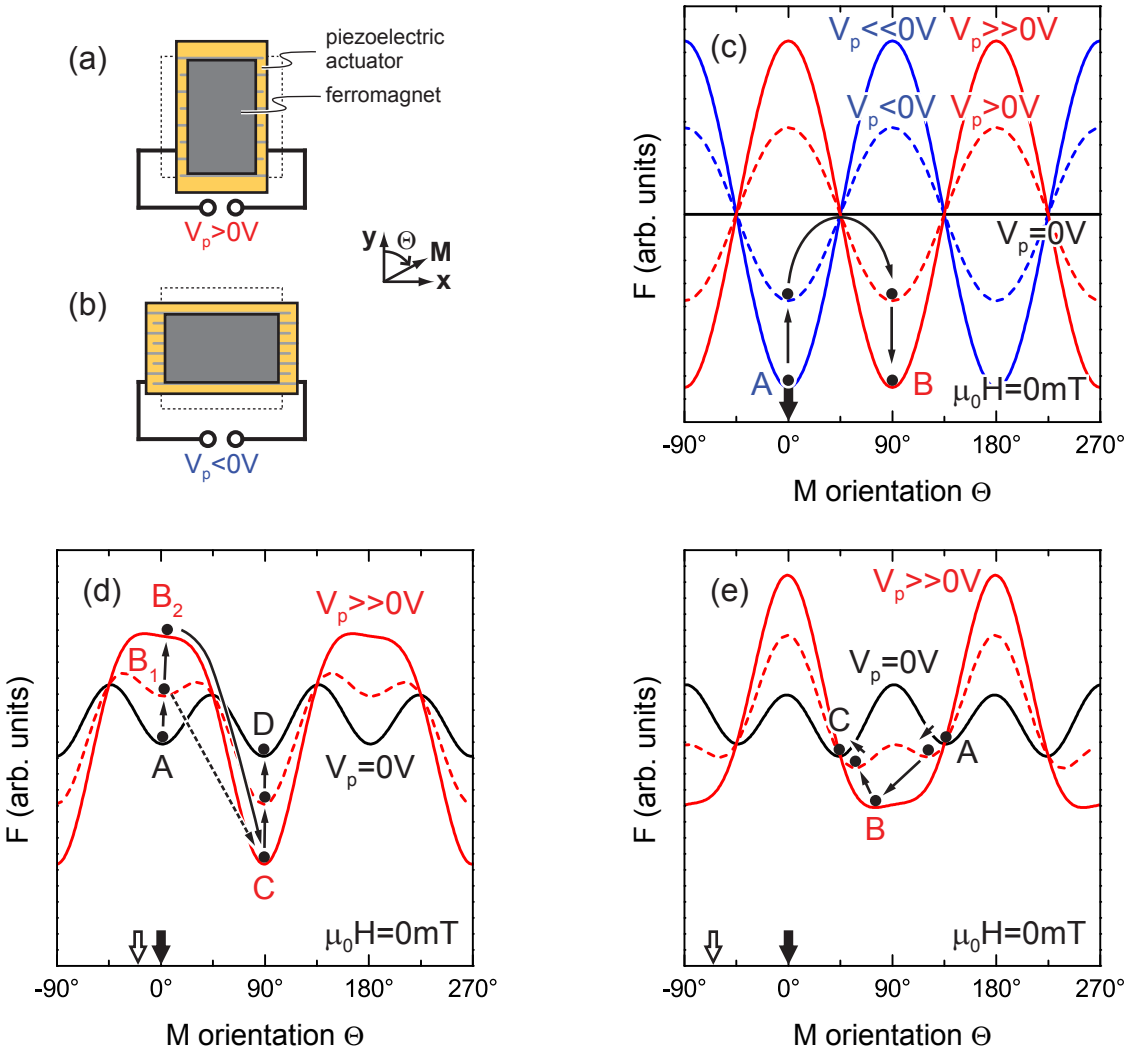

Figure 1.3: (a), (b) The piezoelectric actuator deforms upon the application of a voltage $V_\mathrm{p} \neq 0\,\mathrm{V}$ and thus induces strain in the affixed ferromagnetic thin film. The free energy density contours in the film plane $F(\Theta)$ depict different magnetization switching processes: (c) discontinuous, coherent, and volatile switching from point A to B, (d) discontinuous, noncoherent, and nonvolatile switching from point B_1 to C (dashed black arrow) and discontinuous, coherent, and nonvolatile switching from point B_2 to C (solid black arrow), and (e) continuous, coherent, and nonvolatile switching from point A to C. The position of the full black circle corresponds to the equilibrium magnetization orientation (i.e., a minimum of F). The full downward-oriented arrows depict the dominant elongation direction $\mathbf{y}$, and the open downward-oriented arrows depict the orientation of an additionally included uniaxial magnetic anisotropy with a magnetic hard axis to lift the energy degeneracy.

ing from point A to B. Figure 1.3(d) shows both a discontinuous, noncoherent, and nonvolatile magnetization switching from B_1 to C (dashed black arrow) and a discontinuous, coherent, and nonvolatile magnetization switching from B_2 to C (solid black arrow), and Fig. 1.3(e) displays a continuous, coherent, and nonvolatile magnetization switching process from A to C.

Within the framework of this thesis we investigate in detail these magnetization manipulation concepts for both polycrystalline and single-crystalline ferromagnetic thin films. The thesis is organized as follows: in Chapters 2 and 3 we give short introductions into the phenomena of magnetic anisotropy and elasticity. The most relevant aspects of the experimental techniques employed in this thesis are summarized in Chapter 4. Subsequently, we investigate polycrystalline nickel thin film/piezoelectric actuator hybrids at room temperature in Chapter 5. These systems show large magnetoelastic coupling effects due to the absence of competing net crystalline anisotropies, and we determine the magnetic anisotropy as a function of V_p using ferromagnetic resonance (FMR) spectroscopy and indeed observe a voltage-controlled inversion of the magnetic anisotropy in the film plane. Using magnetometry measurements, we record the evolution of the magnetization as a function of V_p and show a substantial both reversible and irreversible control of the magnetization orientation. The hysteretic nature of the hybrids furthermore allows for a nonvolatile and reversible control of remanent magnetization. Finally, by means of spatially resolved magneto-optical imaging, we evidence that all our findings can be quantitatively and consistently described in a macrospin model. To investigate the influence of strain on single-crystalline ferromagnetic thin films, we employ the dilute magnetic semiconductor $Ga_{1-x}Mn_xAs$ [(Ga,Mn)As]. Due to the strong temperature-dependence of its magnetic anisotropy, we are able to access qualitatively different anisotropy regimes in (Ga,Mn)As/piezoelectric actuator hybrids, as discussed in Chapter 6. We investigate the magnetic anisotropy within the temperature range $5\,\mathrm{K} \leq T \leq 80\,\mathrm{K}$ using anisotropic magnetoresistance techniques and demonstrate both a reversible control and an irreversible, nonvolatile switching of the magnetization orientation at $T = 50\,\mathrm{K}$ and $40\,\mathrm{K}$, respectively. The quantification of the piezo-induced strain and the magnetic anisotropy is used to derive the temperature dependence of the magnetostriction constant. In Chapter 7, we investigate two different approaches towards a nonvolatile, voltage-controlled magnetization switching in a single-crystalline ferromagnet at room temperature. To this end, we use magnetite (Fe_3O_4) thin film/piezoelectric actuator hybrids. Hereby, we exert stress in the film plane either along the $\langle 100 \rangle$ or $\langle 110 \rangle$ crystalline cubic axes. We determine the magnetic anisotropy as a function of V_p using FMR spectroscopy and detect the evolution of the magnetization using magnetometry measurements. We critically discuss the feasibility of a voltage-controlled, nonvolatile magnetization control. The thesis concludes with a summary in Chapter 8.

Chapter 2

Magnetic Anisotropy

The term *magnetic anisotropy* refers to the dependence of the energy of a ferromagnet on the direction of the magnetization. According to the principle of energy minimization, the magnetization will preferably align along directions corresponding to low total energy, so-called *easy axe*s. Directions of large energy are referred to as *hard axes* [99]. The preference of particular directions can generally either be of intrinsic or extrinsic origin. Hereby intrinsic anisotropy stems from, e.g., crystalline symmetry (magnetocrystalline anisotropy), which is superimposed by, e.g., the effect due to sample geometry (shape anisotropy) and the external application of stress (magnetoelastic anisotropy) [100–102].

This chapter aims to introduce the magnetic anisotropy contributions relevant for this thesis. The anisotropy contributions will be treated purely phenomenologically, which allows for a very convenient and detailed discussion in terms of a free energy ansatz by symmetry considerations, and which requires no comprehensive microscopic understanding.

2.1 Introduction to magnetic anisotropy

A simple analogy for a magnetically anisotropic system is illustrated in Fig. 2.1 by a set of compass needles in dipolar interaction [103]. In the absence of an external magnetic field, the needles will align head to tail [Fig. 2.1(a)] to minimize stray field energy, so that the horizontal corresponds to the magnetic easy axis of the system. This situation is visualized in the two-dimensional energy surface in Fig. 2.1(b). For the magnetization pointing along a distinct direction, the free energy is given by the distance from the origin to the surface. For the magnetization $\mathbf{M}$ in a horizontal orientation, it is in a stable state pointing along a minimum of the energy surface and thus along an axis of easy magnetization. Upon the application of an external magnetic field $\mu_0\mathbf{H}$ of sufficient strength [Fig. 2.1(c)] perpendicular to the easy axis, the compass needles align parallel to the external field along a maximum of the (original, $H = 0$) energy [Fig. 2.1(d)]. Such a direction is called a hard axis of magnetization.

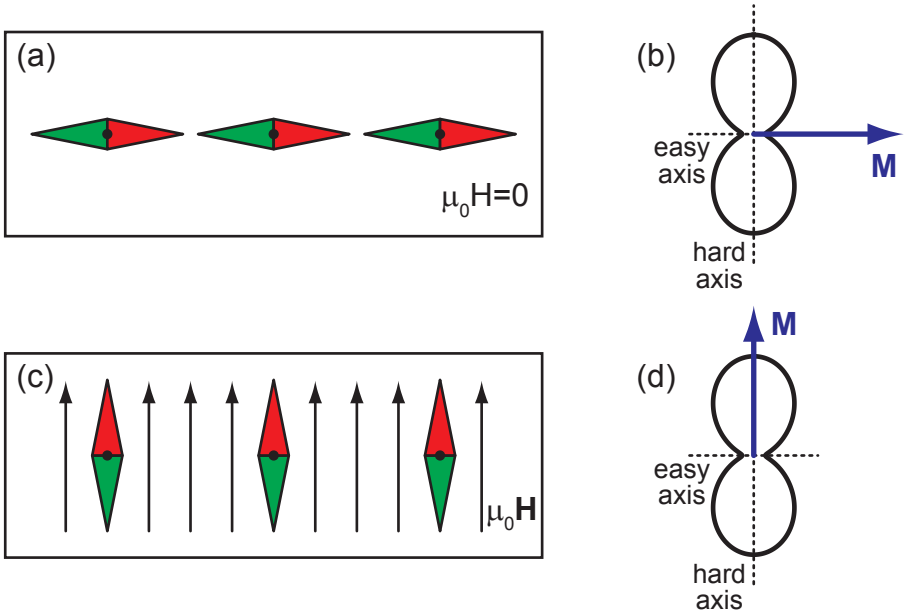

Figure 2.1: A set of compass needles with dipolar interaction as an example for a magnetically anisotropic system. (a) Stable state in the absence of an external magnetic field, (b) corresponding free energy surface with the magnetization pointing along an easy axis of the system. (c) Perpendicular alignment of the needles by application of an external magnetic field along this direction, denoted as (d) hard axis.

2.2 Phenomenology of magnetic anisotropy

Here we focus on two main types of magnetic anisotropies, namely uniaxial and cubic anisotropies. In a phenomenological ansatz, anisotropy effects are parametrized by symmetry considerations. Typically, their respective contributions to the total free energy density are expressed as a power series of the direction cosines of the magnetization.

2.2.1 Uniaxial anisotropy

The free energy density of a uniaxial magnetic anisotropy along $\mathbf{u} = \mathbf{U}/U$ can be expressed by [101, 104, 105]

$$F_{\mathrm{u}} = K_{\mathrm{u1}} \left(\mathbf{m} \cdot \mathbf{u}\right)^2 + K_{\mathrm{u2}} \left(\mathbf{m} \cdot \mathbf{u}\right)^4 + \cdots , \tag{2.1}$$

with the first- and second-order anisotropy constants K_{u1} and K_{u2}, respectively, and the magnetization

$$\mathbf{m} = \frac{\mathbf{M}}{M} = \begin{pmatrix} m_x \\ m_y \\ m_z \end{pmatrix} , \tag{2.2}$$

using the direction cosines m_i $(i = x, y, z)$ of the Cartesian axes. For the ferromagnetic thin films investigated in the framework of this thesis, it has been found

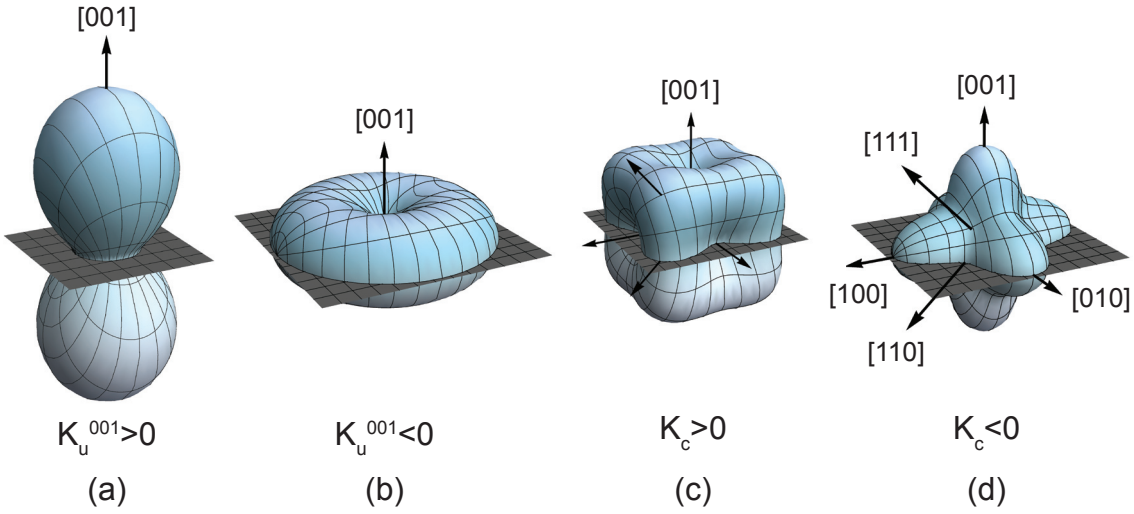

Figure 2.2: First-order free energy density surfaces for a uniaxial anisotropy along [001] with (a) $K_{\mathrm{u}}^{001} > 0$ and (b) $K_{\mathrm{u}}^{001} < 0$, as well as for a cubic anisotropy with (c) $K_{\mathrm{c}} > 0$ and (d) $K_{\mathrm{c}} < 0$. The gray layers indicate the (001) film plane.

sufficient to consider only the first term of the free energy density expansion, so that Eq. (2.1) can be rewritten as

$$\begin{aligned} F_{\mathrm{u}} &= K_{\mathrm{u}} \left(m_x u_x + m_y u_y + m_z u_z\right)^2 \\ &= K_{\mathrm{u}} \cos^2 \vartheta, \end{aligned} \tag{2.3}$$

with the angle ϑ between the magnetization orientation $\mathbf{m}$ and the uniaxial anisotropy axis $\mathbf{u}$. This situation is illustrated in Figs. 2.2(a) and (b) for a uniaxial anisotropy along [001] $\parallel \mathbf{z}$ and thus $F_{\mathrm{u}} = K_{\mathrm{u}} m_z^2$. The vector components refer to the cubic coordinate system with the [100], [010] and [001] directions denoted by $\mathbf{x}$, $\mathbf{y}$ and $\mathbf{z}$, respectively. The free energy density surface in Fig. 2.2(a) with $K_{\mathrm{u}}^{001} > 0$ is a prolate spheroid extended along the [001] direction (magnetic hard axis) with minimum energy in the (001) plane (magnetic easy plane). When $K_{\mathrm{u}}^{001} < 0$, as shown in Fig. 2.2(b), F_{u} forms an oblate spheroid with a magnetic easy axis along [001] and a magnetic hard (001) plane.

Furthermore, regarding three orthogonal uniaxial anisotropy axes, note that because of the relation

$$m_x^2 + m_y^2 + m_z^2 = 1$$

only two of three anisotropy constants K_{u}^i for $i = x, y, z$ are independent. Hence, a uniaxial anisotropy can always be expressed by two uniaxial anisotropies perpendicular to each other.

2.2.2 Cubic anisotropy

In analogy to the uniaxial anisotropy, for cubic symmetry the anisotropy energy density is expanded in powers of the direction cosines m_i $(i = x, y, z)$ [cf. Eq. (2.2)]

of the magnetization along the three Cartesian axes and the application of symmetry operations yields [101, 104, 106]

$$F_{\mathrm{c}} = K_{\mathrm{c1}} \left(m_x^2 m_y^2 + m_y^2 m_z^2 + m_z^2 m_x^2 \right) + K_{\mathrm{c2}} \left(m_x^2 m_y^2 m_z^2 \right) \cdots , \tag{2.4}$$

where K_{c1} and K_{c2} are the first- and second-order cubic anisotropy constants, respectively. As discussed in the framework of uniaxial anisotropies, we here also omit terms of higher order than the first one, so that

$$F_{\mathrm{c}} = K_{\mathrm{c}} \left(m_x^2 m_y^2 + m_y^2 m_z^2 + m_z^2 m_x^2 \right) . \tag{2.5}$$

Using the addition theorem for the direction cosines

$$m_x^4 + m_y^4 + m_z^4 = 1 - 2 \left(m_x^2 m_y^2 + m_y^2 m_z^2 + m_z^2 m_x^2 \right) , \tag{2.6}$$

Eq. (2.5) can be rewritten as

$$F_{\mathrm{c}} = \mathrm{const} - \frac{1}{2} K_{\mathrm{c}} \left(m_x^4 + m_y^4 + m_z^4 \right) , \tag{2.7}$$

and thus expresses the first-order cubic anisotropy in Eq. (2.7) as a linear combination of second-order uniaxial anisotropies along the Cartesian axes given in Eq. (2.1). Figure 2.2 shows the free energy density surfaces with $K_{\mathrm{c}} > 0$ (c) and therefore magnetic easy axes along the $\langle 100 \rangle$ directions, and with $K_{\mathrm{c}} < 0$ (d) and thus magnetic easy axes along the $\langle 111 \rangle$ directions.

2.3 Contributions to the magnetic free energy density

We now introduce the relevant magnetic anisotropy contributions to the total free energy density F of the ferromagnetic material systems investigated. We note that we here refer to F as the free energy density as commonly done in the literature. Correctly, this energy should be denoted as free enthalpy density (also known as Gibbs free energy density) $G = F + p - \mu_0 M H$, where p and M are the pressure and the magnetization, respectively [100, 101]. The total differential of this thermodynamic potential yields $\mathrm{d}G = -S\mathrm{d}T + \mathrm{d}p - \mu_0 M \mathrm{d}H$, with the entropy per unit volume S and the temperature T. The free enthalpy density G, which exhibits the natural variables T, p, and H, thus is the potential that is minimized when a system reaches equilibrium at constant temperature and external magnetic field. Therefore, the free enthalpy represents the energy which evidently meets the experimental conditions.

2.3.1 Zeeman interaction

The Zeeman energy density [100]

$$F_{\mathrm{Zeeman}} = -\mu_0 \mathbf{H} \cdot \mathbf{M}, \tag{2.8}$$

is the magnetostatic energy density of the magnetization in an external magnetic field. This term is the only contribution dependent on the external field, which—to be precise—cannot be considered as an anisotropy contribution, since in the absence of further contributions to the total free energy density and at $H = 0$ no anisotropy prevails.

2.3.2 Shape anisotropy

The discontinuity of the magnetization at the surface of a ferromagnetic sample results in a divergence of $\mathbf{M}$, $\nabla \cdot \mathbf{M} \neq 0$. Maxwell's equation $\nabla \cdot \mathbf{B} = 0$ and thus $\nabla \cdot \mathbf{H} = -\nabla \cdot \mathbf{M}$ can only be fulfilled due to the presence of an equal and opposite divergence of $\mathbf{H}$ [99]. This resulting magnetic field is termed the demagnetizing field $\mathbf{H}_{\mathrm{demag}}$ and arises from (fictive) magnetic surface poles. Hence, this field originates from magnetic dipolar interactions, as evident from the simple analogy of compass needles in Fig. 2.1. The corresponding free energy density contribution [107, 108]

$$F_{\mathrm{demag}} = \frac{1}{2}\mu_0 \mathbf{M} \cdot \mathbf{N} \cdot \mathbf{M} \tag{2.9}$$

is referred to as shape anisotropy or demagnetization contribution, where $\mathbf{N}$ is the sample shape-dependent demagnetization tensor. For a thin film, as discussed in this work, all tensor components are zero except for the direction perpendicular to the film $N_\perp = 1$. Assuming a thin film in the (001) plane results in

$$F_{\mathrm{demag}} = \frac{1}{2}\mu_0 M_{\mathrm{s}}^2 m_z^2. \tag{2.10}$$

This situation is depicted in Fig. 2.2(a), with the shape anisotropy describing a uniaxial anisotropy with a magnetic hard axis perpendicular to the film plane. Thus shape anisotropy favors an in-plane orientation of the magnetization.

2.3.3 Magnetocrystalline anisotropy

In a crystal lattice, the orbital motion of the electrons is subjected to a crystal electric field, which reflects the symmetry of the crystal. Furthermore, due to spin-orbit-coupling the magnetic moments couple to the orbital motion of the electrons and thus to the crystal axes. Hence, the symmetry of the crystal influences the spontaneous magnetization, which energetically prefers certain orientations [100, 109].

Since all ferromagnetic materials discussed in this thesis crystallize in the cubic structure, the magnetocrystalline anisotropy contribution is described in lowest order via [cf. Eq. (2.7)]

$$F_{\mathrm{c}} = -\frac{1}{2}K_{\mathrm{c}}\left(m_x^4 + m_y^4 + m_z^4\right). \tag{2.11}$$

Tetragonal distortion of the lattice due to epitaxial growth of a cubic material may require a splitting into contributions perpendicular to the film plane and within the film plane (e.g., $Ga_{1-x}Mn_xAs$ on GaAs) [110, 111]:

$$F_{\mathrm{c}} = -\frac{1}{2}K_{\mathrm{c}}^{\perp} m_z^4 - \frac{1}{2}K_{\mathrm{c}}^{\parallel}\left(m_x^4 + m_y^4\right). \tag{2.12}$$

Note that for ferromagnetic materials with a comparably large saturation magnetization M_s, e.g., Fe_3O_4 on MgO, a single magnetocrystalline anisotropy constant K_c is sufficient to model the experimental findings, since a splitting into $K_\mathrm{c}^\perp$ and $K_\mathrm{c}^\parallel$ only results in a small correction $(K_\mathrm{c}^\perp - K_\mathrm{c}^\parallel)$ to the large out-of-plane shape anisotropy contribution.

2.3.4 Magnetoelastic anisotropy

A contribution to the energy density also stems from the coupling between the magnetization direction and elastic deformation. This so-called magnetostrictive coupling refers to a ferromagnetic specimen subjected to a magnetic field, which changes its dimensions due to the process of magnetization. The resulting magnetostrictive strains are usually small, reaching saturation values $\lambda = \Delta l/l$ in the order of 10^{-5} for, e.g., Fe and Fe_3O_4 [112, 113], but can reach values over 10^{-3} for alloys containing $4f$ elements, e.g., FeTb [114].

The inverse effect—called the converse magnetostrictive or Villari effect—describes the influence of elastic strain on the magnetization direction [104, 115, 116]. The magnetoelastic energy density for a cubic system to first order is given by [104]

$$\begin{aligned} F_\mathrm{magel} &= B_1 \left[\epsilon_1 \left(m_x^2 - \frac{1}{3} \right) + \epsilon_2 \left(m_y^2 - \frac{1}{3} \right) + \epsilon_3 \left(m_z^2 - \frac{1}{3} \right) \right] \\ &\quad + B_2 \left(\epsilon_4 m_y m_z + \epsilon_5 m_x m_z + \epsilon_6 m_x m_y \right), \end{aligned} \tag{2.13}$$

where m_i again denote the direction cosines of the magnetization with respect to the cubic axes, B_i are the magnetoelastic coupling coefficients, and the uniaxial strains ϵ_i are expressed in matrix notation (see Sec. 3.1). The application of stress will deform the crystal until the magnetoelastic energy F_magel is balanced by the elastic energy F_el [Eq. (3.6)]. Hence, the equilibrium strains are obtained by minimizing the energy

$$F = F_\mathrm{magel} + F_\mathrm{el}, \tag{2.14}$$

which are used to define the relations between the so-called magnetostriction constants λ_{100}, λ_{111} and B_1, B_2 [104]:

$$\lambda_{100} = -\frac{2}{3} \frac{B_1}{(c_{11} - c_{12})}, \qquad \lambda_{111} = -\frac{1}{3} \frac{B_2}{c_{44}}. \tag{2.15}$$

The magnetostriction constants λ_{100} (λ_{111}) given here are defined as the strains measured along [100] ([111]) due to the magnetization along [100] ([111]), starting from a demagnetized state.

For polycrystalline ferromagnetic materials, the magnetostriction is isotropic, calculated by averaging the magnetostrictive strains for different crystal orientations, and thus [104]

$$\bar{\lambda} = \frac{2}{5} \lambda_{100} + \frac{3}{5} \lambda_{111}. \tag{2.16}$$

Chapter 3

Elastic theory

In this chapter, we address the theoretical background regarding the elastic properties of solids. We start with a review of some fundamental aspects of stress, strain, and the related elastic energy density. We then introduce ferromagnetic thin film/piezoelectric actuator hybrid systems as a device concept to realize a voltage-controllable strain in ferromagnetic thin films. We here focus on the piezoelectric constituent, and compile its physical properties and impact on the elastic properties of the affixed ferromagnetic thin films. Finally, particular strain tensors of relevance for this work are derived, as a precise determination of the structural properties is mandatory for a comprehensive and detailed investigation of the voltage controlled magnetic properties in the magnetoelastic framework.

3.1 Stress and strain in solids

In this section, the concept of stress and strain is introduced, following Nye [117]. Generally speaking, a body is in a state of stress if forces are acting on it. Considering a volume element (Fig. 3.1) within a stressed body, we can distinguish between two types of forces: (1) body-forces (e.g., gravity), whose magnitudes are proportional to the *volume* of the element and (2) forces exerted on the surface proportional to the *area* of the surface. The latter, related to a unit area of surface on which they act on, are referred to as stress. In the following, we restrict our discussion to a body in static equilibrium with homogeneous stress throughout the body, thus body-forces or body-torques are not present. Considering a cubic element as illustrated in Fig. 3.1, the stress σ_{ij} denotes a force $\mathbf{F}_i$ in $+\mathbf{x}_i$ direction transmitted across that face of the cube with area A_j and the normal vector in $\mathbf{x}_j$ direction. The components σ_{ij} form the second-rank stress tensor

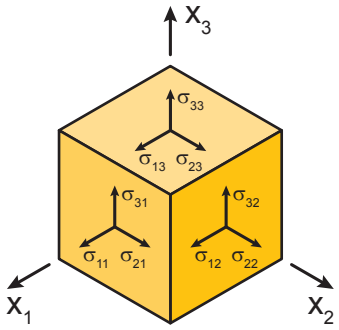

Fig. 3.1: Illustration of the components of stress acting on a cubic element.

$$\boldsymbol{\sigma} = \begin{pmatrix} \sigma_{11} & \sigma_{12} & \sigma_{13} \\ \sigma_{21} & \sigma_{22} & \sigma_{23} \\ \sigma_{31} & \sigma_{32} & \sigma_{33} \end{pmatrix}, \tag{3.1}$$

where the diagonal components σ_{11}, σ_{22}, and σ_{33} are the normal components and σ_{ij} with $i \neq j$ denote the shear components. The above given sign convention results in tensile stress for $\sigma_{ii} > 0$, whereas $\sigma_{ii} < 0$ yields a compressive stress. Due to the confinement to static equilibrium the nine tensor components σ_{ij} are not independent, since they have to meet the condition $\sigma_{ij} = \sigma_{ji}$. Thus we obtain a symmetric tensor with six independent components.

A solid body responds to an applied stress by a deformation. This change in shape is quantified by the strain $e_{ij} = \partial u_i / \partial x_j$, which is defined as a variation of the displacement u_i with position x_i in the body resolved along the x_j direction. In equivalence to the stress tensor $\boldsymbol{\sigma}$, these nine components form a tensor $\mathbf{e}$, whose geometric meaning can be illustrated as follows: (1) the diagonal elements e_{11}, e_{22}, and e_{33} are the relative extensions parallel to $\mathbf{x}_1$, $\mathbf{x}_2$, and $\mathbf{x}_3$, respectively, (2) e_{12} is the rotation about $\mathbf{x}_3$ towards $\mathbf{x}_1$, and (3) e_{21} is the rotation about $\mathbf{x}_3$ towards $\mathbf{x}_2$ (equivalent meanings apply to the other components e_{ij}). It can be shown that $\mathbf{e}$ comprises both the strain (symmetric part of $\mathbf{e}$) as well as a pure rotation of the body (antisymmetric part of $\mathbf{e}$). We therefore define the symmetric part of $\mathbf{e}$ as the strain tensor $\boldsymbol{\epsilon}$: $\epsilon_{ij} = \frac{1}{2}(e_{ij} + e_{ji})$, whose components ϵ_{ii} and $\epsilon_{ij,i\neq j}$ are denoted as *tensile strains* and *shear strains*, respectively.

In the elastic limit, the components of stress are linearly related to the components of strain, generally known as Hooke's law:

$$\sigma_{ij} = c_{ijkl}\epsilon_{kl} \quad \text{and} \quad \epsilon_{ij} = s_{ijkl}\sigma_{kl} \quad (i,j,k,l = 1,2,3), \tag{3.2}$$

where the c_{ijkl} and s_{ijkl} are the stiffness constants and compliance constants, respectively.

So far, we applied the so-called *tensor notation*. However, it can be shown that due to the symmetric nature of the tensors $\boldsymbol{\sigma}$ and $\mathbf{e}$ only 36 of the 81 components s_{ijkl} and c_{ijkl} are independent. Precisely, s_{ijkl} and c_{ijkl} are symmetric both in the first two and the last two suffixes, which allows for a considerable simplification: the so-called *matrix* or *Voigt notation*. The first two and the last two subscripts are contracted according to the following scheme:

tensor notation	11	22	33	23, 32	31, 13	12, 21
matrix notation	1	2	3	4	5	6

.

Hence, the stress and strain components undergo the following changes:

$$\begin{pmatrix} \sigma_{11} & \sigma_{12} & \sigma_{31} \\ \sigma_{12} & \sigma_{22} & \sigma_{23} \\ \sigma_{31} & \sigma_{23} & \sigma_{33} \end{pmatrix} \rightarrow \begin{pmatrix} \sigma_1 & \sigma_6 & \sigma_5 \\ \sigma_6 & \sigma_2 & \sigma_4 \\ \sigma_5 & \sigma_4 & \sigma_3 \end{pmatrix}, \quad \begin{pmatrix} \epsilon_{11} & \epsilon_{12} & \epsilon_{31} \\ \epsilon_{12} & \epsilon_{22} & \epsilon_{23} \\ \epsilon_{31} & \epsilon_{23} & \epsilon_{33} \end{pmatrix} \rightarrow \begin{pmatrix} \epsilon_1 & \frac{1}{2}\epsilon_6 & \frac{1}{2}\epsilon_5 \\ \frac{1}{2}\epsilon_6 & \epsilon_2 & \frac{1}{2}\epsilon_4 \\ \frac{1}{2}\epsilon_5 & \frac{1}{2}\epsilon_4 & \epsilon_3 \end{pmatrix}. \tag{3.3}$$

Now we can express the Equations (3.2) in the more convenient short form

$$\sigma_i = c_{ij}\epsilon_j \quad \text{and} \quad \epsilon_i = s_{ij}\sigma_j \quad (i,j = 1,2,\ldots,6). \tag{3.4}$$

The factor $\frac{1}{2}$ in the strain matrix (3.3) is introduced to avoid additional factors of 2 in the Eqs. (3.4) [117, 118].

3.2 Elastic energy

In the special case of the cubic class, only three independent elastic constants are required to describe the elastic properties:

$$\mathbf{c} = \begin{pmatrix} c_{11} & c_{12} & c_{12} & 0 & 0 & 0 \\ c_{12} & c_{11} & c_{12} & 0 & 0 & 0 \\ c_{12} & c_{12} & c_{11} & 0 & 0 & 0 \\ 0 & 0 & 0 & c_{44} & 0 & 0 \\ 0 & 0 & 0 & 0 & c_{44} & 0 \\ 0 & 0 & 0 & 0 & 0 & c_{44} \end{pmatrix}. \tag{3.5}$$

Hence the elastic energy density $F_{\mathrm{el}} = \frac{1}{2} c_{ij} \epsilon_i \epsilon_j$ [119] for a cubic crystal is given by [120–122]

$$F_{\mathrm{el}} = \frac{1}{2} c_{11} \left(\epsilon_1^2 + \epsilon_2^2 + \epsilon_3^2 \right) + c_{12} \left(\epsilon_1 \epsilon_2 + \epsilon_2 \epsilon_3 + \epsilon_1 \epsilon_3 \right) + \frac{1}{2} c_{44} \left(\epsilon_4^2 + \epsilon_5^2 + \epsilon_6^2 \right). \tag{3.6}$$

3.3 Voltage control of strain

3.3.1 Piezoelectric effect

Piezoelectric materials are a class of low-symmetry non-centrosymmetric materials that can be polarized by application of a mechanical stress [117, 123]. The linear relationship between a stress applied to the piezoelectric material and the resulting polarization charge per unit area is referred to as *direct* piezoelectric effect. The polarization expressed in matrix notation is then given by

$$P_i = d_{ij} \sigma_j \quad (i = 1, 2, 3; j = 1, 2, \ldots, 6), \tag{3.7}$$

where the d_{ij} are the piezoelectric coefficients. Furthermore, piezoelectric materials change their dimensions when an electric Field E is applied. This is denoted as *converse* piezoelectric effect and the resulting strain developed in the piezoelectric due to the applied electric field yields

$$\epsilon_j = d_{ij} E_i \quad (i = 1, 2, 3; j = 1, 2, \ldots, 6). \tag{3.8}$$

The piezoelectric coefficients measured parallel and perpendicular to the electric field are denoted as longitudinal and transverse coefficients, respectively. Examples of piezoelectric materials are quartz (SiO_2), zinc oxide (ZnO), and lead zirconate titanate (PZT). Values of d range from 2 pm/V to > 2000 pm/V in SiO_2 and $\mathrm{Pb\,(Mg, Nb)\,O_3 - PbTiO_3}$ (PMN-PT) single crystals, respectively [123].

Polar materials exhibit a spontaneous polarization, i.e., an electric dipole moment even in the absence of an external electric field. Ferroelectrics are a special case of polar materials, e.g., barium titanate (BTO) and PZT, that possess at least two equilibrium orientations of the spontaneous polarization and in which the direction of the spontaneous polarization can be switched by an external electric field. The crystal

symmetry requires that all ferroelectric materials must be piezoelectric. However, in analogy to ferromagnetics the spontaneous polarization in a ferroelectric is usually not uniformly aligned throughout the material along the same direction. Most of the ferroelectric materials of practical interest have a perovskite structure, such as PZT [124], resulting in six equivalent directions for the spontaneous polarization in the ferroelectric tetragonal state. Hence, ferroelectric domains form to minimize the electrostatic energy of depolarizing fields and the elastic energy, depending on the electrical and mechanical constraints imposed on the material while cooled through the paraelectric-ferroelectric phase transition [123].

3.3.2 Device concept

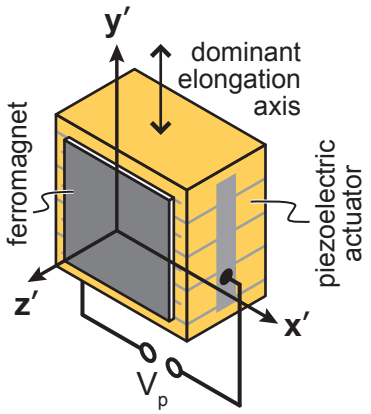

Fig. 3.2: Schematic illustration of a ferromagnetic thin film/piezoelectric actuator hybrid with the $\{\mathbf{x}', \mathbf{y}', \mathbf{z}'\}$ actuator coordinate system.

Figure 3.2 shows the concept of a ferromagnetic thin film/piezoelectric actuator hybrid, which are used to exert a voltage-controlled stress on the ferromagnetic thin film. We use commercially available $\mathrm{Pb}\,(\mathrm{Zr}_x\mathrm{Ti}_{1-x})\,\mathrm{O}_3$ (PZT) poled piezoelectric stack actuators with a size of $x' \times y' \times z' = 3 \times 5 \times 2\,\mathrm{mm}^3$ as the piezoelectric constituent. The co-fired multilayer actuators comprise an alternating approx. 100 μm thick polycrystalline PZT-ceramic/AgPd electrode layers structure [125]. The ferromagnetic film is affixed to the actuator either via cementing using a two-component epoxy [126, 127], or by direct deposition through a shadow mask using electron beam evaporation.

The application of a voltage $V_\mathrm{p} \neq 0\,\mathrm{V}$ results in a deformation of the piezoelectric actuator and thus allows to induce electrically tunable strain in the adjacent ferromagnetic film, since the latter is "rigidly" affixed on the $\mathbf{x}' - \mathbf{y}'$ face of the actuator. Upon the application of a positive (negative) voltage V_p, the actuator expands (contracts) along the dominant elongation direction $\mathbf{y}'$. In particular, a voltage $V_\mathrm{p} > 0$ ($V_\mathrm{p} < 0$) results in an elongation with a related uniaxial strain $\epsilon_2' > 0$ (contraction with $\epsilon_2' < 0$) along $\mathbf{y}'$. Due to elasticity, this tensile (compressive) strain is accompanied by compressive strains $\epsilon_1', \epsilon_3' < 0$ (tensile strains $\epsilon_1', \epsilon_3' > 0$) along the orthogonal in-plane direction $\mathbf{x}'$ and the orthogonal out-of-plane direction $\mathbf{z}'$. Unless stated otherwise, the cubic crystal coordinate system with the [100], [010], and [001] directions of the crystal are denoted by $\mathbf{x}$, $\mathbf{y}$, and $\mathbf{z}$, respectively, whereas the principal elongation axes of the actuator are indicated by $\mathbf{x}'$, $\mathbf{y}'$, and $\mathbf{z}'$, respectively.

Figure 3.3(a) depicts the strain $\epsilon_2'\,(V_\mathrm{p})$ in a PZT actuator (sample A) along $\mathbf{y}'$ in the voltage range of $|V_\mathrm{p}| \leq 150\,\mathrm{V}$, which corresponds to an electric field range of $|E_\mathrm{p}| \lesssim 15\,\mathrm{kV/cm}$, measured at room temperature using a strain gauge [128]. The recorded $\epsilon\,(V_\mathrm{p})$ hysteresis loop is characteristic for ferroelectrics and denoted as the butterfly loop. The simultaneously recorded current $I\,(V_\mathrm{p})$ [Fig. 3.3(b)] exhibits two distinct peaks at minimum strain in Fig. 3.3(a), referred to as depolarization or

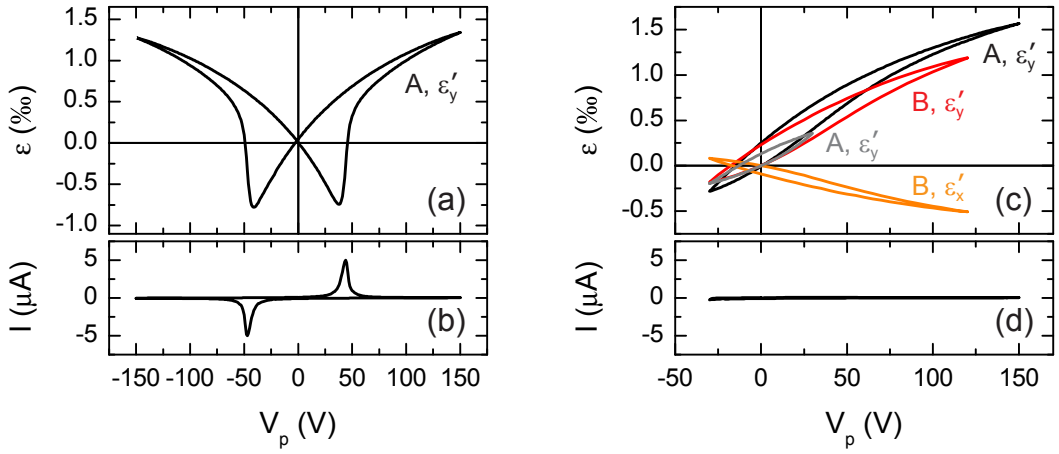

Figure 3.3: (a) $\epsilon_2'(V_\mathrm{p})$ hysteresis loop of a PZT piezoelectric actuator (sample A). (b) The two peaks in the corresponding $I(V_\mathrm{p})$ curve are due to polarization switching. (c) $\epsilon(V_\mathrm{p})$ loops under nonswitching condition. Displayed are the $\epsilon_2'(V_\mathrm{p})$ (black) and the $\epsilon_2'(V_\mathrm{p})$ Rayleigh loops (gray) of sample A, and the $\epsilon_2'(V_\mathrm{p})$ (red) and $\epsilon_1'(V_\mathrm{p})$ (orange) curves of sample B. (d) The $I(V_\mathrm{p})$ curve exhibits no distinct peaks, as the macroscopic polarization orientation is retained. All data were recorded at room temperature using strain gauges.

switching current. They indicate a ferroelectric polarization reversal. The hysteresis loop is due to three types of effects, namely the normal converse piezoelectric effect of the lattice, combined with switching and movement of ferroelectric domain walls [129]. The former is the intrinsic contribution of the linear piezoelectrically induced strain [cf. Eq. (3.8)], whereas the latter two are of extrinsic origin, mainly due to non-180° domains walls and strongly nonlinear and hysteretic [129–132]. The piezoelectric response of ferroelectric PZT ceramics is dominated by domain-wall contributions [131].

To induce a voltage-controlled strain in the ferromagnetic thin films, the piezoelectric actuators are operated in the semi-bipolar regime $-30\,\mathrm{V} \leq V_\mathrm{p} \leq +150\,\mathrm{V}$ at room temperature with a nominal maximum strain $\epsilon_2' = 1.3 \times 10^{-3}$ [133]. Exemplarily, Fig. 3.3(c) shows the $\epsilon_2'(V_\mathrm{p})$ curve for sample A (black). As apparent from the $I(V_\mathrm{p})$ curve in Fig. 3.3(d), the polarization orientation is retained in this operation mode, and thus no switching of the macroscopic polarization occurs. Evidently, the actuator expansion exhibits a nonlinear and hysteretic piezoelectric response. As we will explicitly utilize this property in Sec. 5.7, we here shortly summarize the physical origin of this important characteristic of ferroelectric materials. In the subswitching limit, i.e., at electric fields below the coercive field, hysteresis loops in ferroelectric materials can be very well described by the Rayleigh law [131, 134, 135], and are thus referred to as Rayleigh loops [e.g., gray curve in Fig. 3.3(c)]. Under this condition, the external field induces only vibrations or small displacements of the domain walls, but the overall domain structure is preserved [136]. Generally, the Rayleigh behavior is observed due to a combination of reversible and irreversible domain-wall displacements [131, 137, 138], when domain walls move in the form of small Barkhausen jumps controlled by randomly distributed defects. These act as

pinning centers, which introduce irregular perturbations of the potential energy for domain wall motion [131, 139, 140]. Hence, for small electric fields the domain-wall movement is reversible (nonhysteretic) around an equilibrium position, i.e., at the minimum of a potential well, but nonlinear. When the driving field is sufficiently large to overcome potential barriers and thus to depin domain walls, an irreversible (hysteretic) and nonlinear domain-wall displacement into a new equilibrium position occurs [129, 131]. Although we usually operate our piezoelectric actuators beyond the subcoercive regime [see, e.g., black curve in Fig. 3.3(c)] and thus the shape slightly deviates from a classical Rayleigh loop [gray curve in Fig. 3.3(c)], we meet the nonswitching condition. Hence, the hysteretic stroke in the semi-bipolar voltage regime can be analogously explained.

Regarding the ferromagnetic/piezoelectric hybrid device concept to induce strain in thin films, the strains ϵ_i' $(i = 1, 2, 3)$ are not independent. As will be shown in the following, only one of the strains ϵ_i' remains independent. Due to the actuator's elastic properties, the in-plane strains ϵ_1' and ϵ_2' are related via the Poisson ratio ν according to

$$\epsilon_1' = -\nu\epsilon_2'. \tag{3.9}$$

We use the Poisson ratio of the actuator $\nu = \nu_{\text{piezo}}$, assuming that the strains are transmitted from the actuator into the sample in such a way that the Poisson ratio of the strained sample coincides with the one of the actuator. This is reasonable, as in the experiments the samples with a maximum thickness of about 100 μm are orders of magnitude thinner than the 2 mm thick piezoelectric actuators. The Poisson ratio $\nu_{\text{piezo}} = -d_{31,\text{piezo}}/d_{33,\text{piezo}} = 0.45$ is determined from the piezoelectric coefficients of the actuator $d_{31,\text{piezo}} = -290\,\text{pm/V}$ and $d_{33,\text{piezo}} = +640\,\text{pm/V}$. For illustration, Fig. 3.3(c) shows $\epsilon\,(V_\text{p})$ loops of sample B along $\mathbf{y}'$ (red) and $\mathbf{x}'$ (orange), which are in exact agreement with the given Poisson ratio. Moreover, no stress is applied perpendicular to the film plane. Thus, the out-of-plane strain is found by minimizing the energy density with respect to ϵ_3', i.e., $\sigma_3' = \partial\left(F_\text{el} + F_\text{magel}\right)/\partial\epsilon_3' = 0$ [141] (cf. Sec. 2.3.4). Thus, using Eqs. (3.6) and (2.13) yields

$$\epsilon_3' = -\frac{c_{12}}{c_{11}}\left(\epsilon_1' + \epsilon_2'\right) - \frac{B_1}{c_{11}}\left(m_z'^2 - \frac{1}{3}\right). \tag{3.10}$$

Hence, Eqs. (3.9) and (3.10) show that measuring one strain component ϵ_i' $(i = 1, 2, 3)$ is sufficient to fully determine the strain tensor of the ferromagnetic films. We will utilize this in the following chapters by either recording ϵ_2' using strain gauges or ϵ_3' via high resolution x-ray diffraction.

3.4 Strain tensor

In the following, we derive the strain tensor for a cubic (001)-oriented ferromagnetic thin film with $\mathbf{z} \parallel \mathbf{z}'$, rotated about the out-of-plane [001] direction $\mathbf{z}$ by an angle γ with respect to the $\{\mathbf{x}', \mathbf{y}', \mathbf{z}'\}$ coordinate system of the actuator [Fig. 3.4(a)]. The aim hereby is to express the strain tensor solely as a function of the strain component ϵ_2', which is a function of the applied voltage to the actuator V_p along the actuator's

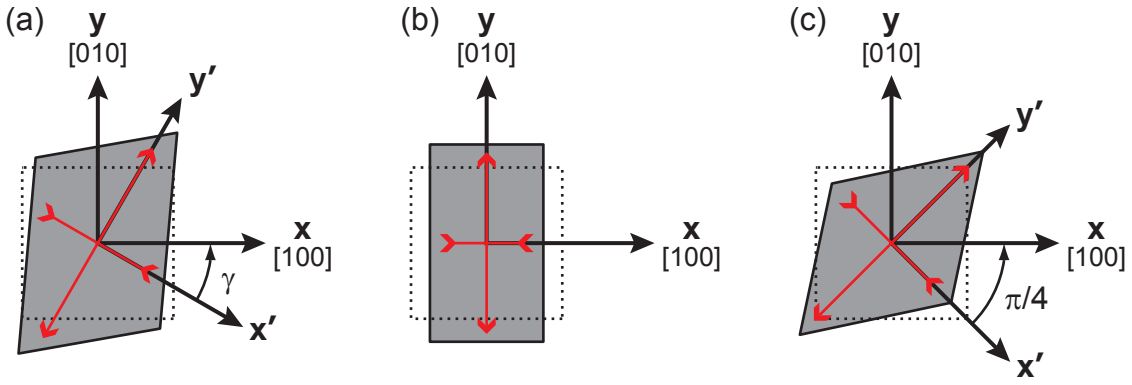

Figure 3.4: Cubic cell (dotted line) exposed to a stress in the $\mathbf{x}-\mathbf{y}$ film plane. The $\{\mathbf{x},\mathbf{y},\mathbf{z}\}$ coordinate system denotes the crystal coordinate system, whereas the $\{\mathbf{x}',\mathbf{y}',\mathbf{z}'\}$ coordinate system indicates the actuator coordinate system. (a) General case with the thin film rotated by an angle γ with respect to the actuator coordinate system. Relevant special cases are shown for (b) $\gamma = 0$ and (c) $\gamma = \pi/4$.

dominant elongation axis $\mathbf{y}'$. The strain induced in the film by the piezoelectric actuator in the $\{\mathbf{x}',\mathbf{y}',\mathbf{z}'\}$ coordinate system is given by the strain tensor

$$\boldsymbol{\epsilon}' = \begin{pmatrix} \epsilon_1' & 0 & 0 \\ 0 & \epsilon_2' & 0 \\ 0 & 0 & \epsilon_3' \end{pmatrix}, \tag{3.11}$$

with the diagonal components denoting the strains along the elongation axes of the actuator $\mathbf{x}'$, $\mathbf{y}'$, and $\mathbf{z}'$. All other components vanish, since in this coordinate system no shear strains are present. To obtain the corresponding crystal strains, i.e., the strains in the crystal coordinate system, we apply a tensor transformation into the $\{\mathbf{x},\mathbf{y},\mathbf{z}\}$ coordinate system [106, 141, 142] using the transformation matrix

$$\mathbf{T}(\gamma) = \begin{pmatrix} \cos(\gamma) & \sin(\gamma) & 0 \\ -\sin(\gamma) & \cos(\gamma) & 0 \\ 0 & 0 & 1 \end{pmatrix}. \tag{3.12}$$

Note that we have to return to the tensor notation to perform the transformation, which yields

$$\begin{aligned} \boldsymbol{\epsilon} &= \mathbf{T}(\gamma)\cdot\boldsymbol{\epsilon}'\cdot\mathbf{T}(\gamma)^{-1} \\ &= \begin{pmatrix} \frac{1}{2}(\epsilon_1'+\epsilon_2') + \frac{1}{2}(\epsilon_1'-\epsilon_2')\cos(2\gamma) & -\frac{1}{2}(\epsilon_1'-\epsilon_2')\sin(2\gamma) & 0 \\ -\frac{1}{2}(\epsilon_1'-\epsilon_2')\sin(2\gamma) & \frac{1}{2}(\epsilon_1'+\epsilon_2') - \frac{1}{2}(\epsilon_1'-\epsilon_2')\cos(2\gamma) & 0 \\ 0 & 0 & \epsilon_3' \end{pmatrix}. \end{aligned} \tag{3.13}$$

Since the film is mechanically free on the upper surface, the stresses σ_3, σ_4, and σ_5 are zero. The corresponding strains can then be deduced according to the mechanical equilibrium condition $\sigma_i = \partial\left(F_{\mathrm{el}} + F_{\mathrm{magel}}\right)/\partial\epsilon_i = 0$ $(i = 3,4,5)$ [cf. Eq. (3.10)]. Substituting these strains into Eq. (3.13) and furthermore considering the relation

given in Eq. (3.9), we finally obtain the strain components in the $\{\mathbf{x}, \mathbf{y}, \mathbf{z}\}$ crystal coordinate system as a function of ϵ_2':

$$\begin{aligned}
\epsilon_1 &= \epsilon_{11} = -\frac{1}{2}\left[-1+\nu+(1+\nu)\cos(2\gamma)\right]\epsilon_2', \\
\epsilon_2 &= \epsilon_{22} = \frac{1}{2}\left[1-\nu+(1+\nu)\cos(2\gamma)\right]\epsilon_2', \\
\epsilon_3 &= \epsilon_{33} = -\frac{c_{12}}{c_{11}}(1-\nu)\,\epsilon_2' - \frac{B_1}{c_{11}}\left(m_z^2-\frac{1}{3}\right), \\
\epsilon_4 &= -\frac{B_2}{c_{44}} m_y m_z, \\
\epsilon_5 &= -\frac{B_2}{c_{44}} m_x m_z, \\
\epsilon_6 &= 2\epsilon_{12} = (1+\nu)\sin(2\gamma)\,\epsilon_2'.
\end{aligned} \tag{3.14}$$

Since for typical values of the parameters in Eqs. (3.14) the terms B_1/c_{11} and B_2/c_{44} are two orders of magnitude smaller than the involved strains ($\frac{B_1}{c_{11}} \approx \frac{B_2}{c_{44}} \sim 10^{-5} \ll \epsilon_2' \sim 10^{-3}$), they are thus omitted in the following.

In the subsequent sections, we discuss special cases of these strain components relevant for this thesis. In particular, we consider a film strained along the cubic axes, i.e., along $\langle 100 \rangle$, and a film strained along the $\langle 110 \rangle$ directions in the film plane.

3.4.1 $\langle 100 \rangle$-strained films

First we consider a situation with the crystalline cubic axes aligned along the actuator's elongation axes ($\mathbf{x}$, $\mathbf{y}$, and $\mathbf{z}$ parallel to $\mathbf{x}'$, $\mathbf{y}'$, and $\mathbf{z}'$, respectively), as shown in Fig. 3.4(b). In this case, the resulting deformation is fully described by the principal strain tensor components, while no shear strains are present. As it will be required in the following chapters, we express the strain components as a function of both ϵ_2' and ϵ_3'. Thus, Eqs. (3.14) yield

$$\begin{aligned}
\epsilon_1 &= -\nu\epsilon_2' \\
&= \frac{c_{11}}{c_{12}}\frac{\nu}{(1-\nu)}\epsilon_3', \\
\epsilon_2 &= \epsilon_2' \\
&= -\frac{c_{11}}{c_{12}}\frac{1}{(1-\nu)}\epsilon_3', \\
\epsilon_3 &= -\frac{c_{12}}{c_{11}}(1-\nu)\,\epsilon_2' \\
&= \epsilon_3', \\
\epsilon_4 &= \epsilon_5 = \epsilon_6 = 0.
\end{aligned} \tag{3.15}$$

3.4.2 ⟨110⟩-strained films

We now address a (001)-oriented cubic crystalline sample with the stresses applied along the ⟨110⟩ directions in the film plane. This situation for $\gamma = +\pi/4$ is illustrated in Fig. 3.4(c). According to the previous subsection, we here also express the strain components as a function of both ϵ_2' and ϵ_3':

$$\begin{aligned}
\epsilon_1 &= \frac{1}{2}(1-\nu)\,\epsilon_2' \\
&= -\frac{1}{2}\frac{c_{11}}{c_{12}}\epsilon_3', \\
\epsilon_2 &= \frac{1}{2}(1-\nu)\,\epsilon_2' \\
&= -\frac{1}{2}\frac{c_{11}}{c_{12}}\epsilon_3', \\
\epsilon_3 &= -\frac{c_{12}}{c_{11}}(1-\nu)\,\epsilon_2' \\
&= \epsilon_3', \\
\epsilon_4 &= \epsilon_5 = 0, \\
\epsilon_6 &= (1+\nu)\,\epsilon_2' \\
&= -\frac{c_{11}}{c_{12}}\frac{(1+\nu)}{(1-\nu)}\epsilon_3'.
\end{aligned} \tag{3.16}$$

Chapter 4

Experimental Techniques

Several complementary experimental techniques are used to investigate the magnetic properties and thus to detect the voltage-controlled magnetization manipulation in our multifunctional hybrids [143, 144]. Ferromagnetic resonance (FMR) spectroscopy allows to sensitively and quantitatively measure the dynamic magnetic response. FMR experiments provide a means to directly deduce the contributions to the free energy density. Hence this technique is the preferred method to quantitatively determine the magnetic anisotropy [145]. However, as FMR spectroscopy is not applicable to directly measure or image the magnetization, superconducting quantum interference device (SQUID) magnetometry and magneto-optical Kerr effect (MOKE) spectroscopy are employed to investigate the magnetization. These detect the static magnetic response and are sensitive to the magnetization itself. SQUID magnetometry allows to quantitatively determine the (integral) magnetization with high precision [105]. Analogous quantitative measurements using MOKE spectroscopy are rather tedious, since the Kerr signal is proportional to the magnetization but the magnetization magnitude has little or no influence. However, MOKE spectroscopy is a very versatile tool in modern magnetic materials research, as it allows for, e.g., spatially resolved imaging and time-resolved magnetometry [146]. To address the electrical transport properties of ferromagnets, magnetotransport is a powerful experimental tool. In particular, since the anisotropic magnetoresistance (AMR) links the electrical resistance and the magnetization orientation [110], magnetoresistance allows to probe both magnetic anisotropy and the magnetization orientation.

As we aim for a voltage-controlled magnetization manipulation in the ferromagnetic/piezoelectric hybrids via the elastic channel, a direct correlation between structural and magnetic properties is mandatory. High-resolution x-ray diffraction (HR-XRD) is used to quantify the variation in lattice constants and thus to determine strains in the samples.

In the following sections, we summarize the important experimental and theoretical aspects of the experimental techniques relevant for this thesis. More thorough treatments can be found in Refs. [100, 108, 147–149].

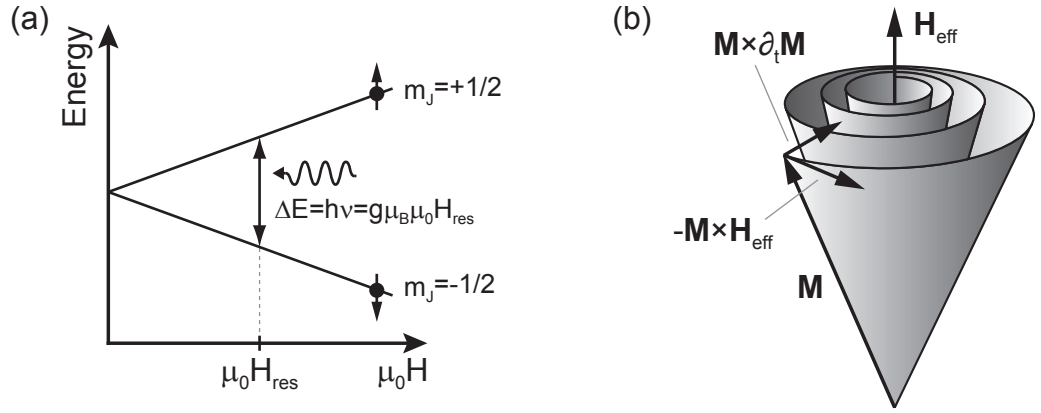

Figure 4.1: (a) Schematic diagram of EPR/FMR. The Zeeman effect leads to a splitting of a twofold degenerate energy level with $J = 1/2$. (b) Damped precession of the magnetization about the effective magnetic field $\mathbf{H}_{\text{eff}}$ [109].

4.1 Ferromagnetic resonance spectroscopy

4.1.1 Basic principle of FMR

We start the discussion of magnetic resonance considering the simple case of isolated atoms. We thus first neglect any internal fields and anisotropy fields. In terms of quantum mechanics, the application of a static external magnetic field $\mathbf{H}$ to an isolated atom with magnetic moment $\boldsymbol{\mu}_J$ leads to an energy splitting of the eigenstates characterized by the magnetic quantum number m_J (Zeeman splitting). For a twofold degenerate energy level with $J = 1/2$, this situation is schematically illustrated in Fig. 4.1(a). The corresponding energy eigenvalues E_J are given by

$$E_J = -\mu_0 \boldsymbol{\mu}_J \cdot \mathbf{H} = g_J \mu_B m_J \mu_0 H, \tag{4.1}$$

with the g-factor g_J and the Bohr magneton μ_B. The irradiation with an alternating electromagnetic field with magnetic component $\mathbf{H}_{\text{rf}}(t) = \mathbf{H}_{\text{rf}} \sin(\omega t)$ perpendicular to $\mathbf{H}$ can induce magnetic dipole transitions ($\Delta m_J = \pm 1$) between the energy eigenstates, if the microwave frequency $\nu = \omega/2\pi$ fulfills the condition

$$h\nu = \Delta E = g_J \mu_B \mu_0 H. \tag{4.2}$$

Considering the magnetic fields typically achievable with electromagnets results in transition frequencies in the radio-frequency (rf) microwave regime, i.e., ν typically lies in the GHz range. The resonant absorption of a microwave field in a system of uncoupled magnetic moments is referred to as electron paramagnetic resonance (EPR) [150], and the corresponding magnetic field is denoted as H_{res}.

Ferromagnetic resonance (FMR) denotes the resonant absorption of microwave radiation in a system of magnetic moments coupled by exchange interaction [109, 145, 151–154]. Because of the large quantum numbers involved in the transition between the energy eigenstates, the resonance phenomenon can be described in a classical picture. The externally applied magnetic field generates a torque acting on

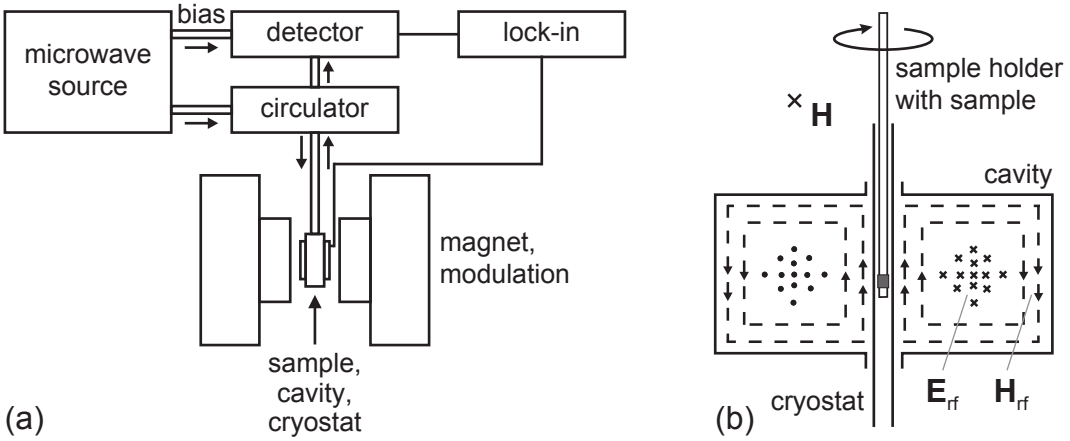

Figure 4.2: (a) Schematic view of the FMR setup [156] and the TE_{102} microwave cavity [157], showing the orientation of the microwave magnetic ($\mathbf{H}_{\mathrm{rf}}$) and electric ($\mathbf{E}_{\mathrm{rf}}$) field, with $\mathbf{H}_{\mathrm{rf}}$ being perpendicular to the static magnetic field $\mathbf{H}$.

the magnetization, resulting in a precession about the magnetic field [Fig. 4.1(b)]. Unlike in EPR, the magnetization does not precess about the externally applied magnetic field but around an effective magnetic field $\mathbf{H}_{\mathrm{eff}}$, which comprises both the external magnetic field $\mathbf{H}$ and additional internal fields due to exchange interaction $\mathbf{H}_{\mathrm{exchange}}$ and anisotropy $\mathbf{H}_{\mathrm{aniso}}$:

$$\mathbf{H}_{\mathrm{eff}} = \mathbf{H} + \mathbf{H}_{\mathrm{exchange}} + \mathbf{H}_{\mathrm{aniso}}. \tag{4.3}$$

Hence, the energy of a transverse microwave rf-field is absorbed when the rf-frequency coincides with the precession frequency, and the corresponding generalized resonance condition is given by

$$\omega = \gamma \mu_0 H_{\mathrm{eff}}, \tag{4.4}$$

with the gyromagnetic ratio $\gamma = g\mu_B/\hbar$.

The time-dependent evolution of the magnetization vector around the effective magnetic field is described by the Landau-Lifshitz-Gilbert (LLG) equation of motion [147, 155]

$$\frac{\partial \mathbf{M}}{\partial t} = -\gamma \mathbf{M} \times (\mu_0 \mathbf{H}_{\mathrm{eff}}) + \frac{G}{\gamma M_{\mathrm{s}}^2} \left(\mathbf{M} \times \frac{\partial \mathbf{M}}{\partial t} \right). \tag{4.5}$$

The last term describes the phenomenological Gilbert damping, with G being the Gilbert damping parameter and M_{s} the saturation magnetization. The damping term accounts for the energy dissipation and thus describes the relaxation of the magnetization orientation in direction of $\mathbf{H}_{\mathrm{eff}}$ [Fig. 4.1(b)]. Consequently, the damping term determines the linewidth of the resonance signal.

4.1.2 Experimental setup

Figure 4.2(a) schematically shows the Bruker ESP 300 spectrometer setup used for all measurements discussed in this thesis. The spectrometer operates in the X-band at a constant microwave frequency of $\nu_{\mathrm{MW}} = 9.3\,\mathrm{GHz}$. A water cooled electromagnet

is used to apply an external static magnetic field of $\mu_0 H \leq 1.4\,\mathrm{T}$. The microwave bridge is equipped with a Gunn-diode array generating microwave radiation with a power of $P_{\mathrm{MW}} < 200\,\mathrm{mW}$, which is fed into the microwave cavity via a circulator and rectangular wave guides. Critical coupling between the wave guide and the resonator is achieved via a mechanically tunable iris, such that out of resonance the microwave radiation is fully absorbed in the resonator. If the resonance condition [Eq. (4.4)] is met for a certain externally applied magnetic field, the sample also absorbs microwave radiation. This leads to a slight detuning of the resonator's impedance matching and hence to a reflection of a part of the microwave radiation in resonance. This part is then guided to the detection diode via the circulator. To optimize the sensitivity, the microwave radiation is split into two parts of equal power, with one part fed into the reference arm to bias the detection diode. The amplitude and the phase of the radiation in the bias arm can be adjusted independently, where the latter allows to perform the measurements either in absorption or dispersion, which corresponds to a measurement of the imaginary or the real part of the high-frequency susceptibility, respectively. All measurements discussed in the following were performed in absorption.

Within this thesis, we used a TE_{102} microwave resonator with a quality factor $Q = \nu_{\mathrm{MW}}/\Delta\nu \approx 4000$. The corresponding mode picture is shown in Fig. 4.2(b). The sample is mounted on a rotatable fused silica sample holder and located on the symmetry axis of the resonator, corresponding to a position of a maximum of the microwave magnetic field $\mathbf{H}_{\mathrm{rf}}$ and a node of the microwave electric field $\mathbf{E}_{\mathrm{rf}}$. The external static magnetic field $\mathbf{H}$ is parallel to $\mathbf{E}_{\mathrm{rf}}$ and perpendicular to $\mathbf{H}_{\mathrm{rf}}$, as required to fulfill the resonance condition. To further allow for temperature dependent measurements, a liquid-He gas-flow glass cryostat is installed on the symmetry axis of the resonator [Fig. 4.2(b)].

To enhance the signal-to-noise ratio, we use signal modulation and lock-in amplifier detection. To this end, the externally applied DC field $\mu_0 H$ is superimposed by an alternating magnetic field $\mu_0 H_{\mathrm{mod}} = 3.2\,\mathrm{mT}$ with the modulation frequency $\nu_{\mathrm{mod}} = 100\,\mathrm{kHz}$.

4.1.3 Resonance lineshape

The lineshape of the microwave absorption signal can be determined by solving the Landau-Lifshitz-Gilbert equation [Eq. (4.5)], which results in a Lorentzian resonant microwave absorption $y\,(\mu_0 H)$ [109, 152]. Due to magnetic field modulation and lock-in detection, the detected signal is equivalent to the first derivative $y'\,(\mu_0 H)$ of the original absorption line (Fig. 4.3). The experimental features of the corresponding curve are the resonance field $\mu_0 H_{\mathrm{res}}$, the peak-to-peak linewidth $\mu_0 \Delta H_{\mathrm{pp}}$, and the peak-to-peak amplitude A_{pp}, as illustrated in Fig. 4.3. The integrated absorption signal $\int y\,(\mu_0 H)\,\mathrm{d}\,(\mu_0 H)$ corresponding to the area A in Fig. 4.3 is proportional to the ferromagnetic sample volume.

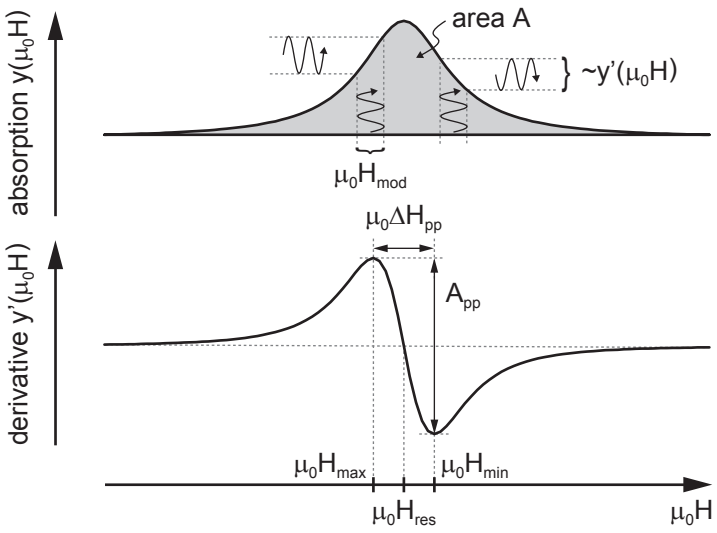

Figure 4.3: Lorentzian lineshape y of resonant microwave absorption and the corresponding signal y' detected using magnetic field modulation [156]. An explanation of the abbreviations is given in the text.

4.1.4 Determination of magnetic anisotropy from FMR

The resonance field of ferromagnetic resonance can be determined from the LLG equation [Eq. (4.5)] by solving the coupled differential equations for the time-dependent magnetization components [158–160]. The intensity, signal shape and resonance linewidth, i.e., all resonance signal characteristics can furthermore be deduced in this formalism. However, as the magnetic anisotropies can be derived from the resonance fields alone and we are mainly interested in the anisotropies for the characterization of the ferromagnetic/piezoelectric hybrids, we neglect the dynamical aspects of ferromagnetic resonance and only discuss $\mu_0 H_{\mathrm{res}}$ in the following. Compared to the vectorial formalism given by the LLG equation of motion, a mathematically simpler method to determine just the resonance field relies on the equation of motion being expressed as a function of the free energy density F instead of the effective field $\mathbf{H}_{\mathrm{eff}}$ [101, 161, 162]. The main advantage of the energy formulation is a straightforward calculation of magnetic anisotropies via the corresponding contributions to free energy, which can be deduced from symmetry considerations (cf. Chapter 2). In this regard, it has proven convenient to introduce polar coordinates, as shown in Fig. 4.4. The Cartesian axes are assumed to coincide with the $\langle 100 \rangle$ crystallographic directions. Capital Greek letters refer to the magnetization orientation $\mathbf{M}(\Theta, \Phi)$, while lower case letters denote the magnetic field direction $\mathbf{H}(\theta, \phi)$. This convention will be used for all FMR simulations throughout this thesis. The total free energy density, which is given in a generalized

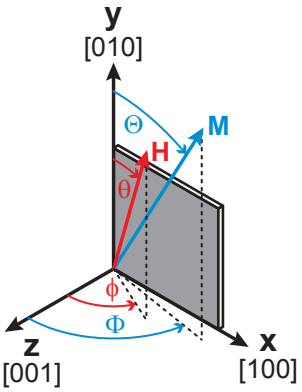

Fig. 4.4: Coordinate system defining the saturation magnetization $\mathbf{M}(\Theta, \Phi)$ and the magnetic field $\mathbf{H}(\theta, \phi)$ with respect to the sample.

form in Sec. 2.3 expressed as functions of the direction cosines, is now described by polar coordinates:

$$\begin{aligned} F\left(M,\Theta,\Phi,H,\theta,\phi\right) &= -\mu_0 H M \left(\sin\Theta\sin\Phi\sin\theta\sin\phi+\cos\Theta\cos\theta\right. \\ &\quad \left.+\sin\Theta\cos\Phi\sin\theta\cos\phi\right)+F_{\text{aniso}}\left(M,\Theta,\Phi\right), \end{aligned} \tag{4.6}$$

where the first term is the Zeeman energy and the second term comprises the anisotropy contributions. The energy formulation of the resonance condition is then given by [161, 163, 164]

$$\left(\frac{\omega}{\gamma}\right)^2 = \frac{1}{M_{\text{s}}^2\sin^2\Theta}\left[\left(\partial_\Phi^2 F\right)\left(\partial_\Theta^2 F\right)-\left(\partial_\Phi\partial_\Theta F\right)^2\right]\Big|_{\Phi_0,\Theta_0}. \tag{4.7}$$

A damping parameter, which accounts for the damping of the magnetization precession, is usually incorporated in this expression. As a damping parameter does not influence the resonance field, it is omitted here for simplicity. Equation (4.7) has to be evaluated at the equilibrium orientation of the saturation magnetization (Θ_0,Φ_0) determined from

$$\partial_\Theta F|_{\Theta=\Theta_0} = \partial_\Phi F|_{\Phi=\Phi_0} = 0. \tag{4.8}$$

The Equations (4.6)–(4.8) correlate the magnetic hardness along the external magnetic field direction and the corresponding FMR field magnitude $\mu_0 H_{\text{res}}$. The magnetic anisotropy contributions in Eq. (4.6) influence a FMR experiment in such a way, that a magnetically easier direction leads to a shift of the resonance field to smaller magnetic fields and a harder direction results in a shift to larger magnetic fields. Therefore, the angular dependence of $\mu_0 H_{\text{res}}$ enables a mapping of the free energy surface. To determine the magnetic anisotropy fields, the sample is mounted on a rotatable sample holder. A series of FMR spectra is then recorded for different orientations of the sample with respect to the external magnetic field in adequate rotation planes. We thus detect the resonance field $\mu_0 H_{\text{res}}$ as a function of the magnetic field orientation (θ,ϕ). Depending on symmetry considerations, we constitute an appropriate free energy density description $F\left(\Theta,\Phi,H,\theta,\phi\right) = F\left(M,\Theta,\Phi,H,\theta,\phi\right)/M$ [cf. Eq. (4.6)] and subsequently simulate $\mu_0 H_{\text{res}}\left(\theta,\phi\right)$ curves in an iterative procedure by simultaneously numerically solving Eqs. (4.7) and (4.8). In particular, solving this set of equations for each orientation of the external magnetic field (θ,ϕ) results in a set of solutions $(\mu_0 H_{\text{res}},\Theta_0,\Phi_0)$ for the corresponding three unknown variables. The anisotropy fields in $F_{\text{aniso}}\left(\Theta,\Phi\right)$ are iteratively adjusted until satisfactory agreement between the measured and simulated $\mu_0 H_{\text{res}}\left(\theta,\phi\right)$ curves is obtained.

4.2 SQUID magnetometry

SQUID magnetometry is employed to quantitatively determine the magnetization $M(H,T)$ of our samples. The Quantum Design MPMS XL-7 SQUID magnetometer provides a magnetic field of $-7\,\text{T} \leq \mu_0 H \leq +7\,\text{T}$ and a temperature range of $1.8\,\text{K} \leq T \leq 400\,\text{K}$ in the sample space. The system is equipped with a second order gradiometer [Fig. 4.5(a)], which suppresses a net flux for any environmental

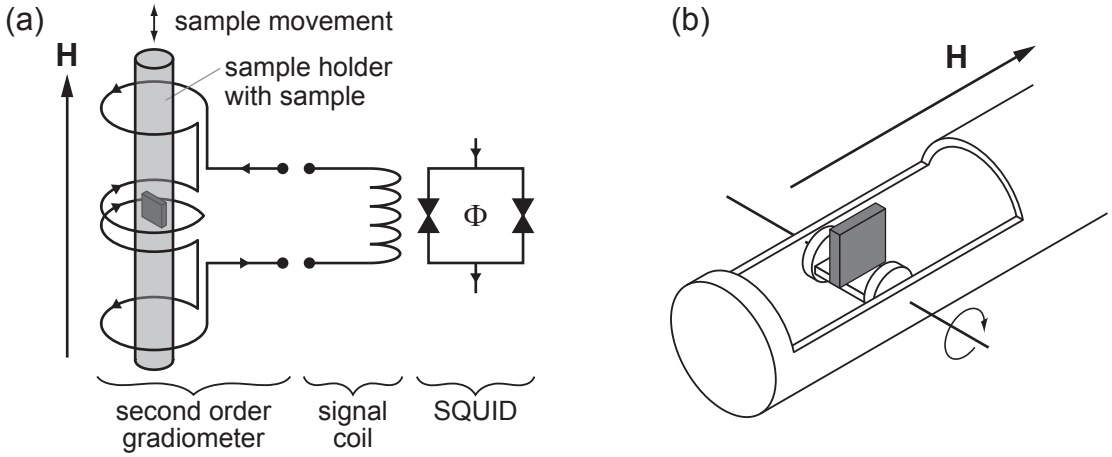

Figure 4.5: (a) Schematic illustration of the SQUID magnetometer. (b) Horizontal rotator to carry out angle-dependent measurements.

constant and first order gradient magnetic fields over the gradiometer length. Hence, the sample holder does not contribute to the net shielding current. During the measurement, the sample is moved inside the gradiometer pickup coils and thus induces a net current signal, which is converted to a magnetic flux via the signal coil, and subsequently is converted to a voltage signal by the SQUID sensor. The magnetometer detects the projection $m = \mathbf{m} \cdot \mathbf{h}$ of the sample's magnetic moment onto the gradiometer axis and thus onto the external magnetic field direction $\mathbf{h} = \mathbf{H}/H$. We subsequently correct m for any diamagnetic and paramagnetic contributions of the sample and calculate the magnetization $M = m/V$ using the ferromagnetic sample volume V.

We employed the SQUID magnetometer in two operation modes. Conventionally, magnetization measurements are performed with the oscillating reciprocating sample measurement (RSM) option with a constant orientation of the external magnetic field during the measurement. Thereby, a nominal resolution of $10^{-8}\,\text{emu} = 10^{-11}\,\text{Am}^2$ is achieved. To carry out angle-dependent magnetization measurements, the setup can be endowed with a horizontal rotator [Fig. 4.5(b)] and operated in the dc mode. The sensitivity hereby is decreased by about one order of magnitude.

4.3 Magneto-Optical Kerr Spectroscopy

4.3.1 Phenomenology

Magneto-optics denotes the dependence of the optical properties on magnetic order. The dependence of the optical properties of light reflected from a solid on the relative orientation of magnetization direction and light polarization is referred to as magneto-optic Kerr effect. Generally, the Kerr effect is characterized by three distinct magneto-optical configurations. In the polar case, the magnetization is perpendicular to the surface [Fig. 4.6(a1)]. In the longitudinal configuration the magnetization is oriented within the film plane and parallel to the plane of light

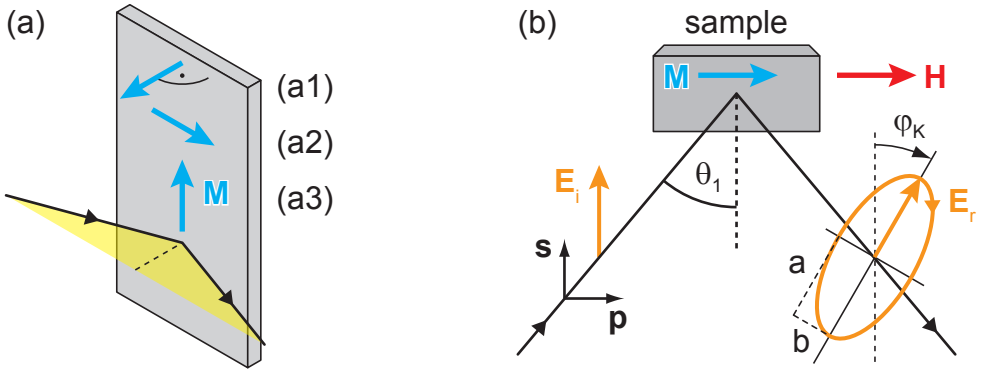

Figure 4.6: (a) Illustration of the different types of Kerr effect geometries, depending on the magnetization orientation with respect to the plane of incidence: (a1) polar, (a2) longitudinal, and (a3) transverse. (b) Phenomenology of the MOKE, defining the Kerr angle φ_K and the ellipticity $\eta_K = b/a$ upon reflection of linearly polarized incident light of a magnetized sample.

incidence [Fig. 4.6(a2)], and, contrarily, perpendicular to the plane of incidence in the transversal geometry [Fig. 4.6(a3)] [165]. Within this thesis, we focus on the longitudinal configuration, as schematically depicted in Fig. 4.6(b). Linearly polarized incident light is subject to two substantial modifications upon reflection from a magnetized solid. First, the polarization plane is rotated by the so-called Kerr angle φ_K with respect to that of the incident light, and second, the polarization state changes from linearly polarized to elliptically polarized. The Kerr ellipticity $\eta_K = b/a$ is determined from a and b, the long and short axis of the polarization ellipse, respectively. These two quantities are represented as the real and imaginary part of the complex Kerr angle [166]

$$\Psi_K = \varphi_K + i\eta_K. \tag{4.9}$$

As both quantities are proportional to the magnetization, MOKE provides a sensitive means to probe the magnetization of a ferromagnetic sample.

4.3.2 Macroscopic Description

Whereas the MOKE microscopically is due to the simultaneous occurrence of exchange splitting and spin-orbit coupling [167, 168], macroscopically the interaction of light with solids is determined by the complex index of refraction $\tilde{n} = n_R + in_I$. The index of refraction is connected with the dielectric tensor $\tilde{\boldsymbol{\varepsilon}}$ and the permeability tensor $\tilde{\boldsymbol{\mu}}$ by $\tilde{\mathbf{n}}^2 = \tilde{\boldsymbol{\varepsilon}} \cdot \tilde{\boldsymbol{\mu}}$. Considering typical values for the Larmor frequency ($\omega \sim$ GHz for external magnetic fields $\mu_0 H \lesssim 1\,\mathrm{T}$), the magnetization cannot follow variations at optical frequencies and thus the permeability tensor is always taken as equal to unity [169, 170]. Therefore the index of refraction yields

$$\tilde{\mathbf{n}}^2 = \tilde{\boldsymbol{\varepsilon}} \tag{4.10}$$

and all magneto-optical effects are incorporated in the complex dielectric tensor.

The dielectric tensor adopts a particular form related to the crystal symmetry. For cubic symmetry, the diagonal elements are identical and the off-diagonal elements are zero. The presence of a magnetization establishes a symmetry break and induces an axial symmetry in the system [166], resulting in off-diagonal elements. For a cubic magnetic material (neglecting higher order terms) the tensor is given by [171, 172]

$$\widetilde{\boldsymbol{\varepsilon}} = \varepsilon \begin{pmatrix} 1 & -\mathrm{i}Qm_z & \mathrm{i}Qm_y \\ \mathrm{i}Qm_z & 1 & -\mathrm{i}Qm_x \\ -\mathrm{i}Qm_y & \mathrm{i}Qm_x & 1 \end{pmatrix}, \tag{4.11}$$

with the direction cosines of the magnetization m_i with respect to the crystallographic axes. ε is the dielectric constant in the absence of a magnetization and Q is the so-called magneto-optic Voigt constant describing the magneto-optical rotation of the polarization plane. Maxwell's equations together with Eqs. (4.10) and (4.11) yields the index of refraction. Such a calculation in first order of Q results in two solutions for right- and left-circularly polarized light, $n^{(+)}$ and $n^{(-)}$, respectively [173]:

$$n^{(\pm)} \approx \sqrt{\varepsilon}\left(1 \pm \frac{1}{2} Q\mathbf{k}\cdot\mathbf{m}\right), \tag{4.12}$$

with the unit vectors of the propagation direction $\mathbf{k}$ and the magnetization $\mathbf{m}$. Hence, a magnetic material exhibits two different refraction indices and thus is birefringent. In a transparent material, both ε and Q are real. Generally, different refraction indices result in deviating propagation velocities for $(+)$ and $(-)$ circularly polarized light [174]. This effect is denoted as linear magnetic birefringence and results in a rotation of the polarization plane. Typically, ε and Q and thus also n are complex. The imaginary parts of $n^{(+)}$ and $n^{(-)}$ cause a different absorption for $(+)$ and $(-)$ polarized light, respectively. Hence, linearly polarized light transforms into elliptically polarized light, referred to as magnetic dichroism.

To deduce quantitative expressions for the complex Kerr rotation Ψ_K, we split the electric field of the incident and reflected light into two components, $\mathbf{E} = E_\mathrm{p}\mathbf{p} + E_\mathrm{s}\mathbf{s}$, with the unit vectors $\mathbf{p}$ and $\mathbf{s}$ parallel and perpendicular to the plane of incidence, respectively. The relation between the electric fields of the incident light $\mathbf{E}$ and the reflected light $\mathbf{E}'$ is given by the Fresnel scattering matrix $\tilde{\mathbf{R}}$ [175]:

$$\begin{pmatrix} E'_\mathrm{p} \\ E'_\mathrm{s} \end{pmatrix} = \begin{pmatrix} \tilde{r}_\mathrm{pp} & \tilde{r}_\mathrm{ps} \\ \tilde{r}_\mathrm{sp} & \tilde{r}_\mathrm{ss} \end{pmatrix} \begin{pmatrix} E_\mathrm{p} \\ E_\mathrm{s} \end{pmatrix}, \tag{4.13}$$

with the reflection coefficients $\tilde{r}_\mathrm{pp}$, $\tilde{r}_\mathrm{ss}$, $\tilde{r}_\mathrm{ps}$, and $\tilde{r}_\mathrm{sp}$. The complex Kerr angle is then defined as $\Psi_\mathrm{K}^\mathrm{p} = \tilde{r}_\mathrm{sp}/\tilde{r}_\mathrm{pp}$ and $\Psi_\mathrm{K}^\mathrm{s} = \tilde{r}_\mathrm{ps}/\tilde{r}_\mathrm{ss}$ for $\mathbf{p}$- and $\mathbf{s}$-polarized incident light, respectively [176]. To account for the different Kerr effect geometries, the scattering matrix $\widetilde{\mathbf{R}}$ is expressed in terms of $\tilde{r}^\mathrm{p}$, $\tilde{r}^\mathrm{l}$, and $\tilde{r}^\mathrm{t}$, which denote the scattering matrices for the polar, longitudinal and transverse geometry, respectively, by a coordinate transformation [175, 177]:

$$\widetilde{\mathbf{R}} = m_\mathrm{p}^2\tilde{\mathbf{r}}^\mathrm{p}\left[Q/m_\mathrm{p}\right] + m_\mathrm{l}^2\tilde{\mathbf{r}}^\mathrm{l}\left[Q/m_\mathrm{l}\right] + m_\mathrm{t}^2\tilde{\mathbf{r}}^\mathrm{t}\left[Q/m_\mathrm{t}\right], \tag{4.14}$$

where the square brackets denote a substitution of Q by Q/m_i $(i = \mathrm{p}, \mathrm{l}, \mathrm{t})$ in the scattering matrices, with $m_\mathrm{p} = M_\mathrm{p}/M_\mathrm{s}$, $m_\mathrm{l} = M_\mathrm{l}/M_\mathrm{s}$, and $m_\mathrm{t} = M_\mathrm{t}/M_\mathrm{s}$ being the direction cosines of the magnetization vector in the $\{\mathbf{p}, \mathbf{l}, \mathbf{t}\}$ coordinate system. For the longitudinal Kerr effect, the components of $\tilde{\mathbf{r}}^\mathrm{l}$ are then given by [175–179]

$$\begin{aligned} \tilde{r}^\mathrm{l}_\mathrm{pp} &= \frac{n_2 \cos\theta_1 - n_1 \cos\theta_2}{n_2 \cos\theta_1 + n_1 \cos\theta_2}, \\ \tilde{r}^\mathrm{l}_\mathrm{ss} &= \frac{n_1 \cos\theta_1 - n_2 \cos\theta_2}{n_1 \cos\theta_1 + n_2 \cos\theta_2}, \\ \tilde{r}^\mathrm{l}_\mathrm{sp} = -\tilde{r}^\mathrm{l}_\mathrm{ps} &= \frac{\mathrm{i} n_1 n_2 Q \cos\theta_1 \tan\theta_2}{(n_1 \cos\theta_1 + n_2 \cos\theta_2)\,(n_2 \cos\theta_1 + n_1 \cos\theta_2)}, \end{aligned} \tag{4.15}$$

with the angle of incidence θ_1, the refractive index of the nonmagnetic medium n_1, the refractive index of the magnetic medium n_2, and the refractive angle θ_2 in the magnetic medium according to Snell's law. Thus, the complex Kerr angle for the longitudinal configuration can be expressed by

$$\begin{aligned} \Psi^{\mathrm{p,long}}_\mathrm{K} &= \frac{\mathrm{i} n_1 n_2 Q \cos\theta_1 \tan\theta_2}{(n_1 \cos\theta_1 + n_2 \cos\theta_2)\,(n_2 \cos\theta_1 - n_1 \cos\theta_2)}, \\ \Psi^{\mathrm{s,long}}_\mathrm{K} &= -\frac{\mathrm{i} n_1 n_2 Q \cos\theta_1 \tan\theta_2}{(n_1 \cos\theta_1 - n_2 \cos\theta_2)\,(n_2 \cos\theta_1 + n_1 \cos\theta_2)}. \end{aligned} \tag{4.16}$$

As apparent, the Kerr rotation vanishes at perpendicular light incidence ($\theta_1 = \theta_2 = 0$). The maximum Kerr rotation is obtained at an angle of incidence $0 < \theta_1 < 90°$, depending on the refractive angle θ_2 [176].

4.3.3 Detection

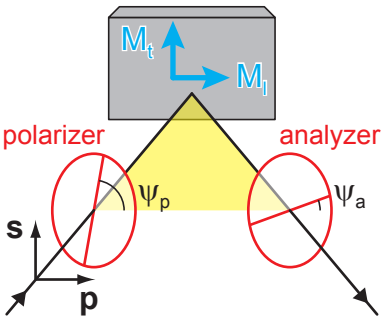

Fig. 4.7: Schematic illustration of a basic MOKE setup. The orientation of the polarizer ψ_p and the analyzer ψ_a are defined with respect to the plane of incidence.

We now turn to the detection of the MOKE signal. In particular, we aim at recording the longitudinal component of the magnetization vector in longitudinal geometry [98, 180–182]. A basic setup configuration to this end is shown in Fig. 4.7, equipped with two polarizers. A polarizer is placed into the illumination path to generate linearly polarized incident light along its transmission axis, rotated by an angle ψ_p with respect to the incidence plane. The reflected light passes through a probing analyzer at an angle ψ_a.

After transmission through the polarizer, the electric field can be expressed as

$$\mathbf{E} = E_0 \cos\psi_\mathrm{p} \mathbf{p} + E_0 \sin\psi_\mathrm{p} \mathbf{s}. \tag{4.17}$$

The interaction of the light with the magnetized material is given by the Fresnel scattering matrix $\widetilde{\mathbf{R}}$ [cf. Eq. (4.14)]. Assuming the magnetization being oriented within the film plane with the components M_l and M_t, the scattering matrix is given by

$$\widetilde{\mathbf{R}} = m_\mathrm{l}^2 \tilde{\mathbf{r}}^\mathrm{l}\left[Q/m_\mathrm{l}\right] + m_\mathrm{t}^2 \tilde{\mathbf{r}}^\mathrm{t}\left[Q/m_\mathrm{t}\right]. \tag{4.18}$$

The components of the electric field $\mathbf{E}'$ after reflection then yield [180]

$$\begin{aligned} E'_{\mathrm{p}} &= \left(m_{\mathrm{t}}^2 \tilde{r}_{\mathrm{pp}}^{\mathrm{t}} + m_{\mathrm{l}}^2 \tilde{r}_{\mathrm{pp}}^{\mathrm{l}}\right) E_0 \cos\psi_{\mathrm{p}} + m_{\mathrm{l}}^2 \tilde{r}_{\mathrm{ps}}^{\mathrm{l}} E_0 \sin\psi_{\mathrm{p}}, \\ E'_{\mathrm{s}} &= m_{\mathrm{l}}^2 \tilde{r}_{\mathrm{sp}}^{\mathrm{l}} E_0 \cos\psi_{\mathrm{p}} + \tilde{r}_{\mathrm{ss}}^{\mathrm{l}} E_0 \sin\psi_{\mathrm{p}}. \end{aligned} \tag{4.19}$$

Subsequently, this reflected light transmits through the analyzer, where only the component parallel to the analyzer passes. The electric field E'' along the analyzer transmission axis is given by

$$E'' = E'_{\mathrm{p}} \cos\psi_{\mathrm{a}} + E'_{\mathrm{s}} \sin\psi_{\mathrm{a}}. \tag{4.20}$$

Substituting Eq. (4.19) into the expression above yields

$$E'' = E_0 \left[\left(m_{\mathrm{t}}^2 \tilde{r}_{\mathrm{pp}}^{\mathrm{t}} + m_{\mathrm{l}}^2 \tilde{r}_{\mathrm{pp}}^{\mathrm{l}}\right) \cos\psi_{\mathrm{p}} \cos\psi_{\mathrm{a}} + m_{\mathrm{l}}^2 \tilde{r}_{\mathrm{ps}}^{\mathrm{l}} \sin\left(\psi_{\mathrm{p}} - \psi_{\mathrm{a}}\right) + \tilde{r}_{\mathrm{ss}}^{\mathrm{l}} \sin\psi_{\mathrm{p}} \sin\psi_{\mathrm{a}}\right]. \tag{4.21}$$

The measured signal is proportional to the intensity of light and thus proportional to the squared modulus of Eq. (4.21). Restricting the discussion to the relevant case of **s**-polarized incident light ($\psi_{\mathrm{p}} = 90°$) makes the signal from the transversal component m_{t} of the magnetization vanish. The resulting expression for the detected signal normalized to the incident intensity I_0 solely depends on the longitudinal component m_{l} of the magnetization:

$$I/I_0 = \left|m_{\mathrm{l}}^2 \tilde{r}_{\mathrm{ps}}^{\mathrm{l}}\right|^2 \cos^2\psi_{\mathrm{a}} + \left|\tilde{r}_{\mathrm{ss}}^{\mathrm{l}}\right|^2 \sin^2\psi_{\mathrm{a}} + \left(\tilde{r}_{\mathrm{ss}}^{\mathrm{l}} \tilde{r}_{\mathrm{ps}}^{\mathrm{l}*} + \tilde{r}_{\mathrm{ss}}^{\mathrm{l}*} \tilde{r}_{\mathrm{ps}}^{\mathrm{l}}\right) m_{\mathrm{l}}^2 \sin\psi_{\mathrm{a}} \cos\psi_{\mathrm{a}}, \tag{4.22}$$

where the symbol $*$ denotes the complex conjugate. Combining Eqs. (4.22) and (4.15) allows for a further simplification. The first term in Eq. (4.22) then appears as $\left|A\left(\theta_1, \theta_2, n_1, n_2\right)\right|^2 \left|Q\right|^2 m_{\mathrm{l}}^2$, with A representing a function of the respective variables. Hence, this term vanishes, since due to small $|Q|$ (typically $|Q| \leq 0.03$ [98]) terms quadratic in Q can be neglected. The second term $\left|B\left(\theta_1, \theta_2, n_1, n_2\right)\right|^2$ gives a nonmagnetic contribution and the third term can be rewritten as $\left[C_1\left(\theta_1, \theta_2, n_1, n_2\right) Q + C_2\left(\theta_1, \theta_2, n_1^*, n_2^*\right) Q^*\right] m_{\mathrm{l}}$. In summary, Eq. (4.22) results in

$$I/I_0 \approx C\left(\theta_1, \theta_2, n_1, n_2, n_1^*, n_2^*, Q, Q^*\right) m_{\mathrm{l}} \sin\left(2\psi_{\mathrm{a}}\right), \tag{4.23}$$

and thus the longitudinal geometry with **s**-polarized incoming light is proportional to the magnetization component m_{l} parallel to the plane of incidence.

4.3.4 Magneto-Optical Contrast

The preceding section covered the detected MOKE signal in longitudinal geometry with **s**-polarized incident light ($\psi_{\mathrm{p}} = 90°$). However, the application of magneto-optical techniques crucially depends on the performance of instrumentation. To determine the optimum settings and sensitivity, we again consider a basic MOKE spectrometer illustrated in Fig. 4.7 with two polarizers as principal components, and neglect elliptical polarization for now [148, 165, 183–188]. For two magnetization states with opposite magnetization direction, i.e., parallel and antiparallel to the

component M_l in Fig. 4.7, the detected intensity of these magnetization states is then given by Malus' law [165]

$$I(\pm M) = I_{0\mathrm{r}} \sin^2(\psi_\mathrm{a} \pm \varphi_\mathrm{K}) + I_\mathrm{rr}, \tag{4.24}$$

where $I_{0\mathrm{r}}$ is the intensity of light reflected by the sample and I_rr denotes the residual intensity transmitted through the analyzer in extinction, which arises from depolarization effects and finite illumination apertures. Upon neglecting depolarization effects from the sample and optical components, $I_\mathrm{rr}/I_{0\mathrm{r}} = \varepsilon$, which is the extinction ratio of the polarizers [165]. ψ_a is the angle of the analyzer transmission axis with respect to the incidence plane, and simultaneously—as we employ **s**-polarized light—the analyzer offset angle from extinction. The angle φ_K denotes the Kerr rotation. The figure of merit for the system is the magneto-optical contrast C_mo [148, 165, 186]

$$C_\mathrm{mo} \equiv \frac{s_\mathrm{mo}}{\bar{I}} = \frac{I(+M) - I(-M)}{\frac{1}{2}[I(+M) + I(-M)]} = \frac{2\sin(2\psi_\mathrm{a})\sin(2\varphi_\mathrm{K})}{1 - \cos(2\psi_\mathrm{a})\cos(2\varphi_\mathrm{K}) + 2\gamma_\mathrm{D}}, \tag{4.25}$$

with the relative magneto-optical signal s_mo and the depolarization fraction $\gamma_\mathrm{D} = I_\mathrm{rr}/I_{0\mathrm{r}}$. Since the Kerr rotation is typically small ($\varphi_\mathrm{K} \sim 10^{-3}$ rad [182]), Eq. (4.25) can be simplified to

$$C_\mathrm{mo} = \frac{2\varphi_\mathrm{K}\sin(2\psi_\mathrm{a})}{\sin^2\psi_\mathrm{a} + \gamma_\mathrm{D}}. \tag{4.26}$$

The contrast is a linear function of φ_K and therefore of the longitudinal magnetization component. Restricting the discussion to small analyzer angles, the maximum contrast is obtained by minimizing C_mo with respect to ψ_a, which yields

$$\begin{aligned} \psi_\mathrm{a,max} &= \sqrt{\gamma_\mathrm{D}}, \\ C_\mathrm{mo,max} &= \frac{2\varphi_\mathrm{K}}{\sqrt{\gamma_\mathrm{D}}}. \end{aligned} \tag{4.27}$$

Equation (4.27) shows that depolarization effects govern the performance of the optical system, as γ_D limits the maximum achievable contrast $C_\mathrm{mo,max}$, and thus the use of high quality polarizers with low extinction ratio is crucial. To give an example, we use $\gamma_\mathrm{D} = \varepsilon = 10^{-6}$ of high quality Glan Thompson polarizers and obtain $\psi_\mathrm{a,max} \approx 0.1°$.

However, to determine the optimum settings for the MOKE spectrometer we have to consider further major aspects. As apparent, a successful application of the MOKE requires the detected intensity I being proportional to the magnetization (cf. Sec. 4.3.3) and hence Eq. (4.24) results in the condition $\psi_\mathrm{a} > \varphi_\mathrm{K}$. Thus a Taylor series expansion of $I(\psi_\mathrm{a})$ around ψ_0 has a first order linear term in the Kerr rotation angle φ_K [165].

Furthermore, in terms of magneto-optical imaging, the best visibility of domains is rarely governed by the criterion of maximum contrast. First, if the analyzer angle ψ_a is too small, the image is too dark and thus larger analyzer angles are preferred as with increasing ψ_a the intensity increases with ψ_a^2 [cf. Eq. (4.24)]. Second, a good

visibility of domains requires a large signal-to-noise ratio S_{mo}/N. We here consider the ideal case of shot noise only, and neglect electronic noise and media noise, i.e., fluctuations in the light source, optical path, and the sample. The absolute magneto-optical signal is given by $S_{\mathrm{mo}} = AN_{\mathrm{p}}s_{\mathrm{mo}}$, where A is a proportionality constant depending on the quantum efficiency and the amplification and conversion process of the detected photons, and N_{p} is the number of incident photons [148, 186]. With the expression for shot noise $N = \sqrt{\frac{1}{2}AN_{\mathrm{p}}\left[I\left(+M\right) + I\left(-M\right)\right]}$ we finally obtain $S_{\mathrm{mo}}/N = \sqrt{AN_{\mathrm{p}}}s_{\mathrm{mo}}/\bar{I}$. Inserting Eq. (4.24), minimizing the expression with respect to ψ_{a}, and allowing small φ_{K} and γ_{D} yields

$$\cos\psi_{\mathrm{a,opt}} = \sqrt{1-\sqrt{\gamma_{\mathrm{D}}}}.$$

Applying again $\gamma_{\mathrm{D}} = \varepsilon = 10^{-6}$ yields $\cos\psi_{\mathrm{a,opt}} \approx 1.8°$. This result coincides with experimental experience, as analyzer angles of $1° \leq \psi_{\mathrm{a,opt}} \leq 2°$ have proven to yield best contrast and signal-to-noise. To further improve the detected signal, a quarter wave plate can be inserted. It removes the ellipticity of the reflected light and thus enhances the signal amplitude.

4.3.5 Experimental setup and image processing

In the framework of this thesis, a basic longitudinal MOKE setup has been built up [189] and extended to allow for spatially resolved MOKE imaging [190].

The conventional MOKE setup [Fig. 4.8(a)] is equipped with a 7 mW cw-diode laser emitting light in the visible red wavelength regime ($\lambda = 670\,\mathrm{nm}$). A neutral density filter is employed to attenuate the laser beam power to about 70 nW. After passing through a focusing lens, the light transmits through a Glan Thompson polarizing prism (extinction ratio $\varepsilon = 10^{-6}$) at $\psi_{\mathrm{p}} = 90°$ resulting in **s**-polarized light. The beam with a final diameter of a few 100 μm then reflects off the sample, such that only the skin depth region, typically in the range of a few nm in most metals, that contributes to the Kerr rotation. Magnetic fields are generated in the plane of the sample using iron-core, air-gap electromagnets driven by a bipolar power supply, while a Hall probe next to the sample measures the actual magnetic field and actively adjusts the output of the magnet power supply via a feedback control. The reflected beam then passes through a quarter wave plate to remove the ellipticity and improve the contrast, and then transmits through the analyzer close to extinction ($\psi_{\mathrm{a}} \approx 1°$). The beam is focused onto a photodiode by means of an objective lens, which converts the intensity of light into a voltage and amplifies it. To increase the signal-to-noise ratio, the photodiode is equipped with a laser line filter.

Figure 4.8(b) schematically depicts how we have extended our conventional longitudinal MOKE setup to enable spatially resolved measurements [191, 192]. A high power LED in the visible red regime (center frequency $\lambda = 627\,\mathrm{nm}$) serves as a light source and provides the required incoherent and collimated light [193], since LEDs exhibit sufficient spectral width to avoid speckle and interference fringes. A slit aperture is inserted in the illumination path, oriented parallel to the plane of

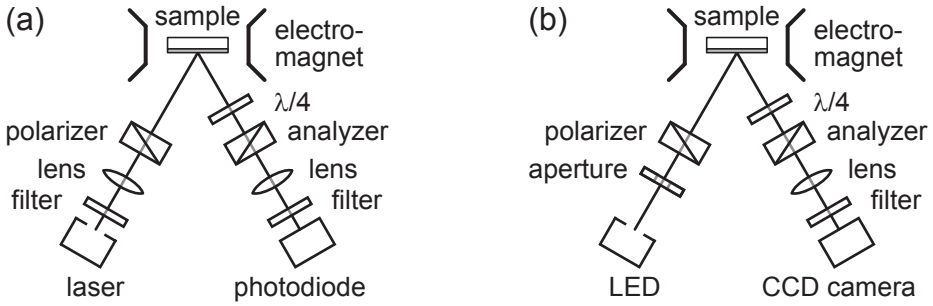

Figure 4.8: Schematic illustrations of the (a) conventional MOKE and (b) MOKE imaging setups.

incidence [194], as a correctly adjusted illumination path is crucial for MOKE imaging. Too small apertures result in diffraction fringes, while large apertures increase the background intensity due to depolarization effects and thus reduce the contrast [148]. The objective lens is slightly tilted to correct the decreased range of focus and the image distortion due to oblique light incidence [148]. The Kerr signal is recorded by a CCD-camera with 658×496 active pixels with a pixel size of $10\,\mu\text{m} \times 10\,\mu\text{m}$ resulting in an image area of $6.58\,\text{mm} \times 4.96\,\text{mm}$, and a digitization of 14 bit. The camera is equipped with appropriate long- and shortpass filters, such that only light within $550\,\text{nm} \leq \lambda \leq 700\,\text{nm}$ can reach the CCD. The spatial resolution of this setup is rather low and is practically limited by the setup geometry, abberations and the achievable numerical aperture. Typically the objective lens is adjusted to yield a transverse magnification between one and three to ensure decent contrast and brightness conditions. Therefore we attain a spatial resolution in the range of several micrometers.

The visualization of magnetic domains is generally limited as the weak magnetic contrasts are usually governed by strong non-magnetic contrasts arising from, e.g., surface imperfections and irregularities, and inhomogeneous light illumination. A process to remarkably reduce these unintended signal contributions is the technique of difference imaging [195–198]. The standard procedure comprises the digital subtraction of two images to obtain a resulting image which exhibits only magnetic contrast. Therefore, a reference image in a magnetically saturated state is recorded and subtraced from all subsequent images.

4.4 Magnetotransport

4.4.1 Anisotropic magnetoresistance

The resistivity of a ferromagnetic material generally depends on the orientation of the magnetization, i.e., it is a function of the angle between the magnetization and the direction of the sensing current. This is referred to as anisotropic magnetoresistance [100, 199, 200]. The mechanism that governs AMR is spin-orbit interaction [201–203]. The relation between the electric field $\mathbf{E}$ and the current density $\mathbf{J} = J\mathbf{j}$

is phenomenologically given by Ohm's law

$$\mathbf{E} = \boldsymbol{\rho} \cdot \mathbf{J}, \tag{4.28}$$

where $\boldsymbol{\rho}$ represents the resistivity tensor.

We first consider the case of polycrystalline ferromagnetic materials, where the resistivity tensor with the sample being in a magnetically saturated state is given by [100]

$$\boldsymbol{\rho} = \begin{pmatrix} \rho_\perp & \rho_\mathrm{H} & 0 \\ \rho_\mathrm{H} & \rho_\perp & 0 \\ 0 & 0 & \rho_\parallel \end{pmatrix},$$

where $\rho_\perp$ and $\rho_\parallel$ are the resistivities for $\mathbf{J} \perp \mathbf{M}$ and $\mathbf{J} \parallel \mathbf{M}$, respectively, and ρ_H is the Hall resistivity. Ohm's law can then be expressed as follows [199, 204]:

$$\mathbf{E} = \rho_\perp \mathbf{J} + \left(\rho_\parallel - \rho_\perp\right) \mathbf{m} \left(\mathbf{J} \cdot \mathbf{m}\right) + \mu_0 \left(R_0 \mathbf{H} + R_\mathrm{s} \mathbf{M}\right) \times \mathbf{J}, \tag{4.29}$$

with the unit magnetization vector $\mathbf{m} = \mathbf{M}/M$. In this equation, the three terms represent the longitudinal magnetoresistance, the planar Hall effect (PHE), and the Hall effect, respectively. The latter is composed of the ordinary and the extraordinary Hall effect, respectively. As for all AMR data presented in this thesis, the magnetization orientation was constrained to lie in the film plane due to an external magnetic field applied in the film plane and/or strong shape anisotropy, we omit the last term in Eq. (4.29) in the following and thus only consider the PHE. Then the resistivities ρ_long and ρ_trans measured parallel and perpendicular to $\mathbf{J}$ are given by [199]

$$\begin{aligned} \rho_\mathrm{long}^\mathrm{poly} &= \rho_\perp + \left(\rho_\parallel - \rho_\perp\right) \cos^2 \beta, \\ \rho_\mathrm{trans}^\mathrm{poly} &= \frac{1}{2} \left(\rho_\parallel - \rho_\perp\right) \sin\left(2\beta\right), \end{aligned} \tag{4.30}$$

with the angle β between $\mathbf{m}$ and $\mathbf{j}$.

According to Neumann's principle, the physical properties of a crystal reflect its morphological symmetry [205]. Hence, the resistivity tensor of single crystals depends on the magnetization orientation with respect to the crystallographic axes, and symmetry considerations are phenomenologically incorporated by expressing $\boldsymbol{\rho}$ as a series expansion in powers of the direction cosines of the magnetization vector m_i [106, 110, 206, 207]. To quantitatively determine the measurable resistivities with an arbitrarily oriented magnetization, the unit vectors $\mathbf{n}$ and $\mathbf{t}$ are introduced (Fig. 4.9), which denote the surface normal and an in-plane direction $\mathbf{t} = \mathbf{n} \times \mathbf{j}$, respectively. The measured voltages parallel and perpendicular to the current direction then are

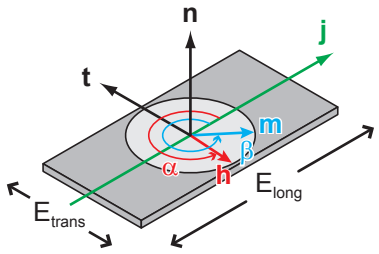

Fig. 4.9: Illustration of an AMR measurement with the corresponding unit vectors and electric fields described in the text.

$E_{\text{long}} = \mathbf{j} \cdot \boldsymbol{E}$ and $E_{\text{trans}} = \mathbf{t} \cdot \boldsymbol{E}$, respectively. Hence, based on Eq. (4.28), the longitudinal and the transverse resistivities can be expressed as [110]

$$\begin{aligned} \rho_{\text{long}} &= \frac{E_{\text{long}}}{J} = \mathbf{j} \cdot \boldsymbol{\rho} \cdot \mathbf{j}, \\ \rho_{\text{trans}} &= \frac{E_{\text{trans}}}{J} = \mathbf{t} \cdot \boldsymbol{\rho} \cdot \mathbf{j}. \end{aligned} \tag{4.31}$$

The resistivity tensor as a series expansion is given by [106, 206]

$$\rho_{ij} = a_{ij} + \sum_k a_{kij} m_k + \sum_k a_{klij} m_k m_l + \cdots . \tag{4.32}$$

For cubic symmetry, the tensors with elements $a_{ij}, a_{kij}, a_{klij}, \cdots$ can be substantially simplified using von Neumann and Onsager relations, so that most components vanish. Thus, the resistivity tensor including terms up to the second order is given by

$$\begin{aligned} \boldsymbol{\rho}^{\text{cubic}} &= A \begin{pmatrix} 1 & 0 & 0 \\ 0 & 1 & 0 \\ 0 & 0 & 1 \end{pmatrix} + B \begin{pmatrix} m_x^2 & 0 & 0 \\ 0 & m_y^2 & 0 \\ 0 & 0 & m_z^2 \end{pmatrix} \\ &\quad + C \begin{pmatrix} 0 & m_x m_y & m_x m_z \\ m_x m_y & 0 & m_y m_z \\ m_x m_z & m_y m_z & 0 \end{pmatrix} + D \begin{pmatrix} 0 & m_z & -m_y \\ -m_z & 0 & m_x \\ m_y & -m_x & 0 \end{pmatrix}, \end{aligned} \tag{4.33}$$

with the resistivity parameters A, B, C, D being linear combinations of the components $a_{ij}, a_{kij}, a_{klij}$. Epitaxial growth of a cubic material on a cubic substrate can result in a tetragonally distorted film. To account for tetragonal symmetry, a correction term is added [110]:

$$\boldsymbol{\rho}^{\text{tetra}} = \boldsymbol{\rho}^{\text{cubic}} + \Delta\boldsymbol{\rho}, \tag{4.34}$$

with

$$\begin{aligned} \Delta\boldsymbol{\rho} &= \begin{pmatrix} 0 & 0 & 0 \\ 0 & 0 & 0 \\ 0 & 0 & a \end{pmatrix} + \begin{pmatrix} 0 & dm_z & 0 \\ -dm_z & 0 & 0 \\ 0 & 0 & 0 \end{pmatrix} \\ &\quad + \begin{pmatrix} b_1 m_z^2 & c m_x m_y & 0 \\ c m_x m_y & b_1 m_z^2 & 0 \\ 0 & 0 & b_2 m_z^2 \end{pmatrix}. \end{aligned} \tag{4.35}$$

Analogously, the resistivity parameters a, b_1, b_2, c, d are linear combinations of the components $a_{ij}, a_{kij}, a_{klij}$. The magnetotransport studies on single-crystalline systems presented in this work were performed on (001)-oriented samples with the current direction $\mathbf{j}$ along [110]. Hence we restrict the discussion to this experimentally

relevant case, and the appropriate equations for ρ_{long} and ρ_{trans} read as

$$\begin{aligned}\rho_{\mathrm{long}}^{\mathrm{tetra}} &= A + \frac{1}{2}(B - C - c) + (C + c)(\mathbf{j}\cdot\mathbf{m})^2 \\ &\quad + \left(\frac{1}{2}(C - B + c) + b_1\right)(\mathbf{n}\cdot\mathbf{m})^2, \\ \rho_{\mathrm{trans}}^{\mathrm{tetra}} &= B(\mathbf{j}\cdot\mathbf{m})(\mathbf{t}\cdot\mathbf{m}) - (D + d)(\mathbf{n}\cdot\mathbf{m}). \end{aligned} \tag{4.36}$$

If we consider an expansion including terms up to the fourth order, furthermore introduce the phenomenological resistivity parameters ρ_i, and regard the magnetization orientation being retained in the film plane, i.e., $\mathbf{n}\cdot\mathbf{m} = 0$, the resistivities can be rewritten as [207]

$$\begin{aligned}\rho_{\mathrm{long}}^{\mathrm{tetra}} &= \rho_0 + \rho_1(\mathbf{j}\cdot\mathbf{m})^2 + \rho_3(\mathbf{j}\cdot\mathbf{m})^4 \\ &= \rho_0 + \rho_1\cos^2\beta + \rho_3\cos^4\beta, \\ \rho_{\mathrm{trans}}^{\mathrm{tetra}} &= \rho_7(\mathbf{j}\cdot\mathbf{m})(\mathbf{t}\cdot\mathbf{m}) \\ &= \frac{1}{2}\rho_7\sin(2\beta). \end{aligned} \tag{4.37}$$

4.4.2 Determination of magnetic anisotropy from AMR

Magnetotransport measurements provide a comprehensive tool for the determination of the magnetic anisotropy. We here employ the procedure established by Limmer *et al.* [110], which relies on angle-dependent magnetoresistance (ADMR) measurements. To this end, we record the resistivities $\{\rho_{\mathrm{long}}(\alpha), \rho_{\mathrm{trans}}(\alpha)\}$ for a rotation of the external magnetic field $\mathbf{H}$ in the film plane at a constant field strength, where α denotes the angle between the magnetic field orientation $\mathbf{h} = \mathbf{H}/H$ and the current direction $\mathbf{j}$, and chose an appropriate free energy density ansatz according to Sec. 2.3:

$$F(M, \beta, H, \alpha) = -\mu_0 HM\cos(\beta - \alpha) + F_{\mathrm{aniso}}(\beta). \tag{4.38}$$

The evolution of ADMR under large magnetic field is exemplarily depicted by the blue lines in Fig. 4.10. At these magnetic field magnitudes, the Zeeman energy dominates the total free energy and the magnetic anisotropy contributions are negligible. Consequently, $\mathbf{M}$ aligns along $\mathbf{H}$ such that $\beta = \alpha$ and continuously follows its motion, resulting in smooth ADMR curves. With decreasing magnetic field the influence of the magnetic anisotropy increases, hence the magnetization orientation increasingly deviates from the field direction and tends to remain oriented close to a magnetic easy axis (termed as e.a. and depicted as green lines in Fig. 4.10). Thus, as shown for small magnetic field by the red curves, ρ_{long} and ρ_{trans} exhibit only small and smooth changes over a broad range of magnetic field orientations close to a magnetic easy axis. In contrast, a magnetic hard axis causes abrupt changes in the magnetization orientation, resulting in substantial changes in ρ_{long} and ρ_{trans}. Figure 4.10 shows $\{\rho_{\mathrm{long}}(\alpha), \rho_{\mathrm{trans}}(\alpha)\}$ curves for an in-plane cubic magnetic anisotropy with the easy axes along 45° and 135° [Figs. 4.10(a) and (b)], and for an in-plane uniaxial anisotropy along 90° [Figs. 4.10(c) and (d)] and 0° [Figs. 4.10(e) and (f)].

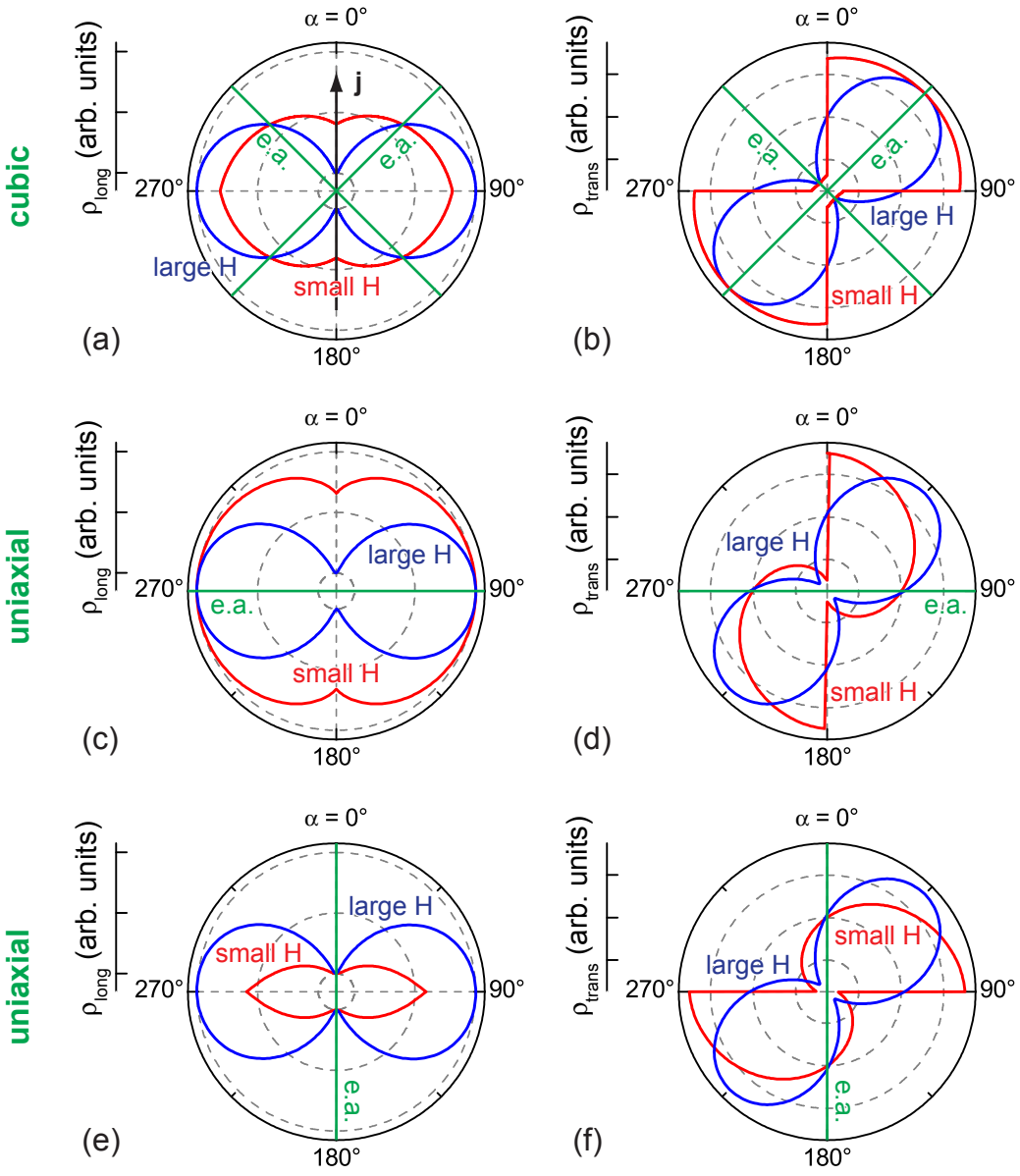

Figure 4.10: Schematic illustration of the ADMR evolution for a rotation of the external magnetic field in the film plane. α denotes the angle between $\mathbf{h}$ and $\mathbf{j}$. The panels show $\{\rho_{\mathrm{long}}(\alpha), \rho_{\mathrm{trans}}(\alpha)\}$ curves, calculated with the same resistivity parameters ($\rho_0, \rho_7 > 0$, $\rho_1, \rho_3 < 0$) for different magnetic anisotropy. The blue curves illustrate traces corresponding to a large applied magnetic field, such that $\mathbf{m} \parallel \mathbf{h}$. Hence, the high-field traces coincide, regardless of the magnetic anisotropy. At small magnetic fields (red curves), $\mathbf{m}$ deviates from $\mathbf{h}$, such that the magnetoresistance curves significantly differ for in-plane cubic magnetic anisotropy [(a), (b)] and in-plane uniaxial anisotropy with the magnetic easy axis along $\alpha = 90°$ [(c), (d)] and $0°$ [(e), (f)].

In the experiment, the magnetization is initially aligned in a well-defined state by applying a sufficiently high magnetic field along a magnetic easy axis. Subsequently, the magnetic field strength is reduced to the measurement field and then the angular scan $\{\rho_{\text{long}}(\alpha), \rho_{\text{trans}}(\alpha)\}$ is started. The resistivity and anisotropy parameters from Eqs. (4.37) and (4.38) are then determined by an iterative fit procedure. In a first step, the resistivity parameters ρ_i in Eqs. (4.37) are determined. To this end, we take advantage of the fact that at sufficiently large field $\mathbf{M}$ aligns along $\mathbf{H}$. Thus, the resistivity parameters can be derived from the corresponding $\{\rho_{\text{long}}(\alpha), \rho_{\text{trans}}(\alpha)\}$ traces, using Eqs. (4.37) with $\beta = \alpha$. In a second step, we modify the anisotropy parameters from Eq. (4.38), which, analogous to the procedure used in the FMR measurements (see Sec. 4.1.4), yields the magnetization orientation β_0 by numerically minimizing F in Eq. (4.38) with respect to β. The anisotropy parameters are adjusted, until a good agreement between the simulations using Eqs. (4.37) with β_0 and the experimental low-field $\{\rho_{\text{long}}(\alpha), \rho_{\text{trans}}(\alpha)\}$ traces is obtained. Then the whole procedure (steps one and two) is iteratively repeated, until no further improvement of the fit can be achieved.

4.5 High resolution x-ray diffraction

The structural properties of our samples were determined via HRXRD in a four-circle Bruker AXS D8 Discover diffractometer. A Cu-K_α x-ray source connected to a Goebel mirror and a 4-bounce Germanium monochromator provide parallel x-ray beams with a wavelength of $\lambda = 0.154056\,\text{nm}$. The beams are incident under an angle ω with respect to the sample mounted on the sample holder of the four-circle diffractometer (Fig. 4.11). The diffracted beam is then detected at an angle 2θ with respect to the incident beam with a resolution of 0.001°.

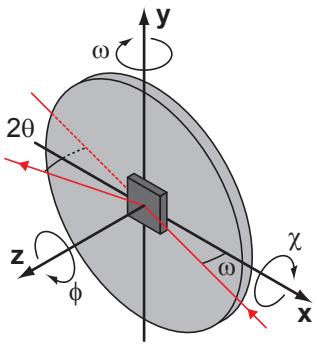

Fig. 4.11: Schematic illustration of the four-circle diffractometer.

Considering geometric scattering theory, we assume a crystal as a regular array of scatterers arranged in lattice planes with spacing d_{hkl}. When x-rays are incident on an atom at an angle θ with respect to the lattice planes, they produce secondary spherical waves. The scattered waves interfere with each other constructively, if the phase shift is a multiple of 2π. This condition is expressed by Bragg's law [149]

$$2d_{hkl}\sin\theta = n\lambda \quad (n \in \mathbb{N}), \tag{4.39}$$

with l, k, and l being the Miller indices.

To determine the lattice constants, we perform 2θ-ω-scans and reciprocal space maps. For an orthorhombic unit cell with lattice constants a, b, and c, the distance d between the lattice planes is given by [149]

$$\frac{1}{d^2} = \frac{h^2}{a^2} + \frac{k^2}{b^2} + \frac{l^2}{c^2}, \tag{4.40}$$

which enables us to calculate the out-of-plane lattice constant in combination with Eq. (4.39) and 2θ-ω-scans ($h = k = 0$):

$$c = \frac{\lambda l}{2 \sin \theta}. \tag{4.41}$$

Reciprocal space maps are represented by the parallel and orthogonal components of the reciprocal lattice vector $\mathbf{q}$, $q_{\parallel}$ and $q_{\perp}$, respectively. Conventionally, these components are expressed in reciprocal lattice units by $q_{\parallel}\,[\mathrm{rlu}] = q_{\parallel}/\frac{4\pi}{\lambda}$ and $q_{\perp}\,[\mathrm{rlu}] = q_{\perp}/\frac{4\pi}{\lambda}$, which are independent of λ. Hence, the in-plane and out-of-plane lattice constants can be calculated by

$$a = \frac{1}{q_{\parallel}\,[\mathrm{rlu}]}\frac{\lambda}{2}h \quad \text{and} \quad c = \frac{1}{q_{\perp}\,[\mathrm{rlu}]}\frac{\lambda}{2}l,$$

respectively.

Chapter 5

Anisotropy inversion and magnetization control in polycrystalline nickel thin films

In this chapter, we discuss the voltage control of magnetization in polycrystalline Ni thin film/piezoelectric actuator hybrids at room temperature. These systems in particular show large magnetoelastic coupling effects due to the absence of competing net crystalline magnetic anisotropies. They thus are ideal model systems to investigate the spin-mechanics scheme in terms of device applications. This chapter is organized as follows: after a short review of the material properties of Ni in Sec. 5.1 and the phenomenology of strain-induced magnetic anisotropy in polycrystalline ferromagnetic thin films in Sec. 5.2, we discuss the magnetic anisotropy as a function of the voltage V_p applied to the actuator, relying on ferromagnetic resonance (FMR) and angle-dependent magnetoresistance (ADMR) experiments in Secs. 5.3 and 5.4, respectively. More precisely, FMR spectroscopy demonstrates the influence of the strain-induced magnetoelastic anisotropy in initially magnetically isotropic films. It furthermore shows that the magnetic anisotropy can be inverted, i.e., the in-plane magnetic easy axes can be switched by 90°, upon changing the polarity of V_p. The anisotropic magnetoresistance measurements in combination with x-ray diffraction measurements show that the voltage-controlled changes in the magnetic anisotropy of the Ni/piezoelectric actuator hybrid can be fully and quantitatively modeled within magnetoelastic theory. Using superconducting quantum interference device (SQUID) magnetometry, the evolution of the magnetization orientation is traced both as a function of V_p and of the external magnetic field in Sec. 5.5. Changing V_p allows to irreversibly switch the magnetization orientation by up to 180° and to reversibly rotate the remanent magnetization orientation within a range of about 80°. All SQUID data can be quantitatively understood in terms of a single-domain (macrospin) Stoner-Wohlfarth type of approach using the free energy density determined from the FMR experiments. In Sec. 5.6 we estimate the domain-wall formation energy, which exceeds the voltage-controlled changes in the free energy density. Hence, this gives further evidence that we can describe the changes in the magnetization orientation in terms of coherent magnetization rotation in a macrospin model in good approximation. In Sec. 5.7 we exploit the intrinsically hysteretic strain-voltage curve of the piezoelectric actuator to deterministically generate two different elastic strain states at zero applied voltage, which in

turn correspond to two distinct remanent magnetization orientation states in the ferromagnetic thin film connected to the actuator. The magnetization state can be described in a macrospin model evidencing two distinct nonvolatile remanent magnetization states enclosing an angle of 15°. Our results thus demonstrate a nonvolatile, reversible, and all-electric-field control of remanent magnetization. Finally, we have studied the validity and limitations of a macrospin approach to the voltage-controlled magnetization manipulation in Sec. 5.8 by using simultaneous spatially resolved MOKE and integral magnetotransport measurements. By correlating an effective magnetization orientation (macrospin) extracted from spatially averaged Kerr images with AMR measurements, we find that a macrospin approach is adequate to describe the magnetization as a function of V_p, with the exception for $\mathbf{H}$ along a magnetically easy direction in a narrow region around the magnetic coercive field—where the magnetization reorientation evolves via domain effects. Thus, on length scales much larger than the typical magnetic domain size, the voltage control of magnetization can be described in terms of a simple Stoner-Wohlfarth type macrospin model.

All measurements shown in this chapter are recorded at room temperature. Some results presented in the following have been published in Refs. [208, 209] and have been submitted for publication [210].

5.1 Nickel: Material properties

The ferromagnetic constituent nickel (Ni) has been chosen as it is a prototype 3d-transition itinerant ferromagnet with a Curie temperature $T_\mathrm{C} = 627\,\mathrm{K}$ [211] well above room temperature. Nickel crystallizes in the face-centered-cubic (fcc) structure with the room temperature lattice constant $a = 0.3524\,\mathrm{nm}$ [212] and exhibits the bulk elastic stiffness constants $c_{11} = 2.50 \times 10^{11}\,\mathrm{N/m^2}$, $c_{12} = 1.60 \times 10^{11}\,\mathrm{N/m^2}$, and $c_{44} = 1.185 \times 10^{11}\,\mathrm{N/m^2}$ [115]. The bulk saturation magnetization of Ni is $M_\mathrm{s} = 493\,\mathrm{kA/m}$ [213], and the magnetostrictive constants amount to $\lambda_{100} = -45.9 \times 10^{-6}$ and $\lambda_{111} = -24.3 \times 10^{-6}$ [115], which result for polycrystalline Ni in a considerable volume magnetostriction $\bar{\lambda} = -32.9 \times 10^{-6}$ [cf. Eq. (2.16)]. Nickel furthermore shows a moderate AMR ratio $\Delta\rho/\rho_0 = 2\,\%$ at room temperature [199] and a g-factor of 2.165 [214].

The Ni films were deposited onto an area of $3\,\mathrm{mm^2} \leq A \leq 5\,\mathrm{mm^2}$ on the actuators using electron beam evaporation at a base pressure of $2 \times 10^{-8}\,\mathrm{mbar} \leq p \leq 7 \times 10^{-8}\,\mathrm{mbar}$. To allow for an optimized interfacial strain coupling between the ferromagnetic and piezoelectric compounds, the ferromagnetic films were directly deposited onto the actuators, which are by default encapsulated with a $< 50\,\mu\mathrm{m}$ thick epoxy-based coating for electrical isolation [133]. The films had thicknesses ranging from 50 nm to 100 nm. Subsequently, we deposited between 5 nm and 10 nm thick Au films in situ to prevent oxidation of the Ni films.

We also address Ni thin films deposited onto single-crystal magnesium oxide (MgO) substrates (Sec. 5.4). MgO crystallizes in the fcc structure with the room temperature lattice constant $a = 0.4212\,\mathrm{nm}$ [215]. It is an insulator and exhibits

the elastic stiffness constants $c_{11} = 2.966 \times 10^{11}\,\mathrm{N/m^2}$, $c_{12} = 0.959 \times 10^{11}\,\mathrm{N/m^2}$, and $c_{44} = 1.562 \times 10^{11}\,\mathrm{N/m^2}$ [216].

5.2 Phenomenology of strain-induced magnetic anisotropy

The magnetoelastic energy density for a polycrystalline ferromagnet is given by Eq. (2.13),

$$F_{\mathrm{magel}} = \frac{3}{2}\bar{\lambda}\left(c_{12}^{\mathrm{Ni}} - c_{11}^{\mathrm{Ni}}\right)\left[\epsilon_1\left(m_x^2 - \frac{1}{3}\right) + \epsilon_2\left(m_y^2 - \frac{1}{3}\right) + \epsilon_3\left(m_z^2 - \frac{1}{3}\right)\right], \tag{5.1}$$

where ϵ_1, ϵ_2, and ϵ_3 denote the strains along the $\mathbf{x}$, $\mathbf{y}$, and $\mathbf{z}$ axis of the piezoelectric actuator (see Fig. 3.2). The effects of shear strains ϵ_i $(i = 4, 5, 6)$ average out in a polycrystalline material and thus are omitted. As we here investigate magnetoelastic effects in polycrystalline ferromagnets, we do not consider any crystalline anisotropies, which also average out in the ensemble of randomly oriented grains. Hence, the $\{\mathbf{x}, \mathbf{y}, \mathbf{z}\}$ crystal coordinate system and the $\{\mathbf{x}', \mathbf{y}', \mathbf{z}'\}$ actuator coordinate system coincide [cf. Fig. 3.4(b)], and thus throughout this chapter we use $\mathbf{x}$, $\mathbf{y}$, and $\mathbf{z}$ to indicate the respective directions of the actuator for convenience. Evidently, Eq. (5.1) comprises a superposition of three uniaxial anisotropies along the actuator's coordinate axes. Thus, since $m_x^2 + m_y^2 + m_z^2 = 1$ (cf. Sec. 2.2.1), and furthermore omitting terms independent of the magnetization direction, Eq. (5.1) can be rewritten as

$$F_{\mathrm{magel}} = K_{\mathrm{magel}}^{y} m_y^2 + K_{\mathrm{magel}}^{z} m_z^2 \tag{5.2}$$

with

$$\begin{aligned} K_{\mathrm{magel}}^{y} &= \frac{3}{2}\bar{\lambda}\left(c_{12}^{\mathrm{Ni}} - c_{11}^{\mathrm{Ni}}\right)(\epsilon_2 - \epsilon_1), \\ K_{\mathrm{magel}}^{z} &= \frac{3}{2}\bar{\lambda}\left(c_{12}^{\mathrm{Ni}} - c_{11}^{\mathrm{Ni}}\right)(\epsilon_3 - \epsilon_1). \end{aligned} \tag{5.3}$$

Using Eqs. (3.15), we can express Eqs. (5.3) as a function of the strain ϵ_2 along the dominant in-plane elongation direction (see Sec. 5.3):

$$\begin{aligned} K_{\mathrm{magel}}^{y} &= \frac{3}{2}\bar{\lambda}\left(c_{12}^{\mathrm{Ni}} - c_{11}^{\mathrm{Ni}}\right)(1 + \nu)\,\epsilon_2, \\ K_{\mathrm{magel}}^{z} &= \frac{3}{2}\bar{\lambda}\left(c_{12}^{\mathrm{Ni}} - c_{11}^{\mathrm{Ni}}\right)\left[-\frac{c_{12}}{c_{11}}(1 - \nu) + \nu\right]\epsilon_2, \end{aligned} \tag{5.4}$$

and as a function of the out-of-plane strain ϵ_3 (see Sec. 5.4):

$$\begin{aligned} K_{\mathrm{magel}}^{y} &= \frac{3}{2}\bar{\lambda}\left(c_{12}^{\mathrm{Ni}} - c_{11}^{\mathrm{Ni}}\right)\left[-\frac{c_{11}}{c_{12}}\frac{(1 + \nu)}{(1 - \nu)}\right]\epsilon_3, \\ K_{\mathrm{magel}}^{z} &= \frac{3}{2}\bar{\lambda}\left(c_{12}^{\mathrm{Ni}} - c_{11}^{\mathrm{Ni}}\right)\left[-\frac{c_{11}}{c_{12}}\frac{\nu}{(1 - \nu)} + 1\right]\epsilon_3. \end{aligned} \tag{5.5}$$

Assuming that the magnetoelastic energy density [Eq. (5.2)] is the only in-plane contribution to the total free energy density F—as we will see in the following section—we now can illustrate the effect of strain on the magnetization orientation. Since in equilibrium the magnetization vector aligns along a local minimum of F, the equilibrium magnetization orientation (Θ_0, Φ_0)[1] can be determined as function of the strain and thus as a function of V_p by minimizing F ($\partial_\Theta F|_{\Theta=\Theta_0} = \partial_\Phi F|_{\Phi=\Phi_0} = 0$ with $\partial^2_\Theta F|_{\Theta=\Theta_0}\,, \partial^2_\Phi F|_{\Phi=\Phi_0} > 0$). According to Sec. 5.1, $\frac{3}{2}\bar{\lambda}\left(c_{12}^{\mathrm{Ni}} - c_{11}^{\mathrm{Ni}}\right) > 0$ for Ni, and thus Eq. (5.1) results in the magnetic easy axis being oriented parallel to compressive strain ($\epsilon < 0$) and orthogonal to tensile strain ($\epsilon > 0$) in the absence of external magnetic fields. Due to the strong uniaxial out-of-plane shape anisotropy for the thin Ni films, this easy axis is a global easy axis oriented in the film plane. Consequently, for a voltage $V_\mathrm{p} > 0$ ($\epsilon_2 > 0$), Eqs. (5.2) and (5.3) yield a magnetic easy axis and thus the equilibrium magnetization orientation along $\mathbf{x}$ (cf. Fig. 3.2), while accordingly for $V_\mathrm{p} < 0$ ($\epsilon_2 < 0$) the magnetization is oriented along $\mathbf{y}$. Hence, we expect a 90° rotation of the easy axis and thus a corresponding magnetization switching upon inverting the polarity of the voltage V_p.

5.3 Determination of magnetic anisotropy from FMR

In this section we quantitatively determine the magnetic anisotropy of the ferromagnetic thin film/piezoelectric hybrid structures using FMR spectroscopy. The sample discussed in detail here was fabricated by directly depositing a 70 nm thick Ni film onto an area of 5 mm^2 onto the the $\mathbf{x} - \mathbf{y}$ face of the actuator, which was subsequently in-situ capped with a 10 nm thick Au film. The data presented in this section were recorded by M. Weiler in the framework of his diploma thesis [217]. Figure 5.1(a) shows four FMR spectra recorded at room temperature with $\mathbf{H} \parallel \mathbf{y}$ and voltages $V_\mathrm{p} = -30\,\mathrm{V}$, 0 V, +30 V, and +90 V applied to the actuator. Each spectrum shows a single strong resonance, whose resonance field $\mu_0 H_\mathrm{res}$ is determined as the arithmetic mean of its maximum and minimum and depicted by the squares in Fig. 5.1(a). Within the voltage range $-30\,\mathrm{V} \leq V_\mathrm{p} \leq +90\,\mathrm{V}$, $\mu_0 H_\mathrm{res}$ shifts to higher magnetic fields by 46 mT, while the peak-to-peak linewidth of $\mu_0 \Delta H_\mathrm{pp} = 23\,\mathrm{mT}$ is not significantly changed as it varies by only 1 mT.

To determine the evolution of $\mu_0 H_\mathrm{res}$ with V_p in more detail, we recorded FMR spectra for V_p increasing from −30 V to +90 V (upsweep) and decreasing back to −30 V (downsweep) in steps of $\Delta V_\mathrm{p} = 10\,\mathrm{V}$. According to Fig. 5.1(a), for $\mathbf{H} \parallel \mathbf{y}$ we obtain an increasing resonance field $\mu_0 H_\mathrm{res}$ for increasing V_p and a decreasing resonance field for decreasing V_p, as shown by the black squares in Fig. 5.1(b). As indicated by the black arrows, full symbols depict the upsweep and open symbols the downsweep of V_p. The hysteresis between up- and downsweep is due to the hysteretic expansion and contraction of the actuator [cf. Fig. 3.3(c)]. Analogous measurements with $\mathbf{H} \parallel \mathbf{x}$ yield the resonance fields shown by the red circles in Fig. 5.1(b). As expected from Eq. (3.9), the resonance field along this magnetic field direction exhibits the converse behavior, i.e., $\mu_0 H_\mathrm{res}$ decreases for increasing

[1] for definition of Θ and Φ, see Fig. 4.4

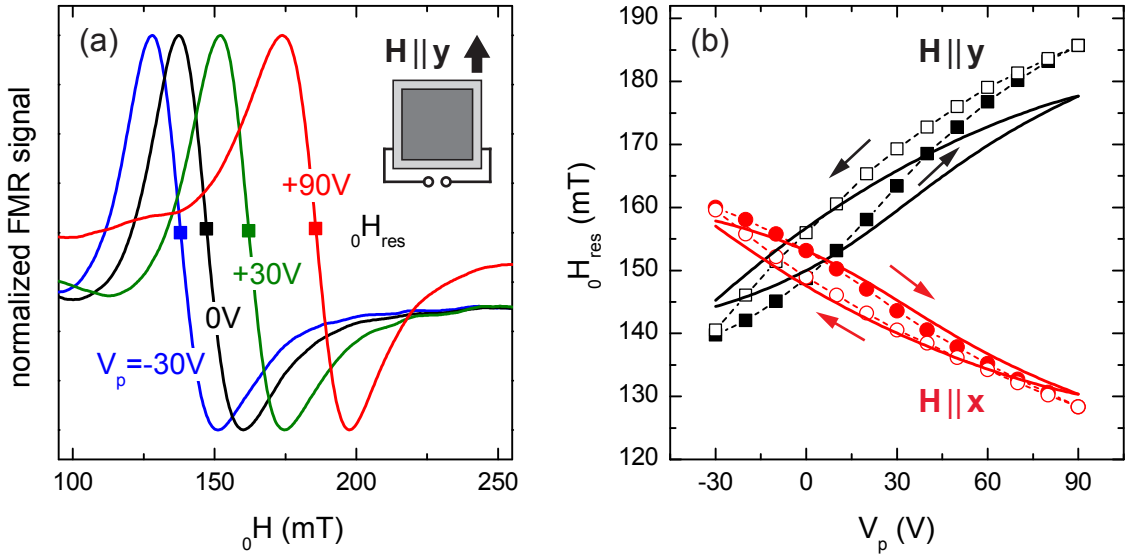

Figure 5.1: (a) Room-temperature, X-band FMR spectra with $\mathbf{H} \parallel \mathbf{y}$ at different voltages V_p. The resonance field $\mu_0 H_\mathrm{res}$ (squares) systematically increases for increasing V_p while the lineshape is not significantly altered. (b) The dependence of $\mu_0 H_\mathrm{res}$ on V_p for $\mathbf{H} \parallel \mathbf{y}$ (black squares) and $\mathbf{H} \parallel \mathbf{x}$ (red circles) for a V_p upsweep (full symbols) and downsweep (open symbols). For $\mathbf{H} \parallel \mathbf{y}$, increasing V_p increases $\mu_0 H_\mathrm{res}$ and thus this direction becomes magnetically harder, while for $\mathbf{H} \parallel \mathbf{x}$, increasing V_p decreases $\mu_0 H_\mathrm{res}$ and thus this direction becomes magnetically easier. The hysteresis of $\mu_0 H_\mathrm{res}$ is due to the hysteretic expansion and contraction of the actuator. The solid lines represent the numerically simulated FMR fields yielding very good agreement with the measurement.

V_p and vice versa. Hence, according to Secs. 5.2 and 4.1.4, for increasing V_p the $\mathbf{y}$ direction becomes magnetically harder while the $\mathbf{x}$ direction simultaneously becomes easier. Neglecting the small hysteretic behavior, we can state as a general rule that for $V_\mathrm{p} > 0\,\mathrm{V}$ the $\mathbf{x}$ direction is magnetically easier than the $\mathbf{y}$ direction, while for $V_\mathrm{p} < 0\,\mathrm{V}$ the $\mathbf{y}$ direction is magnetically easier than the $\mathbf{x}$ direction. At $V_\mathrm{p} = 0\,\mathrm{V}$, we obtain a resonance field of $\mu_0 H_\mathrm{res} \approx 150\,\mathrm{mT}$ for $\mathbf{H} \parallel \mathbf{y}$ as well as for $\mathbf{H} \parallel \mathbf{x}$, and thus at this voltage both orientations are magnetically equal, as expected for easy-plane films.

To quantitatively model the evolution of the FMR fields, we use the total free energy density

$$\begin{aligned} F &= F_\mathrm{Zeeman} + F_\mathrm{demag} + F_\mathrm{magel} \\ &= -\mu_0 H M \left(\sin\Theta \sin\Phi \sin\theta \sin\phi + \cos\Theta \cos\theta + \sin\Theta \cos\Phi \sin\theta \cos\phi\right) \\ &\quad + \frac{1}{2}\mu_0 M^2 \sin^2\Theta \cos^2\Phi \\ &\quad + K^y_\mathrm{magel} \cos^2\Theta + K^z_\mathrm{magel} \sin^2\Theta \cos^2\Phi, \end{aligned} \tag{5.6}$$

which includes only two anisotropy contributions, the uniaxial out-of-plane oriented shape anisotropy and the magnetoelastic anisotropy contribution Eq. (5.2) using Eqs. (5.4). The resonance fields are calculated by numerically evaluating Eqs. (4.7)

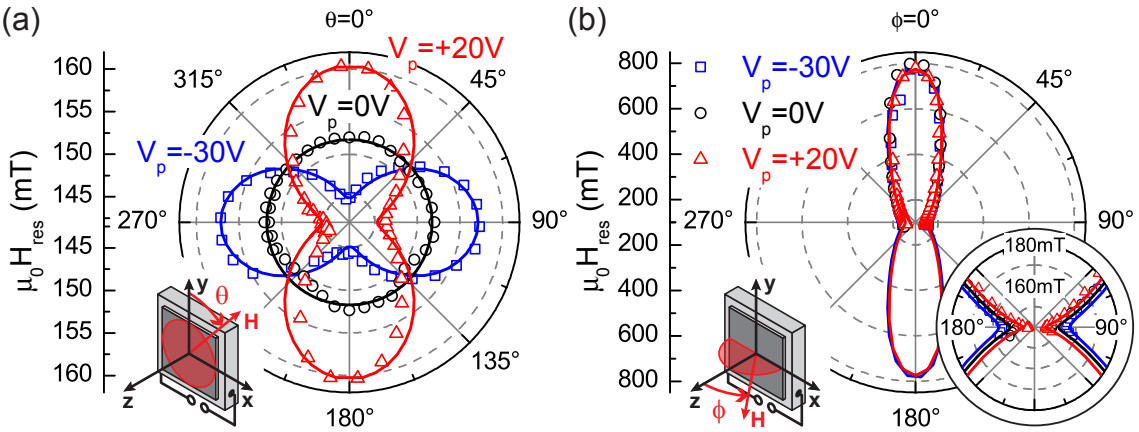

Figure 5.2: Angular dependence of the ferromagnetic resonance fields as a function of the external magnetic field orientation **H** and the voltage V_p. The symbols represent the experimental data (blue squares for $V_\mathrm{p} = -30\,\mathrm{V}$, black circles for $V_\mathrm{p} = 0\,\mathrm{V}$, and red triangles for $V_\mathrm{p} = +20\,\mathrm{V}$), and the lines show the corresponding simulations. (a) The FMR fields $\mu_0 H_\mathrm{res}(\theta)$ for a rotation of **H** in the film plane are independent of θ for $V_\mathrm{p} = 0\,\mathrm{V}$. However, a uniaxial anisotropy is observed for $V_\mathrm{p} \neq 0\,\mathrm{V}$, with the easy axis being rotated by 90° from $\theta = 0°$ to $\theta = 90°$ as V_p is changed from $-30\,\mathrm{V}$ to $+20\,\mathrm{V}$. (b) Corresponding experiments yield $\mu_0 H_\mathrm{res}(\phi)$ for a rotation of **H** in the **y** plane. A strong uniaxial anisotropy with the hard axis perpendicular to the film plane is observed. The inset shows that the resonance fields for **H** in the film plane ($\phi = 90°$ and $\phi = 270°$) are shifted as a function of V_p in accordance to the data shown in (a) for $\theta = 90°$ and $\theta = 270°$.

and (4.8), and plotted as solid lines in Fig. 5.1(b). We use a saturation magnetization $M_\mathrm{s} = 370\,\mathrm{kA/m}$, as determined by SQUID measurements, and a g-factor of 2.165 [214]. The strain $\epsilon_2(V_\mathrm{p})$ was measured using a strain gauge in the voltage range of $-30\,\mathrm{V} \leq V_\mathrm{p} \leq +90\,\mathrm{V}$. The simulation is in excellent agreement with the experiment for $\mathbf{H} \parallel \mathbf{x}$ (solid red line), while for $\mathbf{H} \parallel \mathbf{y}$ (solid black line) the measured $\mu_0 H_\mathrm{res}(V_\mathrm{p})$ dependence shows a slightly greater slope compared to the simulation. If we, however, consider that Eq. (5.6) contains no free fit parameter but only measured quantities and literature values for the material constants, the simulation is in very good agreement with the experimental results.

To quantitatively determine the full magnetic anisotropy as a function of V_p, we recorded FMR traces at constant V_p for several different **H** orientations. Adopting the angle convention from Fig. 4.4 (also shown in the insets in Fig. 5.2), we particularly obtain $\mu_0 H_\mathrm{res}(\theta)$ for a rotation of **H** in the film plane [Fig. 5.2(a), $\phi = 90°$] and $\mu_0 H_\mathrm{res}(\phi)$ for a rotation of **H** in a plane perpendicular to the film plane [Fig. 5.2(b), $\theta = 90°$] at constant voltages $V_\mathrm{p} = -30\,\mathrm{V}$, $0\,\mathrm{V}$, $+20\,\mathrm{V}$, and $+90\,\mathrm{V}$ (the data for the latter voltage are not shown in Fig. 5.2). In Fig. 5.2, blue squares represent the resonance fields obtained for $V_\mathrm{p} = -30\,\mathrm{V}$, black circles those for $V_\mathrm{p} = 0\,\mathrm{V}$, and red triangles those for $V_\mathrm{p} = +20\,\mathrm{V}$.

For a rotation of **H** in the film plane [Fig. 5.2(a)], $\mu_0 H_\mathrm{res}(\theta)$ shows no angular dependence for $V_\mathrm{p} = 0\,\mathrm{V}$, as expected for an isotropic polycrystalline ferromagnetic thin film. Moreover, the resonance fields exhibit minima at $\theta = 0°$ and $\theta = 180°$ for $V_\mathrm{p} = -30\,\mathrm{V}$ and at $\theta = 90°$ and $\theta = 270°$ for $V_\mathrm{p} = +20\,\mathrm{V}$, respectively. Thus, a 180°

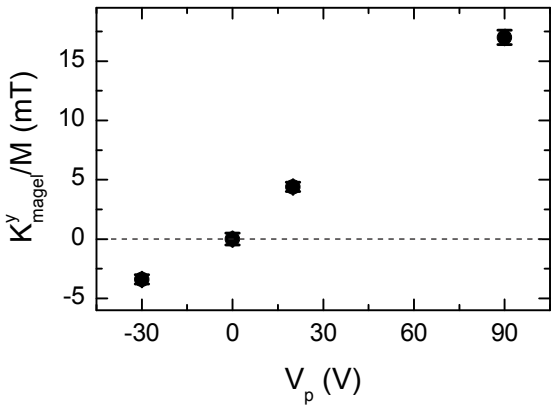

Figure 5.3: The sign of the in-plane anisotropy field K^y_{magel}/M can be inverted by changing the polarity of V_p and thus results in a rotation of the in-plane easy axis by 90°.

periodicity of the resonant fields and hence a uniaxial magnetic anisotropy in the film plane is observed for voltages $V_\mathrm{p} \neq 0\,\mathrm{V}$. As the orientations θ corresponding to minima of $\mu_0 H_\mathrm{res}$ for one voltage coincide with maxima for the other voltage, the direction of the easy axis evidently is rotated by 90° upon a change of V_p from $V_\mathrm{p} = -30\,\mathrm{V}$ to $V_\mathrm{p} = +20\,\mathrm{V}$.

A rotation of **H** from within the film plane ($\theta = 90°$, $\phi = 90°$) to perpendicular to the film plane ($\theta = 90°$, $\phi = 0°$) yields the resonance fields shown in Fig. 5.2(b). We observe a dominating strong uniaxial shape anisotropy with a magnetic hard axis perpendicular to the film plane (almost) independent of V_p. The inset in Fig. 5.2(b) shows that for **H** in the film plane along $\phi = 90°$ and $\phi = 270°$, the resonance fields for $V_\mathrm{p} = -30\,\mathrm{V}$ and $V_\mathrm{p} = +20\,\mathrm{V}$ are shifted by approximately 10 mT in full accordance to the data in Fig. 5.2(a).

To finally obtain the anisotropy fields as a function of V_p, we simulated the angular dependence of $\mu_0 H_\mathrm{res}$ again using the total free energy density given in Eq. (5.6). Hereby, we employ K^y_{magel} as the only fit parameter in Eq. (5.6), and determine the anisotropy fields K^y_{magel}/M depicted in Fig. 5.3. The respective calculated resonance fields are displayed by the lines in Fig. 5.2. The good agreement between simulation and experiment demonstrates that the magnetic anisotropy contributions included in Eq. (5.6) are sufficient to model the magnetic anisotropy of the hybrid system. As evident from Eq. (5.6), the magnetoelastic contribution exclusively determines the in-plane anisotropy, thus a sign change of K^y_{magel} (cf. Fig. 5.3) results in an inversion of the in-plane magnetic anisotropy [cf. Fig. 5.2(a)].

In summary, the FMR experiments conclusively demonstrate that we can invert the in-plane magnetic anisotropy of our hybrid structure solely by inverting the polarity of the voltage V_p applied to the actuator. As the FMR experiment furthermore allows to quantitatively determine all contributions to the total free energy density [Eq. (5.6)], the equilibrium orientation of the magnetization **M** can be calculated a priori for arbitrary **H** and V_p. However, it is not possible to directly measure the magnetization orientation with FMR spectroscopy. To this end, we will apply

SQUID magnetometry in Sec. 5.5 to directly detect the magnetization.

5.4 Determination of magnetic anisotropy from ADMR

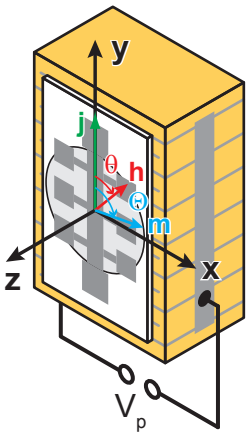

Fig. 5.4: Illustration of the alignment of the Ni Hall bar with the current density $\mathbf{j} \parallel \mathbf{y}$.

We also determine the magnetic anisotropy from magnetotransport experiments in a 50 nm thick Ni film deposited onto a MgO substrate. After patterning the film into 80 μm wide Hall bars with the longitudinal voltage probes separated by 200 μm using optical lithography and Ar milling, we cut the sample into pieces with lateral dimensions of $2 \times 2\,\mathrm{mm}^2$ and polished the MgO substrate down to a thickness of 50 μm. As schematically depicted in Fig. 5.4, the samples were cemented [126] onto piezoelectric actuators (piezoelectric actuator-epoxy-MgO/Ni) annealed for 3 h at 100°C, and the Hall bar was aligned such that the current direction $\mathbf{j}$ and the MgO $\langle 100 \rangle$ crystal axis are parallel to the $\mathbf{y}$ direction of the actuator. We note that for consistency the angular convention from the previous section is used for the magnetotransport measurements discussed in this section [cf. Figs. 4.4 and 5.4]. The sample was then mounted on a rotatable sample stage to carry out the magnetotransport experiments in a superconducting magnet cryostat at $T = 300\,\mathrm{K}$. The resistivities ρ_{long} along the dc bias current density $\mathbf{j}$ and ρ_{trans} perpendicular to $\mathbf{j}$ were recorded via four-point measurements. The magnetic anisotropy is quantitatively derived from $\{\rho_{\mathrm{long}}(\theta), \rho_{\mathrm{trans}}(\theta)\}$ traces recorded in the course of M. Wagner's diploma thesis [218] using ADMR measurements as a function of the magnetic field orientation θ in the film plane at fixed external magnetic field strength. Prior to each angular scan, the magnetization was aligned into a well-defined initial state by applying a field of $\mu_0 H = +3\,\mathrm{T}$ along $\theta = 90°$. Subsequently, we lowered the field to the measurement field and started the angular scan for a rotation of $\mathbf{H}$ in the film plane. Since the magnetization orientation is confined within the film plane due to strong shape anisotropy (cf. Sec. 5.3) and since we aim to obtain the in-plane anisotropy, angular scans in a plane perpendicular to the film plane yield only redundant information and are thus omitted. We investigated two samples with almost identical results, therefore we here focus on the sample which was most extensively characterized.

Figure 5.5 shows $\{\rho_{\mathrm{long}}(\theta), \rho_{\mathrm{trans}}(\theta)\}$ traces measured at $V_{\mathrm{p}} = 0\,\mathrm{V}$ at magnetic field strengths $\mu_0 H = 1000\,\mathrm{mT}$ and 50 mT. Evidently, the curves for different external magnetic field strength differ for both ρ_{long} [Fig. 5.5(a)] and ρ_{trans} [Fig. 5.5(b)], which, contrary to the sample investigated in the precious section [cf. black symbols and the black line in Fig. 5.2(a)], indicates a uniaxial anisotropy already present at $V_{\mathrm{p}} = 0\,\mathrm{V}$. The angular dependence corresponds to the cases (c) and (d) in Fig. 4.10 for $\rho_0, \rho_1, \rho_7 > 0$. Note that in Fig. 4.10 $\rho_1 < 0$, which accounts for the qualitative deviations in ρ_{long} compared to Fig. 5.5(a). We thus identify a voltage-independent

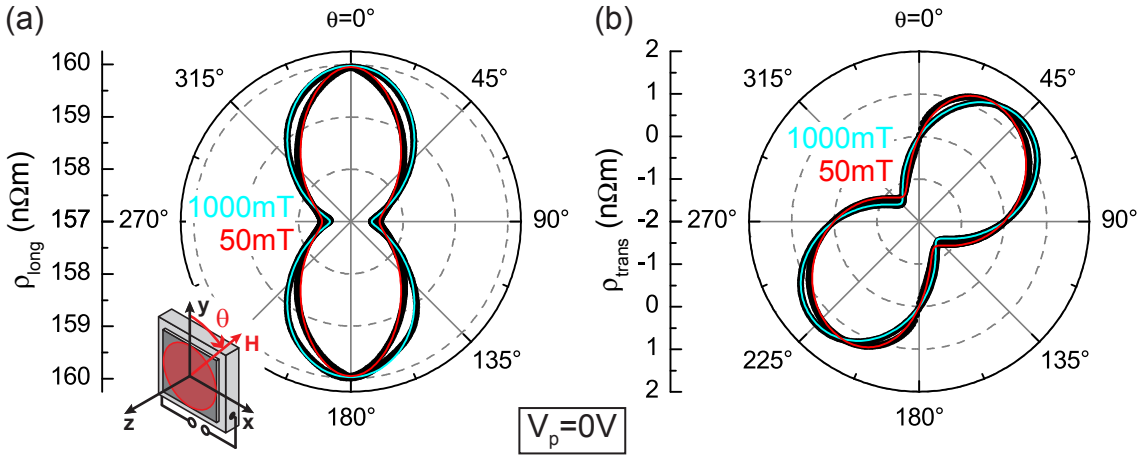

Figure 5.5: (a) Longitudinal resistivity $\rho_{\mathrm{long}}(\theta)$ and (b) transverse resistivity $\rho_{\mathrm{trans}}(\theta)$ for constant external magnetic fields $\mu_0 H = 1000\,\mathrm{mT}$ and $50\,\mathrm{mT}$ rotated within the film plane at $V_{\mathrm{p}} = 0\,\mathrm{V}$. The black symbols represent the experimental data, the blue and red lines show the corresponding simulations for $\mu_0 H = 1000\,\mathrm{mT}$ and $50\,\mathrm{mT}$, respectively.

magnetic hard axis along **y** by the rather abrupt changes observed along $\theta = 0°$ for small magnetic fields. Such a uniaxial anisotropy in the film plane is observed in all samples where a ferromagnetic film is affixed to the actuator via cementing of a substrate and stems from the highly anisotropic thermal expansion coefficient of the piezoelectric actuator stack ($+1\,\mathrm{ppm/K}$ along **y** and $-3\,\mathrm{ppm/K}$ along **x** [219]), as also reported in Ref. [220]. The samples are clamped onto the actuator as the two-component epoxy is cured at $T = 100°\mathrm{C}$. Upon cooling to room temperature, the anisotropic contraction of the actuator builds up tensile strain along the **y** direction in the plane of the ferromagnetic thin film layer, which results in a uniaxial magnetic anisotropy. Since annealing is not necessary in the Ni films directly evaporated onto piezoelectric actuators, the ferromagnetic films are not strained at $V_{\mathrm{p}} = 0\,\mathrm{V}$ and thus the film plane is magnetically isotropic.

To determine the magnetic anisotropy, we recorded $\{\rho_{\mathrm{long}}(\theta), \rho_{\mathrm{trans}}(\theta)\}$ traces at constant magnetic field strength $\mu_0 H = 50\,\mathrm{mT}$ for different voltages $-30\,\mathrm{V} \leq V_{\mathrm{p}} \leq +150\,\mathrm{V}$ applied to the actuator, where representatively the curves for $V_{\mathrm{p}} = -30\,\mathrm{V}$ and $+150\,\mathrm{V}$ are shown in Fig. 5.6 by the black symbols. This magnetic field magnitude was chosen as it is small enough so that the evolution of $\{\rho_{\mathrm{long}}(\theta), \rho_{\mathrm{trans}}(\theta)\}$ clearly exhibits the influence of the strain-dependent magnetic anisotropy, but up- and downsweep still coincide, indicative of negligible domain formation. As shown in Figs. 5.6(a) and (b), the ADMR data exhibit increasingly abrupt changes at $\theta = 0°$ for increasing V_{p}, and thus, in agreement with the sample characterized in the previous section, an increasing magnetically hard uniaxial axis along **y**.

To finally quantitatively model the evolution of the ADMR data, we calculate the resistivities by using Eqs. (4.30),

$$\begin{aligned} \rho_{\mathrm{long}}^{\mathrm{poly}} &= \rho_0 + \rho_1 \cos^2 \Theta, \\ \rho_{\mathrm{trans}}^{\mathrm{poly}} &= \frac{1}{2}\rho_2 \sin(2\Theta), \end{aligned} \tag{5.7}$$

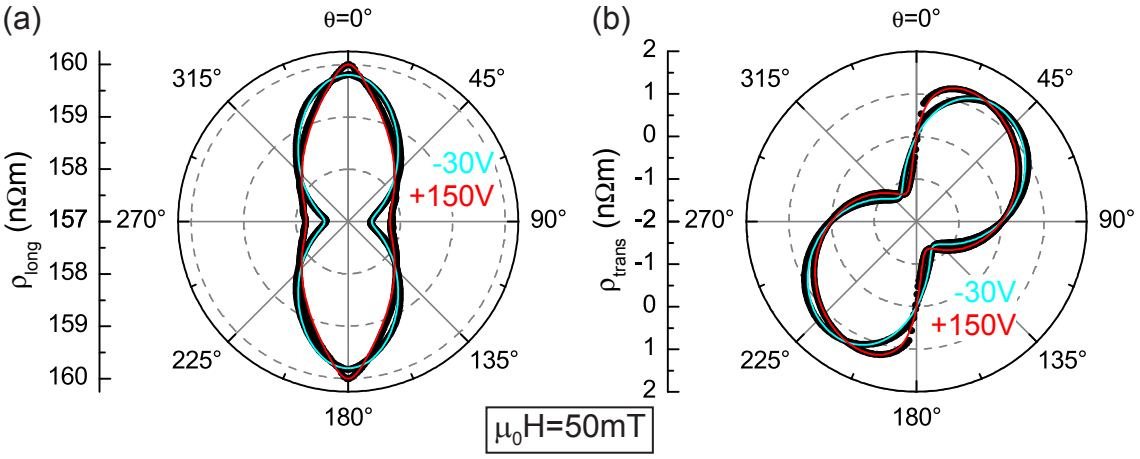

Figure 5.6: (a) Longitudinal resistivity $\rho_{\mathrm{long}}(\theta)$ and (b) transverse resistivity $\rho_{\mathrm{trans}}(\theta)$ for a constant external magnetic field $\mu_0 H = 50\,\mathrm{mT}$ rotated within the film plane at different voltages $V_{\mathrm{p}} = -30\,\mathrm{V}$ and $+150\,\mathrm{V}$. The black symbols denote the experimental data, the blue and red lines represent the corresponding simulations for $V_{\mathrm{p}} = -30\,\mathrm{V}$ and $+150\,\mathrm{V}$, respectively.

where ρ_i $(i = 0, 1, 2)$ are phenomenological resistivity parameters. The direction of the magnetization $\mathbf{M}(\Theta, \Phi)$ and thus the angle Θ in Eqs. (5.7) is calculated by numerically minimizing the corresponding free energy density F with respect to Θ and Φ. Therefore, we again use Eq. (5.6),

$$F = F_{\mathrm{Zeeman}} + F_{\mathrm{demag}} + F_{\mathrm{u}}^{y} + F_{\mathrm{magel}}, \tag{5.8}$$

with an additional uniaxial anisotropy contribution $F_{\mathrm{u}}^{y} = K_{\mathrm{u}}^{y} m_y^2 = K_{\mathrm{u}}^{y} \cos^2\Theta$ in the film plane, which accounts for the voltage-independent magnetic hard axis along $\mathbf{y}$. The simulations of the ADMR curves are then determined by an iterative fit procedure of the resistivity and anisotropy parameters from Eqs. (5.7) and (5.8), as described in Sec. 4.4.2.

To fully model the data within the framework of magnetoelasticity, we quantified the amount of strain induced in the sample by the piezoelectric actuator using x-ray diffraction on the supporting MgO substrate. A direct measurement of the in-plane lattice constants and thus the strains ϵ_1 and ϵ_2 via reciprocal space maps did not prove useful for a quantitative analysis due to the wide spatial expansion of the reflections. As $2\vartheta - \vartheta$ scans allow for a determination of the out-of-plane lattice constant (and thus the corresponding strains ϵ_3) with much higher precision, we use Eqs. (5.5) to determine the magnetoelastic contribution in Eq. (5.8). As evident from Fig. 5.7(a), the MgO (004) reflections clearly shift with V_{p}. The peak position was determined by Split Pearson VII fits [221] as representatively shown in Fig. 5.7(a) by the gray dashed curve for $V_{\mathrm{p}} = +150\,\mathrm{V}$, and the out-of-plane lattice constant c^{MgO} was then calculated according to Sec. 4.5. The out-of-plane strain $\epsilon_3^{\mathrm{MgO}} = (c^{\mathrm{MgO}} - c_0^{\mathrm{MgO}})/c_0^{\mathrm{MgO}}$, where c_0^{MgO} is the lattice constant for $V_{\mathrm{p}} = 0\,\mathrm{V}$, is shown by the full black circles in Fig. 5.7(b) and changes linearly with V_{p}. Using Eqs. (3.15) with $c_{11} = c_{11}^{\mathrm{MgO}}$ and $c_{12} = c_{12}^{\mathrm{MgO}}$, the overall change $\Delta\epsilon_3^{\mathrm{MgO}} = \epsilon_3^{\mathrm{MgO}}(+150\,\mathrm{V}) - \epsilon_3^{\mathrm{MgO}}(-30\,\mathrm{V}) \approx -12 \times 10^{-5}$ observed experimentally corresponds

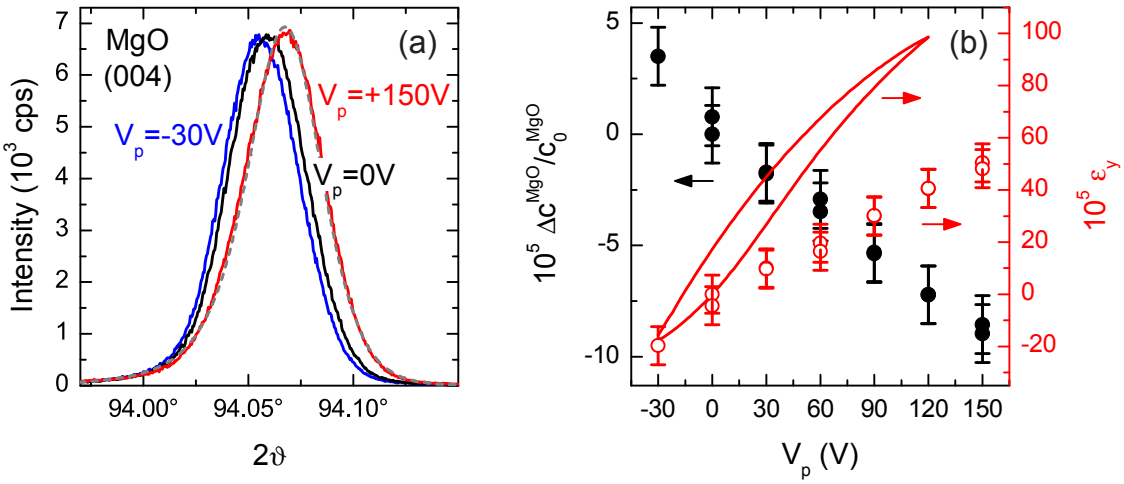

Figure 5.7: (a) XRD $2\vartheta - \vartheta$ scans show a systematic shift with V_p for the MgO (004) reflection (the blue, black, and red lines denote $V_\mathrm{p} = -30\,\mathrm{V}$, $0\,\mathrm{V}$, and $+150\,\mathrm{V}$, respectively). The gray dashed curve represents a fit to determine the peak position. (b) The out-of-plane strain $\epsilon_3^\mathrm{MgO} = (c^\mathrm{MgO} - c_0^\mathrm{MgO})/c_0^\mathrm{MgO}$ (full black symbols) changes linearly with V_p. The corresponding in-plane strain $\epsilon_2 = \epsilon_2^\mathrm{MgO}$ calculated using elastic theory is shown by the open red symbols. For comparison, the red line represents the strain ϵ_2 induced in the sample investigated in Sec. 5.3 measured using a strain gauge.

to $\Delta\epsilon_2^\mathrm{MgO} = \Delta\epsilon_2 \approx 70 \times 10^{-5}$ [open red circles in Fig. 5.7(b)]. This amounts to only about 50% of the strain the directly evaporated Ni thin film investigated in the previous section was exposed to [solid red line in Fig. 5.7(b)]. Assuming that the $50\,\mu$m thick sample does not significantly impede the elongation of the 2 mm thick actuator, the most likely cause for the reduced $\Delta\epsilon_2^\mathrm{MgO}$ value observed is imperfect strain transmission by the cement. Moreover, as apparent from comparing the error bar of ϵ_2^MgO with the hysteretic strain measured using a strain gauge in Fig. 5.7(b), the hysteresis cannot be resolved by x-ray diffraction measurements within the experimental error and the accuracy of the experiment thus accounts for the linear $\epsilon_3^\mathrm{MgO}(V_\mathrm{p})$ behavior and coinciding up- and downsweep.

The simulations using the experimentally determined ϵ_3^MgO and a saturation magnetization $M_\mathrm{s} = 404\,\mathrm{kA/m}$ obtained by SQUID measurements are shown by the solid lines in Figs. 5.5 and 5.6. The value for ρ_0 decreases from $\rho_0\,(50\,\mathrm{mT})$ to $\rho_0\,(1000\,\mathrm{mT})$ by 0.1% due to the influence of negative magnetoresistance. Furthermore, the value for ρ_0 increases from $\rho_0\,(-30\,\mathrm{V})$ to $\rho_0\,(+150\,\mathrm{V})$ by 0.2%. This variation is attributed to the so-called piezoresistance or piezoresistive effect [222–224], which phenomenologically describes the relative change in electrical resistance R of a specimen with length L subjected to a physical strain, $\Delta R/R = \gamma \Delta L/L$, with the gauge factor $\gamma = 2.7$ for evaporated Ni films [225]. For our overall change of $\epsilon_2 \approx 70 \times 10^{-5}$ we obtain $\Delta R/R \approx 0.2\%$ and thus exactly confirm the experimental observation. Within error bars we did not observe a magnetic field dependence of ρ_1 and ρ_2. Furthermore, according to theory $\rho_1 \equiv \rho_2$ [cf. Eqs. (4.30)]. However, our simulations yield an increasing deviation between ρ_1 and ρ_2 for increasing V_p from about 11% at $V_\mathrm{p} = -30\,\mathrm{V}$ to 18% at $+150\,\mathrm{V}$, which is most likely due to the piezoresistive effect.

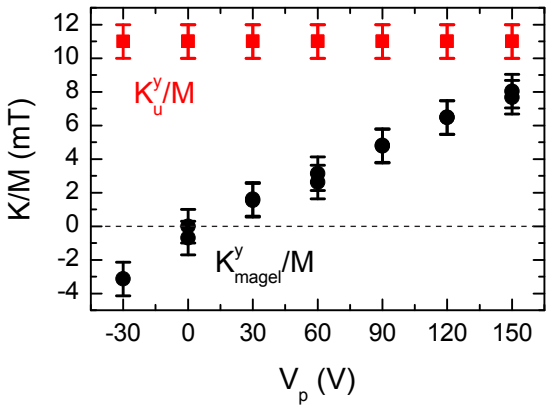

Figure 5.8: In-plane magnetic anisotropy fields of a Ni thin film cemented onto a piezoelectric actuator. The magnetoelastic in-plane anisotropy field K^y_{magel}/M (full black circles) is calculated using Eqs. (5.5) with the experimentally determined strain $\epsilon_3^{\mathrm{MgO}}$ displayed in Fig. 5.7(b). The full red squares denote the voltage-independent uniaxial magnetic anisotropy field K^y_{u}/M.

The voltage-independent anisotropy field $K^y_{\mathrm{u}}/M = 11\,\mathrm{mT}$ (full red squares in Fig. 5.8) is determined from the ADMR traces recorded at $V_{\mathrm{p}} = 0\,\mathrm{V}$ (cf. Fig. 5.5), and the magnetoelastic anisotropy field K^y_{magel}/M calculated using Eqs. (5.5) is shown in Fig. 5.8 by the full black circles. Evidently, as apparent from Figs. 5.5 and 5.6 the simulations are in excellent agreement with the experiment. This full accordance is particularly significant for the ADMR traces at low magnetic field in Figs. 5.5 and 5.6, as the differences between the curves are solely due to the voltage-dependent magnetoelastic contribution to the total free energy density. Since F_{magel} does not contain a fit parameter but is fully determined by the measured out-of-plane strain, we thus are able to entirely and quantitatively explain the strain-induced magnetic-anisotropy modifications in the framework of magnetoelasticity. However, in contrast to the sample characterized in the previous section, an inversion of the in-plane anisotropy is impeded in the current sample, as the voltage-controlled magnetoelastic anisotropy is superimposed by the in-plane anisotropy F^y_{u} (see Fig. 5.8). Hence, the effective in-plane anisotropy contribution $F^y_{\mathrm{u,eff}} = F^y_{\mathrm{u}} + F_{\mathrm{magel}}$ can only be adjusted within $8\,\mathrm{mT} \leq K^y_{\mathrm{u,eff}}/M \leq 19\,\mathrm{mT}$ for $-30\,\mathrm{V} \leq V_{\mathrm{p}} \leq +150\,\mathrm{V}$, but a voltage-induced sign change is not possible.

In summary, we have quantitatively modeled the angular dependences of the longitudinal and transverse resistivities in Ni/MgO/piezoelectric actuator hybrid systems using anisotropic magnetoresistance techniques. In analogy to the previous chapter, we thus are able to quantitatively determine all contributions to the free energy density. Moreover, by precisely determining the strain of the Ni thin film using x-ray diffraction, we find that the voltage-dependent resistivity curves are in full agreement with magnetoelastic theory. ADMR measurements therefore are shown to provide a powerful and comprehensive technique for probing magnetic anisotropy, in full equivalence to FMR spectroscopy.

5.5 Reversible and irreversible control of magnetization orientation

In the preceding sections, we have determined the magnetic anisotropy of our multifunctional hybrid structures via FMR (Sec. 5.3) and ADMR measurements (Sec. 5.4). The total free energy density obtained from these experiments allows to infer the magnetization orientation by minimizing F. However, two major implications result from this approach. First, for FMR spectroscopy the magnetization orientation is calculated a priori for a given external field $\mathbf{H}$ and an applied voltage V_p, but this technique is not suitable for directly measuring the magnetization orientation. Second, the free energy density ansatz relies on a single-domain Stoner-Wohlfarth model [97, 226]. This approach is justified for the FMR measurements, since the applied external field suffices to saturate the magnetization at the FMR fields $\mu_0 H_\mathrm{res} > 100\,\mathrm{mT}$ in the Ni samples investigated. An analogous argument applies to ADMR measurements, as a coincidence of recorded up- and downsweep curves again indicates a negligible domain formation. Moreover, the very good agreement between simulation and experiment for both techniques corroborates the single-domain assumption and thus evidences a saturated magnetic state in good approximation. However, as we are particularly aiming for a magnetization control at small or even vanishing external magnetic field, accompanying effects, e.g., domain formation, are not negligible. Therefore, in this section, we apply SQUID magnetometry, as this technique is directly sensitive to the magnetization M. More precisely, it detects the projection m of the magnetic moment $\mathbf{m}$ onto the direction of the externally applied magnetic field $\mathbf{H}$ [cf. Sec. 4.2][2]. To yield a comprehensive magnetization control we here focus on the hybrid sample discussed in Sec. 5.3, which particularly allows for a magnetic anisotropy inversion, and show that both a reversible and an irreversible control of the magnetization orientation is possible in the hybrid samples, solely by changing V_p.

In a first series of experiments, we recorded M as a function of the external magnetic field magnitude $\mu_0 H$ at fixed orientations of $\mathbf{H}$ and fixed voltages V_p at $T = 300\,\mathrm{K}$. Figure 5.9(a) shows $M(H)$ loops measured with $\mathbf{H} \parallel \mathbf{y}$ at constant voltage $V_\mathrm{p} = -30\,\mathrm{V}$ (blue squares) and $V_\mathrm{p} = +30\,\mathrm{V}$ (red circles). The rectangular loop for $V_\mathrm{p} = -30\,\mathrm{V}$ indicates a magnetic easy axis, while the smooth loop for $V_\mathrm{p} = +30\,\mathrm{V}$ is characteristic of a harder axis [101, 227]. This situation appears inverted for $\mathbf{H} \parallel \mathbf{x}$, as displayed in Fig. 5.9(b). Here, along the $\mathbf{x}$ direction we observe a magnetically easier loop for $V_\mathrm{p} = +30\,\mathrm{V}$ and a harder one for $V_\mathrm{p} = -30\,\mathrm{V}$. Hence, in full consistency with the FMR results shown in Fig. 5.1(b), for $V_\mathrm{p} = -30\,\mathrm{V}$ the $\mathbf{y}$ direction is magnetically easier than the $\mathbf{x}$ direction, while for $V_\mathrm{p} = +30\,\mathrm{V}$ the $\mathbf{x}$ direction is magnetically easier than the $\mathbf{y}$ direction. Moreover, incorporating the results depicted in Fig. 5.2(a), the $M(H)$ loops substantiate the magnetic easy axis being parallel to $\mathbf{y}$ for $V_\mathrm{p} = -30\,\mathrm{V}$ and parallel to $\mathbf{x}$ for $V_\mathrm{p} = +30\,\mathrm{V}$.

Before discussing the experimental magnetometry results as a function of V_p at constant external magnetic field strength, we give an introductory remark on degen-

[2] $M = m/V$ can then be calculated via a normalization to the ferromagnetic sample volume V.

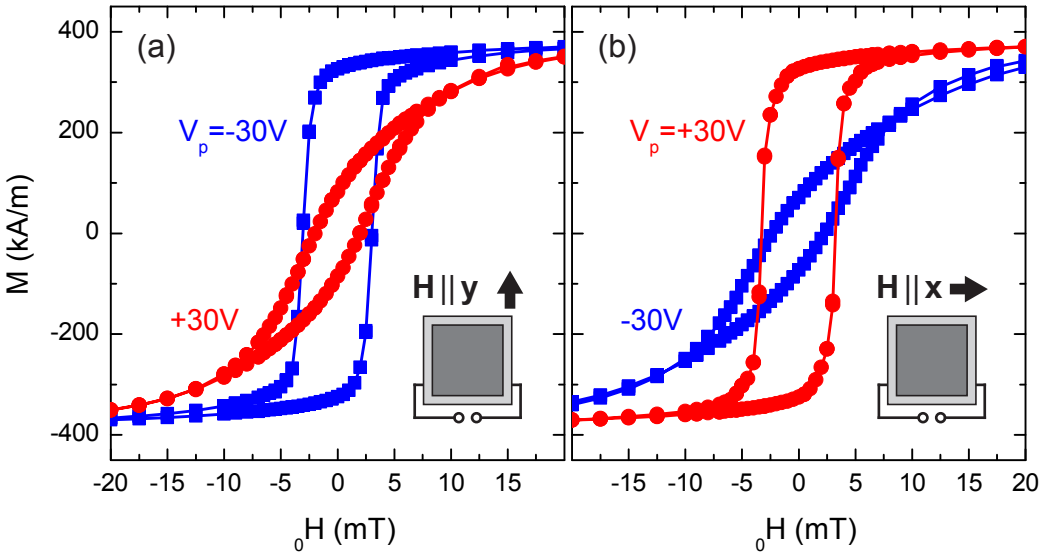

Figure 5.9: $M(H)$ loops recorded at fixed orientations of $\mathbf{H}$ and fixed voltages $V_\mathrm{p} = -30\,\mathrm{V}$ (blue squares) and $V_\mathrm{p} = +30\,\mathrm{V}$ (red circles) using SQUID magnetometry. (a) The $\mathbf{y}$ direction is magnetically easier for $V_\mathrm{p} = -30\,\mathrm{V}$ than for $V_\mathrm{p} = +30\,\mathrm{V}$. (b) The $\mathbf{x}$ direction is magnetically easier for $V_\mathrm{p} = +30\,\mathrm{V}$ than for $V_\mathrm{p} = -30\,\mathrm{V}$.

eracy. Magnetoelastic anisotropies are uniaxial and thus exhibit a 180° periodicity, which results in a twofold degeneracy. Hence, a magnetization reorientation upon repeatedly inverting the polarity of V_p may lead to domain formation and thus potentially results in demagnetization due to the presence of two energetically equally favorable but opposite magnetization directions. Therefore, a reversible magnetization control requires this degeneracy to be lifted, which can be realized by applying a small magnetic field [cf. Eq. (2.8)]—unless $\mathbf{H}$ is directed along the symmetry axes of the system along $\mathbf{x}$ or $\mathbf{y}$, which then again leads to degeneracy upon inverting the polarity of V_p. These considerations are of minor relevance for the experiments, as the measurements shown in the following were carried out in the RSM mode with a fixed orientation of the external magnetic field during the experiments and thus an exact alignment of $\mathbf{H}$ either along $\mathbf{x}$ or $\mathbf{y}$ is practically nearly impossible. However, this issue will be addressed again in the course of this section as it is of relevance for the simulations.

We now turn to the second set of experiments to demonstrate a voltage control of the magnetization orientation. To this end, we recorded M as a function of V_p at constant external magnetic bias field $\mathbf{H}$. The measurements were performed with $\mathbf{H}$ applied along two particular directions, $\mathbf{H} \parallel \mathbf{y}$ and $\mathbf{H} \parallel \mathbf{x}$, within an accuracy of about 2°. Prior to the data acquisition, we magnetized the sample to a well-defined magnetic single-domain state by applying $\mu_0 H_\mathrm{prep} = +7\,\mathrm{T}$ and then swept the magnetic field to the respective measurement field. This preparation field was applied along the easy axis by setting the voltage to $V_\mathrm{p} = -30\,\mathrm{V}$ and $V_\mathrm{p} = +120\,\mathrm{V}$ for $\mathbf{H} \parallel \mathbf{y}$ and $\mathbf{H} \parallel \mathbf{x}$, respectively. The $M(V_\mathrm{p})$ were then recorded for three distinct measurement bias field magnitudes, $\mu_0 H = 0\,\mathrm{mT}$, $-3\,\mathrm{mT}$, and $-5\,\mathrm{mT}$, as these fields are well below, still below but close to, and exceeding the coercive field, respectively

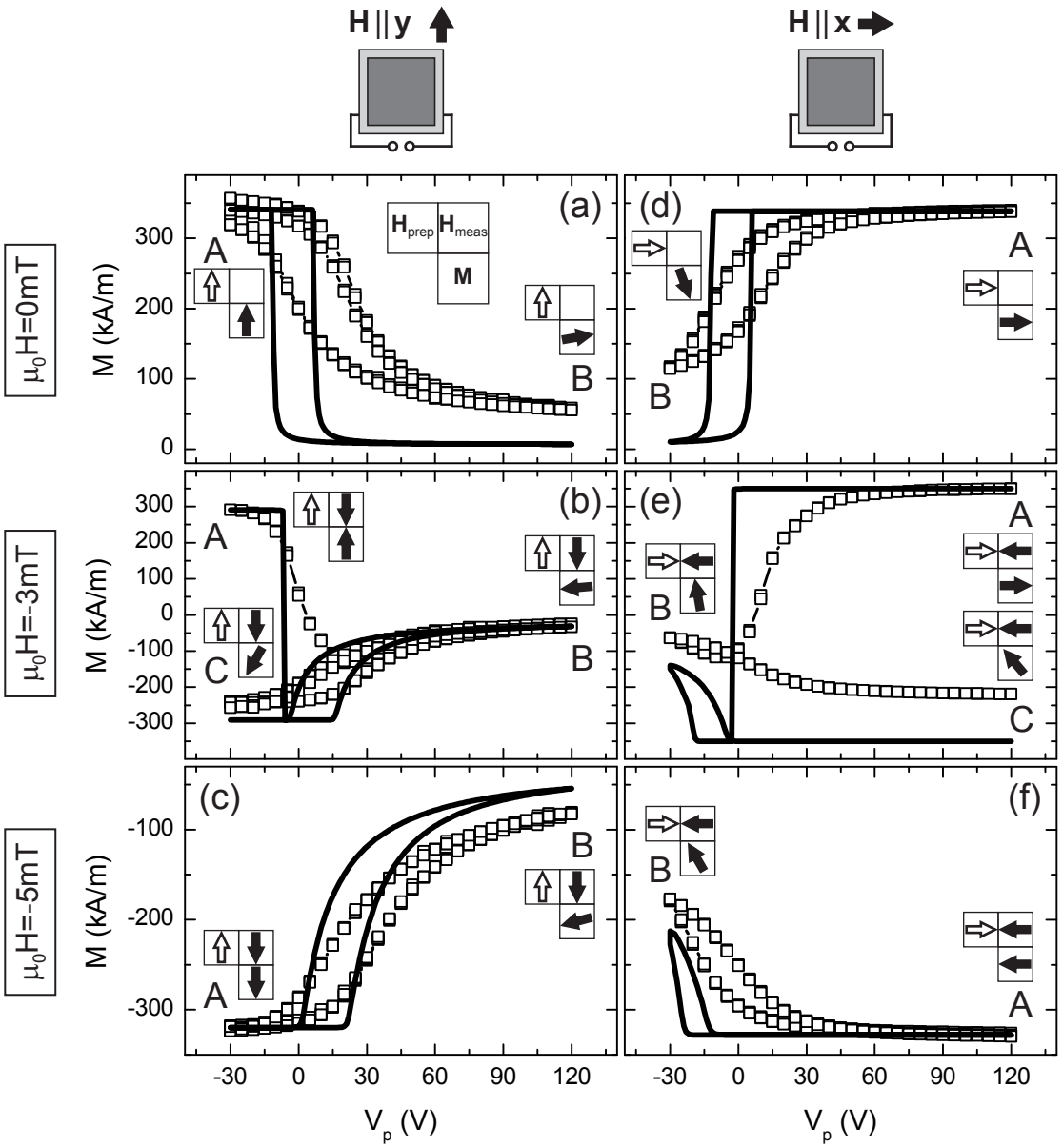

Figure 5.10: $M\,(V_\mathrm{p})$ loops show the projection of the magnetization M onto the direction of the applied magnetic field $\mathbf{H}$ at constant magnetic field magnitude as a function of V_p. The symbols represent the experimental data and the lines show the simulations. For $\mathbf{H} \parallel \mathbf{y}$, $\mathbf{M}$ exhibits a reversible rotation for $\mu_0 H = 0\,\mathrm{mT}$ (a) and $\mu_0 H = -5\,\mathrm{mT}$ (c) between A and B, while for $\mu_0 H = -3\,\mathrm{mT}$ (b) $\mathbf{M}$ undergoes an irreversible reorientation from A to B, followed by a reversible rotation between B and C. The situation appears analogous for $\mathbf{H} \parallel \mathbf{x}$, i.e., $\mathbf{M}$ undergoes a reversible rotation for $\mu_0 H = 0\,\mathrm{mT}$ (d) and $\mu_0 H = -5\,\mathrm{mT}$ (f) between A and B, and an irreversible reorientation for $\mu_0 H = -3\,\mathrm{mT}$ (e) from A to C via B. The arrows in the insets display the orientation of $\mathbf{H}$ and $\mathbf{M}$ at the points A, B, and C, respectively. The open arrow depicts the orientation of $\mathbf{H}_\mathrm{prep}$ during the field preparation at $+7\,\mathrm{T}$. The full arrow to the right indicates the orientation of the measurement bias field $\mathbf{H}$, and the full arrow below depicts the actual orientation of $\mathbf{M}$.

[cf. Fig. 5.9]. The data were acquired subsequently to a renewed preparation at each measurement field. According to Sec. 4.2, the measured quantity $M\,(V_\mathrm{p})$ is the projection of $\mathbf{M}$ onto the $\mathbf{y}$ and the $\mathbf{x}$ direction for $\mathbf{H} \parallel \mathbf{y}$ and $\mathbf{H} \parallel \mathbf{x}$, respectively.

Starting with $\mathbf{H} \parallel \mathbf{y}$, the symbols in Fig. 5.10(a) show $M\,(V_\mathrm{p})$ loops for two complete voltage cycles $-30\,\mathrm{V} \leq V_\mathrm{p} \leq +120\,\mathrm{V}$ recorded at the measurement field $\mu_0 H = 0\,\mathrm{mT}$. Starting at $V_\mathrm{p} = -30\,\mathrm{V}$ (point A), M is positive and thus oriented along the initial preparation field direction. Upon increasing V_p in steps of 5 V to $V_\mathrm{p} = +120\,\mathrm{V}$ (point B), M decreases, which indicates $\mathbf{M}$ reorienting towards the $\mathbf{x}$ direction orthogonal to $\mathbf{H}_\mathrm{prep}$. Upon reducing V_p to its initial value of $-30\,\mathrm{V}$, M increases and returns to its initial value. The V_p cycle was then repeated once more without a renewed preparation, with the recorded loop coinciding with the first cycle. Hence, $\mathbf{M}$ rotates continuously and reversibly between point A and B by approximately 80°. To visualize the orientations of $\mathbf{H}$ and $\mathbf{M}$, small insets are included in the Figs. 5.10(a)–(f) and refer to the respective positions indicated by the points A, B, and C. The open arrow depicts the orientation of $\mathbf{H}_\mathrm{prep}$ during the field preparation at $\mu_0 H_\mathrm{prep} = +7\,\mathrm{T}$. The full arrow to the right indicates the orientation of the measurement bias field $\mathbf{H}$, and the full arrow below depicts the actual orientation of $\mathbf{M}$.

After a renewed preparation, we recorded $M\,(V_\mathrm{p})$ traces at a slightly larger absolute value $\mu_0 H = -3\,\mathrm{mT}$ [Fig. 5.10(b)]. As evident, $\mathbf{H}$ and $\mathbf{M}$ are antiparallel at first at $V_\mathrm{p} = -30\,\mathrm{V}$ (point A). With increasing V_p, M almost vanishes and thus $\mathbf{M}$ is oriented close to the $\mathbf{x}$ direction at $V_\mathrm{p} = +120\,\mathrm{V}$ (point B). Upon reducing V_p again, M becomes negative (point C) and thus proves a parallel orientation of $\mathbf{H}$ and $\mathbf{M}$. During a repeated V_p cycle M now varies between the values at points C and B. Hence the evolution of $\mathbf{M}$ is qualitatively different in the two V_p cycles, with an irreversible magnetization reorientation in the first cycle by about 95°, and a reversible rotation in the second cycle by approximately 50°.

The data shown in Fig. 5.10(c) resemble an inversion of the situation depicted in Fig. 5.10(a). Here we chose an absolute value $\mu_0 H = -5\,\mathrm{mT}$, which results in an initial parallel orientation of $\mathbf{H}$ and $\mathbf{M}$ already present at point A. Two consecutively recorded full voltage cycles between the points A and B fully coincide, and thus $\mathbf{M}$ rotates reversibly by approximately 75°.

To yield a complete dataset, we carried out analogous measurements with $\mathbf{H} \parallel \mathbf{x}$. The data fully corroborate the measurements with $\mathbf{H} \parallel \mathbf{y}$, as they exhibit a reversible $\mathbf{M}$ rotation by approximately 70° and 55° at $\mu_0 H = 0\,\mathrm{mT}$ and $-5\,\mathrm{mT}$ [Figs. 5.10(d) and (f)], respectively, and an irreversible $\mathbf{M}$ reorientation at $\mu_0 H = -3\,\mathrm{mT}$ [Fig. 5.10(e)]. Note that for this bias field along $\mathbf{x}$ we did not measure a consecutive second cycle and thus Fig. 5.10(e) does not show a subsequent reversible rotation analogous to Fig. 5.10(b).

To quantitatively simulate the evolution of M as a function of V_p, we again use the total free energy density given in Eq. (5.6) using $\epsilon_2\,(V_\mathrm{p})$ measured in the voltage range of $-30\,\mathrm{V} \leq V_\mathrm{p} \leq +120\,\mathrm{V}$. The respective free energy density contours corresponding to the experimental conditions depicted in Fig. 5.10 are shown in Fig. 5.11, normalized to the saturation magnetization for $V_\mathrm{p} = -30\,\mathrm{V}$ (blue) and $V_\mathrm{p} = +120\,\mathrm{V}$ (red). To unambiguously visualize the evolution of $\mathbf{M}$ in Fig. 5.11, the free energy

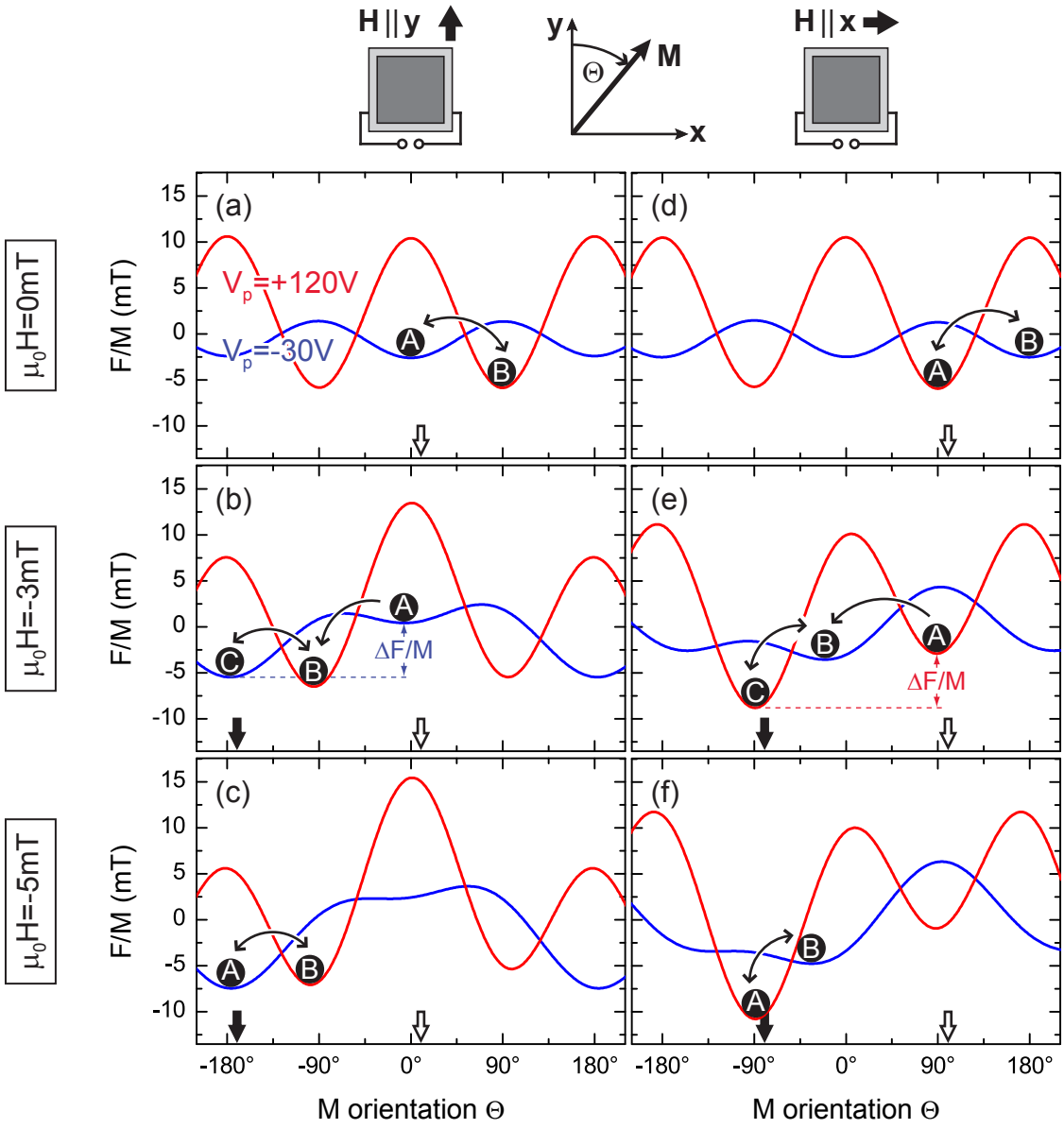

Figure 5.11: Calculated free energy density contours $F/M\,(\Theta)$ normalized to the saturation magnetization in the film plane for $V_\mathrm{p} = -30\,\mathrm{V}$ (blue) and $V_\mathrm{p} = +120\,\mathrm{V}$ (red). The points denoted by the capital letters indicate the equilibrium **M** orientation at the corresponding positions in the $M\,(V_\mathrm{p})$ loops in Fig. 5.10. To clarify the lifting of the free energy density degeneracy by the magnetic field, the curves were obtained using a misalignment of 10° between **H** and the **y** or **x** axis. The open downward-oriented arrows depict the orientation of $\mathbf{H}_\mathrm{prep}$ during the field preparation at +7 T and the full downward-oriented arrows indicate the orientation of the measurement bias field **H**. A reversible **M** rotation between the points A and B [(a), (c), (d), (f)] and B and C [(b), (e)] is due to a rotation of the global minimum of F as a function of V_p. An irreversible **M** reorientation between the points A and B [(b), (e)] results from the discontinuous switching from a local minimum (point A) to a global minimum (point B) as V_p is changed. The free energy density $\Delta F/M = 5.5\,\mathrm{mT}$ in (b), (e) denotes the difference between the local minimum (point A) and the global minimum (point C), which are separated by an energy barrier.

density contours were calculated with a misalignment of the in-plane orientation of the external magnetic field θ of 10°, i.e., $\theta = 10°$ for $\mathbf{H} \parallel \mathbf{y}$ and $\theta = 100°$ for $\mathbf{H} \parallel \mathbf{x}$. Figure 5.11 thus clearly exhibits non-degeneracies in the displayed curves. The experimental $M\,(V_\mathrm{p})$ loops were calculated by tracing the minimum of $F/M\,(\Theta)$ as a function of V_p, and projecting the thus determined $\mathbf{M}$ orientation onto the $\mathbf{y}$ or $\mathbf{x}$ axis to yield M [bold solid lines in Fig. 5.10]. These simulations, however, were obtained with a more realistic misalignment of 1° in θ to lift the degeneracy of F, i.e., $\theta = 1°$ for $\mathbf{H} \parallel \mathbf{y}$ and $\theta = 91°$ for $\mathbf{H} \parallel \mathbf{x}$. The curves for vanishing external bias field [Figs. 5.10(a), (d), 5.11(a), and (d)] were calculated using a magnetic field magnitude of 0.1 mT. For the simulations, we set the initial orientation of $\mathbf{M}$ parallel to $\mathbf{H}$ for $\mu_0 H = 0\,\mathrm{mT}$ and $-5\,\mathrm{mT}$ [$\Theta = 0°$, $-180°$, 90°, and $-90°$ in Figs. 5.10(a), (c), (d), and (f), respectively], and antiparallel for $\mu_0 H = -3\,\mathrm{mT}$ [$\Theta = 0°$ and 90° in Figs. 5.10(b) and (e), respectively]. The magnitude of $\mathbf{M}$ was chosen to equal the initial experimental values at points A and remains constant independent of V_p. Note that as the curves in Fig. 5.11 were obtained with $\theta = 10°$ and in Fig. 5.10 with $\theta = 1°$, the magnetization orientations Θ indicated by A, B, and C in the figures do not always quantitatively coincide.

The simulations shown by the lines in Fig. 5.10 reproduce the reversible $\mathbf{M}$ rotation in Figs. 5.10(a), (c), (d), and (f) as a function of V_p, which is due to a reversible rotation of the global minimum in the free energy density between the points A and B [Figs. 5.10(a), (c), (d), and (f)]. The irreversible reorientations in Figs. 5.10(b) and (e) during the first voltage cycle results from the preparation of $\mathbf{M}$ in a metastable state, i.e., in a local minimum of F (point A) [Figs. 5.10(b) and (e)], which discontinuously switches into the global minimum (point B) upon a V_p sweep. The reversible rotation in the second V_p cycle consequently is due to a rotation of the global minimum between the points B and C. The simulation of the magnetization evolution in Fig. 5.10 is in good agreement with the experimental data. If we furthermore consider the fact that there is no fit parameter included in Eq. (5.6) and that the evolution of $\mathbf{M}$ in our polycrystalline Ni thin film is calculated within a macrospin model, i.e., a single-domain Stoner-Wohlfarth approach, the agreement is quite remarkable. The deviations, however, both in the more rounded shape in the experiment and in the total swing of M is attributed to domain formation during the magnetization reorientation.

Taken together, the experimental $M\,(V_\mathrm{p})$ traces recorded at constant external magnetic field strength and the corresponding simulations within a macrospin model using the free energy density of Eq. (5.6) yield very good agreement. In particular, the application of V_p leads to a reorientation of $\mathbf{M}$, while the discrepancies between the measurements and the macrospin simulations indicate domain formation, which, however, evidently plays only a minor role. More precisely, $\mathbf{M}$ can be reoriented both reversibly and irreversibly by changing V_p. The SQUID magnetometry experiments thus demonstrate that $\mathbf{M}$ can be reoriented irreversibly upon an appropriate preparation of $\mathbf{M}$, and the overall $\mathbf{M}$ reorientation can amount to up to 180°. Moreover, the remanent magnetization orientation, i.e., the magnetization orientation in the absence of an external magnetic field, can be rotated continuously and reversibly by about 80° at room temperature solely via the application of appropriate voltages V_p.

5.6 Coherent and noncoherent magnetization reversal

We have shown in the preceding section that the experimental $M\,(V_\mathrm{p})$ traces recorded at external magnetic field strengths below the magnetic saturation field can be very well modeled within a single-domain (macrospin) Stoner-Wohlfarth model. This section aims to briefly substantiate these findings in terms of the underlying coherent and noncoherent magnetization rotation mechanisms [228]. Figure 5.12(a) shows the $M\,(H)$ loop for $\mathbf{H} \parallel \mathbf{y}$ at $V_\mathrm{p} = -30\,\mathrm{V}$ as already depicted in Fig. 5.9(a) by the blue loop. The solid green line represents a simulation under identical conditions to the calculations shown in Fig. 5.10, i.e., by using the total free energy density in Eq. (5.6) with the measured strain $\epsilon_2\,(-30\,\mathrm{V})$ and an external magnetic field orientation $\theta = 1°$. This macrospin simulation exhibits an abrupt (discontinuous) magnetization reversal at $|\mu_0 H| = 7\,\mathrm{mT}$ and takes place via coherent magnetization switching [226, 229, 230]. This situation is illustrated in Fig. 5.12(b), which shows free energy density contours $F/M\,(\Theta)$ normalized to the saturation magnetization in the film plane for the external magnetic field applied in the film plane along $\theta = 1°$, as indicated by the downward-oriented arrow, for different magnetic field strengths. As apparent from the free energy density contour for $\mu_0 H = -7\,\mathrm{mT}$ (green line), the magnetization undergoes a *coherent and discontinuous switching* due to the appearance of an inflection point in the free energy density, characterized by $\partial_\Theta F = \partial_\Theta^2 F = 0$ [98]. Evidently, this switching field exceeds the experimentally observed one, since the corresponding $M\,(H)$ loop [black squares in Fig. 5.12(a)] exhibits a coercive field $\mu_0 H_\mathrm{c} \approx 3\,\mathrm{mT}$. This indicates that other mechanisms must be considered to model the observed behavior, i.e., the magnetization reversal has to be discussed in terms of domain nucleation and expansion.

The orange free energy density contour in Fig. 5.12(b) illustrates the actual experimental situation for a magnetization reversal at $\mu_0 H = -3\,\mathrm{mT}$. Starting the $M\,(H)$ loop at large positive magnetic field along $\theta = 1°$, the magnetization basically retains its initial orientation along the global minimum at $\Theta = 1°$, which transforms into a local minimum approaching $\Theta = 0°$ as the magnitude of the magnetic field is decreased, resulting in a very small reversible, *coherent and continuous magnetization rotation* due to the gradual angular shift in the free energy density minimum. The global free energy density minimum is lower than the local minimum by $\Delta F/M$ and separated by an energy barrier. If this free energy density difference $\Delta F/M$ accounts for the domain-wall formation energy density and/or domain-wall unpinning energy density (since we have no microscopic evidence, for simplicity this energy density will only be termed domain-wall formation energy density in the following), magnetization reversal takes place via *noncoherent magnetization switching* into the global minimum despite the presence of an energy barrier [98, 231–235]. At that instant, the ferromagnetic sample is comprised of domains with different magnetic moment orientations, until a final homogeneous single-domain state is approached with the magnetization oriented along the global minimum and subsequently the evolution of the magnetization orientation proceeds via coherent rotation to $\Theta = -179°$ for

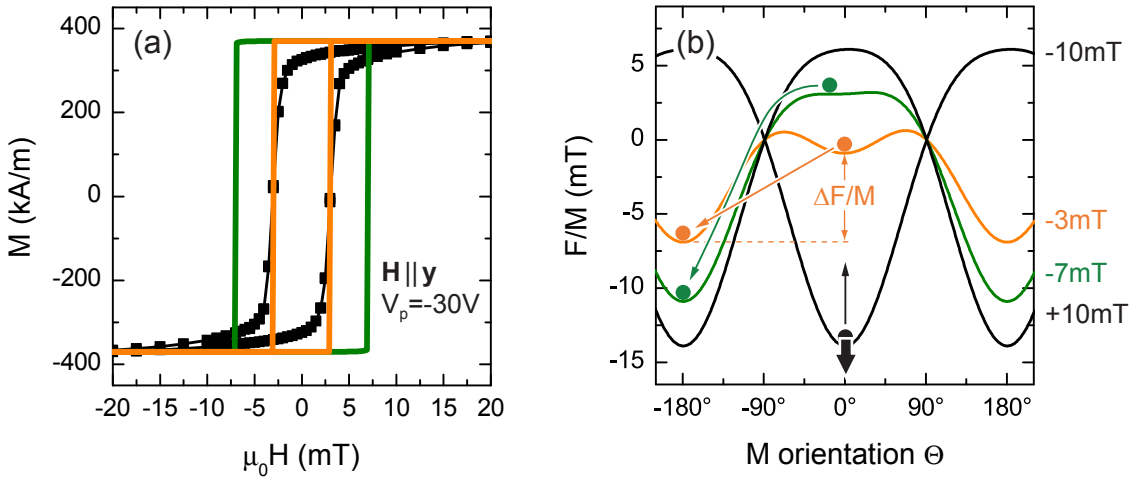

Figure 5.12: (a) $M\,(H)$ loop recorded for $\mathbf{H} \parallel \mathbf{y}$ at $V_\mathrm{p} = -30\,\mathrm{V}$ (black squares) [reproduced from Fig. 5.9(a)]. The solid lines show simulations in a coherent magnetization switching model (green line) and a noncoherent switching model (orange line), calculated for an external magnetic field applied along $\theta = 1°$. (b) Corresponding free energy density contours. In a single-domain (Stoner-Wohlfarth) limit, the magnetization undergoes a coherent magnetization switching at $\mu_0 H = -7\,\mathrm{mT}$ upon the appearance of an inflection point (green line). The more realistic situation is depicted by the orange line for a noncoherent magnetization switching at $\mu_0 H = -3\,\mathrm{mT}$, corresponding to a domain-wall formation energy of $\Delta F/M = 6.0\,\mathrm{mT}$. The downward-oriented arrow indicates the orientation of the external magnetic field.

large negative magnetic fields along $\theta = 1°$ [231, 236, 237].

Therefore, in our simulation we take into account a free parameter $\Delta F/M$, whose value is chosen such that the measured noncoherent magnetization switching field of $|\mu_0 H| = 3\,\mathrm{mT}$ is reproduced by the simulation. We thus obtain $\Delta F/M = 6.0\,\mathrm{mT}$. If we now turn to the $M\,(V_\mathrm{p})$ loops shown in Fig. 5.10, and consider the cases with largest magnetization reorientation, i.e., where we observe an irreversible reorientation process due to the initial preparation of $\mathbf{M}$ into a local minimum [Figs. 5.10(b), (e)], we observe a difference between the local minimum (point A) and the global minimum (point C) in the corresponding free energy density contours [Figs. 5.11(b), (e)] of $\Delta F/M = 5.5\,\mathrm{mT}$. This shows that the voltage-controlled modifications in the free energy density landscape at an external magnetic field $\mu_0 H = -3\,\mathrm{mT}$ do not exceed the domain-wall formation energy $\Delta F/M = 6.0\,\mathrm{mT}$ and thus allows for a quantitative description of the experimentally determined magnetization evolution in very good approximation within a coherent magnetization reorientation model.

We furthermore note that the evolution of ADMR in Sec. 5.4 can be consistently understood in terms of coherent magnetization rotation. To maintain a magnetic single-domain state throughout the measurement, the magnetoresistance traces were recorded at external magnetic field strengths $\mu_0 H \geq 50\,\mathrm{mT}$. The resulting Zeeman energy density contribution thus is sufficiently large to retain the magnetization in the global energy density minimum throughout the angular scan [$F_\mathrm{Zeeman}/M \geq$

$50\,\mathrm{mT} \gg F^{y}_{\mathrm{u,eff}}/M \leq 19\,\mathrm{mT}$ (cf. Fig. 5.8)].

In the framework of this discussion, we also briefly comment on the limitations of this model. The simulated orange hysteresis loop in Fig. 5.12(a) is in reasonable qualitative agreement with the experiment, but produces sharper noncoherent magnetization switching processes than experimentally observed. This is due to two facts: (i) the simple model accounts only for the energy necessary for domain nucleation and neglects processes like pinning and depinning of domain walls by defects during the magnetization reversal. (ii) The model assumes a single, homogeneous magnetic phase, which allows for a description by single-valued parameters [234, 235]. Material defects can result in local fluctuations in the magnetization and the magnetic anisotropy. An improved model accounts for such sample inhomogeneities by introducing a Gaussian distribution of $\Delta F/M$ [234, 235, 238].

Taken together, magnetization reversal can be composed of two processes: coherent magnetization rotation and noncoherent magnetization switching. We will further discuss and substantiate these observations in the following two sections.

5.7 Nonvolatile, reversible control of remanent magnetization orientation

In ferromagnetic/ferroelectric hybrids, the control of the key magnetic properties, such as coercive field, saturation magnetization, or remanent magnetization via electric voltages has been demonstrated recently [58, 64–66, 239–242]. A further major development is the demonstration of a reversible, all-electric-field control of magnetization orientation or reversal, and thus of an electrically controlled magnetization switching [62, 63, 208, 243–250]. However, the literature so far is focused on a nonhysteretic all-electrical magnetization manipulation, i.e, the electric-field induced magnetization changes are volatile in the sense that they return to their initial state upon removing the electric field. Obviously, the next step now is to achieve a nonvolatile or remanent electric-field control of $\mathbf{M}$. First experiments in this direction have already been performed in Ni thin film/ferroelectric hybrid samples [249, 251]. A nonvolatile electric-field control of remanent magnetization can be realized by utilizing the hysteretic expansion and contraction of the piezoelectric actuator, which leads to two distinctly different elastic strain states at $V_{\mathrm{p}} = 0\,\mathrm{V}$ depending on the V_{p} history [cf. Fig. 3.3(c)]. This intrinsically hysteretic strain-voltage curve of the actuator can be exploited to deterministically generate two distinct remanent magnetization orientation states in the ferromagnet intimately connected to the actuator at zero applied voltage [cf. Figs. 5.10(a), (d)]. Hence, a nonvolatile control of remanent magnetization is feasible in polycrystalline Ni thin films with a magnetically isotropic film plane, which enables an electrically read- and writeable memory bit. Contrary to, e.g., ferroelectric random access memory (FERAM), the mechanism utilized here does not rely on a macroscopic polarization reversal of the ferroelectric compound, so that our concept is operational well below the ferroelectric coercive fields.

We have investigated this concept in a sample fabricated by directly depositing

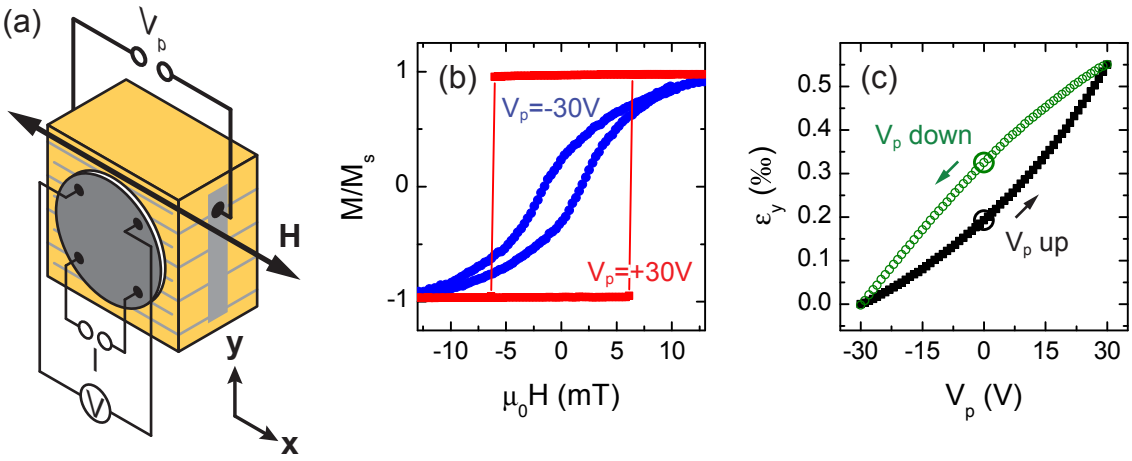

Figure 5.13: (a) Schematic illustration of the ferromagnetic thin film/actuator hybrid with the contact scheme in van der Pauw geometry. The external magnetic field $\mathbf{H}$ is oriented along $\mathbf{x}$ for all measurements. (b) $M\,(H)$ loops recorded at fixed voltages $V_\mathrm{p} = +30\,\mathrm{V}$ (red squares) and $V_\mathrm{p} = -30\,\mathrm{V}$ (blue circles) along $\mathbf{x}$. (c) Hysteretic strain-voltage curve of the actuator showing that the strain $\epsilon_2\,(V_\mathrm{p})$ exhibits two distinct strain states at $V_\mathrm{p} = 0\,\mathrm{V}$ (big open circles) depending on V_p history.

a 100 nm thick Ni film onto a piezoelectric actuator, followed by 5 nm Au in situ to prevent oxidation. Prior to the evaporation process, a 140 nm thick polymethylmethacrylate (PMMA) layer was spin-coated onto the respective actuator face and baked at 110 °C to electrically isolate the Ni film from the actuator electrodes. This layer provides a sufficiently smooth surface mandatory for optical experiments. To enable an electrical read out of the magnetization orientation, electrical contacts in van der Pauw geometry are wire bonded to the Ni film [Fig. 5.13(a)]. To determine the static magnetic properties of the Ni thin film/actuator hybrid we use longitudinal magneto-optical Kerr effect (MOKE) measurements, which detect the projection $M = \mathbf{M} \cdot \mathbf{x}$ of the magnetization onto the magnetic field direction along $\mathbf{H} = H\mathbf{x}$. The incident light from a cw-diode laser hereby is focused on the center of the Ni film onto a spot with a diameter of about 100 μm. We simultaneously recorded the magnetoresistance in four-point measurements, with a constant bias current $\mathbf{I}$ flowing along $\mathbf{x}$. All data were taken at room temperature.

Figure 5.13(b) shows normalized MOKE loops corresponding to $\mathbf{M} \cdot \mathbf{x}/M_\mathrm{s}$ for $V_\mathrm{p} = +30\,\mathrm{V}$ (full red squares) and $-30\,\mathrm{V}$ (full blue circles), in accordance to the SQUID loops shown in Fig. 5.9(b). Figure 5.13(c) depicts the strain $\epsilon_2\,(V_\mathrm{p})$ exerted along $\mathbf{y}$ measured using a strain gauge in the voltage range of $-30\,\mathrm{V} \leq V_\mathrm{p} \leq +30\,\mathrm{V}$ for a V_p upsweep (full black symbols) and downsweep (open green symbols). As the maximum applied voltage is below the ferroelectric coercive field of $E_\mathrm{c} \approx 4.5\,\mathrm{kV/cm}$ corresponding to $V_\mathrm{p} \approx 45\,\mathrm{V}$, the macroscopic polarization of the ferroelectric compound is not switched and only ferroelectric domain-wall motion is induced. The corresponding irreversible displacement contributions generate the observed hysteresis (cf. Sec. 3.3). In particular, the hysteretic $\epsilon_2\,(V_\mathrm{p})$ curve allows us to select one of two distinctly different, remanent elastic strain states at zero applied electric field [big open circles in Fig. 5.13(c)] depending on the voltage history. Via magnetoelas-

tic coupling this is transferred into two distinct remanent magnetization orientation states at $V_\mathrm{p} = 0\,\mathrm{V}$ in the adjacent ferromagnet.

Figures 5.14(a)–(d) show how the magnetic properties change with the hysteretic expansion and contraction of the actuator as a function of V_p. The full black squares depict the MOKE $M\,(H)$ loops for a V_p upsweep, recorded at fixed voltages $V_\mathrm{p} = -30\,\mathrm{V}$, $-15\,\mathrm{V}$, $0\,\mathrm{V}$, and $+30\,\mathrm{V}$, as shown in Figs. 5.14(a), (b), (c), and (d), respectively, whereas open green circles depict the corresponding $M\,(H)$ loops for a V_p downsweep. The dashed lines in panels (a)–(d) are guides to the eye. According to the discussion in Sec. 5.5 [cf. Figs. 5.9(b), 5.13(b)], the $M\,(H)$ loop is magnetically hard at $V_\mathrm{p} = -30\,\mathrm{V}$. The loop becomes increasingly easy with increasing V_p, until it is perfectly rectangular-shaped at $V_\mathrm{p} = +30\,\mathrm{V}$. Upon gradually decreasing V_p again, the loop becomes gradually harder and finally perfectly coincides with the corresponding V_p upsweep loop [Fig. 5.14(a)]. At the intermediate voltages [Figs. 5.14(b), (c)] we observe a considerable difference between the loops recorded for the same V_p value in a V_p up- and downsweep, owing to the hysteretic strain-voltage curve of the actuator. The resistance curves displayed in Figs. 5.14(e)–(h), recorded simultaneously to the $M\,(H)$ loops, show that the AMR of the Ni film also characteristically changes depending on the V_p history, which evidently yields characteristic differences between the $R\,(H)$ loops for the V_p up- and downsweeps [Figs. 5.14(f), (g)]. As discussed in Sec. 4.4, the magnetization state thus can be directly read out electrically.

We next show that the voltage-induced strain affects only the magnetization orientation, but not its magnitude. To this end, we extract the macrospin magnetization orientation $\cos\beta = M/M_\mathrm{s}$ with respect to the current direction along $\mathbf{x}$ from the $M\,(H)$ loops. Hereby, β denotes the angle between $\mathbf{M}$ and $\mathbf{I} \parallel \mathbf{x}$, while we will use the angle $\Theta = \beta + 90^\circ$ [for definition of Θ see Fig. 4.4] in the following to allow for comparison with the previous findings. Obviously, this approach is valid only in a macrospin approximation (no magnetic domain formation). We then calculate the longitudinal AMR using the macrospin expression given in Eqs. (4.30),

$$R = R_\perp + \left(R_\parallel - R_\perp\right) \cos^2\left(\Theta - 90^\circ\right), \tag{5.9}$$

where $R_\perp$ and $R_\parallel$ are the resistance values for $\mathbf{I} \perp \mathbf{M}$ and $\mathbf{I} \parallel \mathbf{M}$, respectively. Using $R_\parallel = 557.5\,\mathrm{m\Omega}$ and $R_\perp = 540.6\,\mathrm{m\Omega}$, we obtain the solid lines in Figs. 5.14(e)–(h). Except for a narrow region (less than 1 mT) around the magnetic coercive fields H_c, where sharp dips appearing in the simulation are not observed in the corresponding experiment, the simulations are in very good agreement with the experimental data. In order to model the magnetization-reversal process, coherent rotation and domain-wall nucleation and/or unpinning usually are combined (see Sec. 5.6). Coherent rotation relies on a continuous rotation of a single homogeneous magnetic domain. The sharp, irreversible features around the magnetic coercive fields often are attributed to domain-wall effects. It furthermore has been shown (e.g., in Ref. [236]) that the magnetization reversal in a ferromagnetic thin film with uniaxial anisotropy is caused by coherent rotation when the external magnetic field is oriented close to the magnetic hard axis [cf. Figs. 5.14(a) and (e)], while for magnetic-field orientations close to an easy axis [and thus for increasingly abrupt changes of the

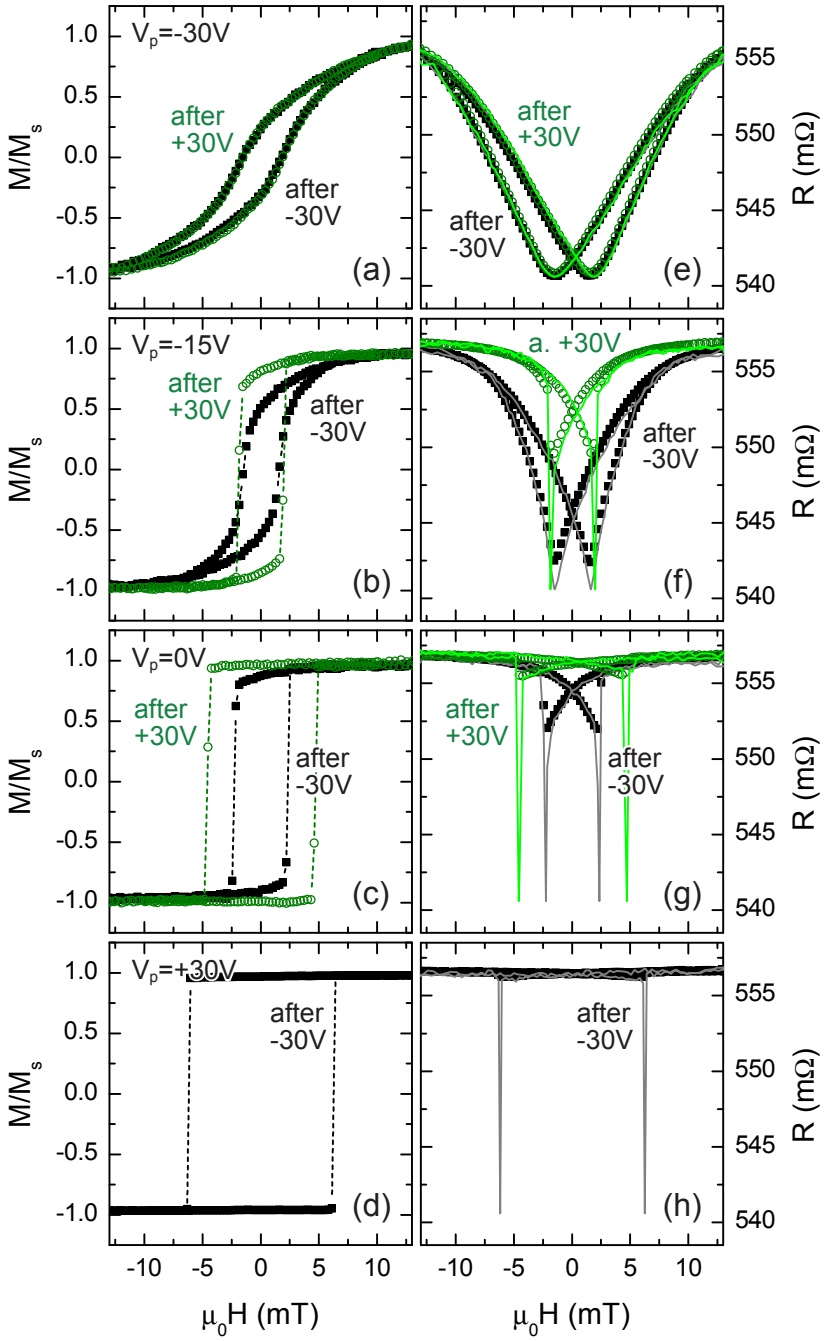

Figure 5.14: (a)–(d) $M\,(H)$ loops at fixed V_p for a V_p upsweep from $V_\mathrm{p} = -30\,\mathrm{V}$ to $V_\mathrm{p} = +30\,\mathrm{V}$ (full black squares) and a subsequent V_p downsweep (open green circles). The dashed lines are guides to the eye. (e)–(h) Simultaneously recorded $R\,(H)$ loops (symbols). The solid lines display simulations of the AMR in a single-domain model showing very good overall agreement with the experiment. The piezo-elastic hysteresis of the actuator results in significant differences between V_p up- and downsweep in the MOKE loops [(b), (c)], which is also reflected in the AMR curves [(f), (g)].

magnetization orientation in the $M(H)$ loops in Fig. 5.14] domain-wall processes take over in the vicinity of the magnetic switching fields. Hence, for increasing V_p one expects that our simple single-domain macrospin modeling will fail to adequately describe the experiments close to H_c—which accounts for the deviations between experiment and simulation at the switching fields in Figs. 5.14(f), (g), and (h). For all other magnetic-field values, however, the overall good agreement demonstrates that we can describe the voltage-controlled magnetization modifications in good approximation as a coherent magnetization reorientation in a single-domain (macrospin) model. The coincidence furthermore shows that $M(H)$ and $R(H)$ measurements yield equivalent information about the magnetization orientation. Note that the information on the magnetization state obtained from MOKE and the AMR measurements is in quite remarkable agreement, considering the fact that the Ni area laterally probed by these two techniques ($\approx 0.008\,\mathrm{mm}^2$ for MOKE and $\approx 3\,\mathrm{mm}^2$ for AMR) differs by more than two orders of magnitude. This suggests that magnetic domains are much smaller than $\approx (100\,\mu\mathrm{m})^2$.

To quantitatively evaluate the characteristic differences in the $M(H)$ loop as a function of V_p evident from Figs. 5.14(a)–(d), we have plotted both the coercive field $\mu_0 H_\mathrm{c}$ and the normalized remanent magnetization $M_\mathrm{r}/M_\mathrm{s}$ observed experimentally in Figs. 5.15(a) and (b), respectively. For both quantities the values for increasing and decreasing V_p are clearly different. In particular, two distinctly different states in M_r, i.e., at $\mu_0 H = 0\,\mathrm{mT}$ and $V_\mathrm{p} = 0\,\mathrm{V}$ are observed, as indicated by the big open circles. This opens the perspective of a nonvolatile, all-voltage controlled remanent magnetization control. In analogy to the $M(V_\mathrm{p})$ loops shown in Fig. 5.10(d), we demonstrate that the magnetization orientation can indeed be remanently altered by solely varying V_p while keeping $\mu_0 H$ constant. To test this conjecture, we also recorded M and R as a function of V_p at zero external magnetic field. Prior to the V_p sweep, we prepared the magnetization into a well-defined initial state along the easy axis by setting the voltage to $V_\mathrm{p} = +30\,\mathrm{V}$ and applying a saturating magnetic field $\mu_0 H = +120\,\mathrm{mT}$. We then swept the magnetic field to $\mu_0 H = 0\,\mathrm{mT}$ and kept it constant at this value, and consecutively recorded two complete $R(V_\mathrm{p})$ voltage cycles $V_\mathrm{p} = +30\,\mathrm{V} \rightarrow -30\,\mathrm{V} \rightarrow +30\,\mathrm{V}$. The $R(V_\mathrm{p})$ loops thus obtained are shown in Fig. 5.15(c) (open green circles and full black squares again indicate the V_p down- and upsweep, respectively). This corroborates the results displayed in Fig. 5.15(b), as a V_p sweep at fixed $\mu_0 H = 0\,\mathrm{mT}$ also yields a hysteretic behavior with two distinctly different magnetic states at $V_\mathrm{p} = 0\,\mathrm{V}$. We observe a considerable total AMR change from $V_\mathrm{p} = +30\,\mathrm{V}$ to $-30\,\mathrm{V}$ of $[R(+30\,\mathrm{V}) - R(-30\,\mathrm{V})]/R(-30\,\mathrm{V}) = 2.5\%$, and a change between the two states at $V_\mathrm{p} = 0\,\mathrm{V}$ of $[R(0\,\mathrm{V},\mathrm{down}) - R(0\,\mathrm{V},\mathrm{up})]/R(0\,\mathrm{V},\mathrm{up}) = 0.6\%$. Moreover, as the two $R(V_\mathrm{p})$ cycles perfectly coincide, the voltage-controlled magnetization rotation appears to be fully reversible, in full agreement with the $M(V_\mathrm{p})$ loops shown in Fig. 5.10(d). Using the $M(V_\mathrm{p})$ loops recorded simultaneously with $R(V_\mathrm{p})$, we again simulate the AMR with $R_\parallel = 557.5\,\mathrm{m\Omega}$ and $R_\perp = 540.6\,\mathrm{m\Omega}$ already used above. The AMR curves thus calculated are displayed by solid lines in Fig. 5.15(c). Evidently, the measured and simulated AMR data are in very good agreement, which again corroborates the validity of the macrospin approach and shows that the **M**

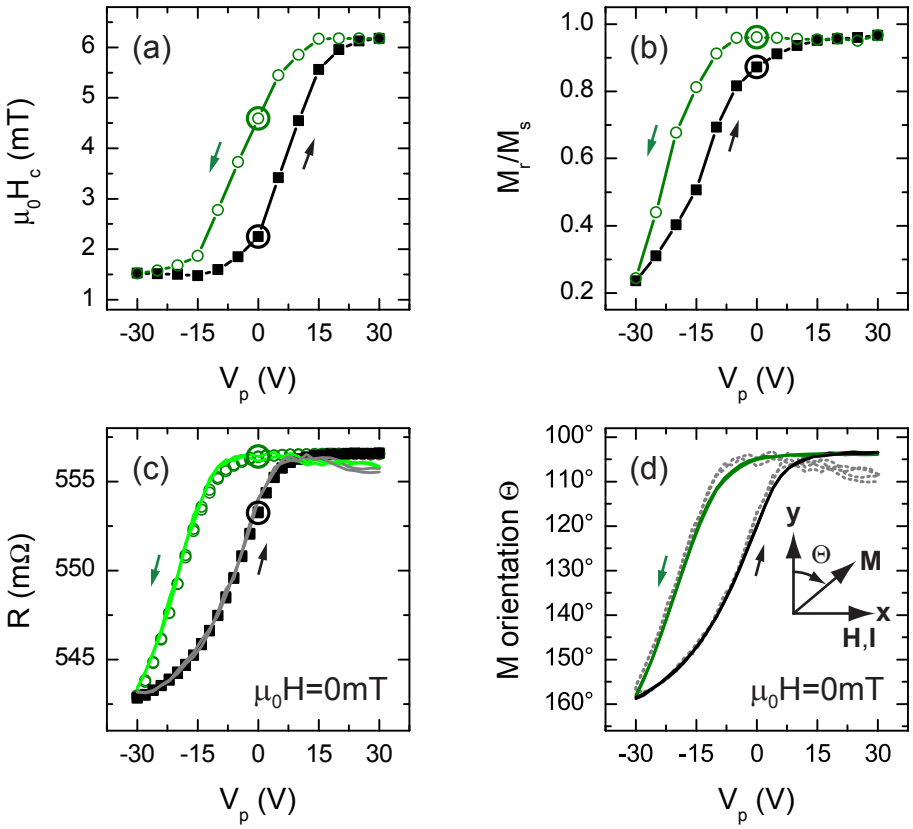

Figure 5.15: Coercive field $\mu_0 H_c$ (a) and normalized remanent magnetization M_r/M_s (b) extracted from the $M(H)$ loops shown in Figs. 5.14(a)–(d). Both quantities exhibit the hysteretic behavior characteristic of the mechano-elastic hysteresis of the actuator. (c) Two consecutive $R(V_p)$ loops recorded at $\mu_0 H = 0\,\mathrm{mT}$, after preparing a single-domain magnetic state. A single voltage cycle starts at $V_p = +30\,\mathrm{V}$, followed by a V_p downsweep (open green circles) and a subsequent upsweep (full black squares). The curves also consistently show a hysteretic behavior. The solid lines depict the AMR calculated based on the corresponding $M(V_p)$ loops, showing very good agreement with the experimental AMR data. (d) Macrospin magnetization orientation Θ, calculated from the measured AMR data displayed in (c) with the AMR parameters given in the text (solid black and green lines), and from the measured MOKE data (dashed gray lines). At $V_p = 0\,\mathrm{V}$, $\mathbf{M}$ can be reversibly switched between two magnetization orientation states, which corresponds to a $\mathbf{M}$ reorientation of $\Delta\Theta = 15°$. In the full voltage range $-30\,\mathrm{V} \leq V_p \leq +30\,\mathrm{V}$, $\mathbf{M}$ can be reversibly adjusted within 55°.

orientation derived from resistance measurements is fully equivalent to that obtained from direct magnetization measurements. This consistency furthermore proves the robustness of the single-domain model, as in the MOKE setup the light beam only probes a $\sim 100\,\mu\mathrm{m}$ diameter region of the Ni film, whereas the four-point resistance measurement integrally probes the magnetic film. A quantitative analysis of the $M(V_p)$ and $R(V_p)$ data is shown in Fig. 5.15(d), which depicts the macrospin magnetization orientation Θ, calculated from the measured AMR data displayed in Fig. 5.15(c) using Eq. (5.9) with the values of the parameters $R_\parallel$ and $R_\perp$ given above (solid black and green lines), and from the measured MOKE data (dashed gray lines). At $V_p = 0\,\mathrm{V}$, we thus obtain a $\mathbf{M}$ orientation $\Theta(V_{p,\mathrm{down}} = 0\,\mathrm{V}) = 105°$

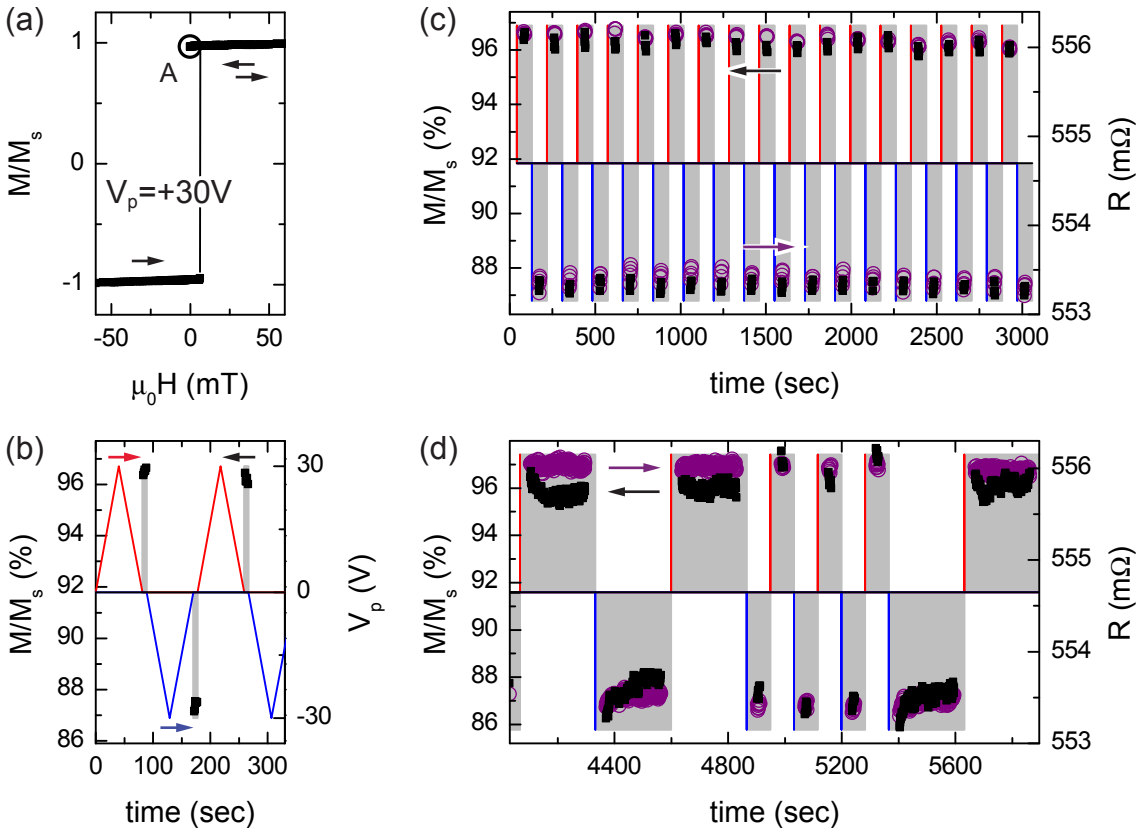

Figure 5.16: (a) Magnetic preparation sweep at $V_\mathrm{p} = +30\,\mathrm{V}$ to establish a well-defined magnetization state. After sweeping from $\mu_0 H = +120\,\mathrm{mT}$ to $0\,\mathrm{mT}$ (point A) the magnetic field is kept fixed at $\mu_0 H = 0\,\mathrm{mT}$. (b) Illustration of the data acquisition process. The data is recorded at $V_\mathrm{p} = 0\,\mathrm{V}$ (gray bar) after applying a voltage sequence either $V_\mathrm{p} = 0\,\mathrm{V} \rightarrow +30\,\mathrm{V} \rightarrow 0\,\mathrm{V}$ (red line) or $V_\mathrm{p} = 0\,\mathrm{V} \rightarrow -30\,\mathrm{V} \rightarrow 0\,\mathrm{V}$ (blue line). (c) Demonstration of repeated electro-elasto-magnetic switching processes, with M (full black symbols) and R (open purple symbols) being recorded five times in each acquisition window (gray). (d) Electro-elasto-magnetic memory-bit response for other acquisition time windows.

for the V_p downsweep and $\Theta\,(V_\mathrm{p,up} = 0\,\mathrm{V}) = 120°$ for the V_p upsweep. In the total voltage swing $-30\,\mathrm{V} \leq V_\mathrm{p} \leq +30\,\mathrm{V}$, we can reversibly rotate the magnetization orientation by 55° [$\Theta\,(V_\mathrm{p} = +30\,\mathrm{V}) = 104°$ and $\Theta\,(V_\mathrm{p} = -30\,\mathrm{V}) = 159°$]. Taken together, our observations show that the magnetization orientation at $V_\mathrm{p} = 0\,\mathrm{V}$ and $\mu_0 H = 0\,\mathrm{mT}$ can be reversibly switched between two distinct states enclosing an angle of 15° only via V_p sweeps, while keeping $\mu_0 H = 0\,\mathrm{mT}$ fixed. For comparison, the $M\,(V_\mathrm{p})$ loops depicted in Fig. 5.10(d) are recorded in the voltage range of $-30\,\mathrm{V} \leq V_\mathrm{p} \leq +120\,\mathrm{V}$ and exhibit two distinct $M\,(V_\mathrm{p} = 0\,\mathrm{V})$ states enclosing an angle of 23°. Overall, this enables a voltage-controlled, nonvolatile magnetization "switching", as will be discussed in the following.

The remanent voltage control of $\mathbf{M}$ is illustrated in Fig. 5.16. We start with a preparation of the magnetization in a single-domain state along a magnetic easy axis at $V_\mathrm{p} = +30\,\mathrm{V}$. To normalize the MOKE magnetization data recorded subsequently, we start with the magnetic field at $\mu_0 H = -120\,\mathrm{mT}$ in a negative saturation

state [Fig. 5.16(a)]. After sweeping the magnetic field beyond positive saturation to $\mu_0 H = +120\,\mathrm{mT}$, we finally set the field back to $\mu_0 H = 0\,\mathrm{mT}$ and keep it constant at this value (point A). The subsequent data acquisition at $\mu_0 H = 0\,\mathrm{mT}$ is illustrated in Fig. 5.16(b). We apply the voltage sequences $V_\mathrm{p} = 0\,\mathrm{V} \rightarrow +30\,\mathrm{V} \rightarrow 0\,\mathrm{V}$ (red lines in the upper half of the panel) and $V_\mathrm{p} = 0\,\mathrm{V} \rightarrow -30\,\mathrm{V} \rightarrow 0\,\mathrm{V}$ (blue lines) to switch the magnetization into one of the two distinct magnetic states determined by the remanent elastic strain, and then simultaneously record M [full black symbols in Fig. 5.16(b)] and R at $V_\mathrm{p} = 0\,\mathrm{V}$. Both $M\,(V_\mathrm{p} = 0\,\mathrm{V})$ and $R\,(V_\mathrm{p} = 0\,\mathrm{V})$ are read out five times per acquisition cycle, which is indicated with a gray bar. We would like to emphasize again that after the initial magnetic preparation sweep, the magnetic field is kept constant at $\mu_0 H = 0\,\mathrm{mT}$ during the whole data-recording process. The $M\,(V_\mathrm{p} = 0\,\mathrm{V})$ (full black symbols) and $R\,(V_\mathrm{p} = 0\,\mathrm{V})$ (open purple symbols) data depicted in Fig. 5.16(c) for a number of switching processes within a total time of about 50 min clearly show that the magnetization can be reversibly and deterministically switched between two distinct orientations and therefore conclusively demonstrate a nonvolatile electric field-control of remanent magnetization with applied voltages below the ferroelectric coercive fields. Figure 5.16(d) presents a part of the measurement sequence with a higher number of readings per acquisition cycle displaying in total each 1600 $M\,(V_\mathrm{p} = 0\,\mathrm{V})$ and $R\,(V_\mathrm{p} = 0\,\mathrm{V})$ readings within an acquisition time of 30 min. These two distinct magnetic states at $V_\mathrm{p} = 0\,\mathrm{V}$ are clearly retained. Note that, however, the MOKE signal tends to drift as a function of time probably owing to small temperature fluctuations, while the resistance signal in all our measurements proved very stable.

Overall, these findings conceptionally demonstrate the feasibility of a spin-mechanics memory with all-electrical read and write at zero external magnetic field, which allows for room-temperature operation, and at electric field strengths well below the ferroelectric coercive fields. More precisely, our findings demonstrate that the magnetization orientation in the ferromagnetic film can be all-electrically, reversibly, and nonvolatilely switched between two remanent orientations at $V_\mathrm{p} = 0\,\mathrm{V}$ and $\mu_0 H = 0\,\mathrm{mT}$.

5.8 Magneto-optical imaging of magnetization reorientation

All experimental findings presented in this chapter so far could be successfully described in terms of a single-domain (macrospin) Stoner-Wohlfarth model. However, since all measurement techniques employed in the previous sections integrally probe the hybrids' ferromagnetic constituent, spatially resolved measurements are mandatory to study the validity and limitations of a macrospin model. Most reports on magnetization changes $M\,(E)$ as a function of the applied electric field rely on either integral measurement techniques or magnetic force microscopy imaging [252–254]. However, to our knowledge little is known about spatially resolved experiments to address local $M\,(E)$ changes on macroscopic (mm^2) areas. To this end, we correlate simultaneously measured spatially resolved magneto-optical Kerr effect imaging and

integral magnetotransport. The data presented in this section were recorded in the course of M. Brasse's diploma thesis [190].

The sample investigated in this context was fabricated as described in the previous section (Sec. 5.7). To determine the static magnetic properties of the Ni thin film/actuator hybrid, we employ spatially resolved magneto-optical Kerr effect (MOKE) imaging. More precisely, we perform longitudinal MOKE spectroscopy, which detects the projection $M = \mathbf{M} \cdot \mathbf{x}$ of the magnetization onto the magnetic field direction $\mathbf{x} = \mathbf{H}/H$, in accordance to the measurement configuration employed in the previous section. All data were recorded at room temperature. Our MOKE setup is equipped with a high power red light emitting diode (center frequency $\lambda = 627\,\mathrm{nm}$). A slit aperture and a Glan Thompson polarizing prism yield an illumination path with s-polarized incident light. After reflecting off the sample, the light passes through a quarter wave plate to remove the ellipticity, and then transmits through a second Glan Thompson polarizing prism close to extinction serving as the analyzer. The Kerr signal is then focused by an objective lens and recorded with a CCD camera with a pixel size of $10\,\mu\mathrm{m} \times 10\,\mu\mathrm{m}$ (see Sec. 4.3.5). While the setup has a rather low spatial resolution of several micrometers, it allows to image samples with lateral dimensions of several mm^2 at once. Such a lateral resolution is mandatory to investigate the piezo-induced $\mathbf{M}\,(V_\mathrm{p})$, since the actuator electrodes are about $10\,\mu\mathrm{m}$ wide, and the active piezoelectric regions are about $100\,\mu\mathrm{m}$ wide. To enable AMR measurements simultaneously to MOKE, we contacted the Ni film on top in four-point geometry [see Fig. 5.13(a)]. All AMR data shown in the following were recorded with a constant bias current $\mathbf{I}$ parallel to $\mathbf{H}$.

As discussed in detail below, we apply several image-processing procedures to extract the relevant magnetic information. On the one hand, we use the difference-image technique, i.e., the digital subtraction of two images, to enhance the magneto-optical contrast and to exclude any non-magnetic signal contributions. To this end, a reference image is recorded in a magnetically saturated state and subtracted from subsequent images [197]. On the other hand, for a quantitative magnetization analysis we normalize the observed image contrast. To this end, we define a region of interest (ROI), which exactly corresponds to the region covered with Ni. Within this ROI, we integrate over all pixels of the CCD-camera image and normalize the resulting value with respect to the ones related to the two opposite single-domain saturation states. This evaluation yields an effective averaged magnetization $-1 \leq M/M_\mathrm{s} \leq 1$. The latter can be considered as an effective macrospin, in which any microscopic magnetic texture has been averaged out. It will be referred to as "integrated MOKE loop" in the following.

In a first series of experiments, we studied the magnetic domain evolution at constant strain, i.e., we recorded MOKE images at constant voltages V_p as a function of the external magnetic field magnitude $\mu_0 H$ for fixed magnetic field orientation $\mathbf{H} \parallel \mathbf{x}$. We refer to these experiments as $M\,(H)$ measurements. We applied a fixed voltage V_p to the actuator, swept the magnetic field to $-H_\mathrm{sat}$ to prepare the magnetization in a single-domain, negative saturation state, and acquired a reference image. Subsequently, the magnetic field was increased in steps, and a MOKE image was recorded at every field value. The corresponding domain evolution (obtained after

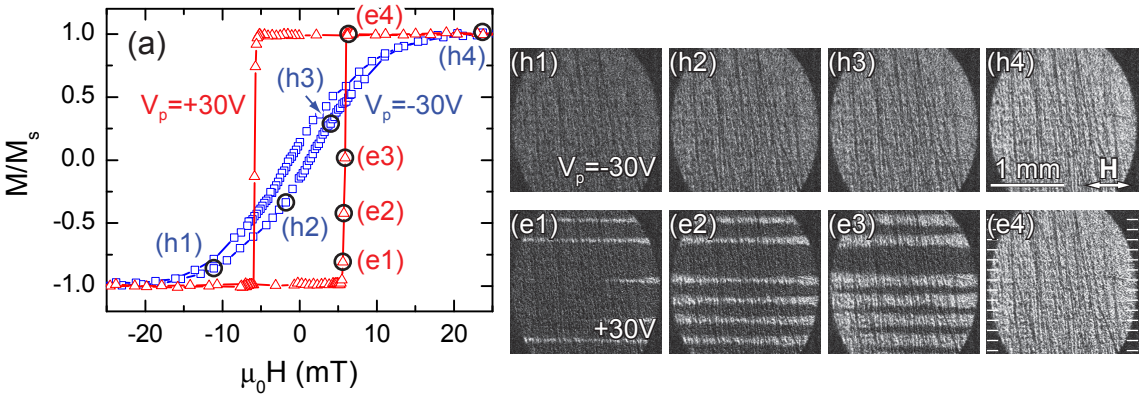

Figure 5.17: Magnetic domain evolution as a function of the external magnetic field magnitude. (a) Integrated MOKE $M\,(H)$ loops for $V_\mathrm{p} = -30\,\mathrm{V}$ (open blue squares) and $V_\mathrm{p} = +30\,\mathrm{V}$ (open red triangles). The lines are guides to the eye. The open black circles indicate the magnetic fields at which the MOKE images (h1)–(h4) and (e1)–(e4) were taken. Hereby, (h1)–(h4) were recorded for $V_\mathrm{p} = -30\,\mathrm{V}$ (**H** parallel to the magnetic hard axis) and (e1)–(e4) were recorded for $V_\mathrm{p} = +30\,\mathrm{V}$ (**H** parallel to the easy axis). The white lines in (e4) indicate the position of the actuator electrodes.

subtraction of the reference image) and the integrated MOKE loops for $V_\mathrm{p} = -30\,\mathrm{V}$ (open blue squares) and $V_\mathrm{p} = +30\,\mathrm{V}$ (open red triangles) are shown in Fig. 5.17. We start the discussion with the data recorded at $V_\mathrm{p} = -30\,\mathrm{V}$, i.e., for a magnetic hard axis along **x**. Figures 5.17(h1)–(h4) show MOKE images for an upsweep of the external magnetic field obtained at magnetic field values h1 $= -10.5\,\mathrm{mT}$, h2 $= -1.5\,\mathrm{mT}$, h3 $= 4.0\,\mathrm{mT}$, and h4 $= 23.0\,\mathrm{mT}$, indicated by circles in the corresponding $M\,(H)$ loop depicted by square symbols in Fig. 5.17(a). In Figs. 5.17(h1)–(h4), the spatially resolved MOKE intensity is homogeneous over the whole Ni film, continuously changing from black to white with increasing magnetic field strength from negative to positive saturation. Hence, the sample is uniformly magnetized throughout the magnetization-reversal process, suggesting coherent and continuous magnetization rotation. Clearly, a single-domain SW approach is appropriate to model this behavior. In contrast, the magnetization reversal along the magnetic easy axis at $V_\mathrm{p} = +30\,\mathrm{V}$ is depicted in Figs. 5.17(e1)–(e4) at magnetic fields close to the coercive field [cf. $M\,(H)$ loop shown by open red triangles in Fig. 5.17(a)]. As apparent, magnetic domains nucleate and gradually propagate until the magnetization-reversal process is finally completed in Fig. 5.17(e4). For such a domain-driven magnetization reversal process the simple SW single macrospin approach appears inadequate, as already inferred from the deviations between the simulated and experimental AMR data at the magnetic coercive field shown in Fig. 5.14. In other words, in view of the domain pattern in Figs. 5.17(e1)–(e4), the macrospin model used in the previous sections to model the magnetization reorientation $M\,(E)$ as a function of electric field at fixed external magnetic field magnitude appears questionable.

To further examine the validity and limitations of the macrospin model for $M\,(E)$, we now address the AMR recorded simultaneously to the MOKE data, referred to as $R\,(H)$ measurements. Figure 5.18(a) again depicts integrated MOKE loops along a magnetic hard axis ($V_\mathrm{p} = -30\,\mathrm{V}$, full blue squares), with zero applied stress

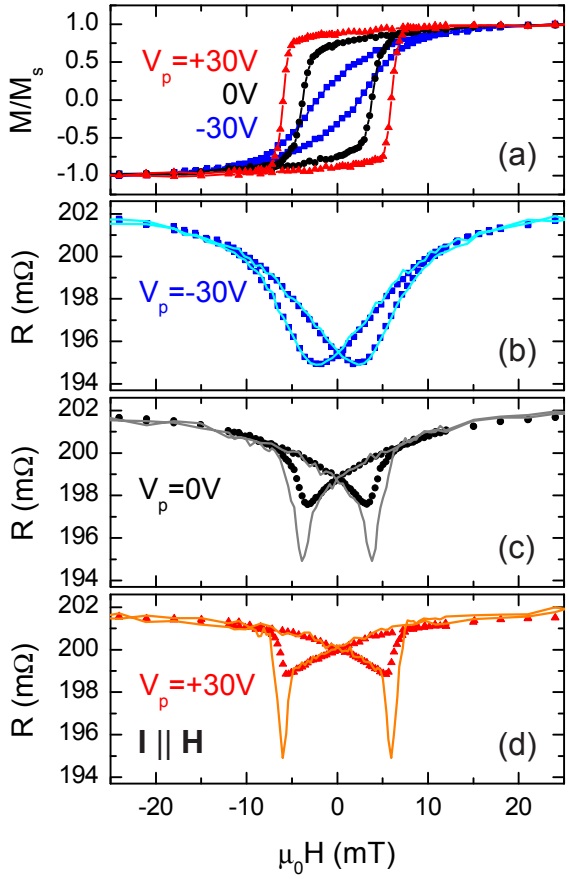

Figure 5.18: (a) Integrated MOKE $M\,(H)$ loops for $V_\mathrm{p} = -30\,\mathrm{V}$ (blue squares), $V_\mathrm{p} = 0\,\mathrm{V}$ (black circles), and $V_\mathrm{p} = +30\,\mathrm{V}$ (red triangles). Simultaneously measured (full symbols) and simulated (solid lines) AMR $R\,(H)$ loops for $V_\mathrm{p} = -30\,\mathrm{V}$ (b), $V_\mathrm{p} = 0\,\mathrm{V}$ (c), and $V_\mathrm{p} = +30\,\mathrm{V}$ (d). Apart from deviations in the vicinity of the coercive fields for $V_\mathrm{p} = 0\,\mathrm{V}$ and $V_\mathrm{p} = +30\,\mathrm{V}$, the simulations in a pseudo-macrospin model are in very good agreement with the measurements.

($V_\mathrm{p} = 0\,\mathrm{V}$, full black circles), and along a magnetic easy axis ($V_\mathrm{p} = +30\,\mathrm{V}$, full red triangles). The corresponding AMR loops, represented by full symbols, are shown in Figs. 5.18(b), (c) and (d) for $V_\mathrm{p} = -30\,\mathrm{V}$, $V_\mathrm{p} = 0\,\mathrm{V}$, and $V_\mathrm{p} = +30\,\mathrm{V}$, respectively. To quantitatively simulate the evolution of the AMR as a function of $\mu_0 H$ in a macrospin-type SW model, we again determined an effective, average magnetization orientation Θ from the $M\,(H)$ loops in Fig. 5.18(a) (see Sec. 5.7). To this end, we use the effective, averaged magnetization orientation in the ROI as a pseudo-macrospin. It should be emphasized at this point that this pseudo-macrospin corresponds to a magnetization orientation averaged over differently oriented magnetic domains, see Figs. 5.17(e1)–(e4). Equation (5.9) with $R_\parallel = 201.9\,\mathrm{m\Omega}$ and $R_\perp = 194.9\,\mathrm{m\Omega}$ then yields the solid lines in Figs. 5.18(b), (c), and (d). As evident from the figure, in full consistency with the findings shown in Fig. 5.14, the AMR calculated using the macrospin model accurately reproduces the measured AMR for **H** parallel to a hard axis ($V_\mathrm{p} = -30\,\mathrm{V}$). For $V_\mathrm{p} = 0\,\mathrm{V}$ and $V_\mathrm{p} = +30\,\mathrm{V}$, **H** is along an increasingly easy axis and we observe an increasing deviation of the AMR simulation from the

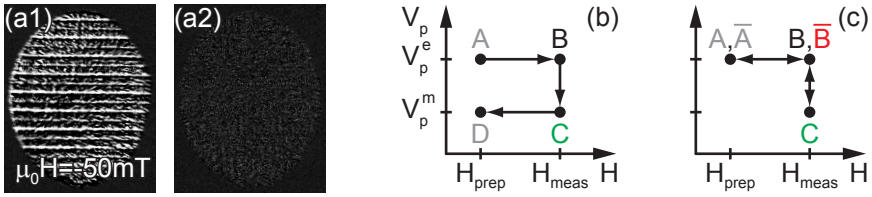

Figure 5.19: (a) Elastic strain-induced Kerr contrast patterns, recorded with the Ni film magnetized to saturation via the application of $\mu_0 H = -50\,\mathrm{mT}$ at $V_\mathrm{p} = +30\,\mathrm{V}$. (a1) Difference image after a sweep to $V_\mathrm{p} = -30\,\mathrm{V}$ and (a2) back to $V_\mathrm{p} = +30\,\mathrm{V}$. (b), (c) Schematic illustrations of measurement sequences used to record magnetic Kerr images as a function of V_p, without the strain-induced signal contributions.

AMR experiment—however only for H in the vicinity of the coercive fields [see Figs. 5.18(c), (d)]. Hence, the AMR experiments corroborate the notion that the pseudo-macrospin is not adequate in the case of substantial microscopic domain formation, i.e., close to the coercive fields. However, for all other field magnitudes and orientations the pseudo-macrospin is adequate. In summary, the magnetization reversal at constant strain in our multifunctional hybrid systems can be modeled in very good approximation using a pseudo-macrospin type of approach, except for a small range of $H \approx H_\mathrm{c}$ with substantial domain formation.

In a second set of experiments we address the voltage control of the magnetization orientation. To this end, we record MOKE images and the AMR as a function of the voltage V_p at constant external magnetic bias field $\mathbf{H}$. However, it turns out that the different strain states at different V_p also give raise to a Kerr signal, as illustrated in Fig. 5.19. In these experiments, we aligned a magnetic easy axis along $\mathbf{H} \parallel \mathbf{x}$ by applying $V_\mathrm{p} = +30\,\mathrm{V}$, and initially magnetized the sample to saturation in a single-domain state and thus established a reference state with a well-defined magnetization orientation by sweeping the magnetic field to $\mu_0 H = -50\,\mathrm{mT}$. After recording a reference image, we swept the voltage to $V_\mathrm{p} = -30\,\mathrm{V}$, keeping $\mu_0 H = -50\,\mathrm{mT}$ constant. Figure 5.19(a1) shows the difference image at $V_\mathrm{p} = -30\,\mathrm{V}$ with respect to the reference at $V_\mathrm{p} = +30\,\mathrm{V}$. After sweeping the voltage back to $V_\mathrm{p} = +30\,\mathrm{V}$, the Kerr difference contrast pattern completely vanishes [Fig. 5.19(a2)], indicating the reversibility of this process. Evidently, the observed Kerr contrast cannot be of magnetic origin, since the magnetic field $\mu_0 H = -50\,\mathrm{mT}$ is way large enough to ensure magnetic saturation at any V_p, such that neither the magnetization orientation nor the magnitude are subject to any magnetoelastic modifications. The Kerr contrast thus must be of non-magnetic origin. Two mechanisms may account for these strain-induced contrast changes. First, the Poisson ratios of the PZT piezoelectric layers and the interdigitated electrodes differ. Thus, the strain induced by $V_\mathrm{p} \neq 0\,\mathrm{V}$ will be slightly inhomogeneous in the $\mathbf{x}-\mathbf{y}$ plane of the actuator, leading to local surface corrugations above the electrodes and thus to a modified intensity of the reflected light. Second, the PMMA layer in between piezo and Ni exhibits strain-induced birefringence, e.g., photoelastic birefringence [255], which also results in a Kerr contrast.

To nevertheless extract the magnetic Kerr signal contributions, we apply two more elaborate measurement sequences. The basic sequence is schematically illustrated

in Fig. 5.19(b). We magnetize the sample to a single-domain state by applying a magnetic preparation field $\mu_0 H_{\mathrm{prep}} = -50\,\mathrm{mT}$ well exceeding the saturation field along the easy axis at $V_{\mathrm{p}}^{\mathrm{e}} = +30\,\mathrm{V}$ (point A), sweep the magnetic field to the measurement bias field H_{meas} (point B), sweep the voltage to the measurement voltage $V_{\mathrm{p}}^{\mathrm{m}}$ (point C), and finally go back to the preparation field $\mu_0 H_{\mathrm{prep}}$ (point D). A Kerr image is acquired at each point. Subsequently, we subtract the images corresponding to equal strain states, such that the resulting images B − A and C − D exhibit only contrast of magnetic origin. Hence, this procedure allows to image the evolution of **M** as a function of strain. To also investigate the reversibility of the voltage-induced magnetization changes, we modify the sequence as sketched in Fig. 5.19(c). After sweeping the voltage to the measurement voltage $V_{\mathrm{p}}^{\mathrm{m}}$ (point C), it is cycled back to $V_{\mathrm{p}}^{\mathrm{e}} = +30\,\mathrm{V}$ (point $\overline{\mathrm{B}}$), and finally the magnetic field is returned to $\mu_0 H_{\mathrm{prep}}$ (point $\overline{\mathrm{A}}$). The difference images B − A and $\overline{\mathrm{B}} - \overline{\mathrm{A}}$ then reveal the degree of reversibility.

Figure 5.20 shows the magnetic Kerr images obtained using the sequence depicted in Fig. 5.19(b) as a function of the voltage V_{p} at different constant magnetic bias fields $\mu_0 H_{\mathrm{meas}} = 3\,\mathrm{mT}$, 4 mT, 5 mT, 6 mT, and 8 mT, depicted in Figs. 5.20(a1)–(a4), (b1)–(b4), (c1)–(c4), (d1)–(d4), and (e1)–(e4), respectively. Hereby, the images (a)–(c) are recorded slightly below the coercive field, while (d) ($\mu_0 H_{\mathrm{meas}} = 6\,\mathrm{mT}$) is directly at the coercive field [$\mu_0 H_{\mathrm{c}} \approx 6\,\mathrm{mT}$ at $V_{\mathrm{p}} = +30\,\mathrm{V}$, cf. Fig. 5.18(a)]. For the latter [Fig. 5.20(d1)], domain nucleation already starts without changing V_{p}. The difference images B − A shown in the first column of Fig. 5.20 are acquired at the preparation voltage $V_{\mathrm{p}}^{\mathrm{e}} = +30\,\mathrm{V}$ after a magnetic field sweep from $\mu_0 H_{\mathrm{prep}} = -50\,\mathrm{mT}$ to the bias field H_{meas}. The difference images C − D in the latter three columns result from a consecutive application of the measurement sequence with different measurement voltages $V_{\mathrm{p}}^{\mathrm{m}} = 0\,\mathrm{V}$, $-8\,\mathrm{V}$, and $-30\,\mathrm{V}$. As evident from Figs. 5.20(a1), (b1), and (c1), no magnetic contrast is yet visible at H_{meas}, indicating a uniform, single-domain magnetization along the initial magnetic field orientation $\mu_0 H_{\mathrm{prep}} < 0\,\mathrm{mT}$, i.e., antiparallel to the bias magnetic field orientation $\mu_0 H_{\mathrm{meas}} > 0\,\mathrm{mT}$. Upon gradually decreasing V_{p}, a noncoherent magnetization-reorientation process sets in for magnetic fields close to the coercive field [see Figs. 5.20(b3), (c2)] via magnetic domain nucleation and propagation, until the process is completed at $V_{\mathrm{p}} = -30\,\mathrm{V}$, as shown in the images in the last column. We note that the domain nucleation preferably proceeds on top of the electrodes, which we attribute to the slight strain inhomogeneities discussed in the context of Fig. 5.19(a1). The final image contrast after the magnetization reorientation is homogeneously white [Figs. 5.20(a4) to (e4)], evidencing a magnetic single-domain state.

Figures 5.20(a1)–(a4), (b1)–(b4), (c1)–(c4), and (e1)–(e4) evidence a fully voltage-controlled magnetization reorientation from an initial magnetic single-domain state to a final single-domain state. As apparent from the Kerr images shown in Fig. 5.20, for externally applied magnetic fields close to H_{c} the magnetization-reorientation process evolves via domain nucleation and propagation. In contrast, for other magnetic field strengths [$\mu_0 H_{\mathrm{meas}} < 4\,\mathrm{mT}$ and $\mu_0 H_{\mathrm{meas}} > 7\,\mathrm{mT}$, see Figures 5.20(a1)–(a4) and (e1)–(e4)]) the Kerr image contrast changes homogeneously as a function of V_{p}, i.e., the magnetization rotates coherently during the V_{p} sweep.

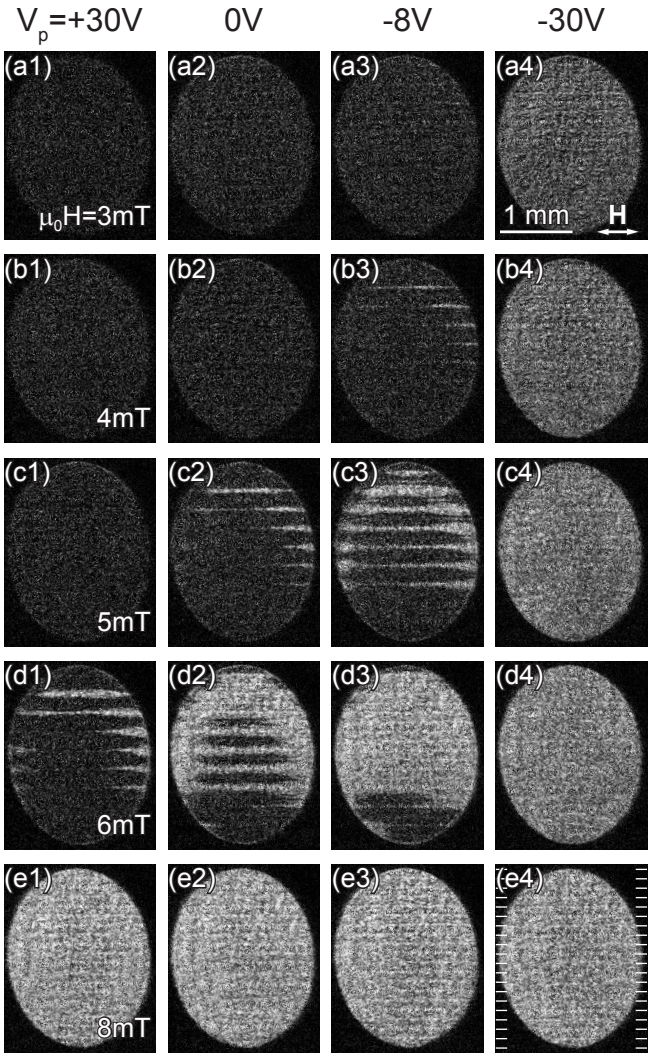

Figure 5.20: Evolution of the magnetization reorientation as a function of the voltage V_p at different, fixed magnetic bias fields after preparing a magnetic single-domain state at $\mu_0 H_\mathrm{prep} = -50\,\mathrm{mT}$. The magnetic Kerr images are obtained using the sequence depicted in Fig. 5.19(b) [images in the first column show difference images B − A, all other images show difference images C − D]. In the vicinity of the coercive field [$\mu_0 H_\mathrm{c} \approx 6\,\mathrm{mT}$ at $V_\mathrm{p} = +30\,\mathrm{V}$, cf. Fig. 5.18(a)] for $\mu_0 H_\mathrm{meas} = 4\,\mathrm{mT}$ [(b1)–(b4)], 5 mT [(c1)–(c4)], and 6 mT [(d1)–(d4)], the voltage-controlled magnetization-reorientation process evidently occurs via magnetic domain nucleation and propagation, and finally attains a single-domain state at $V_\mathrm{p} = -30\,\mathrm{V}$. For other magnetic field strengths, e.g., $\mu_0 H_\mathrm{meas} = 3\,\mathrm{mT}$ [(a1)–(a4)] and $\mu_0 H_\mathrm{meas} = 8\,\mathrm{mT}$ [(e1)–(e4)], the Kerr image contrast changes homogeneously as a function of V_p, i.e., the magnetization rotates coherently during the V_p sweep. The white lines in (e4) indicate the position of the actuator electrodes.

To quantitatively evaluate the Kerr images recorded as a function of V_p, we finally test the applicability of a macrospin picture for the description of $M\,(V_\mathrm{p})$, and address the reversibility of the voltage-induced magnetization reorientation. To this end, we consecutively applied the two measurement sequences illustrated in Figs. 5.19(b) and (c) with different measurement bias fields H_meas. More precisely, for each H_meas we first applied the basic sequence [see Fig. 5.19(b)], i.e., $\mu_0 H_\mathrm{prep} = -50\,\mathrm{mT}$, $V_\mathrm{p}^\mathrm{e} = +30\,\mathrm{V}$ (point A) $\rightarrow \mu_0 H_\mathrm{meas}$, $V_\mathrm{p}^\mathrm{e} = +30\,\mathrm{V}$ (point B) $\rightarrow \mu_0 H_\mathrm{meas}$, $V_\mathrm{p}^\mathrm{m} = -30\,\mathrm{V}$ (point C) $\rightarrow \mu_0 H_\mathrm{prep} = -50\,\mathrm{mT}$, $V_\mathrm{p}^\mathrm{m} = -30\,\mathrm{V}$ (point D). Then we applied the modified sequence [see Fig. 5.19(c)] at the same H_meas, i.e., $\mu_0 H_\mathrm{prep} = -50\,\mathrm{mT}$, $V_\mathrm{p}^\mathrm{e} = +30\,\mathrm{V}$ (point A) $\rightarrow \mu_0 H_\mathrm{meas}$, $V_\mathrm{p}^\mathrm{e} = +30\,\mathrm{V}$ (point B) $\rightarrow \mu_0 H_\mathrm{meas}$, $V_\mathrm{p}^\mathrm{m} = -30\,\mathrm{V}$ (point C) $\rightarrow \mu_0 H_\mathrm{meas}$, $V_\mathrm{p}^\mathrm{e} = +30\,\mathrm{V}$ (point $\overline{\mathrm{B}}$) $\rightarrow \mu_0 H_\mathrm{prep} = -50\,\mathrm{mT}$, $V_\mathrm{p}^\mathrm{e} = +30\,\mathrm{V}$ (point $\overline{\mathrm{A}}$). At each point, a Kerr image is acquired and the resistance is recorded. We refer to these experiments as $M\,(V_\mathrm{p})$ and $R\,(V_\mathrm{p})$ measurements, respectively. The evolution of the corresponding integrated MOKE $M\,(V_\mathrm{p})$ signals obtained from the difference images B − A, $\overline{\mathrm{B}} - \overline{\mathrm{A}}$, and C − D as a function of the measurement field $H = H_\mathrm{meas}$ is shown in Fig. 5.21(a), denoted by B (full black squares), $\overline{\mathrm{B}}$ (full red circles), and C (full green triangles) and referred to as $M_\mathrm{B}\,(H)$, $M_{\overline{\mathrm{B}}}\,(H)$, and $M_\mathrm{C}\,(H)$, respectively. We again determined the magnetization orientation Θ in a macrospin approximation, as displayed in Fig. 5.21(b). The corresponding AMR $R\,(V_\mathrm{p})$ curves simultaneously measured with the Kerr images at the points B and C are depicted in Fig. 5.21(c) by full black squares and full green triangles and referred to as $R_\mathrm{B}\,(H)$ and $R_\mathrm{C}\,(H)$, respectively. For comparison, we also included the integrated MOKE $M\,(H)$ and AMR $R\,(H)$ data recorded as a function of the external magnetic field at constant $V_\mathrm{p} = -30\,\mathrm{V}$ and $+30\,\mathrm{V}$ as open gray squares [denoted as M^- and R^- in Figs. 5.21(a) and (c), respectively] and open gray triangles (M^+ and R^+), respectively.

Using the $M_\mathrm{B}\,(H)$ and $M_\mathrm{C}\,(H)$ curves [Fig. 5.21(a)] recorded simultaneously with $R_\mathrm{B}\,(H)$ and $R_\mathrm{C}\,(H)$, respectively, we again simulate the AMR with Eq. (5.9) and the values of the parameters $R_\parallel$ and $R_\perp$ given above. The AMR curves thus calculated for $R_\mathrm{B}\,(H)$ and $R_\mathrm{C}\,(H)$ are displayed by the solid blue and green lines in Fig. 5.21(c), respectively. Evidently, the measurement and simulation for $R_\mathrm{B}\,(H)$ are in very good agreement, with the exception of a narrow region around H_c, where the macrospin model fails to adequately describe the experiment, in full consistency with the above findings for $M\,(H)$ and $R\,(H)$ measurements (cf. Fig. 5.18). Turning now to $R_\mathrm{C}\,(H)$, we observe a very good quantitative agreement throughout the whole magnetic field range (with small deviations around $\mu_0 H \approx +3\,\mathrm{mT}$). Therefore, except for a magnetic-field range close to H_c we can describe the voltage-induced magnetization changes in very good approximation in a simple macrospin model. This even applies to magnetic field strengths in the vicinity of the coercive field, where the magnetization-reorientation process evidently exhibits magnetic domains [cf. Figs. 5.20(b2)–(b3) and (c2)–(c3)]. It is important to note that since the magnetization evolves from a single-domain state at $V_\mathrm{p} = +30\,\mathrm{V}$ into a single-domain state at $V_\mathrm{p} = -30\,\mathrm{V}$, the magnetization reorientation can still be successfully modeled in macrospin description, which furthermore evidences the versatility of the single-domain model.

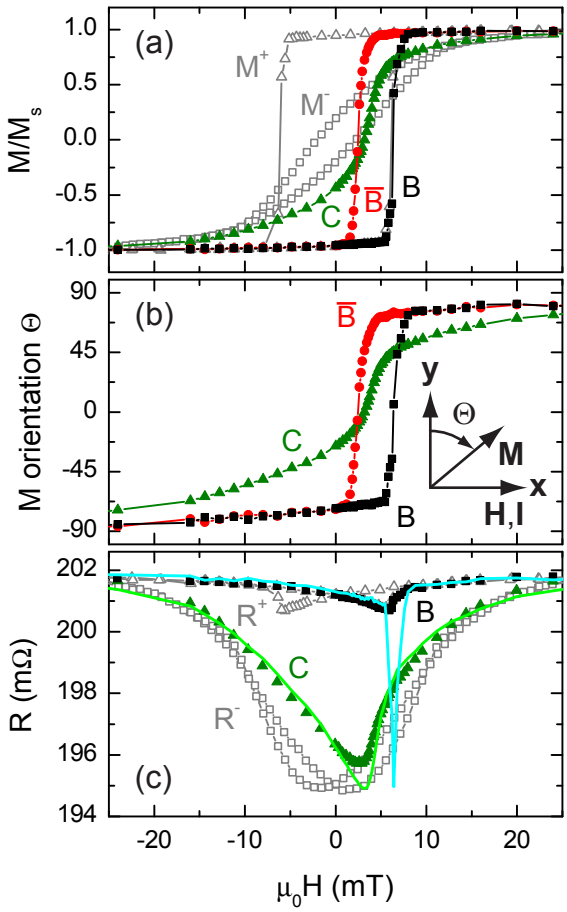

Figure 5.21: Voltage-dependent M and R measurements. The panels show data acquired at the points B (full black squares), $\overline{\text{B}}$ (full red circles), and C (full green triangles) as a function of the measurement field $H = H_{\text{meas}}$ in the sequences depicted in Figs. 5.19(b) and (c). (a) Integrated MOKE $M\,(V_{\text{p}})$ curves obtained from the respective difference images. For comparison, the open gray squares and open gray triangles depict the $M\,(H)$ loops for $V_{\text{p}} = -30\,\text{V}$ (M^-) and $+30\,\text{V}$ (M^+), respectively. (b) Macrospin magnetization orientation Θ, calculated from the measured data displayed in (a) using the pseudo-macrospin model. (c) Corresponding AMR $R\,(V_{\text{p}})$ curves (symbols) and simulations (lines) using the simultaneously recorded $M\,(V_{\text{p}})$ curves [(a), (b)] and the AMR parameters given in the text showing very good overall agreement with the experiment. Hereby, the blue and green solid lines illustrate the simulated evolution of $R_{\text{B}}\,(H)$ and $R_{\text{C}}\,(H)$, respectively. In analogy to (a), the $R\,(H)$ loops for $V_{\text{p}} = -30\,\text{V}$ (R^-) and $+30\,\text{V}$ (R^+) are additionally depicted by open gray squares and open gray triangles, respectively.

As we now have demonstrated the validity of the macrospin approach also for the description of $M\,(V_{\text{p}})$ measurements, we can consistently model the evolution of the magnetization orientation as a function of the voltage V_{p} and the external magnetic field $\mu_0 H$ (Fig. 5.21). We start the discussion with the evolution of $M_{\text{B}}\,(H)$ [full black squares in Fig. 5.21(a)], which coincides with the $M\,(H)$ loop recorded at $V_{\text{p}} = +30\,\text{V}$. The corresponding macrospin magnetization orientation Θ is initially aligned along $-90°$ for large negative external magnetic field [full black squares in Fig. 5.21(b)], continuously rotates to $\approx -70°$ with increasing magnetic field strength,

then abruptly switches into a direction close to $\Theta = 90°$ at the magnetic coercive field, and then continuously rotates towards 90°, the orientation of the external magnetic field. For external magnetic measurement fields $\mu_0 H_{\mathrm{meas}} \lesssim 0\,\mathrm{mT}$, the influence of the Zeeman contribution to the total free energy density in the film plane [cf. Eq. (5.6)] decreases with decreasing absolute value of the external magnetic field, which results in an increasingly dominating magnetoelastic anisotropy contribution. Hence, the magnetization orientation cannot be modified at $\mu_0 H_{\mathrm{prep}} = -50\,\mathrm{mT}$ by application of V_p and can be increasingly rotated to about $\Delta\Theta = 50°$ at $\mu_0 H = 0\,\mathrm{mT}$ [$\Theta_\mathrm{B}(\mu_0 H = 0\,\mathrm{mT}) \approx -75°$ and $\Theta_\mathrm{C}(V_\mathrm{p} = -30\,\mathrm{V}) \approx -25°$]. In this magnetic field range, $M_\mathrm{B}(H)$ and $M_{\overline{\mathrm{B}}}(H)$ fully coincide ($\mathbf{M}_\mathrm{B} \parallel \mathbf{M}_{\overline{\mathrm{B}}}$), i.e., the voltage-induced magnetization reorientation is fully reversible. These findings are consistent with the $M(V_\mathrm{p})$ loops measured via SQUID magnetometry for $\mathbf{H} \parallel \mathbf{x}$ at constant external magnetic field strength $\mu_0 H = 0\,\mathrm{mT}$ and an initially parallel alignment of $\mathbf{H}_{\mathrm{prep}}$ and $\mathbf{M}$ [Fig. 5.10(d)], which also exhibit a reversible rotation of $\mathbf{M}$ between the points A and B. Note that, however, the corresponding magnetization evolution Θ displayed in Fig. 5.11 cannot be directly compared to Fig. 5.21(b) due to the preparation of $\mathbf{M}$ into a well-defined initial state at positive magnetic field $\mu_0 H_{\mathrm{prep}} = +7\,\mathrm{T}$ prior to the measurements shown in Fig. 5.10, while the data shown in Fig. 5.21 are acquired after preparing $\mathbf{M}$ at negative magnetic field $\mu_0 H_{\mathrm{prep}} = -50\,\mathrm{mT}$. In the second field range $0\,\mathrm{mT} \lesssim \mu_0 H_{\mathrm{meas}} \lesssim 8\,\mathrm{mT}$ in Fig. 5.21(b), the angular range within which the magnetization orientation can be rotated by changing $V_\mathrm{p} = +30\,\mathrm{V} \rightarrow -30\,\mathrm{V}$ continuously increases, but the magnetization reorientation is not reversible, since $M_\mathrm{B}(H) \neq M_{\overline{\mathrm{B}}}(H)$. This observation can also be consistently understood in a macrospin model. Here, $\mu_0 H_{\mathrm{prep}} = -50\,\mathrm{mT}$ yields $\mathbf{M}_\mathrm{B}$ antiparallel to $\mu_0 H_{\mathrm{meas}} > 0\,\mathrm{mT}$ aligned along 90°, i.e., $\mathbf{M}_\mathrm{B}$ resides in a local minimum of F at $V_\mathrm{p} = +30\,\mathrm{V}$ and thus in a metastable state. Sweeping V_p from $+30\,\mathrm{V}$ to $-30\,\mathrm{V}$ yields $\mathbf{M}_\mathrm{C}$ aligned along the global minimum of F. However, upon increasing the voltage back to $+30\,\mathrm{V}$, the magnetization does not rotate back in the same way, but evolves into the global minimum of F close to 90°. Therefore, the voltage sweep $V_\mathrm{p} = +30\,\mathrm{V} \rightarrow -30\,\mathrm{V} \rightarrow +30\,\mathrm{V}$ results in an irreversible magnetization-orientation change with $\mathbf{M}_\mathrm{B}$ and $\mathbf{M}_{\overline{\mathrm{B}}}$ essentially being antiparallel at $V_\mathrm{p} = +30\,\mathrm{V}$. The SQUID measurements corresponding to this magnetic field range are displayed in Fig. 5.10(e), showing an irreversible magnetization reorientation from the local minimum in A into the global minimum in B [see Fig. 5.11(e)], followed by a rotation into the global minimum in C. The third magnetic field range $\mu_0 H_{\mathrm{meas}} \gtrsim 10\,\mathrm{mT}$ exceeds $\mu_0 H_\mathrm{c}$ for $V_\mathrm{p} = +30\,\mathrm{V}$, resulting in a (nearly) parallel alignment of $\mathbf{H}_{\mathrm{meas}}$ and $\mathbf{M}_\mathrm{B}$. Here, the evolution of $M(V_\mathrm{p})$ is analogous to the above described for $\mu_0 H_{\mathrm{meas}} \lesssim 0\,\mathrm{mT}$, i.e., sweeping $V_\mathrm{p} = +30\,\mathrm{V} \rightarrow -30\,\mathrm{V} \rightarrow +30\,\mathrm{V}$ rotates $\mathbf{M}_\mathrm{B}$ to $\mathbf{M}_\mathrm{C}$ and back to $\mathbf{M}_\mathrm{B} \parallel \mathbf{M}_{\overline{\mathrm{B}}}$. The angle of rotation decreases with increasing magnetic field strength. The corresponding SQUID loops for an initially antiparallel alignment of $\mathbf{H}_{\mathrm{prep}}$ and $\mathbf{M}$ and a reversible magnetization rotation between the points A and B are given in Fig. 5.10(f) ($\mu_0 H = -5\,\mathrm{mT}$).

Overall, the quantitative comparison of spatially resolved Kerr imaging and AMR measurements demonstrates that the macrospin model cannot only be applied to describe the $M(H)$ and $R(H)$ measurements, but also to the $M(V_\mathrm{p})$ and $R(V_\mathrm{p})$

measurements—with the exception of a narrow range around the magnetic coercive field. Using dedicated measurement sequences to suppress strain-induced contributions to the Kerr signal, the imaging of the magnetization state both as a function of magnetic field and electrical voltage applied to the piezoelectric actuator becomes possible. We extract an effective magnetization orientation (macrospin) by spatially averaging the Kerr images. For experiments both as a function of H and of V_p, we find very good agreement between the AMR calculated using the macrospin and the measured AMR. Our results furthermore are in agreement with the results presented in the previous sections, and show that the magnetization continuously reorients by coherent rotation—except for **H** along a magnetically easy direction in a very narrow region around the magnetic coercive field, where the magnetization reorientation dominantly evolves via domain nucleation and propagation. Taken together, on length scales much larger than the magnetic domain size, the SW macrospin model consistently describes both $M\,(H)$ and $M\,(V_\mathrm{p})$.

5.9 Summary

In summary, we have investigated the magnetic properties of polycrystalline Ni thin film/piezoelectric actuator hybrids at room temperature. We studied the magnetic anisotropy as a function of voltage V_p applied to the actuator both using ferromagnetic resonance spectroscopy and anisotropic magnetoresistance techniques. Our results show that in hybrids with vanishing crystalline magnetic anisotropies in the film plane, i.e., with dominating magneto-elastic anisotropy, the application of V_p induces a uniaxial magnetic anisotropy in the plane of an initially magnetically isotropic ferromagnetic thin film. Furthermore, we demonstrated that this magnetic anisotropy can be inverted (i.e., the magnetic easy axis can be switched by 90°) upon inverting the polarity of V_p. AMR measurements in combination with x-ray diffraction measurements employed to directly measure the strain in the supporting MgO substrate showed that the voltage-dependent changes in the magnetic anisotropy can be fully and quantitatively modeled within magnetoelastic theory. SQUID magnetometry substantiates these findings and evidence that **M** can be reoriented both reversibly and irreversibly solely via changing V_p. Upon an appropriate magnetic-field preparation of **M** into a local minimum of F, **M** can be reoriented irreversibly with V_p, i.e., **M** undergoes a coherent and discontinuous switching process [cf. Fig. 1.3(d)], and the overall voltage-controlled **M** orientation change thus achievable can amount up to 180°. In contrast, if **M** is initially aligned along a global free energy density minimum, the remanent magnetization orientation can be rotated continuously and reversibly within up to 80° via V_p. The $M\,(V_\mathrm{p})$ loops simulated in a single-domain (macrospin) Stoner-Wohlfarth model using the free energy density determined from FMR are in very good agreement with the experiment. An estimation of the domain-wall formation energy using $M\,(H)$ loops showed that the voltage-controlled modifications in the free energy density landscape do not exceed the energy required to nucleate a domain wall, which thus further justifies the applicability of a macrospin model. We furthermore showed that the hysteretic nature

of the piezoelectric actuators allows for a nonvolatile and reversible voltage control of remanent magnetization, demonstrating the feasibility of a spin-mechanics memory with all-electrical read and write at zero external magnetic field. Finally, we have studied the applicability and limitations of a Stoner-Wohlfarth type macrospin model for the description of changes in the magnetic configuration of hybrids by using simultaneous spatially resolved MOKE and integral magnetotransport measurements. We extract an effective magnetization orientation (macrospin) by spatially averaging the Kerr images. For experiments both as a function of H and of V_p, we find very good agreement between the AMR calculated using the macrospin and the measured AMR. Our results show that the magnetization continuously reorients by coherent rotation—except for **H** along a magnetically easy direction in a very narrow region around the magnetic coercive field, where the magnetization reorientation dominantly evolves via domain nucleation and propagation. Taken together, on length scales much larger than the magnetic domain size, the SW macrospin model consistently describes both $M\,(H)$ and $M\,(V_\mathrm{p})$.

Chapter 6

Magnetization control in (Ga,Mn)As thin films

In the previous chapter, we have discussed polycrystalline ferromagnetic thin film/ piezoelectric actuator hybrid structures. The absence of net magnetocrystalline anisotropies makes the spin-mechanics, magnetoelastic anisotropy contribution dominant within the thin film plane in these systems. This concept thus yields a large-angle, voltage-controlled, reversible magnetization orientation control (cf. Sec. 5.5). We now address the impact of in-plane magnetocrystalline anisotropy onto the spin-mechanics scheme. To this end, we employ the dilute magnetic semiconductor (Ga,Mn)As as ferromagnetic constituent. Since the magnetocrystalline anisotropy in (Ga,Mn)As substantially changes as a function of temperature, (Ga,Mn)As/piezoelectric actuator hybrids are an ideal model system for the investigation of different magnetization control regimes. (Ga,Mn)As furthermore exhibits large magnetic domains (a more thorough treatment of the material properties of (Ga,Mn)As with the relevant references will be given in Sec. 6.1), thus its magnetic properties can be comprehensively and quantitatively modeled within the framework of a macrospin approach.

In this chapter, we investigate the voltage control of magnetic anisotropy in (Ga,Mn)As. Taking advantage of the strong temperature dependence of the magnetic anisotropy, it is possible to tune the ratio of the magnetoelastic and magnetocrystalline anisotropy contributions in one and the same sample. In particular, we thus are able to access qualitatively different regimes: at low temperatures ($T \approx 5\,\mathrm{K}$) the magnetoelastic anisotropy term is small compared to the crystalline one, such that the spin-mechanics scheme allows only for minor modifications to the magnetic anisotropy, while at higher temperatures ($T \gtrsim 40\,\mathrm{K}$) the magnetoelastic anisotropy is the dominating anisotropy contribution and thus enables significant changes in the magnetic anisotropy. The chapter is organized as follows: After a short review of the the material properties of (Ga,Mn)As in Sec. 6.1, we summarize the experimental procedures employed and quantify the strain induced by the piezoelectric actuator as a function of temperature in Secs. 6.2 and 6.3, respectively. The procedure to determine the magnetic anisotropy from angle-dependent magnetoresistance (ADMR) experiments and its results are described in Sec. 6.4. At $T = 5\,\mathrm{K}$ we discuss the evolution of $\rho\,(\mu_0 H)$ sweeps and show that the corresponding magnetoresistance switching fields are shifted as a function of the voltage applied to the piezoelectric actuator (Sec. 6.5). In contrast, at $T \gtrsim 40\,\mathrm{K}$ the dominating magnetoelastic contri-

bution (Sec. 6.6) allows to continuously and reversibly rotate the magnetization orientation by about 70° (Sec. 6.7) and enables an irreversible and nonvolatile switching of magnetization orientation by larger angles between two magnetic easy-axis orientations (Sec. 6.8). Last but not least, the magnetostriction constant λ_{111} is derived as a function of temperature from the anisotropy data and the piezo-induced strain in Sec. 6.9. The majority of the results presented in this chapter has been published in Refs. [256, 257]. Results by other groups on similar (Ga,Mn)As/piezoelectric actuator hybrid systems have been reported in Refs. [95, 220, 258].

6.1 (Ga,Mn)As: Material properties

We begin with a short introduction into the prototype ferromagnetic semiconductor (Ga,Mn)As [259]. $Ga_{1-x}Mn_xAs$ films are usually grown onto GaAs, and maintain the lattice structure of their GaAs host lattice and thus exhibit a zinc blende structure [260]. Ferromagnetic order in $Ga_{1-x}Mn_xAs$ is typically observed for $0.02 < x < 0.08$ with a Curie temperature T_C of up to 185 K [261]. To produce $Ga_{1-x}Mn_xAs$ films with x sufficiently high for the formation of ferromagnetism ($x > 0.01$), growth is performed by low-temperature molecular-beam epitaxy (LT-MBE) due to the low solubility of Mn in bulk III-V semiconductors [262–264]. Mn atoms are predominantly incorporated as Mn^{2+} ions on the Ga lattice sites. They act as acceptors and thus both provide localized magnetic moments and itinerant holes [263, 265] mutually coupled by a *p-d* exchange interaction [266]. The long-range magnetic order of the magnetic moments localized on the Mn ions has been successfully modeled within the *p-d* Zener model of the carrier-mediated ferromagnetism by delocalized (or weakly localized) holes [7, 267–271]. To accurately describe their properties, band-structure effects are taken into account, such that the host band structure is parameterized by a multi-band $k \cdot p$ approach and spin-orbit coupling is incorporated. The theory has been very successful in explaining many experimentally observed properties of $Ga_{1-x}Mn_xAs$, e.g., the Curie temperature, the value of the saturation magnetization, magnetic anisotropies, and magnetoelastic effects due to the additional consideration of strain effects in the model. Strain alters the symmetry of the hole wave function in the valence band, which due to the hole-mediated exchange has a strong influence on the magnetic anisotropy [272].

$Ga_{1-x}Mn_xAs$ exhibits rather complex magnetic anisotropy properties, which have been found to depend on many parameters, including temperature, strain, and carrier density [268, 269, 273, 274]. The magnetic anisotropy of $Ga_{1-x}Mn_xAs$ is composed of the following contributions: (i) a cubic magnetic anisotropy, which yields two orthogonal easy axes within the film plane [275]. It is caused by the dependence of the hole energy on the orientation of the magnetization with respect to the $\langle 100 \rangle$ crystal axes [268]. Although the cubic anisotropy field exhibits relatively large values at low temperatures, it decreases rapidly as the temperature increases [265]. (ii) A small in-plane uniaxial anisotropy along [110] is present in most $Ga_{1-x}Mn_xAs$ films on GaAs [276–281], the microscopic origin of which is still controversially discussed. The corresponding anisotropy field is essentially temperature independent,

hence its relative importance increases with temperature and causes the magnetic easy axis to qualitatively change as a function of temperature [277, 278, 280, 281]. Therefore, at low temperatures ($T \lesssim T_C/2$) the magnetic anisotropy is dominated by the cubic contribution with magnetic easy axes along the $\langle 100 \rangle$ directions, while at higher temperatures ($T \gtrsim T_C/2$) the uniaxial anisotropy contribution along [110] prevails [282]. (iii) A uniaxial magnetic anisotropy contribution perpendicular to the film plane due to shape anisotropy, which is comparably small as the saturation magnetization is small due to the fact that the magnetic ions are quite diluted [263]. (iv) Furthermore, the magnetic anisotropy of $Ga_{1-x}Mn_xAs$ significantly depends on strain, such that it qualitatively changes as a function of strain [231, 275, 283–285]. Pseudomorphic growth of $Ga_{1-x}Mn_xAs$ on (001)-oriented cubic substrates leads to a uniaxial magnetic anisotropy perpendicular to the film plane due to biaxial epitaxial strain. $Ga_{1-x}Mn_xAs$ layers grown on GaAs are compressively strained, which results in a uniaxial magnetic hard axis, so that the film plane is a magnetic easy plane [231, 275, 283, 285, 286]. In contrast, $Ga_{1-x}Mn_xAs$ films with tensile strain obtained by using appropriate $Ga_{1-y}In_yAs$ buffers exhibit a uniaxial easy axis and thus the film plane is magnetically hard, so that the magnetization aligns along the film normal at low magnetic fields [275, 283, 285].

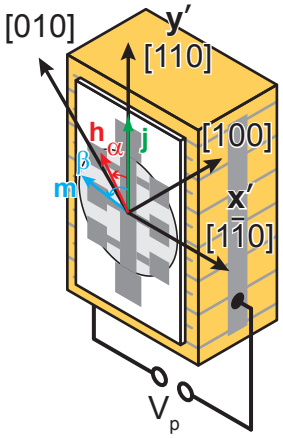

Fig. 6.1: Illustration of the (Ga,Mn)As/piezoelectric actuator hybrid with the current density **j** along [110] parallel to the main expansion direction **y′**.

Furthermore, the spin-orbit coupling in the valence band and the non-cubic symmetry induced by epitaxial strain [270, 287, 288] result in pronounced anisotropic magnetoresistance in $Ga_{1-x}Mn_xAs$ [289–293]. Magneto-optical imaging studies on the magnetic domain structure in $Ga_{1-x}Mn_xAs$ show large and well-defined magnetic domains of several hundred microns during magnetization reversal [282], which results in $Ga_{1-x}Mn_xAs$ being ideally suited for spintronic device concepts and fundamental experiments interpreted in terms of a macrospin (single-domain) approach [cf. Sec. 5.6].

6.2 Experimental details

The 30 nm thick $Ga_{1-x}Mn_xAs$ film with a Mn concentration $x = 0.045$ investigated here was grown by LT-MBE on a (001)-oriented semi-insulating GaAs substrate in the group of W. Limmer at Universität Ulm [110]. The sample exhibits a Curie temperature $T_C \approx 85\,K$, as evident from SQUID magnetometry [cf. Fig. 6.13(a)]. For the magnetotransport studies, the sample was cleaved into rectangular pieces with edges along [110] and [$\bar{1}$10]. We patterned the films into $150 \times 600\,\mu m^2$ Hall bars with the current direction **j** along the [110] crystal axis via optical lithography and wet chemical etching. Subsequently, the GaAs substrate was mechanically polished to a thickness of about 100 μm and the samples were then cemented with a two-

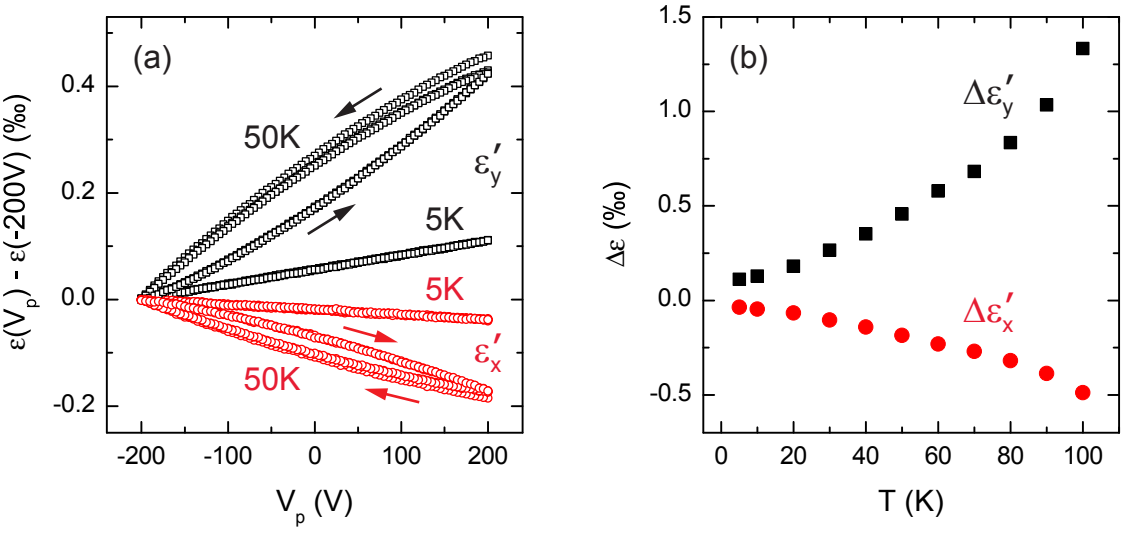

Figure 6.2: (a) $\epsilon_2'(V_\mathrm{p})$ (black squares) and $\epsilon_1'(V_\mathrm{p})$ (red circles) loops along $\mathbf{y}'$ and $\mathbf{x}'$, respectively, at $T = 5\,\mathrm{K}$ and $50\,\mathrm{K}$, measured using strain gauges. To allow for comparison, we plot $\epsilon_i'(V_\mathrm{p}) - \epsilon_i'(-200\,\mathrm{V})$ $(i = 1, 2)$. (b) Temperature dependence of the maximum strain $\Delta\epsilon_i' = \epsilon_i'(V_\mathrm{p} = +200\,\mathrm{V}) - \epsilon_i'(V_\mathrm{p} = -200\,\mathrm{V})$ $(i = 1, 2)$, determined from the third voltage cycle (see text).

component epoxy [126] onto piezoelectric actuators annealed for for 2 h at 120°C in air. The samples were aligned such that the GaAs [110] direction is parallel to the main piezoelectric actuator expansion direction $\mathbf{y}'$ (Fig. 6.1). We here adopt the angle convention introduced by Limmer *et al.* [110], where α and β denote the angles between $\mathbf{j}$ and $\mathbf{h}$ and $\mathbf{j}$ and $\mathbf{m}$, respectively (Fig. 6.1). Note that angles are defined counterclockwise here, whereas they are defined clockwise in the standard coordinate system shown in Fig. 4.4.

The magnetic anisotropy was determined from magnetotransport experiments carried out in a superconducting magnet cryostat, with the hybrid sample mounted on a rotatable sample stage analogous to Sec. 5.4. As illustrated in Fig. 6.1, the external magnetic field always lies within the film plane with the angle α enclosed by the magnetic field orientation $\mathbf{h}$ and the current density $\mathbf{j}$ adjustable within $-140° < \alpha < +140°$. Using a dc bias current density of $j = 4.4 \times 10^3\,\mathrm{Acm}^{-2}$ the resistivities ρ_long along $\mathbf{j}$ and ρ_trans perpendicular to $\mathbf{j}$ were recorded via four-point voltage measurements. We studied the magnetic properties of the sample using conventional magnetoresistance traces $\{\rho_\mathrm{long}(\mu_0 H), \rho_\mathrm{trans}(\mu_0 H)\}$ at a fixed magnetic field orientation α, as well as via ADMR measurements $\{\rho_\mathrm{long}(\alpha), \rho_\mathrm{trans}(\alpha)\}$ at fixed external magnetic field strength. The data presented in this chapter were recorded in the course of M. Althammer's diploma thesis [294].

6.3 Measurement of piezo-induced strain

To determine the temperature dependence of the piezo-induced strain, we again relied on strain gauges [128]. Figure 6.2(a) exemplarily depicts three full $\epsilon_2'(V_\mathrm{p})$

cycles along $\mathbf{y}'$ (black squares) and the corresponding $\epsilon_1'(V_\mathrm{p})$ loops along $\mathbf{x}'$ (red circles) at $T = 5\,\mathrm{K}$ and $50\,\mathrm{K}$. The temperature dependence of the maximum strain $\Delta\epsilon_i' = \epsilon_i'(V_\mathrm{p} = +200\,\mathrm{V}) - \epsilon_i'(V_\mathrm{p} = -200\,\mathrm{V})$ $(i = 1, 2)$ is shown in Fig. 6.2(b). Evidently, both the maximum strain and the hysteresis remarkably decrease with decreasing temperature due to strongly reduced values of the piezoelectric coefficients d at lower temperatures [295]. However, this efficiency reduction is inherently accompanied by a strong increase of the coercive field strength, which results in a high stability against electrical depoling, such that the loss in strain can be partially compensated using a larger voltage swing. Hence, the measurements presented in this chapter are recorded in the bipolar operation regime $-200\,\mathrm{V} \leq V_\mathrm{p} \leq +200\,\mathrm{V}$ within the temperature range $5\,\mathrm{K} \leq T \leq 80\,\mathrm{K}$ [219].

6.4 Determination of magnetic anisotropy from ADMR

To describe the magnetic anisotropy and thus the magnetization orientation in our (Ga,Mn)As thin films, we use the total free energy density [264]

$$\begin{aligned} F &= F_\mathrm{Zeeman} + F_\mathrm{c}^{\parallel} + F_\mathrm{u}^{010} + F_\mathrm{u}^{110}(V_\mathrm{p}) \\ &= -\mu_0 \mathbf{H}\cdot\mathbf{M} + K_\mathrm{c}^{\parallel}\left(m_x^2 m_y^2\right) + K_\mathrm{u}^{010} m_y^2 + K_\mathrm{u}^{110}(V_\mathrm{p})\,(\mathbf{j}\cdot\mathbf{m})^2 \\ &= -\mu_0 H M\cos(\beta-\alpha) + K_\mathrm{c}^{\parallel}\left[\cos^2(\beta+45^\circ)\cos^2(\beta-45^\circ)\right] \\ &\quad + K_\mathrm{u}^{010}\cos^2(\beta-45^\circ) + K_\mathrm{u}^{110}(V_\mathrm{p})\cos^2\beta. \end{aligned} \tag{6.1}$$

This ansatz relies on the magnetization orientation being retained in the film plane, owing to a magnetic hard axis perpendicular to the film plane [110]. This energy contribution is composed of the comparatively weak shape anisotropy due to the rather small magnetization [Fig. 6.13(a)] and a dominating uniaxial anisotropy with a magnetic hard axis caused by the reduction of the crystal symmetry due to epitaxial strain. The latter arises from magnetoelastic effects due to compressive strain of the crystal lattice in the film plane [110, 231, 275]. In Eq. (6.1), the first term describes the Zeeman energy, while the two following terms are the in-plane cubic anisotropy and a uniaxial magnetic anisotropy along [010], represented by the anisotropy constants $K_\mathrm{c}^{\parallel}$ and K_u^{010}, respectively. The last term in Eq. (6.1) accounts for the magnetoelastic contribution to the free energy density $K_\mathrm{u}^{110}(V_\mathrm{p})$ as a function of the applied voltage along the dominant elongation direction $\mathbf{y}'$. We note that the cubic anisotropy field $B_\mathrm{c}^{\parallel}$ used by Limmer *et al.* in Refs. [110, 207] is given by $B_\mathrm{c}^{\parallel} = -(1/2)\,K_\mathrm{c}^{\parallel}/M$, while we here refer to the definition $B_\mathrm{c}^{\parallel} = K_\mathrm{c}^{\parallel}/M$, as used throughout this thesis.

To quantitatively model the evolution of the ADMR measurements and thus determine the magnetic anisotropy, we again rely on the formalism described in Sec. 4.4.2, using the longitudinal and transverse resistivities of a tetragonally distorted film in Eqs. (4.37). Note that a similar approach to determine the in-plane magnetic anisotropy in (Ga,Mn)As has also been followed by Yamada *et al.* [296]. For the ADMR measurements, we first aligned the magnetization into a well-defined initial state in

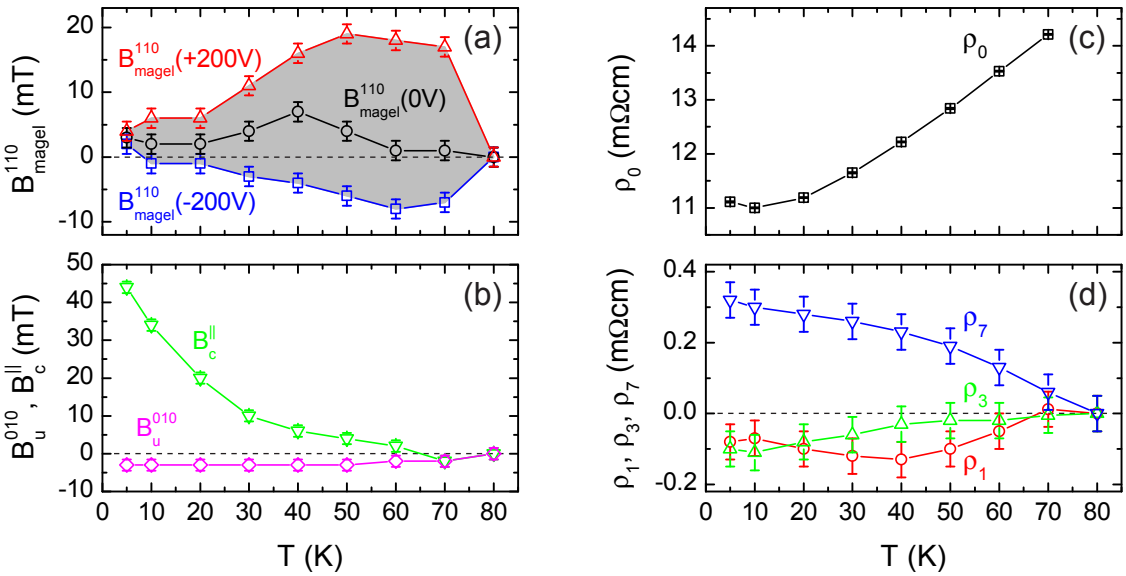

Figure 6.3: Temperature dependence of the anisotropy parameters $B^{110}_{\mathrm{magel}}(V_\mathrm{p}) = K^{110}_\mathrm{u}(V_\mathrm{p})/M$ (a), $B^{010}_\mathrm{u} = K^{010}_\mathrm{u}/M$, and $B^{\parallel}_\mathrm{c} = K^{\parallel}_\mathrm{c}/M$ (b) and the resistivity parameters ρ_0 (c), ρ_1, ρ_3, and ρ_7 (d), as derived from the iterative fitting procedure of the ADMR curves at different external magnetic field strengths. At low temperatures $T \lesssim T_\mathrm{C}/2 \approx 40\,\mathrm{K}$ the cubic anisotropy contribution dominates the magnetic anisotropy, while at higher temperatures $T \gtrsim T_\mathrm{C}/2$ the strain-induced magnetoelastic uniaxial magnetic anisotropy contribution prevails. The gray-shaded area in (a) denotes the range of within $B^{110}_{\mathrm{magel}}(V_\mathrm{p}, T)$ can be adjusted in-situ by application of a voltage $-200\,\mathrm{V} \leq V_\mathrm{p} \leq +200\,\mathrm{V}$ at a certain temperature T. The parameter ρ_0 in (c) was derived from measurements at $V_\mathrm{p} = +200\,\mathrm{V}$ and $\mu_0 H = 100\,\mathrm{mT}$, the parameters ρ_1, ρ_3, and ρ_7 are found to be independent of V_p and H.

an external magnetic field of $\mu_0 H = +7\,\mathrm{T}$ along $\alpha = -140°$. Then we lowered the field to the measurement field and started the angular scan $\{\rho_{\mathrm{long}}(\alpha), \rho_{\mathrm{trans}}(\alpha)\}$.

To give an introductive overview, we here present the temperature dependence of the anisotropy and resistivity parameters, derived from the full set of ADMR measurements $\{\rho_{\mathrm{long}}(\alpha), \rho_{\mathrm{trans}}(\alpha)\}$ recorded for $V_\mathrm{p} = -200\,\mathrm{V}, 0\,\mathrm{V}, +200\,\mathrm{V}$ at different temperatures, while the experimental data will be shown in the following sections. Figure 6.3 displays the temperature dependence of the anisotropy parameters $B^{110}_{\mathrm{magel}}(V_\mathrm{p}) = K^{110}_\mathrm{u}(V_\mathrm{p})/M$ in panel (a), $B^{010}_\mathrm{u} = K^{010}_\mathrm{u}/M$, $B^{\parallel}_\mathrm{c} = K^{\parallel}_\mathrm{c}/M$ in panel (b), and the resistivity parameters ρ_0 in panel (c), ρ_1, ρ_3, and ρ_7 in panel (d). In the fitting procedure, all resistivity parameters except ρ_0 are kept constant for the different values of the applied magnetic field. The field-dependent change in ρ_0 accounts for the influence of negative magnetoresistance typically observed for (Ga,Mn)As [289, 291, 292, 297]. In analogy to Sec. 5.4, ρ_0 here also shows a systematic but small change as a function of V_p due to the piezoresistive effect, e.g., we observe an increase of ρ_0 from $V_\mathrm{p} = -200\,\mathrm{V}$ to $+200\,\mathrm{V}$ by 0.1% at $T = 5\,\mathrm{K}$ and $\mu_0 H = 60\,\mathrm{mT}$. The V_p dependence of ρ_0 at 50 K and an external magnetic field of 10 mT and 100 mT is shown in Figs. 6.10(a) and (c), respectively. We did not observe a magnetic field dependence of ρ_1, ρ_3, and ρ_7. Moreover, within error bars

we did not observe a dependence of ρ_1, ρ_3, and ρ_7 on V_p.

As typically observed for (Ga,Mn)As, the magnetic anisotropy at low temperature ($T \lesssim T_\mathrm{C}/2 \approx 40\,\mathrm{K}$) is dominated by the cubic magnetic anisotropy contribution. As shown in Figs. 6.3(a) and (b), in this temperature regime the ratio of the anisotropy constants amounts to $B^{110}_\mathrm{magel}/B^{\parallel}_\mathrm{c} \approx 1/8$. Consequently, as we will discuss in Sec. 6.5 in this regime the magnetoelastic influence is rather small, and the application of a voltage V_p to the actuator only allows to shift the switching fields in $\rho\,(\mu_0 H)$ curves. At higher temperatures ($T \gtrsim T_\mathrm{C}/2$) the cubic anisotropy term strongly decreases, so that the magnetocrystalline anisotropy is dominated by the uniaxial contribution. Simultaneously the magnetoelastic uniaxial anisotropy contribution substantially increases due to the increase in the piezo-induced strain with temperature [Fig. 6.2(b)]. Thus, in this temperature range we obtain $B^{110}_\mathrm{magel}\,(+200\,\mathrm{V})\,/B^{\parallel}_\mathrm{c} \approx 2/1$. As will be discussed in Secs. 6.6, 6.7, and 6.8, this enables a substantial voltage control of magnetization orientation.

6.5 Magnetotransport at 5K

At $T = 5\,\mathrm{K}$ (Ga,Mn)As exhibits a comparatively large cubic anisotropy [Fig. 6.3(b)] and the piezo-induced strain is small (Fig. 6.2), resulting in only a minor influence of V_p on the magnetic anisotropy. This allows to investigate the influence of strain on a system dominated by cubic anisotropy. We used magnetotransport measurements $\{\rho_\mathrm{long}\,(\mu_0 H)\,, \rho_\mathrm{trans}\,(\mu_0 H)\}$ to this end.

Figures 6.4(a) and (b) show the $\{\rho_\mathrm{long}\,(\mu_0 H)\,, \rho_\mathrm{trans}\,(\mu_0 H)\}$ downsweep curves measured at 5 K and $V_\mathrm{p} = 0\,\mathrm{V}$ for the external magnetic field aligned at $\alpha = 350°$. To understand the evolution of the downsweep curve from positive to negative magnetic fields, we compare the corresponding evolution of $\{\rho_\mathrm{long}\,(\alpha)\,, \rho_\mathrm{trans}\,(\alpha)\}$ in Figs. 6.4(c) and (d) at $\mu_0 H = 7\,\mathrm{T}$. At such high $\mu_0 H$, $\mathbf{M} \parallel \mathbf{H}$, such that $\beta = \alpha$ is fulfilled. Thus, the evolution of the magnetoresistance as a function of the magnetization orientation β is directly traced. Using a macrospin Stoner-Wohlfarth model, we calculate β from F determined from ADMR measurements (Sec. 6.4). In simple terms, $\mathbf{M}$ orients along a local minimum of F. Note that, however, the magnitude of ρ_long in Figs. 6.4(a) and (c) must be corrected for the influence of negative magnetoresistance. The evolution of the magnetization orientation is illustrated in Fig. 6.4(f) and in the free energy density contour plot in Fig. 6.4(e): (A) $\mu_0 H = 100\,\mathrm{mT} \rightarrow -5\,\mathrm{mT}$: rotation of the magnetization from $\beta = 350° \rightarrow 310°$, adjacent to the closest magnetic easy axis at 313° for 0 mT. In this magnetic field range, ρ_long and ρ_trans change smoothly [Figs. 6.4(a), (b)], and consequently β changes smoothly [Figs. 6.4(c), (d)], indicative of a coherent and continuous magnetization rotation (depicted by the black arrows in all panels). Note that the change in $\{\rho_\mathrm{long}\,(\mu_0 H)\,, \rho_\mathrm{trans}\,(\mu_0 H)\}$ [Figs. 6.4(a), (b)] is in agreement (qualitatively for ρ_long and quantitatively for ρ_trans) with the values expected for the corresponding magnetization orientation from the $\{\rho_\mathrm{long}\,(\alpha)\,, \rho_\mathrm{trans}\,(\alpha)\}$ ADMR curves at 7 T ($\beta = \alpha$) [Figs. 6.4(c), (d)]. (B) $\mu_0 H = -5\,\mathrm{mT}$: discontinuous resistivity changes yield the first switching process by $\Delta\beta \approx 85°$ into a direction close to the magnetic easy

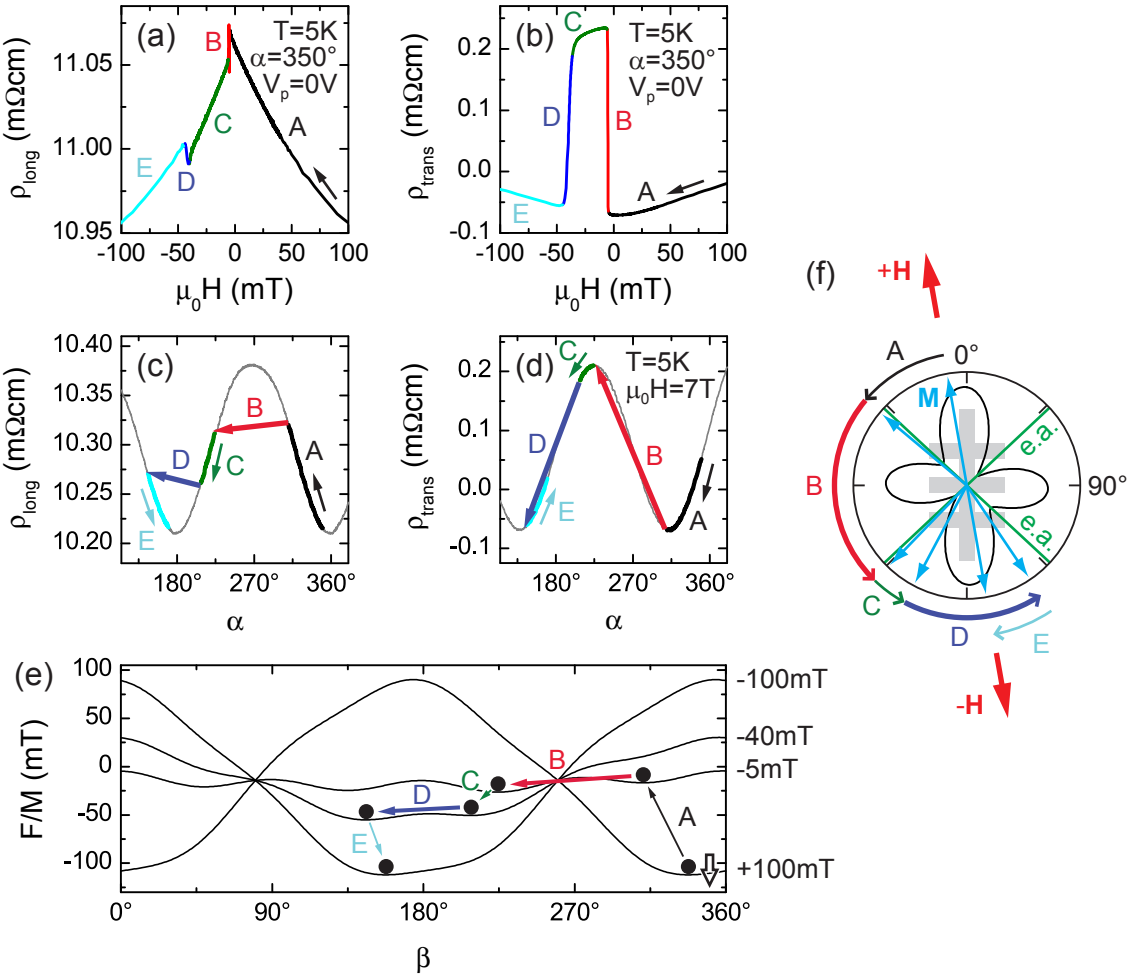

Figure 6.4: (a) $\rho_{\mathrm{long}}\,(\mu_0 H)$ and (b) $\rho_{\mathrm{trans}}\,(\mu_0 H)$ downsweep curves measured at 5 K and $V_{\mathrm{p}} = 0\,\mathrm{V}$ for the external magnetic field aligned at $\alpha = 350°$. (c) $\rho_{\mathrm{long}}\,(\alpha)$ and (d) $\rho_{\mathrm{trans}}\,(\alpha)$ curves recorded at $\mu_0 H = 7\,\mathrm{T}$, such that $\beta = \alpha$ is fulfilled. An explanation of the evolution is given in the text. (e) Free energy density contours $F/M\,(\beta)$ for the external magnetic field applied along $\alpha = 350°$ (indicated by the downward-oriented arrow) at field strengths $+100\,\mathrm{mT}$, $-5\,\mathrm{mT}$, $-40\,\mathrm{mT}$, and $-100\,\mathrm{mT}$. (f) Illustration of the evolution of magnetization orientation during the external magnetic field sweep. Also shown are the free energy density contour and the magnetic easy axes at zero external magnetic field. In all panels, regular arrows depict coherent and continuous magnetization rotations [steps (A), (C), (E)], while bold arrows represent noncoherent magnetization switching processes [steps (B), (D)].

axis at 227° for 0 mT. We refer to the corresponding field as a switching field in the following. The energy barrier between the two respective minima in the free energy density contour for −5 mT evidence a noncoherent magnetization switching (see Sec. 5.6 and Refs. [105, 231, 234, 298–300]), indicated by the bold red arrows. In analogy to (A), the evolution of the magnetization orientation in Figs. 6.4(c) and (d) elucidates the fact that the jump observed in ρ_{trans} is much larger than the one observed in ρ_{long}, since for the magnetization jump ρ_{trans} almost changes from its minimum to its maximum value, while ρ_{long} exhibits similar values. (C)

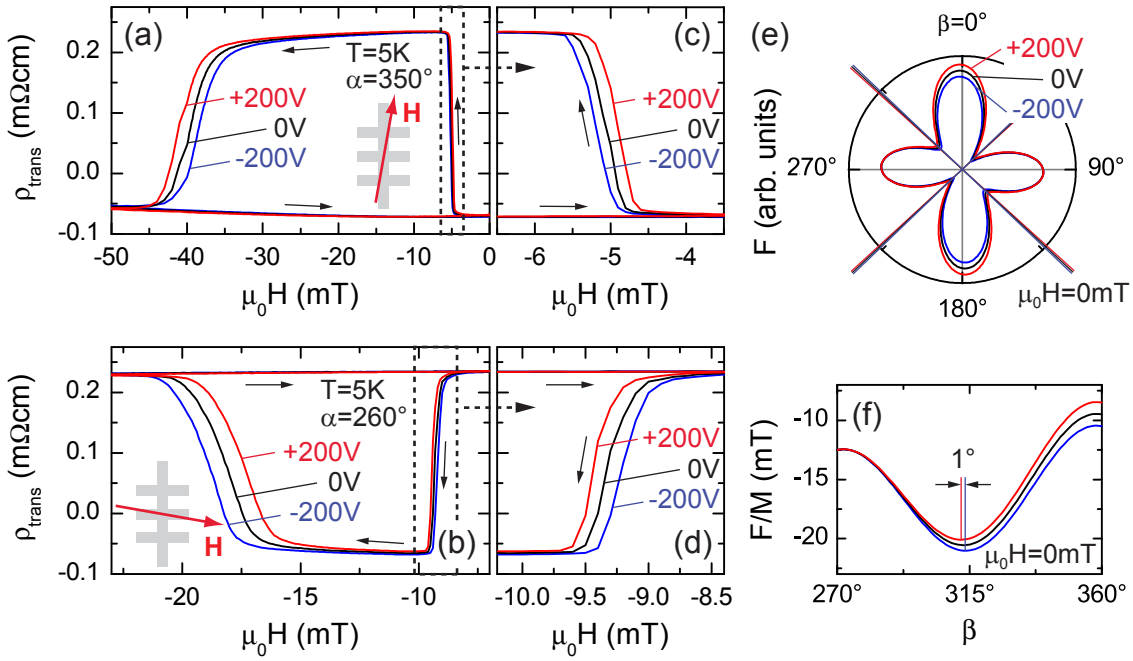

Figure 6.5: (a), (c) Enlarged sections of the $\rho_{\mathrm{trans}}(\mu_0 H)$ curves measured at 5 K for the external magnetic field H aligned at $\alpha = 350°$ showing the piezo-voltage dependence of the first (c) and second (a) switching field. (b), (d) For $\alpha = 260°$ the order of switching fields depending on the piezo voltage is inverted. The arrows indicate the direction of the field sweeps. (e), (f) Free energy density contours $F(\beta)$ as a function of the magnetization orientation β for zero external magnetic field at different voltages V_{p} exhibit an overall tilting of the relative orientation of the magnetic easy axes $\Delta\beta$ by about 1°.

$\mu_0 H = -5\,\mathrm{mT} \rightarrow -40\,\mathrm{mT}$: slight rotation of the magnetization (corresponding to a decrease in β) within the minimum of the free energy density close to 227°. (D) $\mu_0 H = -40\,\mathrm{mT}$: second switching process by $\Delta\beta \approx 60°$ into a direction close to the magnetic easy axis at 133° for 0 mT, which again occurs as a noncoherent magnetization switching due to the presence of an energy barrier separating the two respective minima [Fig. 6.4(e)]. (E) $\mu_0 H = -40\,\mathrm{mT} \rightarrow -100\,\mathrm{mT}$: rotation of magnetization from $\beta \approx 145° \rightarrow 170°$, the orientation of the external magnetic field.

We now turn to the dependence of the switching fields on V_{p}. At 5 K the influence of V_{p} on the magnetic anisotropy is only marginal as visualized in the free energy density contour plots at zero external magnetic field in Figs. 6.5(e) and (f). The application of a voltage V_{p} leads to a slight tilting of the relative orientation of the magnetic easy axes by only about 1° in the voltage range $-200\,\mathrm{V} \leq V_{\mathrm{p}} \leq +200\,\mathrm{V}$ [Fig. 6.5(f)]. Figures 6.5(a) and (c) show the first (B) and the second (D) switching field of $\rho_{\mathrm{trans}}(\mu_0 H)$ for the same magnetic field orientation $\alpha = 350°$ recorded at the voltages $V_{\mathrm{p}} = +200\,\mathrm{V}$ (red curve), 0 V (black), and $-200\,\mathrm{V}$ (blue). For positive (negative) V_{p} the first switching field shifts to lower (higher) and the second switching field to higher (lower) absolute values of the magnetic field. In analogy to Sec. 5.6, this observation can be explained in terms of noncoherent magnetization switching. As the magnetic field strength is approaching the first switching

field at $\mu_0 H \approx -5\,\mathrm{mT}$, at a certain magnetic field magnitude a positive (negative) V_p induces a uniaxial magnetic anisotropy with a magnetic hard (easy) axis along $\mathbf{j}$ [Fig. 6.5(e)], leading to a decreasing (increasing) difference in the free energy density $\Delta F/M$ between the local minimum at $\beta \approx 315°$ the magnetization resides in and the adjacent global minimum at $\beta \approx 225°$. If $\Delta F/M$ exceeds the domain-wall formation energy, the magnetization will switch into the energetically more favorable global minimum. Therefore, a decreasing (increasing) free energy density difference $\Delta F/M$ leads to a shift of the corresponding switching field to smaller (larger) absolute values of the magnetic field, in agreement with experimental observation. Following the simple approach of Cowburn *et al.* [233], a modified ansatz yields an absolute switching-field shift of 0.1 mT for $V_\mathrm{p} = +200\,\mathrm{V} \rightarrow -200\,\mathrm{V}$ using a domain-wall formation energy $\Delta F/M = 9.9\,\mathrm{mT}$ for the first switching field and a shift of 1.6 mT using $\Delta F/M = 4.5\,\mathrm{mT}$ for the second switching field. The phenomenological domain-wall formation energies are obtained such that the measured switching fields at $V_\mathrm{p} = 0\,\mathrm{V}$ are reproduced by simulations of the magnetization reversal in a noncoherent switching model according to Sec. 5.6. The switching-field shifts thus determined are in reasonable agreement with the experimental values 0.3 mT and 2.7 mT for the first and second switching fields, respectively [Figs. 6.5(a), (c)]. For the external magnetic field aligned along $\alpha = 350° - 90° = 260°$, the order of the switching fields is inverted compared to $\alpha = 350°$ [Figs. 6.5(b) and (d)]. This is due to the fact that the order of the differences in the free energy density $\Delta F/M$ between the minima at $\beta \approx 225°$ and $\beta \approx 135°$ is inverted, too, corroborating our analysis.

Figures 6.6(a) and (b) show ADMR measurements $\{\rho_\mathrm{long}(\alpha), \rho_\mathrm{trans}(\alpha)\}$ recorded at $T = 5\,\mathrm{K}$ and $V_\mathrm{p} = 0\,\mathrm{V}$ for rotations at external magnetic field strengths $\mu_0 H = 1\,\mathrm{T}$ and 60 mT (black circles). Following the discussion in Sec. 4.4.2, the angular dependence at small $\mu_0 H$ already indicates that the in-plane anisotropy is dominated by a cubic contribution with magnetic easy axes along $\langle 100 \rangle$ [cf. Figs. 4.10(a) and (b)]. This is corroborated by the simulation, where the simulated curves (red lines) are obtained from the iterative fitting procedure described in Secs. 4.4.2 and 6.4 using the parameter values given in Fig. 6.3. The piezo-voltage dependence of $\{\rho_\mathrm{long}(\alpha), \rho_\mathrm{trans}(\alpha)\}$ at 60 mT is shown in Figs. 6.6(c) and (d) recorded at $V_\mathrm{p} = +200\,\mathrm{V}$ (red curve) and $-200\,\mathrm{V}$ (blue). In agreement with the above discussion, the curves at different V_p exhibit only marginal changes.

6.6 Magnetotransport at higher temperatures

Due to the strong temperature dependence of magnetic anisotropy in (Ga,Mn)As, the magnetic anisotropy landscape can be adjusted to a regime in which piezo-induced strain qualitatively alters magnetic anisotropy. This becomes obvious from magnetotransport measurements at $T = 30\,\mathrm{K}$. At this temperature, the decreasing influence of the cubic anisotropy contribution with increasing V_p can be well observed.

Figure 6.7(a) shows $\rho_\mathrm{long}(\mu_0 H)$ up- and downsweep curves measured at 30 K and

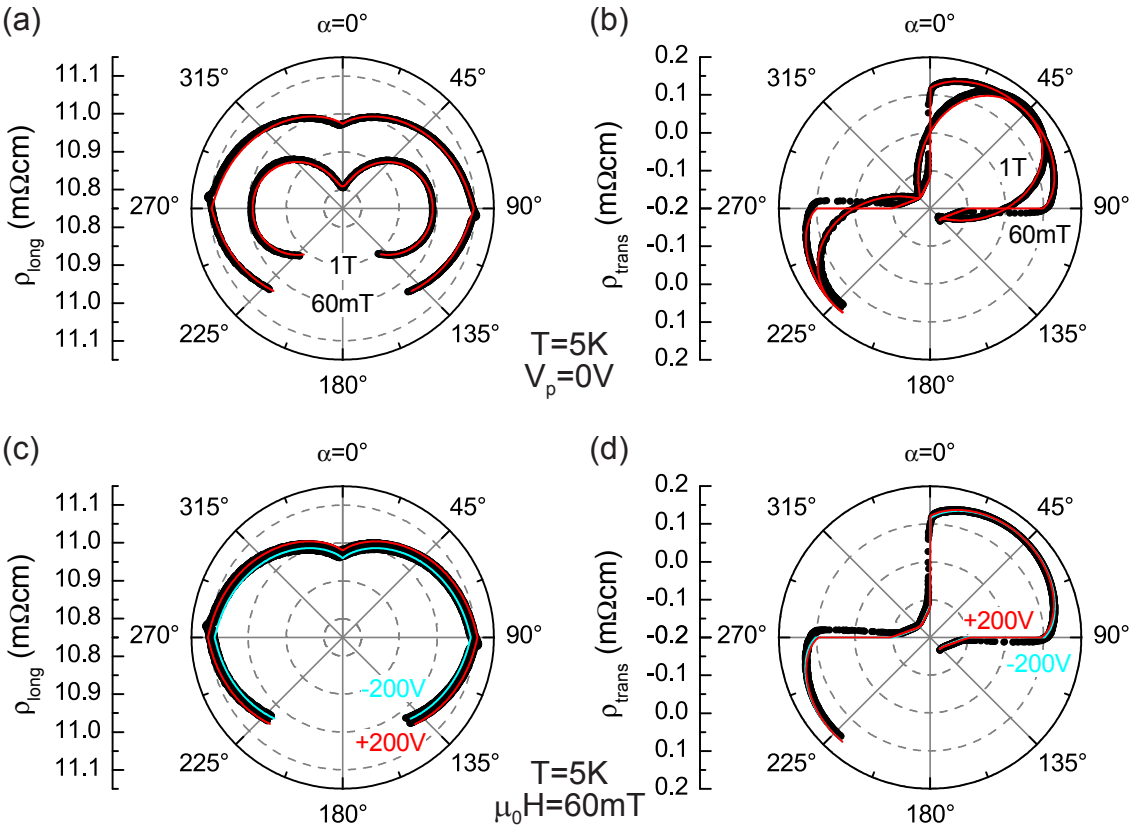

Figure 6.6: Longitudinal resistivity $\rho_{\mathrm{long}}(\alpha)$ and transverse resistivity $\rho_{\mathrm{trans}}(\alpha)$ at 5 K for a constant external magnetic field rotated within the film plane. The black circles represent the experimental data, the solid curves the result of the corresponding simulations using the parameter values given in Fig. 6.3. (a), (b) ADMR curves for magnetic fields $\mu_0 H = 1\,\mathrm{T}$ and 60 mT at $V_{\mathrm{p}} = 0\,\mathrm{V}$. (c), (d) ADMR curves for $\mu_0 H = 60\,\mathrm{mT}$ at $V_{\mathrm{p}} = +200\,\mathrm{V}$ (red curve) and $-200\,\mathrm{V}$ (blue).

$V_{\mathrm{p}} = -200\,\mathrm{V}$ (blue), 0 V (black), and $+200\,\mathrm{V}$ (red) for the external magnetic field aligned at $\alpha = 315°$. The corresponding free energy density contours are plotted in Figs. 6.7(c) to (e) for different magnetic field strengths and in Fig. 6.7(b) for zero external magnetic field. Regarding the downsweep curves in Fig. 6.7(a), only one sharp jump can be observed (compare the two jumps at 5 K in Fig. 6.5) and the number of abrupt changes in the $\rho_{\mathrm{long}}(\mu_0 H)$ curves decreases from $V_{\mathrm{p}} = -200\,\mathrm{V} \rightarrow +200\,\mathrm{V}$, indicative of increasingly dominating uniaxial anisotropy [as apparent from Fig. 6.7(b)]. Since the evolution of $\rho_{\mathrm{long}}(\mu_0 H)$ from positive to negative magnetic fields has been discussed in detail in the previous section, we here only briefly summarize the major characteristics. For $V_{\mathrm{p}} = -200\,\mathrm{V}$ [Figs. 6.7(a), (c)], the magnetization reverses from $\beta = 315°$ to 135° via coherent and continuous rotations [steps (A), (C), (E)], a coherent switching (B), and a noncoherent switching (D). The evolution appears qualitatively similar for $V_{\mathrm{p}} = 0\,\mathrm{V}$, but changes for $+200\,\mathrm{V}$ due to an evidently dominating uniaxial anisotropy [cf. Fig. 6.7(b)], resulting in a "simpler" free energy density landscape [Fig. 6.7(e)], which exhibits less features. Here, we observe coherent and continuous rotations [steps (A), (C)], a noncoherent

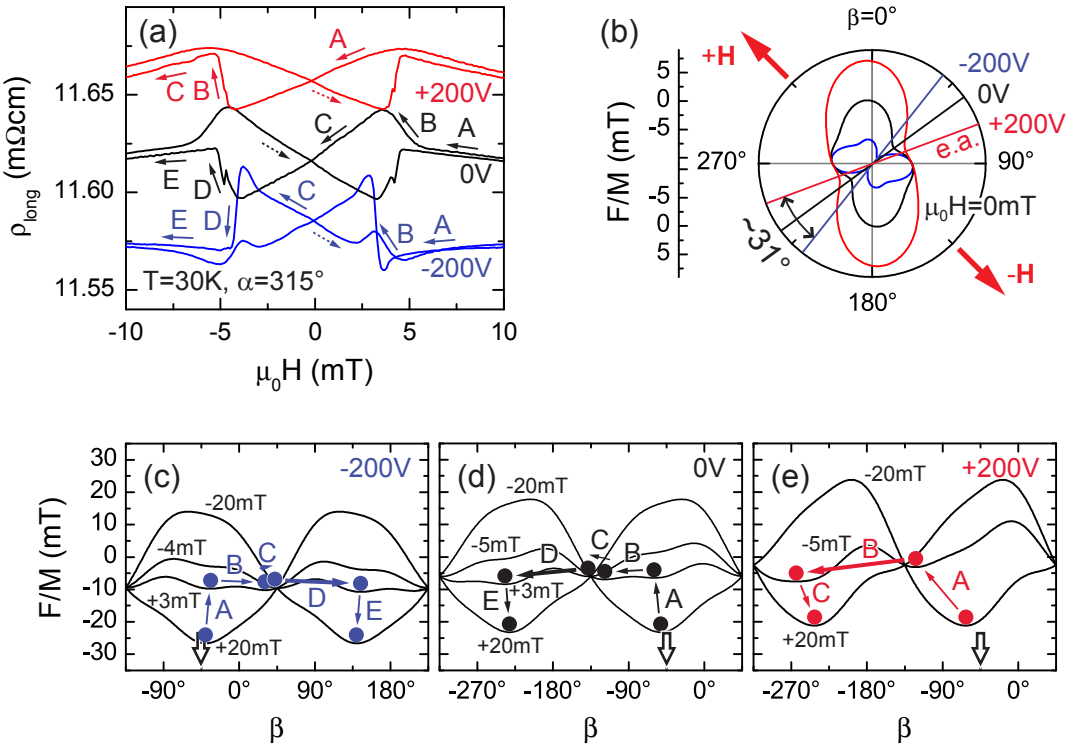

Figure 6.7: (a) $\rho_{\mathrm{long}}(\mu_0 H)$ curves measured at 30 K and different V_{p} for the external magnetic field aligned at $\alpha = 315°$. (b) Corresponding free energy density contours and the magnetic easy axes at zero external magnetic field. The overall shift of the magnetic easy axis amounts to $\Delta\beta \approx 30°$. (c), (d), (e) Free energy density contours $F/M(\beta)$ for characteristic magnetic field strengths at $V_{\mathrm{p}} = -200$ V (c), 0 V (d), and +200 V (e). The downward-oriented arrows indicate the external magnetic field orientation. In all panels the blue, black, and red color refers to $V_{\mathrm{p}} = -200$ V, 0 V, and +200 V, respectively.

switching (B), but no coherent switching processes. The increasing influence of the piezo-induced strain with temperature results in a considerable tilt of the relative orientation of the magnetic easy axis at 30 K, which amounts to about 30°.

As evident from Fig. 6.3, the V_{p}-induced strain yields maximum influence on the magnetic anisotropy at $T \approx 50$ K. Figure 6.8 shows ADMR $\{\rho_{\mathrm{long}}(\alpha), \rho_{\mathrm{trans}}(\alpha)\}$ measurements at 50 K. For $\mu_0 H = 100$ mT, the magnetization orientation is still predominantly determined by the orientation of the external magnetic field α [compare $\{\rho_{\mathrm{long}}(\alpha), \rho_{\mathrm{trans}}(\alpha)\}$ curves at 1 T in Figs. 6.6(a), (b)], while the ADMR traces recorded at $\mu_0 H = 10$ mT [Figs. 6.8(a), (b)] exhibit a dominating uniaxial magnetic anisotropy contribution [compare blue traces for large H in Figs. 4.10(c) to (f)]. The magnetization orientation and thus also the magnetic anisotropy is strongly influenced by the piezo-induced strain, which can be deduced from the qualitatively different behavior of $\{\rho_{\mathrm{long}}(\alpha), \rho_{\mathrm{trans}}(\alpha)\}$ at different V_{p}. As shown in Figs. 6.8(c) and (d) for an external magnetic field of $\mu_0 H = 10$ mT at $V_{\mathrm{p}} = +200$ V, ρ_{long} and ρ_{trans} exhibit abrupt changes in resistivity for a magnetic field orientation $\alpha \approx 355°$, indicating a nearby hard magnetic axis. The smooth changes in resistivity around

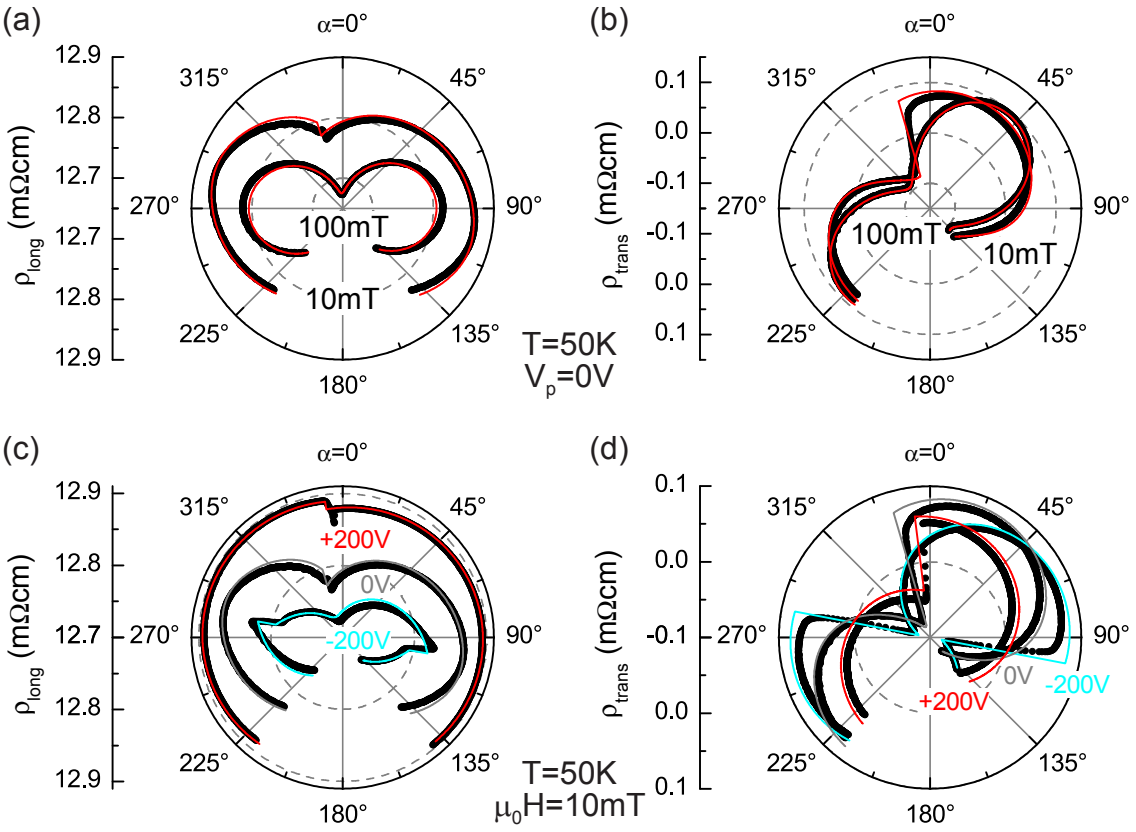

Figure 6.8: Longitudinal resistivity $\rho_{\mathrm{long}}(\alpha)$ and transverse resistivity $\rho_{\mathrm{trans}}(\alpha)$ at 50 K for a constant external magnetic field rotated within the film plane at different voltages V_{p}. The black circles represent the experimental data, the solid curves the result of the corresponding simulation. (a), (b) ADMR curves for $\mu_0 H = 100\,\mathrm{mT}$ and 10 mT at $V_{\mathrm{p}} = 0\,\mathrm{V}$. (c), (d) ADMR curves for $\mu_0 H = 10\,\mathrm{mT}$ at different voltages $V_{\mathrm{p}} = +200\,\mathrm{V}$ (red curve), 0 V (gray), and $-200\,\mathrm{V}$ (blue).

$\alpha \approx 90°$ indicate a nearby magnetic easy axis [cf. Figs. 4.10(c) and (d)]. In contrast, the curvature for $V_{\mathrm{p}} = -200\,\mathrm{V}$ evolves approximately vice versa with a discontinuous resistivity change at $\alpha \approx 280°$ [cf. Figs. 4.10(e) and (f)], indicating a rotation of the magnetic easy axis by about 75°. In analogy to the previous section, the anisotropy parameters are determined independently for each V_{p} via the iterative fitting procedure of the ADMR curves at different external magnetic field strengths. The simulations using the parameter values given in Fig. 6.3 are represented by the solid lines in Fig. 6.8.

The free energy density contours in Fig. 6.9 allow for a more quantitative analysis of the V_{p}-induced magnetic anisotropy modifications at $T = 50\,\mathrm{K}$. The contours calculated for zero external magnetic field in Fig. 6.9(a) result in a rotation of the magnetic easy axis by about 60° upon a variation of V_{p} between $+200\,\mathrm{V}$ and $-200\,\mathrm{V}$. As typical for a uniaxially dominated magnetic system, the corresponding free energy density surface exhibits two energetically equivalent (global) minima separated by 180°. The application of a magnetic field yields a symmetry break and thus only one global minimum prevails. This situation is illustrated in Fig. 6.9(b) for $\mu_0 H = 10\,\mathrm{mT}$

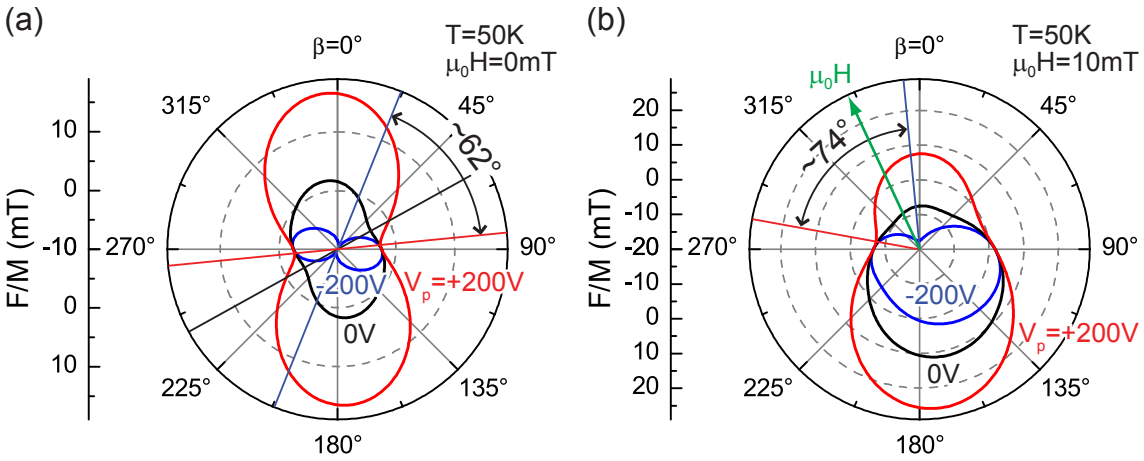

Figure 6.9: Free energy density contours $F/M\,(\beta)$ at $T = 50\,\mathrm{K}$. (a) At zero external magnetic field, the orientation of the magnetic easy axis changes by about 60° if the voltage V_p is varied between $+200\,\mathrm{V}$ and $-200\,\mathrm{V}$. (b) For $\mu_0 H = 10\,\mathrm{mT}$ applied along $\alpha = 335°$, the easy axis rotates by about 75°.

oriented along $\alpha = 335°$ and confirms the above analysis as we indeed obtain a rotation of the easy axis by about 75°.

6.7 Reversible control of magnetization orientation

As we have seen in the previous section, at $T = 50\,\mathrm{K}$ we are able to rotate the orientation of the magnetic easy axis by about 60° in the absence of a magnetic field and by about 75° at an applied field strength of $\mu_0 H = 10\,\mathrm{mT}$ solely by changing the voltage V_p applied to the piezoelectric actuator. However, a voltage control of the magnetization orientation cannot be necessarily inferred from a control of the magnetic easy axis. In this temperature range the free energy density $F/M\,(\beta)$ exhibits a 180° periodicity due to the dominating uniaxial anisotropy [cf. Fig. 6.9(a)]. This results in a potential decay into magnetic domains aligned either parallel or antiparallel to the magnetic easy axis (compare Sec. 5.5). To prevent such domain formation, we apply a magnetic field of constant, small magnitude $\mu_0 H = 10\,\mathrm{mT}$ at $\alpha = 335°$, which lifts the degeneracy in the free energy density such that only one global free energy density minimum prevails. According to Fig. 6.9(b), under these circumstances the global minimum is oriented along $\beta = -80°$ for $V_\mathrm{p} = +200\,\mathrm{V}$ and $\beta = -5°$ for $V_\mathrm{p} = -200\,\mathrm{V}$.

The qualitative, direct correspondence between $\{\rho_\mathrm{long}, \rho_\mathrm{trans}\}$ and the magnetization orientation enables to in situ monitor the evolution of magnetization orientation as a function of V_p via simple resistance measurements. Therefore, the versatility of magnetoresistance measurements allows not only to determine the free energy density but also to directly probe the magnetization vector, and thus provides a means to verify the voltage control of $\mathbf{M}$.

Figures 6.10(a) and (b) [(c), (d)] show $\rho_\mathrm{long}\,(V_\mathrm{p})$ and $\rho_\mathrm{trans}\,(V_\mathrm{p})$ measured at $T = 50\,\mathrm{K}$ for a constant field magnitude $\mu_0 H = 10\,\mathrm{mT}$ [$\mu_0 H = 100\,\mathrm{mT}$] applied along

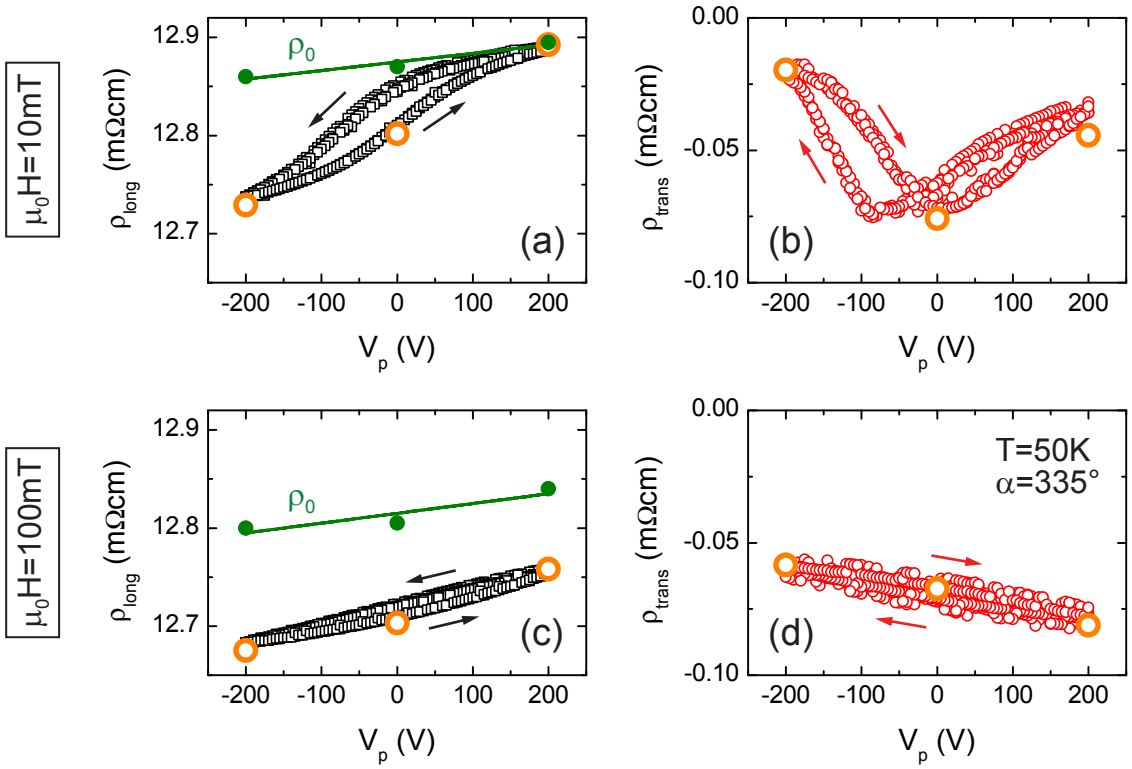

Figure 6.10: Evolution of (a) $\rho_{\mathrm{long}}(V_{\mathrm{p}})$ (open black squares) and (b) $\rho_{\mathrm{trans}}(V_{\mathrm{p}})$ (open red circles) as a function of V_{p} between $+200\,\mathrm{V}$ and $-200\,\mathrm{V}$ for $\mu_0 H = 10\,\mathrm{mT}$ applied along $\alpha = 335°$. The green circles in (a) display the resistivity parameters ρ_0 derived from ADMR measurements and the solid green lines show the corresponding linear fit. (c), (d) Corresponding measurements for $\mu_0 H = 100\,\mathrm{mT}$. In all panels the open orange circles at $V_{\mathrm{p}} = +200\,\mathrm{V}$, $0\,\mathrm{V}$, and $-200\,\mathrm{V}$ depict the resistivity values obtained from the ADMR measurements at $\alpha = 335°$.

$\alpha = 335°$. The data consist of three full voltage cycles ($V_{\mathrm{p}} = +200\,\mathrm{V} \rightarrow -200\,\mathrm{V} \rightarrow +200\,\mathrm{V}$) in steps of $5\,\mathrm{V}$, evidencing the good reproducibility of the measurements, where ρ_{long} and ρ_{trans} are represented by open black squares and open red circles, respectively. The open orange circles at $V_{\mathrm{p}} = +200\,\mathrm{V}$, $0\,\mathrm{V}$, and $-200\,\mathrm{V}$ depict the resistivity values at $\alpha = 335°$ obtained from the ADMR measurements, showing the excellent agreement between the measurement modes $\rho(V_{\mathrm{p}})$ and $\rho(\alpha)$. The hysteresis observed in all measurements as a function of V_{p} stems from the hysteretic piezoelectric response of the actuator.

To calculate the (macrospin) magnetization orientation $\beta(V_{\mathrm{p}})$ from these measurements, we invert Eqs. (4.37) to obtain $\beta(\rho_{\mathrm{long}})$ and $\beta(\rho_{\mathrm{trans}})$. However, an unambiguous determination of β in this way is not straightforward. This is due to the fact that (i) the value of ρ_0 depends on V_{p} (see Sec. 6.4), and (ii) in the region of interest $-90° < \beta < 0°$ within which the magnetization is expected to orient along, the arccosine function resulting from the equation for ρ_{long} is unambiguous, but the arcsine function from the equation for ρ_{trans} yields two potential orientations. To address issue (i), we assume a linear dependence $\rho_0(V_{\mathrm{p}}) \propto V_{\mathrm{p}}$. The resistivity parameters ρ_0 derived from ADMR measurements at $V_{\mathrm{p}} = +200\,\mathrm{V}$, $0\,\mathrm{V}$, $-200\,\mathrm{V}$, and

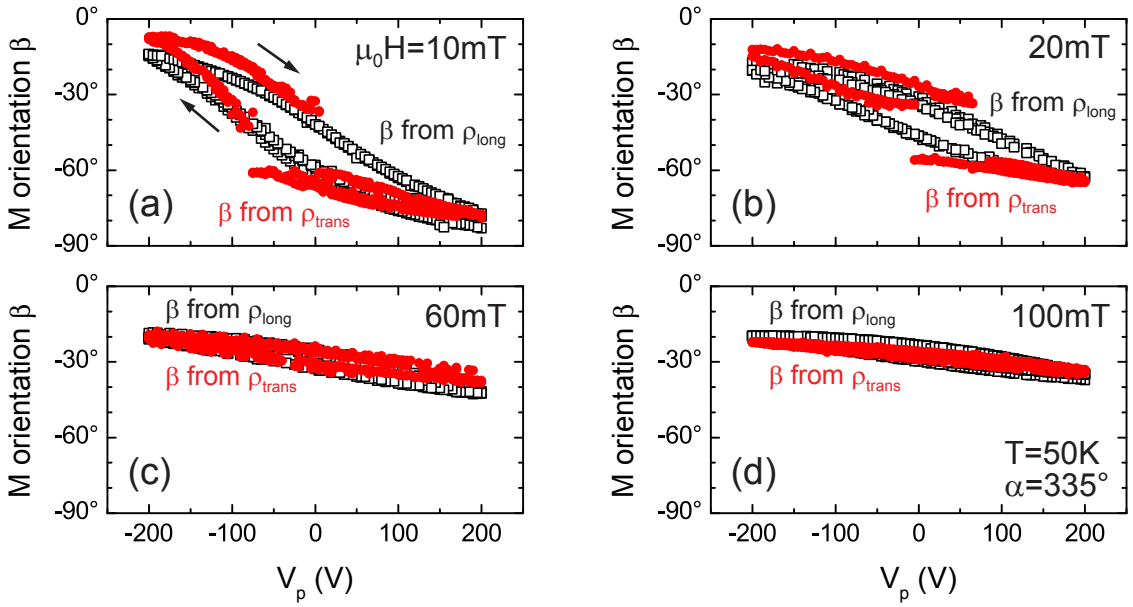

Figure 6.11: The magnetization orientation β as a function of V_p at $T = 50\,\mathrm{K}$ for different magnetic field strengths $\mu_0 H$ applied along $\alpha = 335°$ calculated from $\rho_\mathrm{long}(V_\mathrm{p})$ (open black squares) and $\rho_\mathrm{trans}(V_\mathrm{p})$ (full red circles). The good agreement between the β values calculated from ρ_long and ρ_trans demonstrates that $\mathbf{M}$ can be continuously and reversibly rotated by about 70° solely by varying V_p between $+200\,\mathrm{V}$ and $-200\,\mathrm{V}$. For increasing $\mu_0 H$ the maximum angle of rotation is decreased to $\Delta\beta \approx 15°$ for $\mu_0 H = 100\,\mathrm{mT}$.

the corresponding linear fit are shown by green circles and solid green lines, respectively, in Figs. 6.10(a) and (c). We resolve issue (ii) by adding ±90° to the values $\beta(\rho_\mathrm{trans})$ if appropriate, requesting that $\beta(\rho_\mathrm{trans}) \equiv \beta(\rho_\mathrm{long})$ within experimental error.

Figure 6.11 shows the magnetization orientation $\beta(V_\mathrm{p})$ as a function of V_p at $T = 50\,\mathrm{K}$ obtained from the $\rho_\mathrm{long}(V_\mathrm{p})$ (open black squares) and $\rho_\mathrm{trans}(V_\mathrm{p})$ (full red circles) data for different magnetic field strengths $\mu_0 H$ applied along $\alpha = 335°$. The abrupt jumps in ρ_trans at $V_\mathrm{p} \approx -75\,\mathrm{V}$ and $V_\mathrm{p} \approx 0\,\mathrm{V}$ and the thus emerging gaps around $\beta = -45°$ for $\mu_0 H = 10\,\mathrm{mT}$ and $20\,\mathrm{mT}$ are an artifact of the arcsine transformation because the minimal value of $\rho_\mathrm{trans}(V_\mathrm{p} \approx 0\,\mathrm{V}) = -0.07\,\mathrm{m\Omega cm}$ in Fig. 6.10(b) is somewhat larger than the value $\frac{1}{2}\rho_7 \approx -0.09\,\mathrm{m\Omega cm}$ in the second expression in Eqs. (4.37) determined from the ADMR measurements at 50 K (cf. Fig. 6.3). Figure 6.11 unambiguously shows that the magnetization orientations $\beta(V_\mathrm{p})$ obtained from ρ_long and ρ_trans are consistent. These findings corroborate our above analysis and clearly demonstrate that we indeed are able to continuously and reversibly adjust the magnetization orientation at will within about 70° solely via the application of a voltage to the piezoelectric actuator. With increasing magnetic field strength, the Zeeman contribution in Eq. (6.1) increasingly competes with the magnetoelastic contribution to the free energy density. Thus the angular range within which the magnetization orientation can be rotated as a function of V_p decreases from $\Delta\beta \approx 70°$ for $\mu_0 H = 10\,\mathrm{mT}$ to $\Delta\beta \approx 15°$ for $\mu_0 H = 100\,\mathrm{mT}$.

6.8 Nonvolatile magnetization switching

In the previous section, we have shown a continuous and reversible voltage control of the magnetization orientation. The **M** reorientation at 50 K is limited to a maximum change of about $\Delta\beta \approx 70°$. In this section we will show that the application of appropriate magnetic field strengths also allows for an all-voltage controlled **M** rotation by larger angles on the basis of a continuous, coherent, and nonvolatile but irreversible switching of magnetization orientation.

The full red squares in Fig. 6.12(a) show the transverse resistivity loop $\rho_{\mathrm{trans}}(\mu_0 H)$ at $T = 40\,\mathrm{K}$ and $V_\mathrm{p} = +200\,\mathrm{V}$, with the external magnetic field oriented along $\alpha = 335°$. As indicated by the red arrows, $\mu_0 H$ was swept from $-300\,\mathrm{mT}$ to $+300\,\mathrm{mT}$ and back to $-300\,\mathrm{mT}$. The resistivity jumps at the coercive field $|\mu_0 H| = \mu_0 H_\mathrm{c} \approx 5\,\mathrm{mT}$ are due to noncoherent magnetization switching processes between two minima at $\beta \approx 90°$ and $\beta \approx 250°$ in the free energy density surface [compare the red contour in Fig. 6.12(b) at $V_\mathrm{p} = +200\,\mathrm{V}$ and $\mu_0 H = -4\,\mathrm{mT}$]. The hysteresis of $\rho_{\mathrm{trans}}(\mu_0 H)$ between up- and downsweeps is caused by the magnetization residing in the local one of these two minima until the free energy density difference between the minima exceeds the domain-wall formation energy. To induce a switching process of magnetization orientation back to its initial direction via magnetic fields, an opposing magnetic field magnitude in excess of the coercive field has to be applied. As we will show in the following, the additional degree of freedom offered by the piezoelectric actuator allows inducing an irreversible magnetization switching already at external magnetic fields well below the magnetic coercive field.

Starting from the same magnetic preparation ($\mu_0 H = -300\,\mathrm{mT}$, $V_\mathrm{p} = +200\,\mathrm{V}$), the upsweep [green symbols in Fig. 6.12(a)] is stopped in a second experiment at $\mu_0 H = -4\,\mathrm{mT}$ (position denoted B_1). Keeping the magnetic field constant at this value, the piezo voltage is swept from $V_\mathrm{p} = +200\,\mathrm{V}$ to $-200\,\mathrm{V}$ with the corresponding increase in ρ_{trans} shown in Fig. 6.12(c) [$\mathrm{B}_1\,(V_\mathrm{p} = +200\,\mathrm{V}) \rightarrow \mathrm{B}_2\,(V_\mathrm{p} = 0\,\mathrm{V}) \rightarrow \mathrm{B}_3\,(V_\mathrm{p} = -200\,\mathrm{V})$]. Sweeping V_p back to $+200\,\mathrm{V}$, $\rho_{\mathrm{trans}}(\mu_0 H)$ remains in this high resistance state [$\mathrm{B}_3\,(V_\mathrm{p} = -200\,\mathrm{V}) \rightarrow \mathrm{B}_4\,(V_\mathrm{p} = 0\,\mathrm{V}) \rightarrow \mathrm{B}_5\,(V_\mathrm{p} = +200\,\mathrm{V})$]. This evolution can be understood in terms of an irreversible and nonvolatile magnetization switching via a coherent and continuous magnetization rotation [see Table 1.1 and Fig. 1.3(e)], as illustrated by the free energy density contours in Fig. 6.12(b) calculated at $\mu_0 H = -4\,\mathrm{mT}$. Starting from $V_\mathrm{p} = +200\,\mathrm{V}$ (B_1), the magnetization orientation rotates from $\beta \approx 90°$ (B_1) over $\beta \approx 100°$ at $V_\mathrm{p} = 0\,\mathrm{V}$ (B_2) to $\beta \approx 200°$ at $V_\mathrm{p} = -200\,\mathrm{V}$ (B_3). Sweeping V_p back to $+200\,\mathrm{V}$, due to the emerging potential barrier at $\beta \approx 180°$, the magnetization does not rotate back in the same way, but evolves into the minimum at $\beta \approx 250°$ ($\mathrm{B}_3 \rightarrow \mathrm{B}_4 \rightarrow \mathrm{B}_5$). Therefore, the V_p sweep from $+200\,\mathrm{V}$ to $-200\,\mathrm{V}$ and back to $+200\,\mathrm{V}$ results in a coherent, continuous and irreversible magnetization switching by about 160° from the global free energy density minimum to the local one at $+200\,\mathrm{V}$. Due to the magnetocrystalline anisotropy, distinctly different minima of F are retained at $V_\mathrm{p} = 0\,\mathrm{V}$ and $\mu_0 H = 0\,\mathrm{mT}$. Hence, the voltage-controlled magnetization switching process discussed above results in an *irreversible* and *nonvolatile* switching of *remanent* magnetization orientation by 180° between the two magnetic easy axes. We note that these experimental results

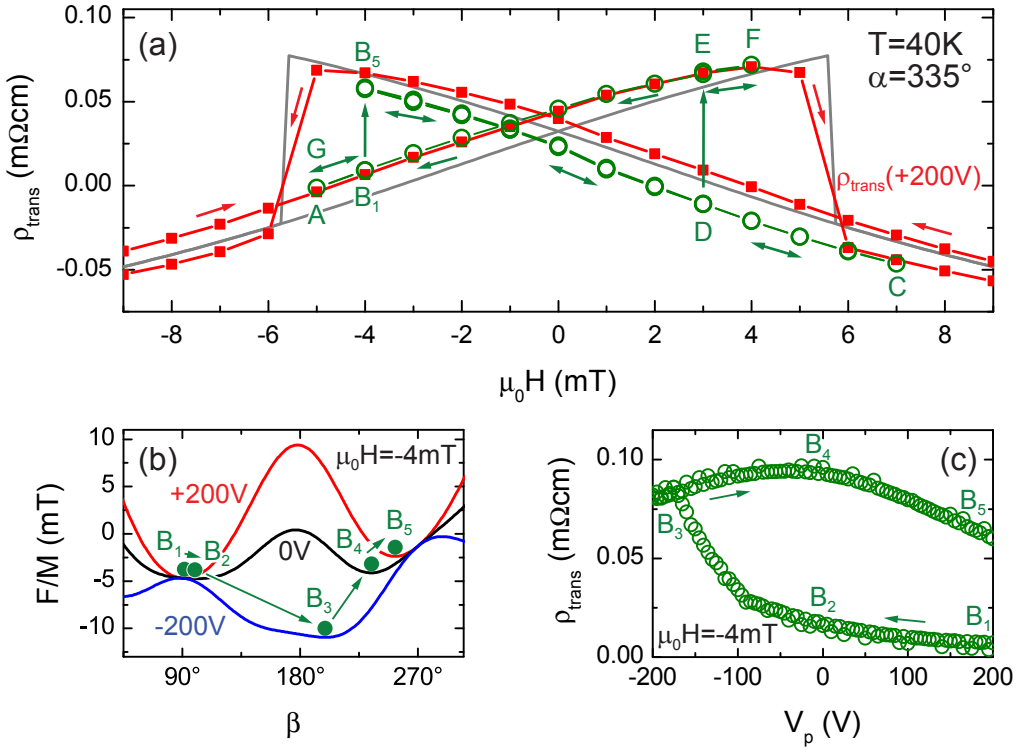

Figure 6.12: (a) Transverse resistivity loop $\rho_{\mathrm{trans}}(\mu_0 H)$ with $V_{\mathrm{p}} = +200\,\mathrm{V}$ and the external magnetic field oriented along $\alpha = 335°$ (full red squares, the solid red lines are guides to the eye). The open green circles describe the evolution of $\rho_{\mathrm{trans}}(\mu_0 H)$ during the measurement sequence A to G described in the text. The solid gray curve shows a simulation using the parameter values given in Fig. 6.3 and a domain-wall formation energy of $\Delta F/M = 3.3\,\mathrm{mT}$. (b) Free energy density contours $F/M\,(\beta)$ at different voltages $V_{\mathrm{p}} = +200\,\mathrm{V}$, $0\,\mathrm{V}$, and $-200\,\mathrm{V}$ for $\mu_0 H = -4\,\mathrm{mT}$. (c) Evolution of $\rho_{\mathrm{trans}}(\mu_0 H)$ during the V_{p} sweep from $V_{\mathrm{p}} = +200\,\mathrm{V}$ (B_1) $\rightarrow 0\,\mathrm{V}$ (B_2) $\rightarrow -200\,\mathrm{V}$ (B_3) $\rightarrow 0\,\mathrm{V}$ (B_4) $\rightarrow +200\,\mathrm{V}$ (B_5).

are comparable to those reported in Ref. [258].

To verify the magnetization switching process from the minimum at $\beta \approx 90°$ (B_1) into the minimum at $\beta \approx 250°$ (B_5) upon cycling V_{p} from $+200\,\mathrm{V}$ to $-200\,\mathrm{V}$ and back to $+200\,\mathrm{V}$ [Fig. 6.12(b)], we sweep $\mu_0 H$ from $-4\,\mathrm{mT}$ to $+7\,\mathrm{mT}$ ($\mathrm{B}_5 \rightarrow$ C). As expected, ρ_{trans} decreases and approximately follows the resistivity curve obtained in the conventional magnetotransport $\rho_{\mathrm{trans}}(\mu_0 H)$ measurement for the opposite sweep direction in this magnetic field range. The fact that ρ_{trans} does not exactly coincide with the downsweep curve might be attributed to first indications of multidomain effects, which begin to become important at these small magnetic fields. In particular, the downsweep curve depicted as the solid red line in Fig. 6.12(a) was measured after saturating the magnetization at $+300\,\mathrm{mT}$, so that multidomain effects should be less important. As we sweep $\mu_0 H$ back to $-4\,\mathrm{mT}$ (C $\rightarrow \mathrm{B}_5$) and up to $+3\,\mathrm{mT}$ again ($\mathrm{B}_5 \rightarrow$ D), ρ_{trans} remains on this resistivity branch.

The magnetization switching process discussed above is denoted irreversible in the sense that the initial magnetization orientation at $\beta \approx 90°$ (B_1) cannot be restored by changing V_{p} alone. Here we show that upon an additional, appropriate change

of the external magnetic field strength a further, voltage-controlled magnetization switching can be induced. After sweeping $\mu_0 H$ from $-4\,\mathrm{mT}$ to $+3\,\mathrm{mT}$ ($\mathrm{B}_5 \rightarrow \mathrm{D}$), which transforms the local minimum at $\beta \approx 250°$ [B_5 in Fig. 6.12(b)] into the global one at $\beta \approx 270°$ and the global one at $\beta \approx 90°$ [B_1 in Fig. 6.12(b)] into the local one at $\beta \approx 75°$, we performed a second switching process via cycling V_p again ($+200\,\mathrm{V} \rightarrow -200\,\mathrm{V} \rightarrow +200\,\mathrm{V}$). In analogy to the irreversible process at $-4\,\mathrm{mT}$ described above, the magnetization switches from the global minimum at $\beta \approx 270°$ into the local minimum at $\beta \approx 75°$ (D $\rightarrow$ E), which thus yields an irreversible magnetization switching by $\approx 195°$. Sweeping $\mu_0 H$ to $+4\,\mathrm{mT}$ (F) after this second switching process and back to $-5\,\mathrm{mT}$ (G), ρ_trans as expected follows the corresponding upsweep branch.

Finally we will show that a description of these strain-induced magnetization reorientations of up to about 195° in terms of a coherent magnetization rotation within a macrospin (single-domain) model is indeed justified. The solid gray curve in Fig. 6.12(a) displays a simulation of $\rho_\mathrm{trans}\,(\mu_0 H)$ using the parameter values given in Fig. 6.3. To obtain the experimentally observed switching field $|\mu_0 H| \approx 5\,\mathrm{mT}$, we incorporate a domain-wall formation energy $\Delta F/M = 3.3\,\mathrm{mT}$ in our calculations, in analogy to Sec. 5.6. This free energy density difference accounts for the domain-wall formation energy and is clearly larger than the strain-induced maximum difference in the free energy density $\Delta F/M = 2.3\,\mathrm{mT}$ between two minima [cf. Fig 6.12(b)]. Hence, the application of V_p cannot induce a noncoherent magnetization switching process and thus a (predominant) single-domain state is maintained. We furthermore note that the agreement between simulation and experiment at the low magnetic fields illustrated in Fig. 6.12 is quite remarkable, considering the fact that the parameter values used for the calculation are obtained from ADMR measurements at $\mu_0 H \geq 60\,\mathrm{mT}$ and the only fit parameter is the domain-wall formation energy, which solely adjusts the switching field. These observations evidence the versatility of the macrospin model, which relies on a coherent magnetization rotation extended to include noncoherent switching processes.

To conclude, the above experiments clearly demonstrate that the piezo voltage not only allows to control the magnetic anisotropy and thus the magnetization orientation, but also to induce an irreversible magnetization switching.

6.9 Determination of the magnetostriction constant

In the previous sections we have determined the temperature dependence of the magnetoelastic anisotropy contribution B^{110}_magel as a function of V_p [Fig. 6.3(a)] and quantified the piezo-induced strain (Fig. 6.2), which can now be used to derive the magnetostriction constant λ_{111}. Starting with the general expression for the magnetoelastic free energy density in Eq. (2.13), we substitute the strains ϵ_i ($i = 1, 2, \ldots, 6$) with the ones deduced for a $\langle 110 \rangle$-strained film from Eqs. (3.13) with $\gamma = \pi/4$, i.e., $\epsilon_1 = \epsilon_2 = \frac{1}{2}\,(\epsilon'_1 + \epsilon'_2)$, $\epsilon_3 = \epsilon'_3$, $\epsilon_4 = \epsilon_5 = 0$, and $\epsilon_6 = \epsilon'_2 - \epsilon'_1$, which together with the magnetization being constrained within the film plane ($m_z = 0$) yields $F_\mathrm{magel} = B_2\,(\epsilon'_2 - \epsilon'_1)\,m_x m_y$. Note that, since $\epsilon_1 = \epsilon_2$, $m_x^2 + m_y^2 = 1$, and $m_z = 0$

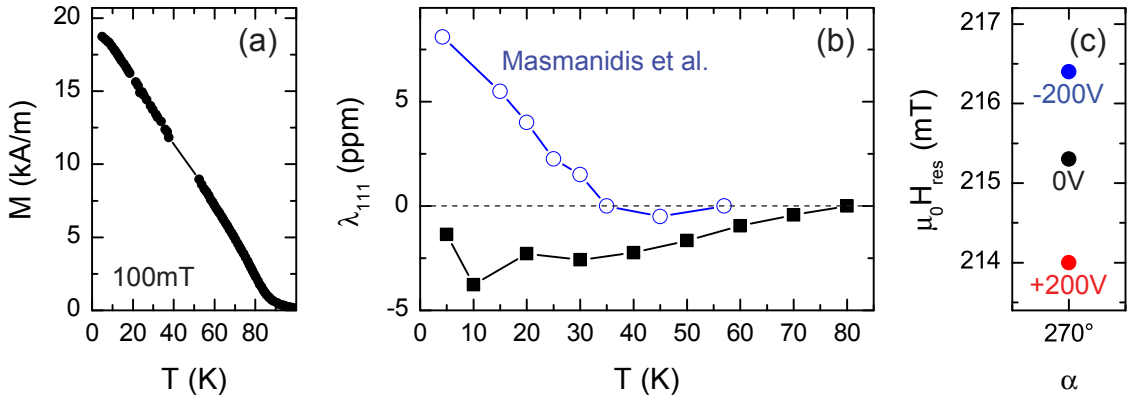

Figure 6.13: (a) $M\,(T)$ curve determined via SQUID magnetometry at a fixed magnetic field strength of $\mu_0 H = 100\,\mathrm{mT}$ with $\mathbf{H}$ along the [110] direction. (b) Temperature dependence of the magnetostriction constant λ_{111} (full black squares) compared to the values obtained by Masmanidis *et al.* [301] (open blue circles). (c) FMR measurements on a further hybrid sample with identical relative alignment of the (Ga,Mn)As thin film and the piezoelectric actuator at $T = 6\,\mathrm{K}$ with $\mathbf{H} \parallel [1\bar{1}0]$ [302]. The FMR field $\mu_0 H_{\mathrm{res}}$ decreases for increasing V_{p} and thus this direction becomes magnetically easier.

the first term in Eq. (2.13) is isotropic and thus vanishes. Therefore, in our hybrid configuration with strain induced along the (Ga,Mn)As in-plane $\langle 110 \rangle$ directions, in-plane magnetotransport experiments are insensitive to the magnetostriction constant λ_{100}, which thus cannot be determined. We furthermore use the second relation in Eqs. (2.15) and with $m_x m_y = \cos(\beta + 45°)\cos(\beta - 45°) = \cos^2\beta - \frac{1}{2}$ we obtain

$$\frac{F_{\mathrm{magel}}}{M} = -\frac{3\lambda_{111} c_{44}}{M}\left(\epsilon_2' - \epsilon_1'\right)\left[\cos^2\beta - \frac{1}{2}\right] = B_{110} m_j^2, \tag{6.2}$$

where the isotropic part again was omitted. This expression constitutes a uniaxial magnetic anisotropy contribution along [110] with the direction cosine of the magnetization with respect to the $\mathbf{j}$ axis $m_j = \mathbf{j} \cdot \mathbf{m} = \cos\beta$ and the corresponding uniaxial anisotropy parameter $B_{110} = -3\lambda_{111} c_{44}\left(\epsilon_2' - \epsilon_1'\right)/M$. Using now the temperature dependence of the piezo-induced strain $\Delta\epsilon_i' = \epsilon_i'\left(T, V_{\mathrm{p}} = +200\,\mathrm{V}\right) - \epsilon_i'\left(T, V_{\mathrm{p}} = -200\,\mathrm{V}\right)$ $(i = 1, 2)$ [Fig. 6.2(b)], of the magnetoelastic anisotropy parameter $\Delta B_{110} = B_{110}\left(T, V_{\mathrm{p}} = +200\,\mathrm{V}\right) - B_{110}\left(T, V_{\mathrm{p}} = -200\,\mathrm{V}\right)$ [Fig. 6.3(a)], and of the magnetization $M\,(T)$ determined via SQUID magnetometry at a fixed magnetic field strength of $\mu_0 H = 100\,\mathrm{mT}$ with $\mathbf{H}$ along the [110] direction [Fig. 6.13(a)], Eq. (6.2) results in

$$\lambda_{111}(T) = -\frac{\Delta B_{110}(T)\, M(T)}{3c_{44}\left[\Delta\epsilon_2'(T) - \Delta\epsilon_1'(T)\right]}. \tag{6.3}$$

For c_{44}, we use the elastic stiffness constant of bulk GaAs. Since it only varies slightly with temperature, a fixed value of $c_{44} = 59.9 \times 10^9\,\mathrm{N/m^2}$ [303] is used in all calculations. The temperature dependence observed is summarized in Fig. 6.13(b) and compared to the results of Masmanidis *et al.* [301]. To our knowledge, this is only the second time that λ_{111} is measured for (Ga,Mn)As. Comparing the two results, the λ_{111} magnitudes of the measurements in our $\mathrm{Ga_{0.955}Mn_{0.045}As}$ thin film (full black

squares) and $Ga_{0.948}Mn_{0.052}As$/(001)GaAs nanoelectromechanical beam resonators (open blue circles) are in reasonable agreement, but the values evidently differ in sign for $T \lesssim 35\,\mathrm{K}$. We can only speculate about this observation. Masmanidis *et al.* [301] observed qualitative changes both in the magnetoelastic coupling and magnetic anisotropy as a function of temperature. Hence, the well-known dependence of the magnetic anisotropy properties on the carrier concentration in (Ga,Mn)As (see, e.g., Refs. [273, 274]) can also be expected for the magnetostriction. We recently reported on the influence of hole concentration p on the magnetic anisotropy in (Ga,Mn)As [285]. p has been increased by postgrowth annealing and thus a significant change from $\lambda_{100} \approx -3\,\mathrm{ppm}$ to $\lambda_{100} \approx -5\,\mathrm{ppm}$ for $p \approx 3.5 \times 10^{20}\,\mathrm{cm}^{-3}$ and $p \approx 5.8 \times 10^{20}\,\mathrm{cm}^{-3}$, respectively, has been shown. These findings demonstrate the sensitivity of λ on the material parameters and thus might account for the observed discrepancy in Fig. 6.13(b). However, the magnetocrystalline anisotropy constant is predicted to change sign as a function of p [268]. This is not observed, as Masmanidis *et al.* determined a cubic anisotropy field $B_c^{\parallel} > 0$ [301], in consistency with our findings [cf. Fig. 6.3(b)]. We note that the $\lambda_{111}(T)$ curve we have published in Fig. 8 in Ref. [257] deviates from the one displayed in Fig. 6.13 due to a mistake in Eq. (A6) in Ref. [257] [cf. Eq. (6.2)]. For correction, the $\lambda_{111}(T)$ curve in Fig. 8 in Ref. [257] has to be multiplied by a factor $-(1/2)$.

We furthermore note that we have also performed FMR measurements on a further (Ga,Mn)As/piezoelectric actuator hybrid sample with identical configuration ($[110] \parallel \mathbf{y}'$) [302]. Figure 6.13(c) shows the FMR field $\mu_0 H_{\mathrm{res}}$ at $T = 6\,\mathrm{K}$ with the external magnetic field aligned along $[1\bar{1}0]$ ($\alpha = 270°$) at different voltages V_{p}. Using ADMR measurements, for increasing V_{p} we observed an increasing magnetically hard uniaxial axis $\Delta B_{110} > 0$ along [110] [cf. Fig. 6.3(a)], while using FMR spectroscopy the inverse situation is observed for $\mathbf{H} \parallel [1\bar{1}0]$ [Fig. 6.13(c)], i.e., increasing V_{p} decreases $\mu_0 H_{\mathrm{res}}$ and thus this direction becomes magnetically easier. Hence, for $\beta = 270°$ we obtain $\Delta B_{1\bar{1}0} < 0$ and Eq. (6.2) consistently results in $\lambda_{111} < 0$. Therefore, the FMR experiments corroborate the findings from our magnetotransport studies.

6.10 Summary

In summary, we have investigated the magnetic properties of a (Ga,Mn)As/piezoelectric actuator hybrid structure. We studied the temperature dependence of the magnetic anisotropy including the magnetoelastic contribution using anisotropic magnetoresistance techniques. The magnetostriction constant λ_{111} was derived from the anisotropy data and compared to the values reported in the literature. We found a different sign of λ_{111}, which might be attributed to a deviating hole concentration p. We intentionally take advantage of the strong temperature dependence of the magnetic anisotropy of (Ga,Mn)As to access different regimes of the relative strength of the magnetoelastic and the magnetocrystalline anisotropy contribution. At $T = 5\,\mathrm{K}$ the magnetoelastic term constitutes only a minor contribution compared to the dominating cubic term, but we showed that the switching fields of $\rho(\mu_0 H)$

loops are shifted by the application of a voltage V_p also at this temperature. At higher temperatures ($T \gtrsim 40\,\mathrm{K}$)—where the magnetoelastic term dominates magnetic anisotropy—we obtained a maximum rotation of the easy axes at 50 K by about 75° and demonstrated a continuous, fully reversible control of magnetization orientation indeed by about 70°, solely via application of a voltage to the piezoelectric actuator. We furthermore demonstrated an irreversible and nonvolatile voltage-controlled switching of magnetization orientation at 40 K by 180° upon the application of an appropriate external magnetic field. In addition, we verified the macrospin approach being sustained upon these voltage-induced changes of the magnetization orientation, which thus can consistently be described in terms of a coherent magnetization rotation. This voltage control of magnetization orientation is directly transferable to other ferromagnetic/piezoelectric hybrid structures opening the way to new innovative multifunctional device concepts based on single-crystalline ferromagnets, such as all electrically controlled magnetic memory elements, as the voltage-induced irreversible magnetization switching constitutes the basic principle of a nonvolatile memory element. Note that depending on the application intended, care must be taken to adjust the ratio of the magnetoelastic and the magnetocrystalline anisotropy contribution. As exemplarily shown in this chapter for a (Ga,Mn)As/piezoelectric actuator hybrid sample, in order to maximize the angle of reversible magnetization reorientation, the magnetocrystalline anisotropy contribution should be as small as possible (see polycrystalline ferromagnetic thin film/piezoelectric actuator hybrid structures in Chapter 5), while in order to realize a memory device concept based on nonvolatile magnetization switching in single-crystalline ferromagnets, a finite but small magnetocrystalline anisotropy should be present.

Chapter 7

Magnetization control and switching in magnetite thin films

In the previous chapter, we have demonstrated a nonvolatile, irreversible magnetization switching in single-crystalline (Ga,Mn)As thin film/piezoelectric actuator hybrids—which, however, could only be realized at temperatures below room temperature ($T = 40\,\mathrm{K}$) and upon the application of an external magnetic field. A true, reversible switching of the magnetization orientation between two (or more) remanent states solely by means of an electric field has not been reported to date. However, theoretical calculations suggest that such a nonvolatile magnetization control should be possible [304–308]. In this chapter we present our studies on magnetization switching concepts in ferromagnetic single-crystalline thin films, that pave the way for the experimental realization of an all-electrically controlled, nonvolatile magnetization switching at zero external magnetic field and at room temperature. To this end, we discuss the voltage control of magnetic anisotropy and the magnetization in single-crystalline magnetite (Fe_3O_4) thin film/piezoelectric actuator hybrids and compare different magnetoelastic switching concepts for stress exerted along the in-plane $\langle 100 \rangle$ and $\langle 110 \rangle$ cubic axes.

This chapter is organized as follows: after a short review of the material properties of magnetite in Sec. 7.1, we discuss two different approaches to realize a nonvolatile magnetization switching in Sec. 7.2 via a (i) continuous or a (ii) discontinuous magnetization rotation in samples with stress applied along the in-plane $\langle 100 \rangle$ and $\langle 110 \rangle$ crystal directions, respectively. Experimental details regarding the sample preparation and the experimental procedures employed are summarized in Sec. 7.3. We investigate the magnetic anisotropy as a function of the voltage V_p applied to the actuator from ferromagnetic resonance (FMR) experiments in Secs. 7.4 and 7.5. Hereby, in combination with HRXRD measurements to quantify the strain induced in the samples, we find that the voltage-controlled modifications of the magnetic anisotropy can be quantitatively modeled within magnetoelastic theory. The measurements show a rotation of the easy axes by a few degrees for the concept (i) and a significant modification of the relative strength of the magnetic easy axes for the concept (ii). However, in the present samples the voltage-induced anisotropy modifications are not large enough to qualitatively alter the free energy density landscape. Therefore, a true magnetization switching without magnetic domain formation appears unlikely at zero external magnetic field. To directly measure the magnetization at vanishing external field as a function of V_p, we employ SQUID magnetometry in

Sec. 7.6. The results thus obtained corroborate the FMR experiments, as they indeed demonstrate insignificant influence on the magnetization orientation in the sample corresponding to concept (i) and magnetic domain formation impeding a coherent magnetization switching in the sample corresponding to concept (ii). Nevertheless, our results demonstrate that the realization of an all-electrically controlled, non-volatile magnetization switching at room temperature is possible. Important results presented in the following have been published in Ref. [309] and are in preparation for publication [310].

7.1 Magnetite: Material properties

The oxide ferrimagnet magnetite (Fe_3O_4) exhibits a high Curie temperature $T_C \approx 860\,K$ [311] well above room temperature and crystallizes in the inverse cubic spinel structure [312] at room temperature with the lattice constant $a = 0.8396\,nm$ [313]. The unit cell consists of 24 iron and 32 oxygen atoms, with its chemical sum formula $\left[Fe^{3+}\right]_A \left[Fe^{3+}Fe^{2+}\right]_B O_4$ indicating two valence states of Fe. More precisely, the tetrahedrally coordinated A sites are occupied by Fe^{3+} ($3d^5$) ions, while the octahedrally coordinated B sites are equally occupied by Fe^{2+} ($3d^6$) and Fe^{3+} ($3d^5$) ions [312]. The ferromagnetic moments on the A and B sites align antiparallel to each other [314], resulting in compensated Fe^{3+} moments and thereby forming a ferrimagnet with a saturation magnetic moment of $\sim 4\mu_B$ (Bohr magneton) per formula unit [315]. However, since magnetite macroscopically exhibits ferromagnetic behavior, we will refer to it as ferromagnet. Magnetite is a promising material for room-temperature spintronic applications [6], e.g., spin-injection devices, since it is predicted to be a half-metallic ferromagnet (100% spin polarization at the Fermi energy) [316], while spin-resolved photoemission spectroscopy yields a spin polarization near the Fermi energy of $-(80 \pm 5)\,\%$ for epitaxial Fe_3O_4 (111) films and $-(55 \pm 10)\,\%$ for Fe_3O_4 (100) films at room temperature [317]. At a temperature $T_V \approx 125\,K$ magnetite undergoes a structural phase transition (Verwey transition) from cubic to monoclinic symmetry below T_V, which is accompanied by a discontinuity in both the conductivity ($\sigma = 250\,\Omega^{-1}cm^{-1}$ at room temperature [318]) and the magnetization [319]. Recently, ferroelectric switching in $Fe_3O_4/SrTiO_3$ thin films at $T \leq 38\,K$ has been shown, with a switchable polarization of about $11\,\mu Ccm^{-2}$ below $20\,K$ [320]. Hence, at low temperatures magnetite exhibits both ferromagnetic and ferroelectric properties and therefore is an intrinsic (single-phase) multiferroic material. As we will investigate magnetite at room temperature, only its ferromagnetic properties are relevant to this work.

Bulk magnetite exhibits the elastic stiffness constants $c_{11} = 27.2 \times 10^{10}\,N/m^2$, $c_{12} = 17.8 \times 10^{10}\,N/m^2$, and $c_{44} = 6.1 \times 10^{10}\,N/m^2$ [321]. The bulk saturation magnetization is $M_s \simeq 471\,kA/m$ [322], and the magnetostriction constants amount to $\lambda_{100} = -19.5 \times 10^{-6}$ and $\lambda_{111} = +77.6 \times 10^{-6}$ [113]. Magnetite furthermore shows a g-factor of 2.12 [322].

We here focus on Fe_3O_4 thin films pseudomorphically grown on (001)-oriented MgO substrates. This results in tetragonally distorted films, as the magnetite lattice

constant corresponds to almost twice the one of the MgO substrate (cf. Sec. 5.1). Hence, coherently strained magnetite films exhibit an isotropic tensile strain of 0.33% within the film plane. The magnetic anisotropy of magnetite thin films is very well studied [313, 315, 323–327]. It is composed of the following two contributions: (i) a cubic magnetic anisotropy and (ii) an effective uniaxial magnetic anisotropy contribution perpendicular to the film plane. The latter is composed of the shape anisotropy $\frac{1}{2}\mu_0 M_\mathrm{s}^2$ and a uniaxial contribution $K_\mathrm{u}^{001} < 0$ due to pseudomorphic growth. This yields an overall magnetic hard uniaxial axis, since $\frac{1}{2}\mu_0 M_\mathrm{s}^2 \gg |K_\mathrm{u}^{001}|$.

7.2 Magnetization switching concepts

We here discuss the spin-mechanics scheme for two qualitatively different approaches towards a nonvolatile, voltage-controlled magnetization switching. To compare these two switching concepts in one and the same magnetic film, we consider a single-crystalline ferromagnetic thin film with cubic anisotropy $K_\mathrm{c} < 0$ and apply stress along different directions with respect to the crystallographic axes. We note that hereby γ again denotes the angle enclosed by the crystalline film coordinate system $\{\mathbf{x}, \mathbf{y}, \mathbf{z}\}$ (see Fig. 4.4) and the actuator coordinate system $\{\mathbf{x}', \mathbf{y}', \mathbf{z}'\}$ (cf. Sec. 3.4), as shown in Fig. 7.1. Figure 7.2 exemplarily shows free energy density contours within the film plane for two special cases, namely $\gamma = 0°$ [Fig. 7.2(a)] and $\gamma = 45°$ [Fig. 7.2(d)]. Regarding these two configurations, it is important to note, that the induced uniaxial strains in the cubic crystals are symmetric with respect to the crystallographic axes. As a result during the switching process, the magnetoelastic contribution may transform a minimum in the free energy density contour and thus the equilibrium magnetization orientation into two energetically equivalent minima. This degeneracy likely leads to domain formation and thus potentially results in demagnetization. Hence, to achieve a nonvolatile magnetization switching it is mandatory to lift this degeneracy, e.g., by applying a small magnetic field or by inducing an additional uniaxial magnetic axis. Hence, in our simulations we introduce an additional uniaxial anisotropy contribution in the film plane given by Eq. (2.3),

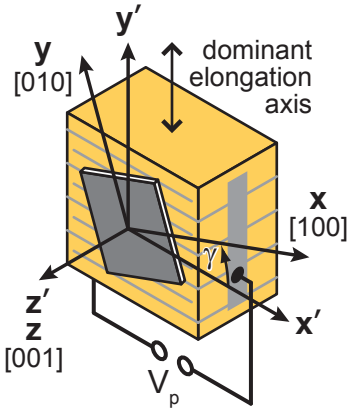

Fig. 7.1: Schematic illustration of a Fe_3O_4 thin film/piezoelectric actuator hybrid, with the thin film and the actuator ($\{\mathbf{x}, \mathbf{y}, \mathbf{z}\}$ and $\{\mathbf{x}', \mathbf{y}', \mathbf{z}'\}$ coordinate system, respectively) enclosing an angle γ.

$$F_\mathrm{u}^\mathrm{ip} = K_\mathrm{u}^\mathrm{ip} \left(m_x u_x + m_y u_y + m_z u_z\right)^2 , \tag{7.1}$$

with the direction cosines $u_1 = \sin\theta_\mathrm{u}$, $u_2 = \cos\theta_\mathrm{u}$, $u_3 = 0$, and the uniaxial anisotropy constant K_u^ip. For illustration purposes, we here use $\theta_\mathrm{u} = 10°$ and $K_\mathrm{u}^\mathrm{ip} > 0$ with $\left|K_\mathrm{u}^\mathrm{ip}/K_\mathrm{c}\right| = 1/15$. We furthermore considered a vanishing external magnetic field $\mu_0 H = 0\,\mathrm{mT}$ in the free energy density calculations. To meet the experimental conditions of Fe_3O_4 thin films, we choose $K_\mathrm{u}^{001} > 0$, $K_\mathrm{c} < 0$, $B_1 > 0$, and $B_2 < 0$.

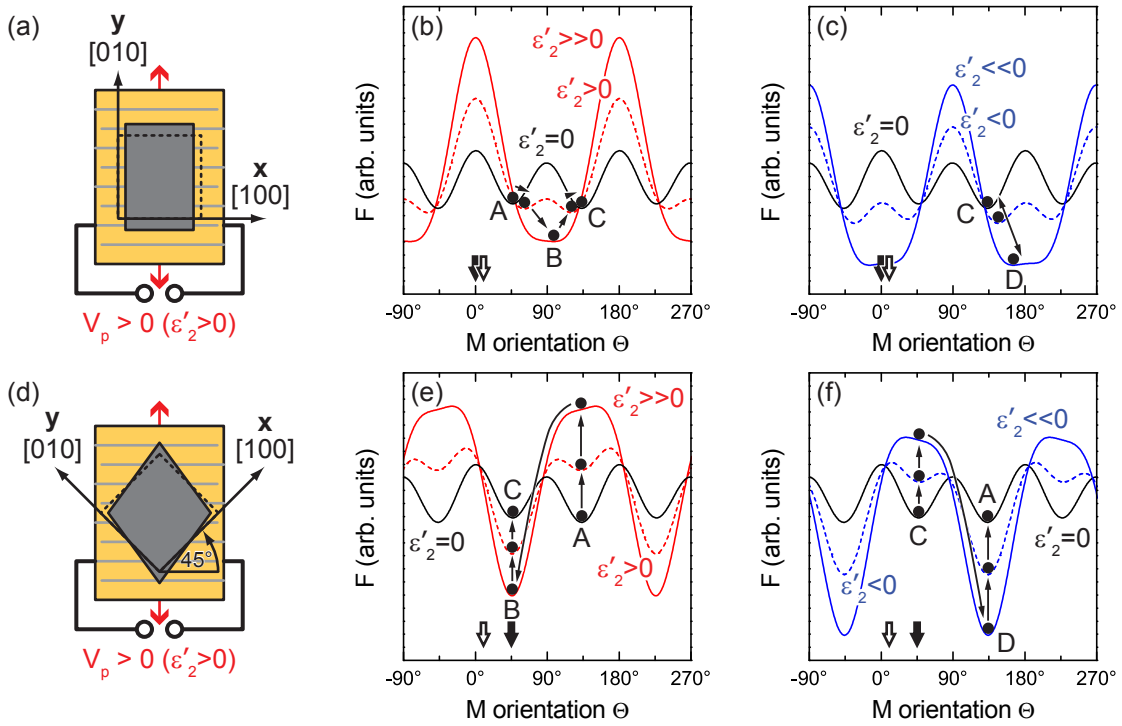

Figure 7.2: (a) Schematic illustration of lateral stress applied to a cubic thin film along the in-plane crystallographic ⟨100⟩ axes, concept (i). (b), (c) Corresponding free energy density contours as a function of the magnetization orientation Θ in the film plane, with capital letters indicating the equilibrium magnetization orientations. (b) Continuous, coherent, and nonvolatile magnetization forward switching upon $\epsilon_2' > 0$. (c) Magnetization back switching is not possible upon $\epsilon_2' < 0$ (irreversible switching process). (d) A deformation of a cubic crystal along the ⟨110⟩ axes in the film plane, concept (ii). (e) Discontinuous, coherent, and nonvolatile magnetization forward switching upon $\epsilon_2' > 0$. (f) Discontinuous, coherent, and nonvolatile magnetization back switching upon $\epsilon_2' < 0$ (reversible switching process). The full downward-oriented arrows in the free energy density contour panels denote the orientation of the main elongation ϵ_2' along 0° and 45° for the configurations (a) and (d), respectively. The open arrows indicate the orientation of the superimposed uniaxial anisotropy, which is $\theta_u = 10°$ for both cases.

Figure 7.2(a) depicts a sketch with $\gamma = 0°$ and hence $\epsilon_4 = \epsilon_5 = \epsilon_6 = 0$ (no shear strains). Thus the crystal is elongated and contracted along the cubic axes ($\mathbf{x}'$, $\mathbf{y}'$ and $\mathbf{z}'$ parallel to $\mathbf{x}$, $\mathbf{y}$, and $\mathbf{z}$, respectively). Corresponding angular dependencies of the free energy density F on the magnetization orientation Θ are shown in Figs. 7.2(b) and (c). The forward switching process with $V_p > 0$ and thus $\epsilon_2' > 0$ is illustrated in Fig. 7.2(b), where we assume an initial magnetization orientation along a magnetically easy axis. Here, we choose $\mathbf{M}$ along $\Theta = 47°$ (point A), which is energetically stable while no stress is applied to the film. Note that the equilibrium magnetization orientation along $\Theta = 47°$ deviates from a pure magnetocrystalline anisotropy with an easy axis along $\Theta = 45°$ due to the superimposed uniaxial anisotropy. With an increasing strain ϵ_2' induced in the film (which corresponds to an increasing applied voltage $V_p > 0$ in the experiment), the easy axis and thus the equilibrium magnetization orientation Θ continuously rotates towards $\Theta = 98°$ (point B). The

corresponding free energy density contour in Fig. 7.2(b) [and also the contour for maximum strain in Fig. 7.2(c)] is calculated with $|B_1\epsilon_2'/K_c| = 3/5$. On gradually reducing ϵ_2' back to 0, the symmetry break due to the uniaxial anisotropy energetically favors the emerging minimum directed towards $\Theta = 180°$, such that the magnetization orientation continuously rotates to the energetically stable direction $\Theta = 133°$ (point C) at $\epsilon_2' = 0$. Hence, this type of magnetization switching can be classified as a *continuous, coherent, and nonvolatile switching* process [see Fig. 1.3(e)]. To verify the possibility of a back switching [i.e., to return to the initial magnetization orientation to point A ($\Theta = 47°$)], the induced strain ϵ_2' is inverted in Fig. 7.2(c) and increased towards $\epsilon_2' < 0$. As shown, the easy axis gradually rotates from $\Theta = 133°$ (point C) to $\Theta = 165°$ (point D). However, upon reducing ϵ_2' back to 0, the easy axis rotates back to $\Theta = 133°$ (point C), thus the magnetization remains in point C and a further switching process is not possible. Consequently, this configuration with $\gamma = 0°$ allows for a single, *irreversible* magnetization switching.

The second approach with $\gamma = 45°$ is schematically shown in Fig. 7.2(d). This configuration exerts stress along the in-plane $\langle 110 \rangle$ directions and thus introduces a non-vanishing shear strain component $\epsilon_6 \neq 0$. Analogously, the angular dependencies of the free energy density on the magnetization orientation Θ for $\epsilon_2' > 0$ and $\epsilon_2' < 0$ are shown in Figs. 7.2(e) and (f), respectively. Again we first discuss the switching process with $\epsilon_2' > 0$ (forward switching) and an initial equilibrium magnetization orientation along $\Theta = 133°$ (point A). With a positively increasing strain ϵ_2', the easy axis basically retains its initial orientation, while the free energy density minimum becomes flat and gradually transforms into a maximum. Upon a certain critical induced strain (for illustration purposes, we plot the free energy density contour for $|B_2\epsilon_2'/K_c| = 3/5$), the easy axis changes discontinuously to $\Theta = 46°$ (point B), indicating an abrupt magnetization switching. The orientation of the easy axis essentially stays along $\Theta = 46°$ while reducing ϵ_2' back to 0, and finally reaches its equilibrium orientation at $\Theta = 47°$ (point C). Consequently, Fig. 7.2(e) illustrates a *discontinuous, coherent, and nonvolatile switching* process [see Fig. 1.3(d)]. Subsequently, we here also continuously increase the inverted induced strain $\epsilon_2' < 0$ [Fig. 7.2(f)], and, likewise, starting from point C the easy axis abruptly rotates to $\Theta = 47°$ (point D) at a certain critical strain. Finally, the magnetization orientation remains in the free energy density minimum at $\Theta = 133°$ (point A). Thus, in this case, magnetization back switching occurs. A *reversible* magnetization switching in the complete absence of a magnetic field thus becomes possible. Analogous calculations for similar configurations are presented in Refs. [304–307]. However, to our knowledge no experimental results have been published yet.

7.3 Experimental details

The 44 nm thick Fe_3O_4 thin film studied here was deposited on a (001)-oriented MgO substrate by laser molecular beam epitaxy, as described in detail elsewhere [328, 329]. For the sample discussed here, we used KrF laser pulses with a fluence of 2.5 J/cm^2 and a repetition rate of 2 Hz to ablate material from a stoichiometric

Fe_3O_4 target. The growth took place in Ar atmosphere at a pressure of 0.06 mbar and at a substrate temperature of 320 °C.

To allow for an in-situ variation of the strain, we cut the sample into pieces with lateral dimensions of $2 \times 2\,\mathrm{mm}^2$, and mechanically polished the MgO substrate to a thickness of about 50 μm. The samples were then cemented onto PZT stack actuators using a two-component epoxy [126, 127] annealed at $T = 100\,^\circ\mathrm{C}$ in air. The samples discussed here were cemented with the magnetite film facing the piezoelectric actuator (piezoelectric actuator-epoxy-Fe_3O_4/MgO). In the following, we discuss two samples corresponding to concepts (i) and (ii), i.e., the samples were cemented onto the actuators, such that stress is exerted along the $\langle 100 \rangle$ crystal axes ($\gamma = 0^\circ$ in Fig. 7.1) in one sample and along $\langle 110 \rangle$ ($\gamma = 45^\circ$) in the other. The samples thus are referred to as sample $\langle 100 \rangle$ and sample $\langle 110 \rangle$. Note that for this chapter, the definition of the angles used to define the orientation of the magnetization $\mathbf{M}\,(\Theta, \Phi)$ and the magnetic field $\mathbf{H}\,(\theta, \phi)$ with respect to the crystal axes is illustrated in Fig. 4.4.

The structural and magnetic properties of the samples were determined via HR-XRD and SQUID magnetometry, respectively. We used FMR spectroscopy to quantitatively determine the magnetic anisotropy. Angle-dependent dc magnetization measurements were performed using SQUID magnetometry endowed with a horizontal rotator (see Sec. 4.2). All FMR and magnetometry data were recorded at room temperature.

7.4 Manipulation of magnetic anisotropy I (stress along $\langle 100 \rangle$)

In this section, we focus on sample $\langle 100 \rangle$ [see Fig. 7.2(a)] as a model system to investigate the manipulation of the magnetic anisotropy in a ferromagnetic thin film/piezoelectric actuator hybrid at room temperature. The strain in the sample is quantified as a function of the voltage V_p applied to the actuator using HRXRD, and the corresponding evolution of the magnetic anisotropy is determined by FMR spectroscopy. By this means, we are able to directly and quantitatively correlate structural and magnetic properties within a magnetoelastic description. We show a continuous and reversible rotation of the magnetic easy axes as a function of V_p by 6° at room temperature. Most of the results presented here have been published in Ref. [309].

7.4.1 In-situ measurement of piezo-induced strain

In analogy to the previous chapter, we here also start with quantifying the strain in the ferromagnetic sample induced by the piezoelectric actuator. We relied on x-ray diffraction to measure the structural properties of the supporting MgO substrate, which thus allows to determine the strain induced in the Fe_3O_4 thin film as a function of the voltage V_p applied to the actuator (cf. Sec. 5.4).

Fig 7.3 shows XRD measurements of the as-grown Fe_3O_4/MgO (001) sample. Conventional $2\vartheta - \vartheta$ x-ray diffraction scans [Fig. 7.3(a)], together with reciprocal space

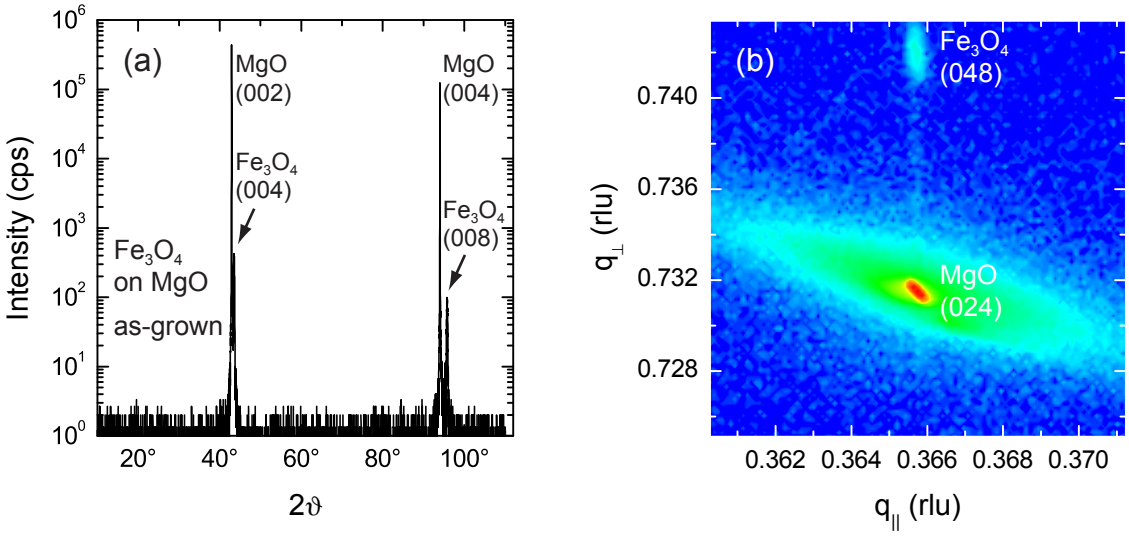

Figure 7.3: (a) $2\vartheta - \vartheta$ scan of the as-grown Fe_3O_4/MgO (001) sample. The Fe_3O_4 (004) and (008) reflections indicated by the arrows are at slightly higher angle 2ϑ than the (002) and (004) reflections of the MgO substrate. (b) Reciprocal space map of the Fe_3O_4 (048) and MgO (024) reflections. The Fe_3O_4 and the MgO reflections occur at the same in-plane $q_{\parallel}$, showing that the magnetite film is coherently strained.

maps [Fig. 7.3(b)], yield an out-of-plane Fe_3O_4 lattice constant of 0.8305 nm and an in-plane lattice constant of 0.8425 nm. The latter corresponds to twice the lattice constant of the MgO substrate within experimental error. The magnetite film is thus coherently strained, as directly evident from the reciprocal space map around the Fe_3O_4 (048) and MgO (024) reflections displayed in Fig. 7.3(b). The mosaic spread is very small, with a full width at half maximum $\Delta\omega = 0.04°$ of the rocking curve of the Fe_3O_4 (004) reflection. The magnetization measurements yield a saturation magnetization $M_s = 305\,\mathrm{kA/m}$, which is considerably smaller than the saturation magnetization of nearly 500 kA/m of bulk magnetite [311]. Such a reduced saturation magnetization is often observed in thin Fe_3O_4 films [330, 331]. It is attributed either to deviations from bulk stoichiometry [315, 332] or to the presence of structural defects, in particular antiphase boundaries [333–335].

We now turn to the dependence of the out-of-plane lattice constant on V_p, i.e., we quantify the amount of strain induced in the sample by the piezoelectric actuator. In analogy to Sec. 5.4, a direct measurement of the in-plane lattice constants and thus the strains $\epsilon_1 = \epsilon_1'$ and $\epsilon_2 = \epsilon_2'$ via reciprocal space maps was not appropriate for a quantitative analysis, as due to the significant width of the reflections a sufficiently small experimental error cannot be attained. As in Sec. 5.4 we rely on $2\vartheta - \vartheta$ scans to determine the out-of-plane strain $\epsilon_3 = \epsilon_3'$, and deduce ϵ_1 and ϵ_2 from measured ϵ_3 via elasticity theory. Since the intensity of the Fe_3O_4 reflections is too low to allow for a measurement of the Fe_3O_4 film lattice constants with sufficient accuracy, we investigated the much stronger MgO reflections in $2\vartheta - \vartheta$ scans. As evident from Fig. 7.4(a), the MgO reflections clearly shift with V_p. To minimize systematic errors, we used the Nelson-Riley formalism to determine the out-of-plane lattice constant c^{MgO} from these measurements [336]. Figure 7.4(b) shows the out-of-plane strain

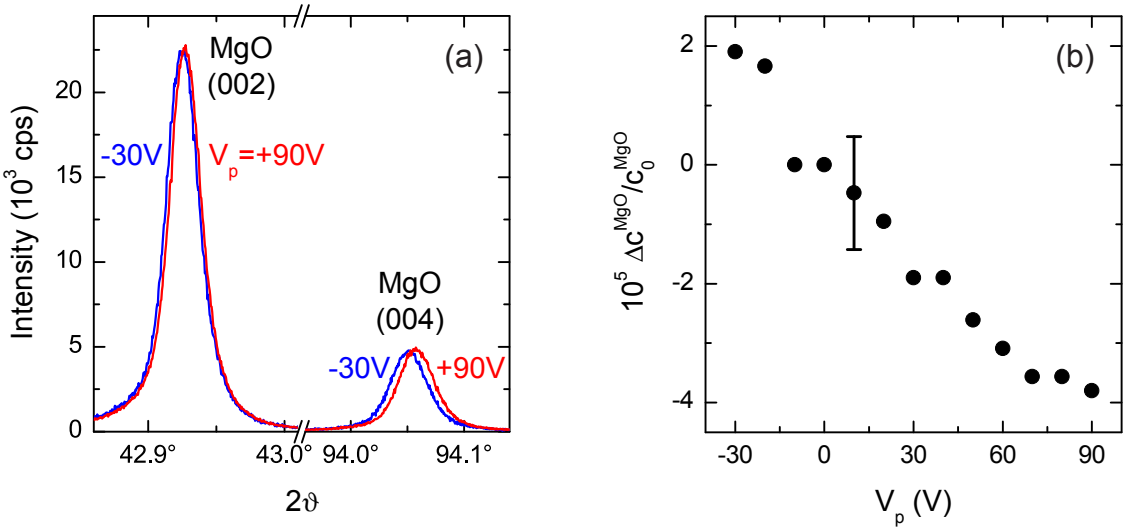

Figure 7.4: (a) The application of a finite voltage V_p to the piezoelectric actuator allows to stress the sample in situ. The piezo-induced strain manifests itself as a change in the sample's lattice constants, as directly evident from the $2\vartheta-\vartheta$ scans at $V_\mathrm{p}=-30\,\mathrm{V}$ and $V_\mathrm{p}=+90\,\mathrm{V}$. (b) The out-of-plane MgO lattice constant c^MgO changes linearly with the voltage V_p applied to the actuator. The relative lattice constant change $\Delta c^\mathrm{MgO}/c_0^\mathrm{MgO}=(c^\mathrm{MgO}-c_0^\mathrm{MgO})/c_0^\mathrm{MgO}$ is equivalent to the out-of-plane strain ϵ_3^MgO. The error bar corresponds to an upper estimate of the error in the determination of the lattice constants following the Nelson-Riley formalism, taking into account the uncertainties in the determination of the individual (002) and (004) reflections.

$\epsilon_3^\mathrm{MgO}=(c^\mathrm{MgO}-c_0^\mathrm{MgO})/c_0^\mathrm{MgO}$, where c_0^MgO is the lattice constant for $V_\mathrm{p}=0\,\mathrm{V}$, which consistently with Sec. 5.4 changes linearly with V_p. As discussed in Sec. 3.4.1, in the framework of elasticity theory ϵ_3^MgO is sufficient to quantitatively derive the strain $\epsilon_2^\mathrm{MgO}=-(c_{11}^\mathrm{MgO}/c_{12}^\mathrm{MgO})\,(1-\nu)^{-1}\,\epsilon_3^\mathrm{MgO}$ [see Eqs. (3.15)] induced within the plane along [010]. Using the literature values for c_{11}^MgO and c_{12}^MgO given in Sec. 5.1, from the overall change $\Delta\epsilon_3^\mathrm{MgO}=\epsilon_3^\mathrm{MgO}\,(+90\,\mathrm{V})-\epsilon_3^\mathrm{MgO}\,(-30\,\mathrm{V})\approx-6\times10^{-5}$ observed experimentally [see Fig. 7.4(b)] we derive $\Delta\epsilon_2^\mathrm{MgO}\approx+33\times10^{-5}$. This amounts to only about 39% of the nominal stroke $\Delta\epsilon_2^\mathrm{piezo}\approx+87\times10^{-5}$ of the actuator in the voltage range $-30\,\mathrm{V}\le V_\mathrm{p}\le+90\,\mathrm{V}$ assuming a perfect linear expansion of the actuator [133]. Such a reduced strain-transmission efficiency has also been observed in Sec. 5.4, and is most likely due to imperfect strain transmission by the cement. Careful optimization of the cementing procedure thus should allow to increase the strain introduced into the Fe_3O_4 film by up to a factor of about 2.5 in future experiments. Furthermore, a reduction of the MgO substrate thickness could have a beneficial effect on the strain magnitude as well.

7.4.2 Determination of magnetic anisotropy

We now turn to the ferromagnetic resonance spectra of the Fe_3O_4 thin film/piezoelectric actuator hybrid. Figure 7.5(a) shows how the room-temperature FMR spectrum of the sample for $\mathbf{H}\parallel[\bar{1}00]$ changes as a function of the voltage V_p applied to the actuator. The FMR spectrum consists of a single resonance with a peak-to-peak

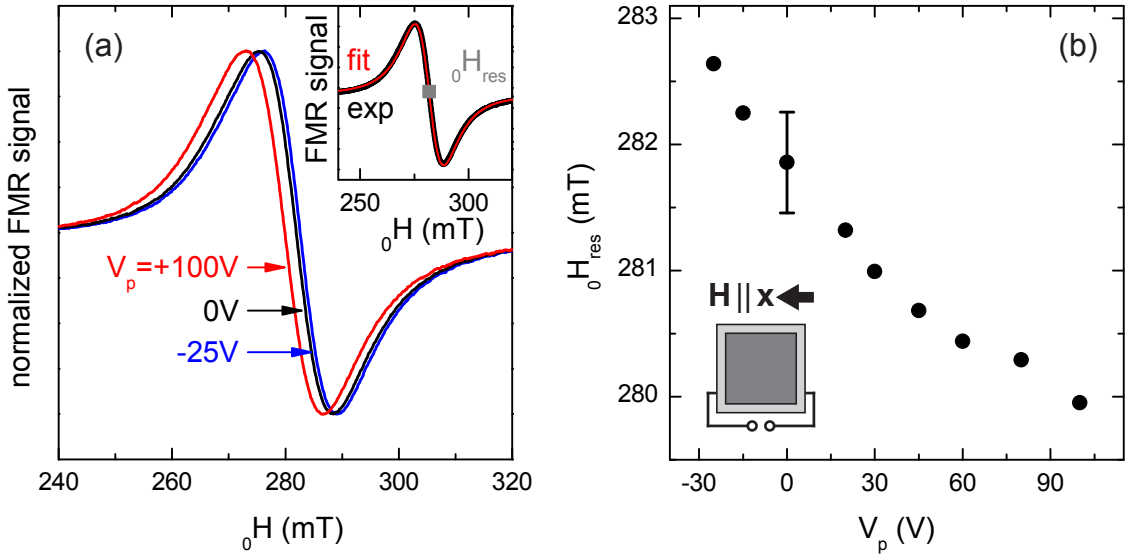

Figure 7.5: (a) Room-temperature FMR spectra of a Fe_3O_4 film mounted on a piezoelectric actuator for $\mathbf{H} \parallel [\bar{1}00]$ for three different bias voltages V_p applied to the actuator. The FMR spectra systematically shift with V_p. The inset shows that the FMR spectrum can be fitted with the derivative of a Lorentz curve. (b) The FMR field $\mu_0 H_\mathrm{res}$ changes linearly with V_p in good approximation. The error bar corresponds to the total change in the FMR peak-to-peak linewidth with V_p as an upper estimate of the uncertainty in the determination of $\mu_0 H_\mathrm{res}$.

linewidth of $\mu_0 \Delta H_\mathrm{pp} \approx 13\,\mathrm{mT}$, which is well described by a Lorentzian lineshape [inset in Fig. 7.5(a)]. In equivalence to Fig. 5.1(b), for $\mathbf{H} \parallel \mathbf{x}$ the FMR shifts to lower (higher) magnetic fields upon the application of $V_\mathrm{p} > 0\,\mathrm{V}$ ($V_\mathrm{p} < 0\,\mathrm{V}$). Within the voltage range $-25\,\mathrm{V} \leq V_\mathrm{p} \leq +100\,\mathrm{V}$, the FMR field $\mu_0 H_\mathrm{res}$ is proportional to V_p in good approximation [Fig. 7.5(b)].

The overall shift of the FMR field with V_p in single-crystalline Fe_3O_4 thin films is much smaller than in the polycrystalline Ni thin film/piezoelectric actuator hybrid systems investigated in Sec. 5.3. Therefore, we here present a brief and more thorough analysis and thus justify strain-induced changes of the magnetic anisotropy as exclusive cause for FMR-field shifts. In this way, spurious effects, such as a variation of the FMR lineshape, the microwave cavity tuning, or the temperature, can be ruled out by the following arguments. First, the peak-to-peak linewidth $\mu_0 \Delta H_\mathrm{pp}$ changes by less than 0.8 mT for $-25\,\mathrm{V} \leq V_\mathrm{p} \leq +100\,\mathrm{V}$, so that a variation of the FMR *lineshape* cannot account for the maximum shift of the FMR field $\mu_0 \Delta H_\mathrm{res} = \mu_0 H_\mathrm{res}\,(-25\,\mathrm{V}) - \mu_0 H_\mathrm{res}\,(+100\,\mathrm{V}) = 2.7\,\mathrm{mT}$ observed. Second, the resonance frequency of the microwave cavity is constant to about 10^{-4} over the whole V_p range, and thus cannot account for the FMR line shift of $\frac{2.7\,\mathrm{mT}}{281\,\mathrm{mT}} \approx 10^{-2}$. Third, the quasi-linear dependence $H_\mathrm{res}\,(V_\mathrm{p}) \propto V_\mathrm{p}$ allows to rule out temperature fluctuations as an explanation for the effect. Most importantly, however, the evolution of $\mu_0 H_\mathrm{res}\,(V_\mathrm{p})$ with the orientation of the external magnetic field, which we discuss in detail in the next paragraph, allows to unambiguously identify strain-induced anisotropy modifications as the origin of the FMR line shift.

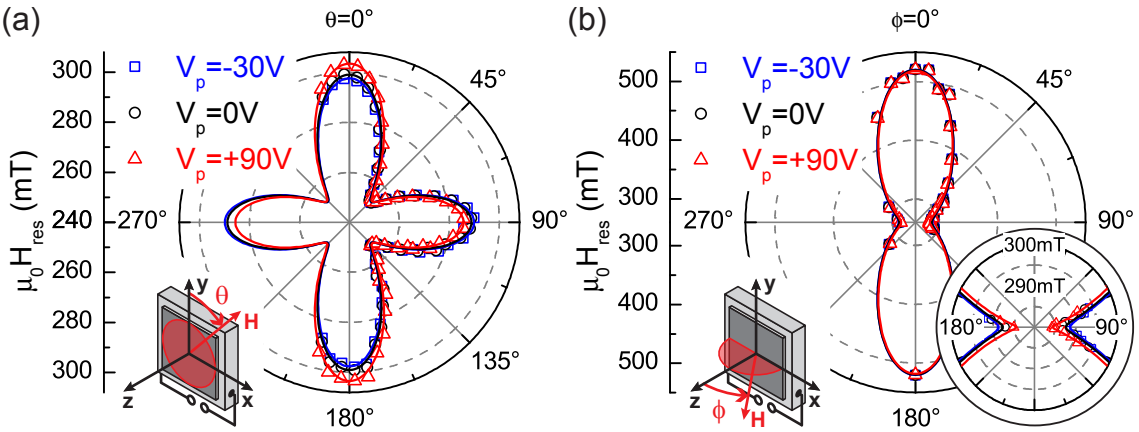

Figure 7.6: (a), (b) The FMR field $\mu_0 H_{\rm res}$ sensitively depends on the orientation of the external magnetic field $\mathbf{H}$ and the voltage $V_{\rm p}$ applied to the piezoelectric actuator (blue squares for $V_{\rm p} = -30\,{\rm V}$, black circles for $V_{\rm p} = 0\,{\rm V}$ and red triangles for $V_{\rm p} = +90\,{\rm V}$). The full lines represent the numerically simulated FMR fields (blue line for $V_{\rm p} = -30\,{\rm V}$, black line for $V_{\rm p} = 0\,{\rm V}$ and red line for $V_{\rm p} = +90\,{\rm V}$), as described in more detail in the text. (a) $\mu_0 H_{\rm res}(\theta)$ for a rotation of $\mathbf{H}$ within the (001) film plane and (b) $\mu_0 H_{\rm res}(\phi)$ for a rotation of $\mathbf{H}$ in the (010) plane perpendicular to the film plane. The inset shows that the resonance fields for $\mathbf{H}$ in the film plane ($\phi = 90°$ and $\phi = 270°$) are shifted as a function of $V_{\rm p}$ in accordance to the data shown in (a) for $\theta = 90°$ and $\theta = 270°$.

Figure 7.6 shows that the FMR field $\mu_0 H_{\rm res}$ characteristically changes as a function of magnetic field orientation $\mathbf{H} = \mathbf{H}(\theta, \phi)$, which allows to quantify the magnetic anisotropy in the Fe_3O_4 film. For clarity, only the data for $V_{\rm p} = 0\,{\rm V}$ and the two bias voltages $V_{\rm p} = -30\,{\rm V}$ and $V_{\rm p} = +90\,{\rm V}$ are displayed in the figure (shown as open black circles, open blue squares, and open red triangles, respectively). Figure 7.6 shows that the FMR line shift $\mu_0 \Delta H_{\rm res} = \mu_0 H_{\rm res}(-30\,{\rm V}) - \mu_0 H_{\rm res}(+90\,{\rm V})$ is qualitatively different for different orientations of the external field: $\mu_0 \Delta H_{\rm res}$ is large and negative ($\approx -6\,{\rm mT}$) for $\mathbf{H} \parallel [010]$, vanishes for $\mathbf{H} \parallel [110]$, and becomes positive ($\approx +4\,{\rm mT}$) for $\mathbf{H} \parallel [100]$ [Fig. 7.6(a)]. Moreover, $\mu_0 \Delta H_{\rm res}$ also vanishes if the field is applied perpendicular to the film plane along [001] [Fig. 7.6(b)]. The effect of $V_{\rm p}$ on the FMR spectrum thus is qualitatively different for $\mathbf{H}$ applied along the three cubic axes of the Fe_3O_4 film. Note also that for $\mathbf{H}$ in the film plane, the FMR exhibits a characteristic fourfold symmetry as expected for a cubic material, although the magnitude of the resonance fields does not coincide every 90°.

To model the angular dependence of the FMR fields, we use the total free energy density

$$\begin{aligned} F &= F_{\rm Zeeman} + F_{\rm u,eff}^{001} + F_{\rm c} + F_{\rm u}^{010} + F_{\rm magel}\left(\epsilon_3^{\rm MgO}\right) \\ &= -\mu_0 H M \left(\sin\Theta \sin\Phi \sin\theta \sin\phi + \cos\Theta \cos\theta + \sin\Theta \cos\Phi \sin\theta \cos\phi\right) \\ &\quad + K_{\rm u,eff}^{001} \sin^2\Theta \cos^2\Phi + \frac{1}{4} K_{\rm c} \left[\sin^2(2\Theta) + \sin^4\Theta \sin^2(2\Phi)\right] \\ &\quad + K_{\rm u}^{010} \cos^2\Theta + F_{\rm magel}\left(\epsilon_3^{\rm MgO}\right), \end{aligned} \tag{7.2}$$

which is composed of four anisotropy contributions. The effective uniaxial aniso-

tropy contribution $K_{\mathrm{u,eff}}^{001} = \frac{1}{2}\mu_0 M^2 + K_{\mathrm{u}}^{001}$ along [001] comprises the demagnetization contribution $\frac{1}{2}\mu_0 M^2$ and the uniaxial contribution $K_{\mathrm{u}}^{001} < 0$ resulting from pseudomorphic growth of the Fe_3O_4 film, which leads to isotropic tensile strain within the film plane. These two terms can not be separated with FMR as they have the same symmetry, but in magnetite, the main contribution to $K_{\mathrm{u,eff}}^{001}$ usually arises from shape anisotropy $\frac{1}{2}\mu_0 M^2 > 0$ establishing a magnetic hard axis perpendicular to the film plane in the [001] direction. K_{c} is the first-order cubic anisotropy constant. K_{u}^{010} represents a uniaxial anisotropy within the film plane along [010], which is observed in all cemented hybrids due to the anisotropic thermal expansion of the piezoelectric actuator stack (see Sec. 5.4). The last term in Eq. (7.2), $F_{\mathrm{magel}}(\epsilon_3^{\mathrm{MgO}})$, describes the influence of the voltage-tunable strain induced by the piezoelectric actuator, which is again based on Eq. (2.13). The aim hereby is to express F_{magel} only in terms of the strain component $\epsilon_3^{\mathrm{MgO}}$ *perpendicular* to the film plane, as the latter can be quantitatively measured via x-ray diffraction. Since in this hybrid sample stress is applied along the ⟨100⟩ cubic crystal axes, we refer to the strain components given in Eqs. (3.15). As the Fe_3O_4 film is coherently strained, i.e., $\epsilon_1^{\mathrm{Fe_3O_4}} = \epsilon_1^{\mathrm{MgO}}$ and $\epsilon_2^{\mathrm{Fe_3O_4}} = \epsilon_2^{\mathrm{MgO}}$, $\epsilon_3^{\mathrm{Fe_3O_4}}$ thus can be calculated to

$$\epsilon_3^{\mathrm{Fe_3O_4}} = -\frac{c_{12}^{\mathrm{Fe_3O_4}}}{c_{11}^{\mathrm{Fe_3O_4}}}\left(\epsilon_1^{\mathrm{Fe_3O_4}} + \epsilon_2^{\mathrm{Fe_3O_4}}\right) = \frac{c_{12}^{\mathrm{Fe_3O_4}}}{c_{11}^{\mathrm{Fe_3O_4}}}\frac{c_{11}^{\mathrm{MgO}}}{c_{12}^{\mathrm{MgO}}}\epsilon_3^{\mathrm{MgO}}. \tag{7.3}$$

Hence, using Eqs. (2.13), (3.15), and (7.3), the magnetoelastic contribution can be written as

$$\begin{aligned} F_{\mathrm{magel}}\left(\epsilon_3^{\mathrm{MgO}}\right) &= \chi\frac{3}{2}\lambda_{100}^{\mathrm{Fe_3O_4}}\left(c_{12}^{\mathrm{Fe_3O_4}} - c_{11}^{\mathrm{Fe_3O_4}}\right)\left(\frac{c_{11}^{\mathrm{MgO}}}{c_{12}^{\mathrm{MgO}}}\frac{1}{1-\nu}\right) \\ &\quad\times\left[\nu\left(\sin^2\Theta\sin^2\Phi - \frac{1}{3}\right) - \left(\cos^2\Theta - \frac{1}{3}\right)\right. \\ &\quad\left. + (1-\nu)\,\frac{c_{12}^{\mathrm{Fe_3O_4}}}{c_{11}^{\mathrm{Fe_3O_4}}}\left(\sin^2\Theta\cos^2\Phi - \frac{1}{3}\right)\right]\epsilon_3^{\mathrm{MgO}}, \end{aligned} \tag{7.4}$$

with the proportionality factor χ.

The resonance fields are obtained numerically from Eq. (7.2) using Eq. (7.4) by numerically evaluating Eqs. (4.7) and (4.8). The resonance fields calculated in this way for $V_{\mathrm{p}} = 0\,\mathrm{V}$ ($\epsilon_3^{\mathrm{MgO}} = 0$) using the voltage-independent anisotropy fields $K_{\mathrm{u,eff}}^{001}/M = 80.2\,\mathrm{mT}$, $K_{\mathrm{c}}/M = -14.9\,\mathrm{mT}$, and $K_{\mathrm{u}}^{010}/M = 3.2\,\mathrm{mT}$, are shown as solid black lines in Fig. 7.6. The good agreement between the simulated and the measured resonance fields demonstrates that the magnetic anisotropy contributions included in Eq. (7.2) are sufficient to model the magnetic anisotropy of the Fe_3O_4 film within the accuracy of the experiment. The magnetic anisotropy constants for $V_{\mathrm{p}} = 0\,\mathrm{V}$ agree well with the values quoted in the literature [313, 324, 326, 327]—with the exception of the uniaxial anisotropy contribution K_{u}^{010} within the film plane, which is not observed in as-grown Fe_3O_4 films as the thermal expansion typically is isotropic [327]. This was verified by angle-dependent FMR measurements of the sample in the as-grown state, where $K_{\mathrm{u,eff}}^{001}/M = 73.2\,\mathrm{mT}$, $K_{\mathrm{c}}/M = -14.7\,\mathrm{mT}$,

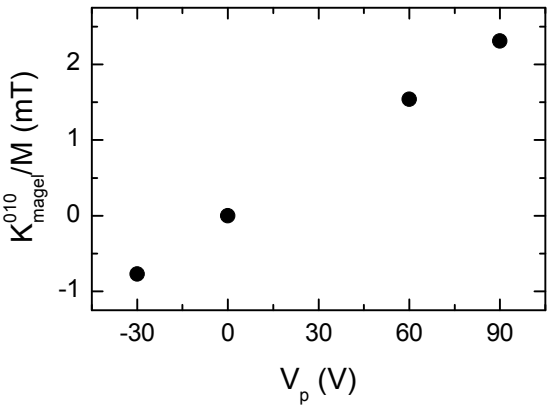

Figure 7.7: The in-plane magnetoelastic anisotropy field $K^{010}_{\mathrm{magel}}/M$ calculated using Eqs. (7.6) with the experimentally determined strain $\epsilon_3^{\mathrm{MgO}}$ shown in Fig. 7.4(b).

and $K_{\mathrm{u}}^{010}/M = 0\,\mathrm{mT}$ were found. Thus, K_{u}^{010} stems from the anisotropic thermal expansion of the piezoelectric actuator.

To calculate the angular dependence of the FMR fields for $V_{\mathrm{p}} \neq 0\,\mathrm{V}$, we use the measured out-of-plane strain $\epsilon_3^{\mathrm{MgO}} = \Delta c^{\mathrm{MgO}}/c_0^{\mathrm{MgO}}$ [Fig. 7.4(b)]. The factor χ is furthermore introduced in Eq. (7.4) since the calculated resonance fields depend very sensitively on the elastic stiffness constants [321, 337]. χ accounts for the fact that the magnetoelastic properties of ferromagnetic thin films typically deviate from the corresponding bulk values [338–341]. We note, however, that this was not the case for the polycrystalline Ni thin film/piezoelectric actuator hybrid systems investigated in Sec. 5.3. Using $\chi = 0.7$, we obtain excellent agreement with the experiment, as evident from the solid blue and red lines in Fig. 7.6 calculated with the above values for $V_{\mathrm{p}} = -30\,\mathrm{V}$ and $V_{\mathrm{p}} = +90\,\mathrm{V}$, respectively.

To illustrate the magnitude of the magnetoelastic anisotropy contribution in the Fe_3O_4 film, we follow the approach of Sec. 5.2 and express Eq. (7.4) as a superposition of one uniaxial magnetic anisotropy in the film plane along [010] and one perpendicular to the film plane in the [001] direction,

$$\begin{aligned} F_{\mathrm{magel}}\left(\epsilon_3^{\mathrm{MgO}}\right) &= F_{\mathrm{magel}}^{010}\left(\epsilon_3^{\mathrm{MgO}}\right) + F_{\mathrm{magel}}^{001}\left(\epsilon_3^{\mathrm{MgO}}\right) \\ &= \left[K_{\mathrm{magel}}^{010}\left(\epsilon_3^{\mathrm{MgO}}\right)\right]\left(m_y^2 - \frac{1}{3}\right) + \left[K_{\mathrm{magel}}^{001}\left(\epsilon_3^{\mathrm{MgO}}\right)\right]\left(m_z^2 - \frac{1}{3}\right) \end{aligned} \tag{7.5}$$

with

$$\begin{aligned} K_{\mathrm{magel}}^{010}\left(\epsilon_3^{\mathrm{MgO}}\right) &= \chi\frac{3}{2}\lambda_{100}^{\mathrm{Fe_3O_4}}\left(c_{12}^{\mathrm{Fe_3O_4}} - c_{11}^{\mathrm{Fe_3O_4}}\right)\left(\frac{c_{11}^{\mathrm{MgO}}}{c_{12}^{\mathrm{MgO}}}\frac{1}{1-\nu}\right)(-1-\nu)\,\epsilon_3^{\mathrm{MgO}}, \\ K_{\mathrm{magel}}^{001}\left(\epsilon_3^{\mathrm{MgO}}\right) &= \chi\frac{3}{2}\lambda_{100}^{\mathrm{Fe_3O_4}}\left(c_{12}^{\mathrm{Fe_3O_4}} - c_{11}^{\mathrm{Fe_3O_4}}\right)\left(\frac{c_{11}^{\mathrm{MgO}}}{c_{12}^{\mathrm{MgO}}}\frac{1}{1-\nu}\right) \\ &\quad \times\left[-1-(1-\nu)\,\frac{c_{12}^{\mathrm{Fe_3O_4}}}{c_{11}^{\mathrm{Fe_3O_4}}}\right]\epsilon_3^{\mathrm{MgO}}. \end{aligned} \tag{7.6}$$

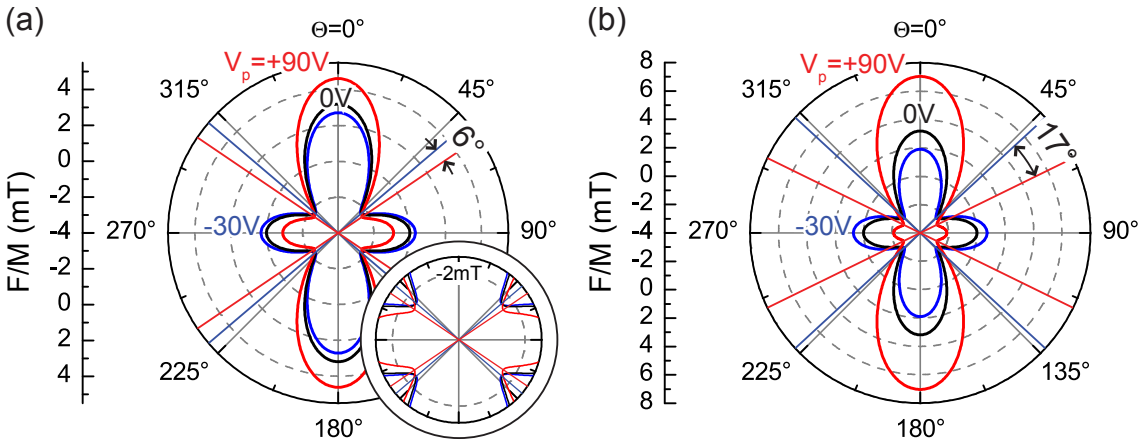

Figure 7.8: Numerical simulations of the dependence of the free energy density $F/M\,(\Theta)$ on the magnetization orientation within the film plane for zero applied magnetic field. Panel (a) shows the free energy density using the anisotropy parameters determined from FMR. In panel (b), we assumed a perfect strain transmission from piezoelectric actuator to sample and no strain relaxation within the sample ($\epsilon_1^{\mathrm{MgO}} = \epsilon_1^{\mathrm{piezo}}$, $\epsilon_2^{\mathrm{MgO}} = \epsilon_2^{\mathrm{piezo}}$), which results in much larger changes in the magnetic anisotropy. The orientation of the magnetic easy axes [shown as solid lines in panels (a) and (b)] clearly depends on the stress exerted by the piezoelectric actuator. The inset in (a) clarifies the rotation of the easy axes by 6° within the voltage range $-30\,\mathrm{V} \leq V_\mathrm{p} \leq +90\,\mathrm{V}$.

The in-plane magnetoelastic anisotropy field $K_{\mathrm{magel}}^{010}/M$ as a function of V_p is shown in Fig. 7.7. Hence, the overall change of the magnetoelastic contribution amounts to $\Delta K_{\mathrm{magel}}^{010}/M = 3\,\mathrm{mT}$ within the voltage range $-30\,\mathrm{V} \leq V_\mathrm{p} \leq +90\,\mathrm{V}$, which cannot induce qualitative changes in the magnetic anisotropy due to the presence of the voltage-independent, competing cubic and uniaxial anisotropy contributions in the film plane K_c and K_u^{010}, respectively.

The piezo-induced changes in the magnetic anisotropy have a distinct impact on the free energy density and the magnetization orientation. Using the experimentally determined anisotropy constants given above, we find that the magnetization vector is in the film plane (close to ⟨110⟩) for vanishing external magnetic field $\mu_0 H = 0\,\mathrm{mT}$. However, the equilibrium magnetization in-plane orientation Θ_0 characteristically changes for finite V_p, as shown by the free energy density curves shown in Fig. 7.8(a). Upon the application of $V_\mathrm{p} \neq 0$ we observe a change of the relative strength of the magnetic hard axes, as evident from the different magnitudes of the maxima of the free energy, while they retain their orientation. The easy axes—i.e., the free energy density minima—almost retain their strength, but the orientation Θ of the easy axes clearly is dependent on V_p. This is the basis for the continuous and reversible rotation of $\mathbf{M}$ in the spin-mechanics scheme. The free energy density contours in Fig. 7.8(a) exhibit a rotation of the easy axes and thus of the equilibrium magnetization orientation Θ_0 by $\Delta\Theta = 6°$ for $-30\,\mathrm{V} \leq V_\mathrm{p} \leq +90\,\mathrm{V}$ at room temperature in the present sample. Assuming perfect strain transmission from the piezoelectric actuator into the sample ($\epsilon_1^{\mathrm{MgO}} = \epsilon_1^{\mathrm{piezo}}$ and $\epsilon_2^{\mathrm{MgO}} = \epsilon_2^{\mathrm{piezo}}$), Θ_0 can be shifted by 17° [Fig. 7.8(b)]. Hence, a continuous and reversible voltage control of magnetization orientation is possible, but a voltage-controlled magnetization

switching is out of reach in the present sample.

Taken together, these results show that a fully reversible, continuous, voltage-based control of the magnetization orientation is possible at room temperature in crystalline ferromagnets attached to piezoelectric actuators. This voltage control of magnetization does not require the application of variable magnetic fields. However, we note that care must be taken to ensure that a well-defined global free energy density minimum always is present to preserve a homogeneous magnetization and prevent the formation of a multi-domain state. As we have seen in the previous chapter for (Ga,Mn)As thin film/piezoelectric actuator hybrids, the ratio of the magnetoelastic and magnetocrystalline anisotropy contributions is a crucial aspect for the realization of a substantial impact on the magnetization orientation. However, since in the investigated ferromagnetic thin films with stress exerted along $\langle 100 \rangle$ the magnetocrystalline anisotropies typically are large, the voltage-induced magnetoelastic contribution can only modify the free energy density landscape to some extent, but will not result in qualitative changes as observed in the previous chapter. Hence, to maximize the angular range accessible by the voltage-induced magnetization rotation, a smaller magnetocrystalline anisotropy contribution is required.

Because the piezoelectric actuator is cemented onto the ferromagnetic crystal, it is possible to align the direction of the voltage-controllable, external stress along any direction within the ferromagnetic film plane. This allows to engineer the type of strain exerted in the sample. For example, if the actuator elongation axis is aligned along a $\langle 100 \rangle$ axis in a cubic crystal [Fig. 3.4(b)], shear-strain contributions are suppressed. This was the case in all the experiments discussed above. In contrast, shear-strain effects will play an important role, e.g., if the piezoelectric actuator elongation is along a $\langle 110 \rangle$ axis.

7.5 Manipulation of magnetic anisotropy II (stress along $\langle 110 \rangle$)

In view of the two different switching concepts shown in Fig. 7.2, we here discuss a Fe_3O_4 thin film with stress applied along the $\langle 110 \rangle$ crystal axes [denoted as sample $\langle 110 \rangle$, see Fig. 7.2(d)]. This approach is favorably suited for applications, since it (i) provides the possibility of a nonvolatile forward and back switching of the magnetization, and (ii) switching can be attained at lower critical strain due to $\lambda_{111} > |\lambda_{100}|$. Since we have demonstrated in the last section that the voltage-controlled manipulation of the magnetic anisotropy in Fe_3O_4 thin film/piezoelectric actuator hybrids can be quantitatively modeled using magnetoelastic theory, we here omit an extensive structural characterization using HRXRD. Instead, we will follow a more phenomenological ansatz and use the magnetoelastic anisotropy constants as fit parameters.

To quantitatively determine the magnetic anisotropy as a function of V_p, we again recorded the FMR field $\mu_0 H_\mathrm{res}(\theta)$ for a rotation of the magnetic field $\mathbf{H}(\theta, \phi = 90^\circ)$ in the film plane at constant actuator voltages V_p within the full semi-bipolar voltage

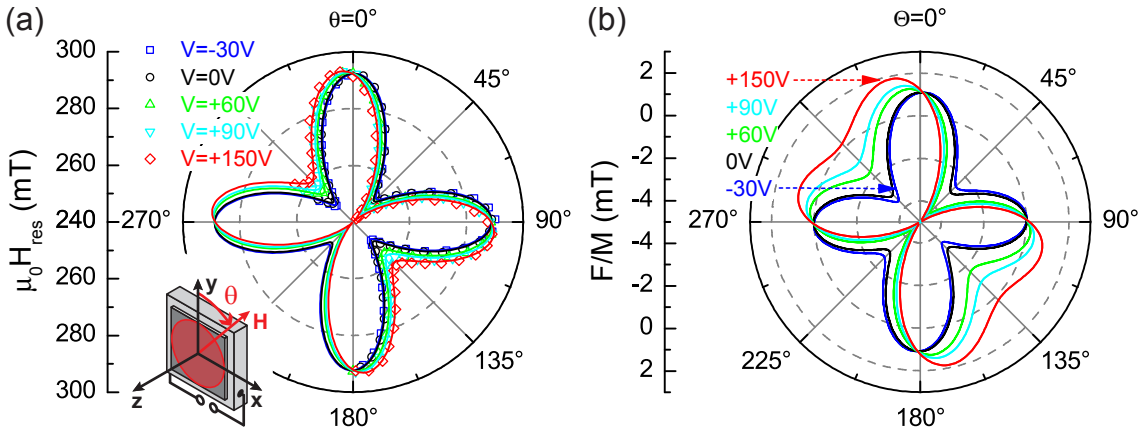

Figure 7.9: (a) FMR field $\mu_0 H_{\mathrm{res}}$ for sample ⟨110⟩ for a rotation of $\mathbf{H}$ in the film plane as a function of the voltage V_{p} applied to the actuator (symbols). The lines show the simulated FMR fields. (b) Corresponding free energy density curves for vanishing external field $\mu_0 H = 0$. Upon the application of a voltage V_{p} the easy axes reside in their initial orientation while their relative strengths change.

range $-30\,\mathrm{V} \leq V_{\mathrm{p}} \leq +150\,\mathrm{V}$. The result is shown by the symbols in Fig. 7.9(a). To model the angular dependence of the FMR fields, we use a total free energy density corresponding to Eq. (7.2),

$$\begin{aligned} F &= F_{\mathrm{Zeeman}} + F_{\mathrm{u,eff}}^{001} + F_{\mathrm{c}} + F_{\mathrm{u}}^{\mathrm{ip}} + F_{\mathrm{magel}} \\ &= -\mu_0 H M \left(\sin\Theta \sin\Phi \sin\theta \sin\phi + \cos\Theta \cos\theta + \sin\Theta \cos\Phi \sin\theta \cos\phi\right) \\ &\quad + K_{\mathrm{u,eff}}^{001} \sin^2\Theta \cos^2\Phi + \frac{1}{4} K_{\mathrm{c}} \left[\sin^2(2\Theta) + \sin^4\Theta \sin^2(2\Phi)\right] \\ &\quad + K_{\mathrm{u}}^{\mathrm{ip}} \left(\sin\theta_{\mathrm{u}} \sin\Theta \sin\Phi + \cos\theta_{\mathrm{u}} \cos\Theta\right)^2 + F_{\mathrm{magel}}(\epsilon_2') \,. \end{aligned} \tag{7.7}$$

Hereby, $F_{\mathrm{u,eff}}^{001}$ and F_{c} again represent the uniaxial hard magnetic anisotropy perpendicular to the film plane and the magnetocrystalline anisotropy contributions, respectively, as typically observed in single-crystalline ferromagnetic thin films. Equivalently to Eq. (7.2), $F_{\mathrm{u}}^{\mathrm{ip}}$ denotes a thermally induced uniaxial anisotropy in the film plane along $\theta_{\mathrm{u}} = 5°$ [cf. Eq. (7.1)]. Finally, $F_{\mathrm{magel}}(\epsilon_2')$ represents the magnetoelastic contribution as a function of the strain ϵ_2' along the actuator's dominant elongation axis $\mathbf{y}'$ and is composed of Eqs. (2.13) and (3.16). Since for ⟨110⟩-strained films (i.e., $\gamma = 45°$) $\epsilon_1 \equiv \epsilon_2$ [cf. Eqs. (3.16)], the magnetoelastic anisotropy contributions along [100] and [010] can be incorporated in the effective out-of-plane contribution $K_{\mathrm{u,eff}}^{001}$ (see Sec. 2.2.1). Hence,

$$\begin{aligned} F_{\mathrm{magel}}(\epsilon_2') &= F_{\mathrm{magel}}^{110}(\epsilon_2') + F_{\mathrm{magel}}^{001}(\epsilon_2') \\ &= \left[K_{\mathrm{magel}}^{110}(\epsilon_2')\right](m_x m_y) + \left[K_{\mathrm{magel}}^{001}(\epsilon_2')\right]\left(m_z^2 - \frac{1}{3}\right), \end{aligned} \tag{7.8}$$

with the magnetoelastic in-plane anisotropy contribution along [110] corresponding to the strain component ϵ_6,

$$K_{\mathrm{magel}}^{110}(\epsilon_2') = -3\lambda_{111}^{\mathrm{Fe_3O_4}} c_{44}^{\mathrm{Fe_3O_4}} \epsilon_6 = -3\lambda_{111}^{\mathrm{Fe_3O_4}} c_{44}^{\mathrm{Fe_3O_4}} (1+\nu)\,\epsilon_2'. \tag{7.9}$$

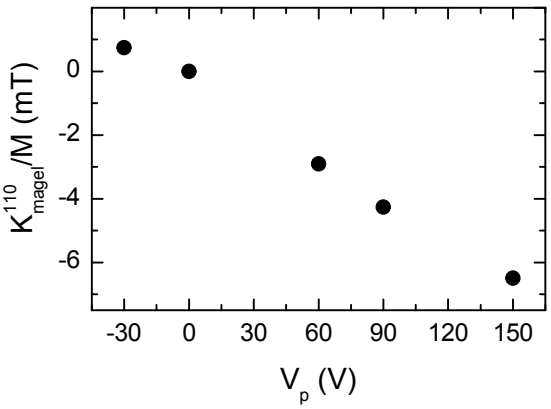

Figure 7.10: The in-plane magnetoelastic anisotropy field $K^{110}_{\mathrm{magel}}/M$ of sample $\langle 110 \rangle$ as a function of V_p.

We employ K^{110}_{magel} as fit parameter, and further using the voltage-independent anisotropy fields $K^{001}_{\mathrm{u,eff}}/M = 75.3\,\mathrm{mT}$, $K_\mathrm{c}/M = -14.5\,\mathrm{mT}$, and $K^{\mathrm{ip}}_\mathrm{u}/M = 1.1\,\mathrm{mT}$ yields the corresponding simulated FMR fields displayed by the solid lines in Fig. 7.9(a). The anisotropy field $K^{110}_{\mathrm{magel}}/M$ as a function of V_p thus obtained is shown in Fig. 7.10 and exhibits an overall change of the magnetoelastic contribution of $\Delta K^{110}_{\mathrm{magel}}/M \approx 7\,\mathrm{mT}$ within the voltage range $-30\,\mathrm{V} \leq V_\mathrm{p} \leq +150\,\mathrm{V}$.

The corresponding free energy density curves in the film plane for zero external magnetic field applied are depicted in Fig. 7.9(b). According to the analogous case in Sec. 7.2, upon the application of a voltage V_p, the energy minima mainly retain their orientation. Slight deviations arise from the uniaxial anisotropy contribution $F^{\mathrm{ip}}_\mathrm{u}$. More importantly, the relative strengths of the magnetic easy axes considerably change, as illustrated for the energy density minimum at $\Theta = 133°$, which remarkably loses depth for $V_\mathrm{p} = +150\,\mathrm{V}$ and approaches transforming into a maximum. Unfortunately, in the present sample $\langle 110 \rangle$, the strain-induced anisotropy was just not large enough to really invert the energy landscape. Nevertheless, in terms of a magnetization switching, the concept realized in sample $\langle 110 \rangle$ is clearly more advantageous, with a magnetization switching process being much more likely to happen.

To conclude, angular-dependent FMR measurements allow to quantitatively determine the contributions to the total free energy density. The corresponding equilibrium magnetization orientation can be obtained by calculating the free energy density minima. However, FMR spectroscopy does not allow to directly measure the magnetization orientation. We again note that the free energy density ansatz [Eqs. (7.2) and (7.7)] is applicable only to a homogeneously magnetized single-domain magnetization. This approach is valid for the FMR measurements, since the applied external field suffices to saturate the magnetization to $M = 305\,\mathrm{kA/m}$ measured with SQUID magnetometry at the FMR resonance fields $\mu_0 H_\mathrm{res} > 200\,\mathrm{mT}$ for the present samples. As we are particularly aiming at a magnetization switching at vanishing external magnetic field, it is not a priori clear that a single-domain model is adequate. In particular, magnetic domain formation might not be negligible.

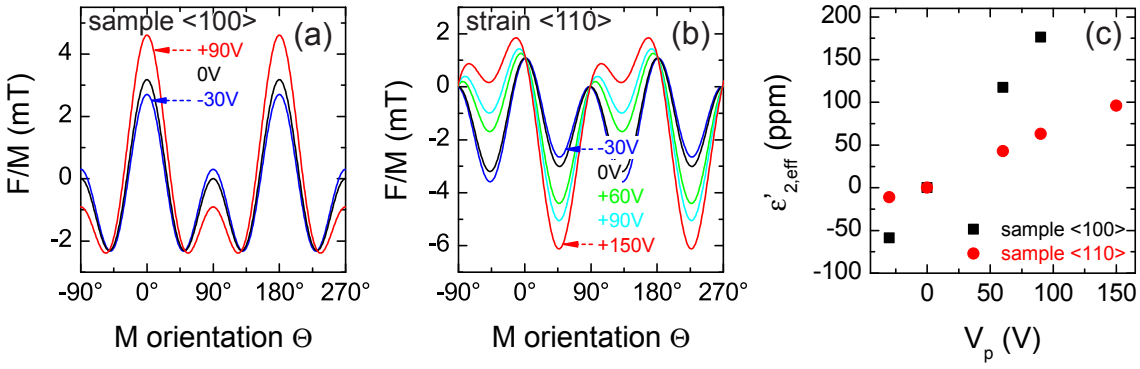

Figure 7.11: (a), (b) Free energy density contours for sample ⟨100⟩ and sample ⟨110⟩, reproduced from Figs. 7.8(a) and 7.9(b), respectively. (c) Effective strain $\epsilon'_{2,\mathrm{eff}}$ along the dominant elongation axis $\mathbf{y}'$ for sample ⟨100⟩ (black squares) and sample ⟨110⟩ (red circles).

Therefore, in the following section, we apply SQUID magnetometry measurements as means of directly detect the magnetization as a function of V_p.

7.6 Towards voltage-controlled, nonvolatile magnetization switching

We start the discussion of the actual magnetization behavior with a short comparison of the two samples discussed in detail in the preceding two sections. To this end, Figs. 7.11(a) and (b) again show the free energy density contours at different V_p and zero external magnetic field for sample ⟨100⟩ and sample ⟨110⟩, respectively [see Figs. 7.8(a) and 7.9(b)]. We observed a rotation of the magnetic easy axes as a function of V_p while their strength is retained for stress applied along ⟨100⟩ [Fig. 7.11(a)]. In contrast, for stress applied along ⟨110⟩, the relative strengths of the easy axes change while their orientation is retained [Fig. 7.11(b)]. To quantitatively compare these two magnetization manipulation concepts, a direct comparison of the two magnetoelastic anisotropy constants K^{010}_{magel} [see Eqs. (7.6) and Fig. 7.7] and K^{110}_{magel} [see Eq. (7.9) and Fig. 7.10] is not adequate, since they incorporate different values of the magnetostriction constant λ and the elastic stiffness constant c along different crystalline directions. Instead, we exclude such direction-specific material parameters by considering a phenomenological effective strain $\epsilon'_{2,\mathrm{eff}}$ along the dominant elongation axis $\mathbf{y}'$ [$\epsilon'_{2,\mathrm{eff}} = -\chi c_{11}^{\mathrm{MgO}}/c_{12}^{\mathrm{MgO}}\,(1-\nu)^{-1}\,\epsilon_3^{\mathrm{MgO}} = \chi\epsilon'_2$ for sample ⟨100⟩ using Eqs. (3.15), and $\epsilon'_{2,\mathrm{eff}} = \epsilon'_2$ for sample ⟨110⟩ using Eq. (7.9)]. We again note that we used the literature values for the magnetostriction constants and the elastic stiffness constants in all our calculations. The values for the effective strain $\epsilon'_{2,\mathrm{eff}}$ in Fig. 7.11(c) thus deviate from the actual values, as quantitatively determined for sample ⟨100⟩ by the factor $\chi = 0.7$ in Sec. 7.4.2. Figure 7.11(c) shows the strain $\epsilon'_{2,\mathrm{eff}}$ in this way obtained. It exhibits a significant difference in the strain transmission across the actuator-sample interface between the samples investigated. As evident, the strain $\Delta\epsilon'_{2,\mathrm{eff}} = \epsilon'_{2,\mathrm{eff}}\,(+90\,\mathrm{V}) - \epsilon'_{2,\mathrm{eff}}\,(-30\,\mathrm{V})$ induced in

the sample ⟨110⟩ [red circles in Fig. 7.11(c)] amounts to only 30 % of the one in the sample ⟨100⟩ [black squares in Fig. 7.11(c)] within the voltage range $-30\,\mathrm{V} \leq V_\mathrm{p} \leq +90\,\mathrm{V}$. These results demonstrate that upon optimizing the strain transmission efficiency larger magnetoelastic effects could be realized.

To directly investigate the magnetization behavior as a function of applied voltage V_p, we utilize SQUID magnetometry. This technique detects the projection $m = \mathbf{m}\cdot\mathbf{h}$ of the magnetic moment $\mathbf{m}$ onto the direction of the external magnetic field $\mathbf{H} = H\mathbf{h}$. We subsequently correct m for any diamagnetic and paramagnetic contributions of the sample and calculate the magnetization $M = m/V$ using the ferromagnetic sample volume V. Moreover, SQUID magnetization measurements as a function of $\mathbf{H}$ orientation provide a technique to record the magnetization orientation $\mathbf{M}$. For these angle-dependent magnetization measurements, we magnetized the sample along an easy axis to a single-domain state by applying $\mu_0 H = +1\,\mathrm{T}$ and then swept the magnetic field to $\mu_0 H = 0\,\mathrm{T}$ at a fixed voltage V_p. Subsequent to this preparation of the magnetization we started the acquisition of $m(\theta)$ data, keeping V_p constant.

Starting the discussion with sample ⟨100⟩, we applied a constant actuator voltage V_p, oriented the external magnetic field along $\theta = 50°$ (energy density minimum for $V_\mathrm{p} = -30\,\mathrm{V}$), swept the preparation field to $\mu_0 H = +1\,\mathrm{T}$ and then back to 0 T. Subsequently, we recorded $m(\theta)$ as a function of the angle θ in the film plane between $\mathbf{H}$ and the cubic axis [010] $\parallel$ $\mathbf{y}$ [symbols in Fig. 7.12(a)]. The full lines represent fits using a cosine function. Since in the absence of an external magnetic field the magnetization preferably aligns along a magnetic easy axis, maxima in the $M(\theta)$ curves correspond to minima in the free energy density contours $F(\Theta)$. The respective maxima of the $M(\theta)$ curves are evaluated in Fig. 7.12(b), regarding their orientation (black squares) and magnitude (red circles) as a function of V_p. M_max changes by only 1 % in the full voltage range $-30\,\mathrm{V} \leq V_\mathrm{p} \leq +150\,\mathrm{V}$ of the actuator and thus is almost independent of V_p. Taking furthermore the excellent agreement between experiment and fits into account, we conclude that domain formation plays only a negligible role. As evident from Fig. 7.12(a), we can model the experimental data very well in a single-domain approach. In other words, a macroscopic, homogeneous magnetization $\mathbf{M}$ oriented along the respective free energy minimum at a given voltage V_p consistently accounts for the experimental data. Figures 7.12(a) and (b) thus show that the equilibrium magnetization orientation Θ rotates by 10° within the full voltage range $-30\,\mathrm{V} \leq V_\mathrm{p} \leq +150\,\mathrm{V}$. These observations corroborate the FMR results, which yielded a shift of the easy axes by 6° for $-30\,\mathrm{V} \leq V_\mathrm{p} \leq +90\,\mathrm{V}$ [Fig. 7.8(a)], in good agreement with the rotation of the magnetization orientation by 9° in this voltage range measured via SQUID magnetometry [Fig. 7.12(b)]. Thus, the SQUID measurements conclusively substantiate the notion that the present sample is not suitable for magnetization switching, since the induced strain in the sample only induces a rotation of the magnetization in the order of 10° and thus is too small to allow for a substantial magnetization switching effect.

We now turn to sample ⟨110⟩. The preparation field was in a first set of experiments applied along $\theta = 133°$ [Fig. 7.12(c)]. As the free energy density at this orientation continuously evolves from a deep minimum towards a shallow one

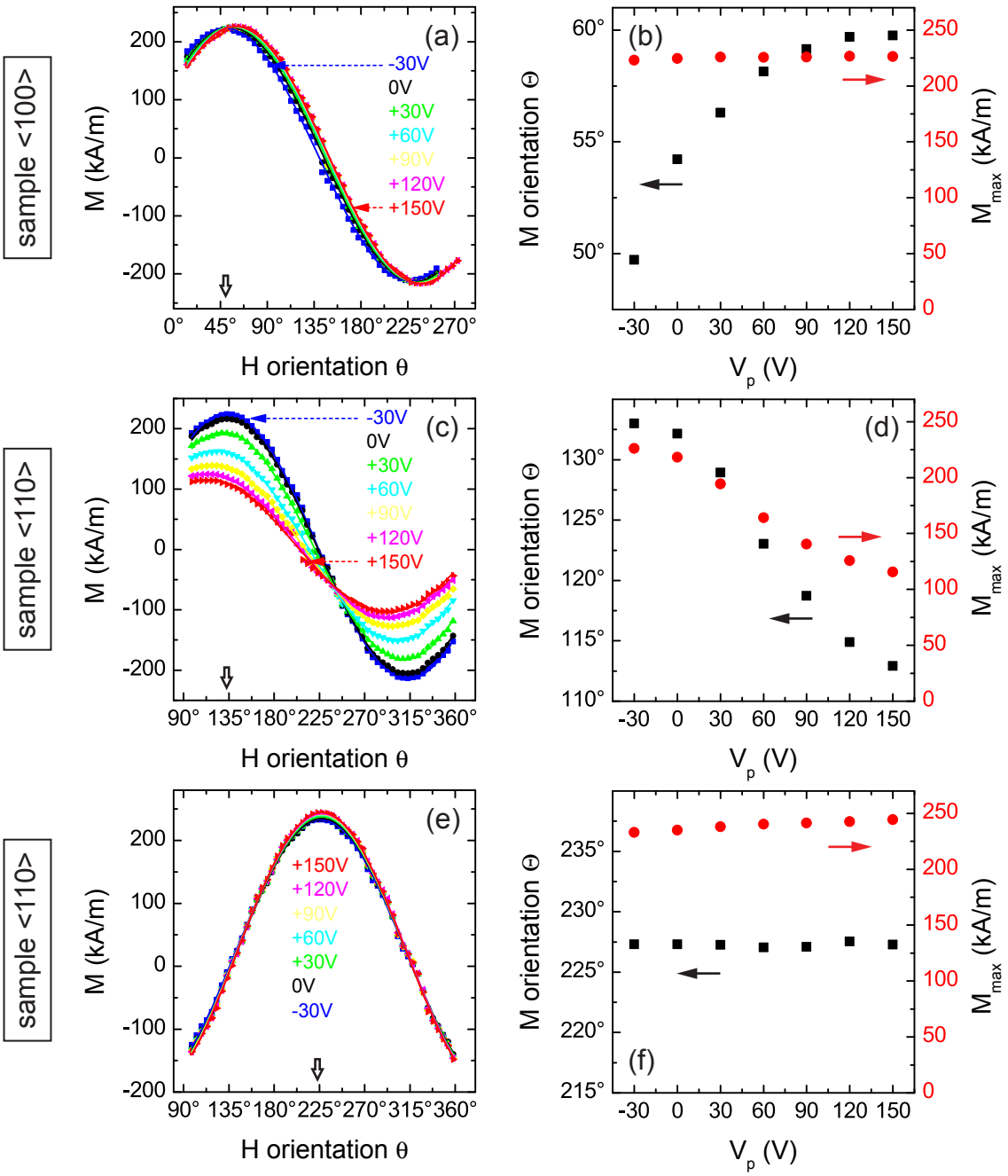

Figure 7.12: Angle-dependent SQUID measurements showing the magnetization projection M onto the SQUID measurement axis $\mathbf{H}$ as a function of θ at different voltages V_p. Prior to recording M, the sample was magnetized to a single-domain state, with the magnetic field oriented along the direction indicated by the open downward-oriented arrows. All measurements were carried out in zero magnetic field. The symbols represent the experimental data and the lines denote fits to cosine functions. The respective panels on the right show the macroscopic magnetization orientation Θ of the maximum of $M(\theta)$, and the corresponding magnitude M_max. (a), (b) Represent sample $\langle 100 \rangle$, (c), (d) sample $\langle 110 \rangle$ with the preparation field oriented along the local minimum and (e), (f) along the global minimum. A detailed discussion is given in the text.

(and eventually towards a maximum) with increasing V_p [cf. Fig. 7.11(b)], this minimum will be referred to as local minimum in the following. The subsequent angle-dependent SQUID measurements at constant V_p are evaluated in Fig. 7.12(d). These data show a qualitatively different behavior compared to the measurements on sample ⟨100⟩ depicted in Fig. 7.12(a), as both the magnitude M_max as well as the corresponding orientation Θ significantly change as a function of V_p. Upon increasing V_p from $-30\,\mathrm{V}$ to $+150\,\mathrm{V}$, M_max decreases by 49 % of its initial value, while the orientation of M_max rotates by 20° towards the free energy density minimum at 47° [cf. Fig. 7.11(b)]. Although the evolution of M can again be fitted with a cosine function, showing that the data are in excellent agreement with a macroscopic magnetization model, however, the reduction of M_max clearly evidences magnetic domain formation and a corresponding reduction of the net magnetization M_max with increasing V_p, as compared to the saturation magnetization. The sample uniformly magnetized after the magnetic preparation at $V_\mathrm{p} = -30\,\mathrm{V}$ remains in a single-domain state upon decreasing the magnetic preparation field, with the magnetization $\mathbf{M}$ finally residing in the minimum $\Theta = 133°$ at zero magnetic field [cf. free energy density contour for $V_\mathrm{p} = -30\,\mathrm{V}$ in Fig. 7.11(b)]. As the applied voltage V_p increases, the local energy density minimum at $\Theta = 133°$ looses depth and thus magnetically hardens, while the energy minima at $\Theta = 47°$ and 227°, referred to as global minima in the following, magnetically soften and therefore favor a domain formation [cf. Fig. 7.11(b)]. As apparent from Figs. 7.12(c) and (d), the orientation of decreasing M_max systematically shifts to lower angle with increasing V_p, indicating a magnetic domain state preferably oriented along the global minimum at $\Theta = 47°$ [Fig. 7.11(b)], in agreement with the orientation of the magnetic hard uniaxial axis K_u^ip detected by FMR measurements. Taken together, these experimental findings are clearly not consistent with a single-domain free energy density approach as it was used in Fig. 7.11(b).

To substantiate this interpretation, we repeated the angle-dependent SQUID measurements in a second set of experiments in sample ⟨110⟩, with the magnetic preparation field now applied along $\theta = 223°$, close to the free energy density minimum at $\Theta = 227°$ [cf. Fig. 7.11(b)]. As shown in Figs. 7.12(e) and (f), the angular dependence for varying applied voltages V_p coincides in good approximation. The magnetization $\mathbf{M}$ retains its orientation at $\Theta = 227°$ in the global energy density minimum independent of V_p, while the magnitude of the magnetization at this orientation M_max changes by only 5 % within the full voltage range. Considering the free energy density contours of Fig. 7.11(b), the energy barrier for domain formation is much larger in this case, such that the magnetization can still be modeled as a single domain in good approximation. Hence, the experiments in this configuration with a field preparation along the global minimum are in good agreement with the FMR results, i.e., Stoner-Wohlfarth type calculations.

Taken together, sample ⟨110⟩ does not show a uniform magnetization switching, however, the SQUID measurements provide clear evidence for a strain-induced switching of domains towards a global free energy density minimum. Thus, a voltage-controlled, nonvolatile magnetization switching is clearly a viable option, whose experimental realization will be further addressed in Chapter 8.

7.7 Summary

In summary, we have investigated the voltage-controlled manipulation of magnetic anisotropy and magnetization in crystalline Fe_3O_4 thin film/piezoelectric actuator hybrids, with particular emphasis on the experimental feasibility of a nonvolatile magnetization switching at room temperature. A coherent and nonvolatile magnetization switching in such hybrids can be realized via either a continuous or a discontinuous magnetization rotation. The possibility to induce strain along different directions in the film plane with respect to the crystallographic axes depending on cementing procedure, allows to investigate these switching concepts. We have discussed the qualitatively different switching behavior for two different configurations, namely strain exerted along the in-plane crystalline Fe_3O_4 $\langle 100 \rangle$ and along the in-plane $\langle 110 \rangle$ directions. These two concepts were experimentally studied using both FMR and SQUID magnetometry at room temperature. The magnetic anisotropy and thus the free energy density of the ferromagnetic thin films as a function of the applied voltage in a magnetically saturated state was determined by FMR spectroscopy. For stress applied along the $\langle 100 \rangle$ directions, we find that the voltage-controlled modifications of the magnetic anisotropy can be quantitatively modeled within magnetoelastic theory using FMR spectroscopy in combination with HR-XRD measurements. We observe a continuous and reversible rotation of the easy axes by 6°. In contrast, for strain induced along $\langle 110 \rangle$, our results show a significant modification of the relative strength of the magnetic easy axes. However, a true magnetization switching without magnetic domain formation appears impossible in any of the two investigated samples in vanishing external magnetic field. To verify these findings we directly measured the magnetization M as a function of the applied voltage in zero external magnetic field by employing SQUID magnetometry. The magnetometry experiments corroborate the FMR results for sample $\langle 100 \rangle$, while they show a decreased saturation magnetization with increasing voltage applied and thus a decay into domains with a considerable fraction of domains having switched towards a preferential orientation. This shows that inefficient strain transfer and magnetic domain formation are major obstacles towards a magnetization switching. Therefore, to overcome these experimental drawbacks, some additional measures have to be taken. We will address important steps towards the experimental realization of an all-electrically controlled, nonvolatile magnetization switching in the following chapter.

Chapter 8

Conclusions and outlook

In this thesis, we studied the realization of an all-electric field control of magnetization in ferromagnetic/ferroelectric hybrid systems by exploiting the spin-mechanics concept. This approach is based on utilizing an electric-field-controlled magnetoelastic coupling and thus a strain-mediated, indirect magnetoelectric coupling in these multifunctional hybrids. Hereby, we particularly focused on a control of the magnetization *orientation*, i.e., we studied the feasibility and limitations of a *macrospin* magnetization manipulation. More precisely, we systematically investigated the magnetic properties of ferromagnetic thin film/piezoelectric actuator hybrid systems. As ferromagnetic constituents we employed polycrystalline nickel, single-crystalline (Ga,Mn)As, and single-crystalline magnetite thin films. Since a detailed summary of our results has already been given at the end of each chapter, we here compile the more general aspects of this work.

In specific, we fabricated ferromagnetic thin film/piezoelectric actuator hybrid systems and investigated the strain-mediated voltage control of magnetization. We quantified the magnetic anisotropy as a function of the voltage V_p applied to the piezoelectric actuator both using ferromagnetic resonance spectroscopy and anisotropic magnetoresistance techniques. The evolution of the magnetization as a function of V_p was determined via superconducting quantum interference device (SQUID) magnetometry and magneto-optical Kerr effect (MOKE) spectroscopy. To this end, a MOKE setup has been built up and subsequently extended to allow for spatially resolved MOKE imaging in the framework of this thesis. Using x-ray diffraction (XRD), we also quantitatively studied elastic strain induced in hybrids by piezoelectric actuators.

Polycrystalline ferromagnetic thin film/piezoelectric actuator hybrids constitute an ideal model system to study large magnetoelastic coupling effects. In particular, due to the absence of competing net crystalline anisotropies it is possible to maximize the impact of strain-induced uniaxial anisotropies on the magnetization orientation changes as a function of the voltage V_p applied to the actuator. In polycrystalline Ni thin film/piezoelectric actuator hybrids, via FMR experiments we demonstrated a voltage-controlled inversion of the magnetic anisotropy in the film plane, i.e., a switching of the magnetic easy axes by 90° upon changing the polarity of V_p, as discussed in Chapter 5. We employed SQUID magnetometry to record the evolution of the magnetization orientation $\mathbf{M}\left(V_\mathrm{p}\right)$ as a function of V_p, and showed that the magnetization orientation can be rotated continuously and reversibly within up to 80° at zero external magnetic field at room temperature solely

by changing V_p. Larger magnetization orientation changes of up to 180° could be realized upon the application of an appropriate external magnetic field. However, the latter type of magnetization reorientations is denoted irreversible in the sense that the initial magnetization orientation cannot be restored by changing V_p alone. Furthermore, despite the magnetically isotropic film plane at $V_p = 0\,V$ we realized a nonvolatile and reversible all-electric field control of remanent magnetization, making use of the intrinsically hysteretic nature of the actuator's ferroelectric constituent. All M (V_p) data could be quantitatively understood within a single-domain (macrospin) Stoner-Wohlfarth type of approach. Spatially resolved magneto-optical imaging fully corroborated this conception, showing that the magnetization evolves continuously and coherently. The only exception is for the external magnetic field **H** oriented along a magnetically easy direction in a narrow region around the magnetic coercive field. In this case, the magnetization reorients via domain nucleation and propagation. Therefore, on length scales much larger than the typical magnetic domain size, the voltage control of magnetization can be consistently described in terms of a simple Stoner-Wohlfarth type macrospin model.

Since the magnetocrystalline anisotropy of the dilute magnetic semiconductor (Ga,Mn)As substantially changes as a function of temperature, (Ga,Mn)As thin film/piezoelectric actuator hybrids are an ideal model system to study the interplay between magnetocrystalline and magnetoelastic anisotropy contributions (Chapter 6). Furthermore, (Ga,Mn)As exhibits large magnetic domains, which thus allows for a comprehensive interpretation of its magnetic properties in terms of a macrospin (single-domain) approach. We investigated the magnetic anisotropy in (Ga,Mn)As/piezoelectric actuator hybrids as a function of temperature using anisotropic magnetoresistance techniques. At $T = 50\,K$, where the magnetoelastic anisotropy contribution prevails, the magnetization orientation can be rotated continuously and reversibly within up to 70°, solely via application of appropriate voltages V_p. Moreover, the cubic magnetocrystalline anisotropy of (Ga,Mn)As enables nonvolatile magnetization reorientations. Hereby, we exemplarily demonstrated an irreversible and nonvolatile voltage-controlled switching of magnetization orientation at 40 K by 180° upon the application of an external magnetic field strength below the magnetic coercive field.

A key requirement for spintronic device applications is a nonvolatile and reversible all-electric-field control of remanent magnetization at room temperature, i.e., the feasibility to deterministically select one of several distinct magnetization orientation states in single-crystalline ferromagnets, which are retained at zero magnetic and electric fields and allow for a switching solely via the application of electric fields. In this regard, we discussed two different approaches in Chapter 7 to experimentally realize a nonvolatile, all-voltage-controlled magnetization switching at room temperature in the absence of magnetic fields and presented fundamental experiments towards this goal. To this end, we employed Fe_3O_4 ferromagnetic thin film/piezoelectric actuator hybrids, with strain induced along the in-plane ⟨100⟩ or ⟨110⟩ cubic axes. We again used FMR spectroscopy to determine the free energy density F. The free energy density then allows to infer the equilibrium magnetization orientation in a single-domain Stoner-Wohlfarth model, which yields a continuous

rotation of the magnetic easy axes and a significant modification of the relative strength of the easy axes, respectively. However, in combination with SQUID magnetometry measurements we found that the angle of **M** orientation rotation is not large enough to induce a magnetization switching in the former, and magnetic domain formation impedes a coherent magnetization switching in the latter approach, which thus represent major obstacles.

Overall, optimizing the ratio of the magnetoelastic and magnetocrystalline anisotropy contributions is thus a crucial challenge. To summarize, the key requirements for strain-controlled magnetic memory elements are (i) a Curie temperature well above room temperature, (ii) a high magnetostriction, (iii) a small cubic anisotropy (however, thermal stability required for, e.g., 10 years data retention is obtained when $\Delta E \gtrsim 65 k_\mathrm{B} T$, where ΔE is the energy barrier between two stable magnetic configurations [14, 342]), and (iv) a large domain-wall formation energy.

To overcome the issues just mentioned, we therefore address practicable engineering concepts in the outlook and demonstrate that a voltage-controlled, nonvolatile magnetization switching is a viable and versatile scheme for spintronic devices. More precisely, in the following we present simulations, showing that skillful alignment of the strain within the films should enable a magnetization switching at lower strain and impede magnetic domain formation.

Outlook

The experimental results discussed in Chapter 7 show that an alignment of the strain axes along crystallographic axes favor magnetic domain formation. Therefore we now discuss configurations with an angle $\gamma \notin \{0°, 45°\}$ enclosed by the crystallographic axes of the film and the elongation axes of the actuator.

The corresponding concept is illustrated for $\gamma = 20°$ in Fig. 8.1. The curves are calculated using the total free energy density in the film plane

$$\begin{aligned} F &= F_\mathrm{Zeeman} + F_\mathrm{c} + F_\mathrm{magel} \\ &= -\mu_0 H M \left(\sin\Theta \sin\Phi \sin\theta \sin\phi + \cos\Theta \cos\theta + \sin\Theta \cos\Phi \sin\theta \cos\phi\right) \\ &\quad + \frac{1}{4} K_\mathrm{c} \left[\sin^2(2\Theta) + \sin^4\Theta \sin^2(2\Phi)\right] + F_\mathrm{magel}(\epsilon_2'), \end{aligned} \tag{8.1}$$

with the magnetoelastic free energy density contribution and the strain components given in Eqs. (2.13) and (3.14), respectively. For the free energy density curves shown in Figs. 8.1(a) and (b) we used a ratio of the magnetoelastic and magnetocrystalline anisotropy contributions of $|B_1\epsilon_2'/K_\mathrm{c}| = |B_2\epsilon_2'/K_\mathrm{c}| \leq 0.35$. Note that in the present case ($\gamma \notin \{0°, 45°\}$), the orientation of the elongation axes already breaks the symmetry, so the superposition of an additional uniaxial axis [Eq. (7.1)] is not mandatory to impede magnetic domain formation. Thus we adopt a pure cubic anisotropy at $V_\mathrm{p} = 0\,\mathrm{V}$ [black lines in Figs. 8.1(a), (b)], assume zero external magnetic field and an initial magnetization orientation along $\Theta = 135°$ [point A in Fig. 8.1(a)]. Upon inducing a strain $\epsilon_2' > 0$ in the film, the easy axis first coherently rotates, until it switches discontinuously and coherently to B at a certain critical

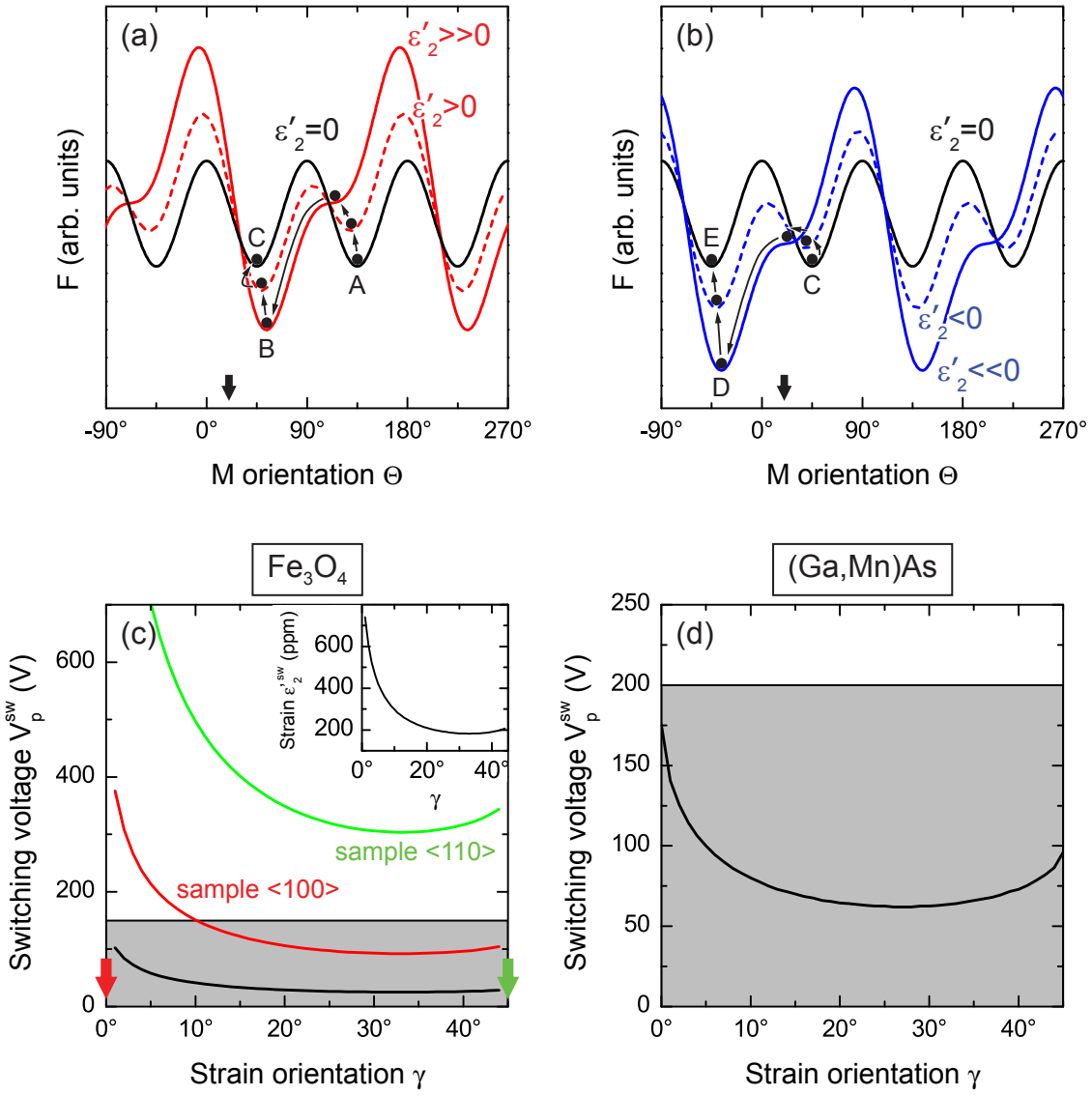

Figure 8.1: Schematic picture for all-voltage controlled magnetization switching. (a), (b) Calculated free energy density contours as a function of the magnetization orientation Θ in the film plane for $\gamma = 20°$ (marked by the downward-oriented arrows), with a first discontinuous, coherent, and nonvolatile magnetization switching process (A→B→C) upon $\epsilon_2' > 0$ and a second one (C→D→E) along the same direction of rotation for $\epsilon_2' < 0$. (c) Calculated switching voltage $V_\mathrm{p}^\mathrm{sw}(\gamma)$ as a function of the strain orientation γ for Fe_3O_4. The curves represent simulations for different strain transmission efficiencies. The black curve depicts perfect strain transmission, the red and green curves represent the experimentally realized strains in the sample $\langle 100\rangle$ and sample $\langle 110\rangle$, respectively (cf. Chapter 7; the downward-oriented arrows denote the samples' respective dominant elongation orientation). The gray-shaded area indicates the experimentally accessible region, and the inset depicts the effective switching strain $\epsilon_2'^\mathrm{sw}(\gamma)$. (d) Analogous calculations for (Ga,Mn)As. The curve is calculated with the experimental parameters obtained at $40\,\mathrm{K} \lesssim T \lesssim 50\,\mathrm{K}$. The $V_\mathrm{p}^\mathrm{sw}(\gamma)$ curve displayed in the panel is experimentally fully accessable ($|V_\mathrm{p}| \leq 200\,\mathrm{V}$ at $T \approx 50\,\mathrm{K}$).

strain. When the strain is reduced back to 0, the easy axis rotates to C at $\Theta = 45°$. Upon subsequently increasing the strain $\epsilon_2' < 0$ with opposite sign, the situation appears qualitatively different from the situations illustrated in Fig. 7.2, as we do not observe a back switching to the initial orientation A, but a further switching process along the original direction of rotation via D to point E at $\Theta = -45°$ [Fig. 8.1(b)]. Hence, iteratively applying strain with alternating sign provides a concept to discontinuously rotate the equilibrium magnetization orientation via nonvolatile switching processes [308]. Such magnetization switching processes are "quasi-reversible", since four consecutive switching processes (in a ferromagnet with cubic symmetry) evidently restore the initial magnetization orientation state. Hence, this constitutes a very elegant voltage-control scheme of magnetization orientation.

We now discuss the dependence of the switching voltage V_p^sw on the strain orientation γ both for Fe_3O_4 and for (Ga,Mn)As. We start with the calculations for Fe_3O_4 [Fig. 8.1(c)]. Hereby, $V_\mathrm{p}^\mathrm{sw}(\gamma)$ and $\epsilon_2'^\mathrm{sw}(\gamma)$ denote the switching voltage and the switching strain [inset of Fig. 8.1(c)] upon which a coherent and discontinuous switching process occurs due to the appearance of an inflection point in the free energy density contour [cf. Figs. 8.1(a), (b)]. The solid black lines in Fig. 8.1(c) and its inset are calculated assuming perfect strain transmission, i.e., $\epsilon_2' = 1.3 \times 10^{-3}$ in the full voltage range of the piezoelectric actuator $-30\,\mathrm{V} \leq V_\mathrm{p} \leq +150\,\mathrm{V}$ at room temperature. The curves are calculated using the total free energy density given in Eq. (8.1), with the cubic anisotropy field $K_\mathrm{c}/M = -14.7\,\mathrm{mT}$ taken as the averaged value corresponding to the two samples investigated in Chapter 7. Evidently, the voltage V_p^sw required to induce a magnetization switching process significantly decreases with increasing angle γ, exhibits a minimum at $\gamma = 33°$, and finally slightly increases with γ approaching 45°. Overall, V_p^sw can have comparatively moderate values lower than $\approx 100\,\mathrm{V}$ for our hybrids, suggesting that a purely voltage-controlled, nonvolatile switching of $\mathbf{M}$ should be experimentally feasible, since $V_\mathrm{p}^\mathrm{sw}(\gamma) \lesssim 150\,\mathrm{V}$ is experimentally accessible (depicted by the gray-shaded area) in the whole angular range. However, the feasibility of a magnetization switching crucially depends on the transformation efficiency of the applied stress into the strain induced in the thin film across the actuator-sample interface. As apparent from Fig. 7.11(c), the effective strains $\epsilon_{2,\mathrm{eff}}'$ induced in the samples investigated in this thesis are significantly different, as the strain in sample $\langle 110 \rangle$ amounts to only about 30 % of the one induced in sample $\langle 100 \rangle$ in the voltage range $-30\,\mathrm{V} \leq V_\mathrm{p} \leq +90\,\mathrm{V}$. We attribute this to variations in the strain transmission efficiency of the cement, and possibly also to reduced substrate thicknesses. This behavior is reflected in the calculated switching voltage V_p^sw as a function of γ [Fig. 8.1(c)]. The strain transmission experimentally achieved in sample $\langle 100 \rangle$ ($\gamma = 0°$) suggests that a magnetization switching should be possible for $\gamma \gtrsim 10°$ [solid red line in Fig. 8.1(c)], while a magnetization switching is impossible for all experimental realizations for the strain transmission efficiency of sample $\langle 110 \rangle$ [solid green line in Fig. 8.1(c)]. To conclude our findings, the configuration with $\gamma = 33°$ is most suitable to promote magnetization switching in our Fe_3O_4 thin films, as it requires comparatively lowest strain $\epsilon_2'^\mathrm{sw}$ induced in the film and inherently introduces a symmetry-break, which impedes magnetic domain formation. To furthermore lower the switching

strain $\epsilon_2'^{\mathrm{sw}}$, the properties of the ferromagnetic film itself must be fine-tuned, as $\epsilon_2'^{\mathrm{sw}}$ linearly depends on the cubic anisotropy constant K_c and inversely depends on the magnetostriction constants λ_{100} and λ_{111}. Most promising candidates regarding the realization of a magnetization switching therefore evidently are materials with a small cubic anisotropy and high magnetostriction constants.

For this reason, (Ga,Mn)As thin film/piezoelectric actuator hybrids again appear as an ideal model system to study such a "rotatable" nonvolatile magnetization switching due to the well-tunable ratio of the magnetoelastic and magnetocrystalline anisotropy contributions in (Ga,Mn)As thin films. Analogous calculations for (Ga,Mn)As are shown in Fig. 8.1(d), with the corresponding total free energy density given in Eq. (8.1). To maximize the influence of the magnetoelastic anisotropy contribution we refer to the temperature range $40\,\mathrm{K} \lesssim T \lesssim 50\,\mathrm{K}$ [cf. Figs. 6.3(a), (b)]. The solid black line in Fig. 8.1(d) is calculated using $K_\mathrm{c}/M = +5\,\mathrm{mT}$ [Fig. 6.3(b)], a maximum achievable strain $\epsilon_2' = 0.4 \times 10^{-3}$ in the full voltage range $-200\,\mathrm{V} \leq V_\mathrm{p} \leq +200\,\mathrm{V}$ of the piezoelectric actuator at lower temperatures (Fig. 6.2), and a saturation magnetization $M = 10\,\mathrm{kA/m}$ [Fig. 6.13(a)]. We furthermore employ an isotropic magnetostriction constant $\lambda = -2 \times 10^{-6}$. This assumption is reasonable, since (i) λ_{111} experimentally determined amounts to $\approx -2 \times 10^{-6}$ in the currently regarded temperature range [Fig. 6.13(b)], and (ii) we independently deduced $\lambda_{100} \approx -3 \times 10^{-6}$ [285]. The corresponding $V_\mathrm{p}^{\mathrm{sw}}(\gamma)$ curve shown in Fig. 8.1(d) is experimentally fully accessible ($|V_\mathrm{p}| \leq 200\,\mathrm{V}$ at $T \approx 50\,\mathrm{K}$). Therefore, our simulations based on the quantitative information on material properties obtained in this thesis suggest that a voltage-controlled, nonvolatile magnetization switching should be possible.

The all-electrical magnetization switching is only one of the key challenges in multifunctional hybrid research. Within the last few years, multifunctional magnetoelectric composite thin films have attracted an ever-increasing interest, which thus triggered a rapid development of research activities. However, many fundamental, important issues remain to be solved. In the following, we highlight some of them.

A precise control of the domain structures in multifunctional hybrid systems is essential for device applications [42]. Particularly, ferromagnetic domain-wall engineering offers interesting application potential for nonvolatile, fast, and low-power consuming memory devices [343].

The dynamics of magnetoelectric coupling is an important issue [42]. Of particular interest hereby is the timescale of the electric (magnetic) field-induced magnetization (polarization) switching process. First, fundamental studies addressing this issue are presented in Refs. [62, 244, 246, 344]. A further important issue is the time-dependent ferromagnetic (ferroelectric) domain evolution as a function of external electric (magnetic) field.

A further question we here address refers to size effects of the magnetoelectric response [42], i.e., whether there exist any critical dimensions in micro- or nanostructures below which magnetoelectric coupling effects might vanish or undergo fundamental changes. A conceptual elementary device structure for the investigation of such issues is presented in Fig. 8.2. The device consists of a ferromagnetic Hall bar [patterned from, e.g., (Ga,Mn)As thin films], which is in a central, locally

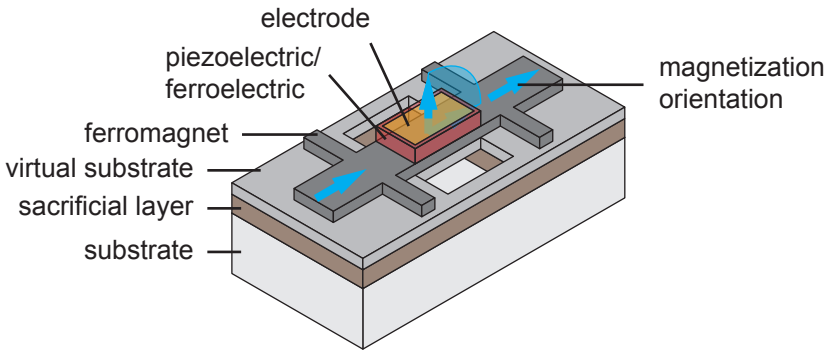

Figure 8.2: Sketch of a thin film ferromagnetic/ferroelectric free-standing hybrid structure (from Ref. [257]). Details of the device are given in the text.

confined area intimately connected to a piezoelectric or ferroelectric material. The ferromagnetic film is deposited on a virtual substrate [e.g., (Ga,In)As], which allows for a pseudomorphic growth of the ferromagnetic thin film and thus for a strain-engineering of its as-grown magnetic anisotropy (e.g., to reduce the strong uniaxial anisotropy in growth direction). However, such device structures suffer from the drawback that strain-mediated magnetoelectric coupling is significantly reduced or even suppressed due to the clamping effect of the rigid substrate [20, 47, 345]. To reduce mechanical clamping effects and thus to maximize magnetoelastic coupling effects, the multifunctionally active part is free-standing by removing a subjacent sacrificial layer (e.g., AlAs) via etching techniques. The piezo- or ferroelectric material can be deposited by, e.g., either hydrothermal methods (e.g., PZT [346]) or spin-coating of organic ferroelectrics [e.g., poly(vinylidene fluoride/trifluoroethylene) [347]]. Tuning of the lateral dimensions of the central part allows to investigate magnetoelectric coupling effects on different length scales. Tuning of the ferromagnetic thin film thickness allows to study different magnetoelectric coupling effects: direct electric-field effects can be studied for very thin films ([82], see Sec. 1.2), while strain-mediated, magnetoelastic coupling effects prevail for thicker films.

Finally, elastic strain is relevant also in the emerging field of spin caloritronics [348–350]. Very recently, the spin Seebeck effect, i.e., the spin analogue of the conventional "charge" Seebeck effect, has been attributed to the coupling of spins and phonons [351]. This coupling has been demonstrated by directly injecting a sound wave into a ferromagnet/Pt bilayer, and detecting the so-called acoustic spin pumping signal in the Pt film [351]. These first results of acoustic spin-current generation may pave the way to "acoustic spintronics", offering novel spin-based device concepts.

List of publications

- A. Brandlmaier, S. Geprägs, M. S. Brandt, R. Gross, and S. T. B. Goennenwein, *Towards voltage-controlled nonvolatile magnetization switching*, in preparation for publication.

- A. Brandlmaier, M. Brasse, S. Geprägs, M. Weiler, R. Gross, and S. T. B. Goennenwein, *Magneto-optical imaging of voltage-controlled magnetization reorientation*, submitted for publication (2011).

12. A. Brandlmaier, S. Geprägs, G. Woltersdorf, R. Gross, and S. T. B. Goennenwein, *Nonvolatile, reversible electric-field controlled switching of remanent magnetization in multifunctional ferromagnetic/ferroelectric hybrids*, Journal of Applied Physics **110**, 043913 (2011).

11. M. Weiler, F. D. Czeschka, A. Brandlmaier, I.-M. Imort, G. Reiss, A. Thomas, G. Woltersdorf, R. Gross, and S. T. B. Goennenwein, *Magnetic microstructure and magnetotransport in Co_2FeAl Heusler compound thin films*, Applied Physics Letters **98**, 042501 (2011).

10. L. Dreher, T. A. Hilker, A. Brandlmaier, S. T. B. Goennenwein, H. Huebl, M. Stutzmann, and M. S. Brandt, *Electroelastic Hyperfine Tuning of Phosphorus Donors in Silicon*, Physical Review Letters **106**, 037601 (2011).

9. M. Opel, S. Geprägs, E. P. Menzel, A. Nielsen, D. Reisinger, K.-W. Nielsen, A. Brandlmaier, F. D. Czeschka, M. Althammer, M. Weiler, S. T. B. Goennenwein, J. Simon, M. Svete, W. Yu, S.-M. Hühne, W. Mader, and R. Gross, *Novel multifunctional materials based on oxide thin films and artificial heteroepitaxial multilayers*, Physica Status Solidi A **208**, 232 (2011).

8. S. Geprägs, A. Brandlmaier, M. Opel, R. Gross, and S. T. B. Goennenwein, *Electric field controlled manipulation of the magnetization in $Ni/BaTiO_3$ hybrid structures*, Applied Physics Letters **96**, 142509 (2010).

7. M. Glunk, J. Daeubler, L. Dreher, S. Schwaiger, W. Schoch, R. Sauer, W. Limmer, A. Brandlmaier, S. T. B. Goennenwein, C. Bihler, and M. S. Brandt, *Magnetic anisotropy in (Ga,Mn)As: Influence of epitaxial strain and hole concentration*, Physical Review B **79**, 195206 (2009).

6. M. Weiler, A. Brandlmaier, S. Geprägs, M. Althammer, M. Opel, C. Bihler, H. Huebl, M. S. Brandt, R. Gross, and S. T. B. Goennenwein, *Voltage controlled inversion of magnetic anisotropy in a ferromagnetic thin film at room temperature*, New Journal of Physics **11**, 013021 (2009).

5. A. Nielsen, A. Brandlmaier, M. Althammer, W. Kaiser, M. Opel, J. Simon, W. Mader, S. T. B. Goennenwein, and R. Gross, *All oxide ferromagnet/ semiconductor epitaxial heterostructures*, Applied Physics Letters **93**, 162510 (2008).

4. C. Bihler, M. Althammer, A. Brandlmaier, S. Geprägs, M. Weiler, M. Opel, W. Schoch, W. Limmer, R. Gross, M. S. Brandt, and S. T. B. Goennenwein, *$Ga_{1-x}Mn_xAs$/piezoelectric actuator hybrids: A model system for magnetoelastic magnetization manipulation*, Physical Review B **78**, 045203 (2008).

3. A. Brandlmaier, S. Geprägs, M. Weiler, A. Boger, M. Opel, H. Huebl, C. Bihler, M. S. Brandt, B. Botters, D. Grundler, R. Gross, and S. T. B. Goennenwein, *In situ manipulation of magnetic anisotropy in magnetite thin films*, Physical Review B **77**, 104445 (2008).

2. S. T. B. Goennenwein, M. Althammer, C. Bihler, A. Brandlmaier, S. Geprägs, M. Opel, W. Schoch, W. Limmer, R. Gross, and M. S. Brandt, *Piezo-voltage control of magnetization orientation in a ferromagnetic semiconductor*, Physica Status Solidi (RRL) **2**, 96 (2008).

1. S. T. B. Goennenwein, S. W. Schink, A. Brandlmaier, A. Boger, M. Opel, R. Gross, R. S. Keizer, T. M. Klapwijk, A. Gupta, H. Huebl, C. Bihler, and M. S. Brandt, *Electrically detected ferromagnetic resonance*, Applied Physics Letters **90**, 162507 (2007).

Acknowledgements

I would like to thank all the people who contributed to this work and supported me during my Ph.D. time, in particular:

- Prof. Dr. Rudolf Gross for giving me the opportunity to work in the WMI's 'Magnetiker' group and his very kind support. He gave me the freedom to follow my research interests, while his deep scientific insight and many fruitful discussions were always helpful.
- Dr. habil. Sebastian T. B. Gönnenwein for his excellent supervision and overall support. I particularly thank him for all the scientific discussions, for his motivation and guidance, and for providing me with numerous stimuli and ideas. He always had his door open and provided help whenever needed.
- Stephan Geprägs for all the uncountable hours spent discussing physics and non-physics, for sharing his experimental skills and his profound knowledge on all available measurement setups. I am grateful for his enormous support and for the fun we had.
- Dr. Matthias Opel for his kind help and support, especially regarding all types of computer problems, and for always taking care of a good atmosphere in the group.
- All the diploma students (in order of appearance): Mathias Weiler, Matthias Althammer, Matthias Pelkner, Matthias Brasse, and Michael Wagner for their substantial contributions to this work during their diploma theses. It was a great pleasure to work with you.
- Prof. Dr. Martin S. Brandt for generously assigning me measurement time in his ESR lab, for all the useful discussions in the Walt(h)er seminar, and for his profound pool of enjoyable stories.
- Dr. Hans Hübl and Dr. Christoph Bihler for numerous discussions on ferromagnetic resonance, magnetic anisotropy, and all frequency-related issues.
- Konrad Klein, Lukas Dreher, and Felix Höhne for the good atmosphere and for their helping hands in the ESR lab.
- Dr. Wolfgang Limmer, Dr. Wladimir Schoch, and Michael Glunk for the growth of the (Ga,Mn)As samples and many fruitful discussions.
- Dr. Georg Woltersdorf for his very helpful support regarding the magneto-optical Kerr effect and for the growth of the GMR samples.

- Thomas Brenninger for his continuous professional support on all technical issues and for the small breaks in between which I enjoyed a lot.

- The WMI workshop staff, in particular Robert Müller and Helmut Thies, for doing an outstanding job in fabricating numerous components and setups.

- All my fellow 'Magnetiker' Ph.D. colleagues, in particular Matthias Althammer, Franz Czeschka, Stephan Geprägs, and Mathias Weiler, and last but not least Thomas Niemczyk from the qubit group, for sharing a great time and many laughs at the WMI.

- All the current office mates: Prof. Dr. B. S. Chandrasekhar, Hans-Martin Eiter, Stephan Geprägs, and Florian Kretzschmar for the great atmosphere and all the fun we had.

- The whole WMI staff for the great support and the friendly working atmosphere.

- Meltem for everything beyond physics, especially for her continuous encouragement, patience, and understanding.

- My parents for their unlimited support in every imaginable aspect.

Bibliography

[1] M. N. Baibich, J. M. Broto, A. Fert, F. N. V. Dau, F. Petroff, P. Etienne, G. Creuzet, A. Friederich, and J. Chazelas, Phys. Rev. Lett. **61**, 2472 (1988).

[2] G. Binasch, P. Grünberg, F. Saurenbach, and W. Zinn, Phys. Rev. B **39**, 4828 (1989).

[3] G. A. Prinz, Science **282**, 1660 (1998).

[4] M. Ziese, Philos. Trans. R. Soc. London, Ser. A **358**, 137 (2000).

[5] S. A. Wolf, D. D. Awschalom, R. A. Buhrman, J. M. Daughton, S. von Molnár, M. L. Roukes, A. Y. Chtchelkanova, and D. M. Treger, Science **294**, 1488 (2001).

[6] I. Žutić, J. Fabian, and S. Das Sarma, Rev. Mod. Phys. **76**, 323 (2004).

[7] T. Dietl and H. Ohno, Mater. Today **9**, 18 (2006).

[8] S. M. Thompson, J. Phys. D: Appl. Phys. **41**, 093001 (2008).

[9] M. Julliere, Phys. Lett. A **54**, 225 (1975).

[10] B. Dieny, V. S. Speriosu, S. S. P. Parkin, B. A. Gurney, D. R. Wilhoit, and D. Mauri, Phys. Rev. B **43**, 1297 (1991).

[11] J. S. Moodera, L. R. Kinder, T. M. Wong, and R. Meservey, Phys. Rev. Lett. **74**, 3273 (1995).

[12] G. A. Prinz, J. Magn. Magn. Mater. **200**, 57 (1999).

[13] S. Parkin, X. Jiang, C. Kaiser, A. Panchula, K. Roche, and M. Samant, Proc. IEEE **91**, 661 (2003).

[14] C. Chappert, A. Fert, and F. N. V. Dau, Nat. Mater. **6**, 813 (2007).

[15] S. Ikeda, J. Hayakawa, Y. M. Lee, F. Matsukura, Y. Ohno, T. Hanyu, and H. Ohno, IEEE Trans. Electron Devices **54**, 991 (2007).

[16] J.-G. Zhu, Proc. IEEE **96**, 1786 (2008).

[17] A. Ney, C. Pampuch, R. Koch, and K. H. Ploog, Nature **425**, 485 (2003).

[18] N. A. Spaldin and M. Fiebig, Science **309**, 391 (2005).

[19] W. Eerenstein, N. D. Mathur, and J. F. Scott, Nature **442**, 759 (2006).

[20] R. Ramesh and N. A. Spaldin, Nat. Mater. **6**, 21 (2007).

[21] H. Béa, M. Gajek, M. Bibes, and A. Barthélémy, J. Phys.: Condens. Matter **20**, 434221 (2008).

[22] H. Schmid, Ferroelectrics **162**, 317 (1994).

[23] N. A. Spaldin, S.-W. Cheong, and R. Ramesh, Phys. Today **63**, 38 (2010).

[24] M. Fiebig, J. Phys. D: Appl. Phys. **38**, R123 (2005).

[25] Y.-H. Chu, L. W. Martin, M. B. Holcomb, and R. Ramesh, Mater. Today **10**, 16 (2007).

[26] L. W. Martin, S. P. Crane, Y.-H. Chu, M. B. Holcomb, M. Gajek, M. Huijben, C.-H. Yang, N. Balke, and R. Ramesh, J. Phys.: Condens. Matter **20**, 434220 (2008).

[27] J. M. Rondinelli, M. Stengel, and N. A. Spaldin, Nat. Nanotechnol. **3**, 46 (2008).

[28] C. A. F. Vaz, J. Hoffman, C. H. Ahn, and R. Ramesh, Adv. Mater. **22**, 2900 (2010).

[29] M. Fiebig, T. Lottermoser, D. Fröhlich, A. V. Goltsev, and R. V. Pisarev, Nature **419**, 818 (2002).

[30] T. Lottermoser, T. Lonkai, U. Amann, D. Hohlwein, J. Ihringer, and M. Fiebig, Nature **430**, 541 (2004).

[31] T. Zhao, A. Scholl, F. Zavaliche, K. Lee, M. Barry, A. Doran, M. P. Cruz, Y. H. Chu, C. Ederer, N. A. Spaldin, R. R. Das, D. M. Kim, S. H. Baek, C. B. Eom, and R. Ramesh, Nat. Mater. **5**, 823 (2006).

[32] M. Gajek, M. Bibes, S. Fusil, K. Bouzehouane, J. Fontcuberta, A. Barthélémy, and A. Fert, Nat. Mater. **6**, 296 (2007).

[33] N. Mathur, Nature **454**, 591 (2008).

[34] A. Kingon, Nature **401**, 658 (1999).

[35] J. F. Scott, Science **315**, 954 (2007).

[36] X. Chen, A. Hochstrat, P. Borisov, and W. Kleemann, Appl. Phys. Lett. **89**, 202508 (2006).

[37] J. F. Scott, Nat. Mater. **6**, 256 (2007).

[38] M. Bibes and A. Barthélémy, Nat. Mater. **7**, 425 (2008).

[39] W. F. Brown, R. M. Hornreich, and S. Shtrikman, Phys. Rev. **168**, 574 (1968).

[40] N. A. Hill, J. Phys. Chem. B **104**, 6694 (2000).

[41] W. Eerenstein, M. Wiora, J. L. Prieto, J. F. Scott, and N. D. Mathur, Nat. Mater. **6**, 348 (2007).

[42] J. Ma, J. Hu, Z. Li, and C.-W. Nan, Adv. Mater. **23**, 1062 (2011).

[43] C.-W. Nan, M. I. Bichurin, S. Dong, D. Viehland, and G. Srinivasan, J. Appl. Phys. **103**, 031101 (2008).

[44] J. Zhai, Z. Xing, S. Dong, J. Li, and D. Viehland, J. Am. Ceram. Soc. **91**, 351 (2008).

[45] S. Priya, R. Islam, S. Dong, and D. Viehland, J. Electroceram. **19**, 147 (2007).

[46] G. Srinivasan, Ann. Rev. Mater. Res. **40**, 153 (2010).

[47] H. Zheng, J. Wang, S. E. Lofland, Z. Ma, L. Mohaddes-Ardabili, T. Zhao, L. Salamanca-Riba, S. R. Shinde, S. B. Ogale, F. Bai, D. Viehland, Y. Jia, D. G. Schlom, M. Wuttig, A. Roytburd, and R. Ramesh, Science **303**, 661 (2004).

[48] F. Zavaliche, H. Zheng, L. Mohaddes-Ardabili, S. Y. Yang, Q. Zhan, P. Shafer, E. Reilly, R. Chopdekar, Y. Jia, P. Wright, D. G. Schlom, Y. Suzuki, and R. Ramesh, Nano Lett. **5**, 1793 (2005).

[49] F. Zavaliche, T. Zhao, H. Zheng, F. Straub, M. P. Cruz, P.-L. Yang, D. Hao, and R. Ramesh, Nano Lett. **7**, 1586 (2007).

[50] M. K. Lee, T. K. Nath, C. B. Eom, M. C. Smoak, and F. Tsui, Appl. Phys. Lett. **77**, 3547 (2000).

[51] D. Dale, A. Fleet, J. D. Brock, and Y. Suzuki, Appl. Phys. Lett. **82**, 3725 (2003).

[52] R. V. Chopdekar and Y. Suzuki, Appl. Phys. Lett. **89**, 182506 (2006).

[53] S. Sahoo, S. Polisetty, C.-G. Duan, S. S. Jaswal, E. Y. Tsymbal, and C. Binek, Phys. Rev. B **76**, 092108 (2007).

[54] H. F. Tian, T. L. Qu, L. B. Luo, J. J. Yang, S. M. Guo, H. Y. Zhang, Y. G. Zhao, and J. Q. Li, Appl. Phys. Lett. **92**, 063507 (2008).

[55] F. D. Czeschka, S. Geprägs, M. Opel, S. T. B. Goennenwein, and R. Gross, Appl. Phys. Lett. **95**, 062508 (2009).

[56] C. A. F. Vaz, J. Hoffman, A.-B. Posadas, and C. H. Ahn, Appl. Phys. Lett. **94**, 022504 (2009).

[57] C. Israel, N. D. Mathur, and J. F. Scott, Nat. Mater. **7**, 93 (2008).

[58] C. Israel, S. Kar-Narayan, and N. D. Mathur, Appl. Phys. Lett. **93**, 173501 (2008).

[59] C. Thiele, K. Dörr, O. Bilani, J. Rödel, and L. Schultz, Phys. Rev. B **75**, 054408 (2007).

[60] Y. Chen, J. Wang, M. Liu, J. Lou, N. X. Sun, C. Vittoria, and V. G. Harris, Appl. Phys. Lett. **93**, 112502 (2008).

[61] M. Liu, O. Obi, J. Lou, Y. Chen, Z. Cai, S. Stoute, M. Espanol, M. Lew, X. Situ, K. S. Ziemer, V. G. Harris, and N. X. Sun, Adv. Funct. Mater. **19**, 1826 (2009).

[62] Y. Chen, T. Fitchorov, C. Vittoria, and V. G. Harris, Appl. Phys. Lett. **97**, 052502 (2010).

[63] S.-K. Kim, J.-W. Lee, S.-C. Shin, H. W. Song, C. H. Lee, and K. No, J. Magn. Magn. Mater. **267**, 127 (2003).

[64] J.-W. Lee, S.-C. Shin, and S.-K. Kim, Appl. Phys. Lett. **82**, 2458 (2003).

[65] H. Boukari, C. Cavaco, W. Eyckmans, L. Lagae, and G. Borghs, J. Appl. Phys. **101**, 054903 (2007).

[66] Y. Chen, J. Gao, T. Fitchorov, Z. Cai, K. S. Ziemer, C. Vittoria, and V. G. Harris, Appl. Phys. Lett. **94**, 082504 (2009).

[67] V. Novosad, Y. Otani, A. Ohsawa, S. G. Kim, K. Fukamichi, J. Koike, K. Maruyama, O. Kitakami, and Y. Shimada, J. Appl. Phys. **87**, 6400 (2000).

[68] T. Brintlinger, S.-H. Lim, K. H. Baloch, P. Alexander, Y. Qi, J. Barry, J. Melngailis, L. Salamanca-Riba, I. Takeuchi, and J. Cumings, Nano Lett. **10**, 1219 (2010).

[69] M. Shayegan, K. Karrai, Y. P. Shkolnikov, K. Vakili, E. P. D. Poortere, and S. Manus, Appl. Phys. Lett. **83**, 5235 (2003).

[70] B. Botters, F. Giesen, J. Podbielski, P. Bach, G. Schmidt, L. W. Molenkamp, and D. Grundler, Appl. Phys. Lett. **89**, 242505 (2006).

[71] W. H. Meiklejohn and C. P. Bean, Phys. Rev. **102**, 1413 (1956).

[72] C. Binek and B. Doudin, J. Phys.: Condens. Matter **17**, L39 (2005).

[73] P. Borisov, A. Hochstrat, X. Chen, W. Kleemann, and C. Binek, Phys. Rev. Lett. **94**, 117203 (2005).

[74] H. Béa, M. Bibes, F. Ott, B. Dupé, X.-H. Zhu, S. Petit, S. Fusil, C. Deranlot, K. Bouzehouane, and A. Barthélémy, Phys. Rev. Lett. **100**, 017204 (2008).

[75] Y.-H. Chu, L. W. Martin, M. B. Holcomb, M. Gajek, S.-J. Han, Q. He, N. Balke, C.-H. Yang, D. Lee, W. Hu, Q. Zhan, P.-L. Yang, A. Fraile-Rodriguez, A. Scholl, S. X. Wang, and R. Ramesh, Nat. Mater. **7**, 478 (2008).

[76] D. Lebeugle, A. Mougin, M. Viret, D. Colson, and L. Ranno, Phys. Rev. Lett. **103**, 257601 (2009).

[77] S. M. Wu, S. A. Cybart, P. Yu, M. D. Rossell, J. X. Zhang, R. Ramesh, and R. C. Dynes, Nat. Mater. **9**, 756 (2010).

[78] H. Tanaka, J. Zhang, and T. Kawai, Phys. Rev. Lett. **88**, 027204 (2001).

[79] H. Ohno, D. Chiba, F. Matsukura, T. Omiya, E. Abe, T. Dietl, Y. Ohno, and K. Ohtani, Nature **408**, 944 (2000).

[80] D. Chiba, M. Yamanouchi, F. Matsukura, and H. Ohno, Science **301**, 943 (2003).

[81] D. Chiba, M. Sawicki, Y. Nishitani, Y. Nakatani, F. Matsukura, and H. Ohno, Nature **455**, 515 (2008).

[82] I. Stolichnov, S. W. E. Riester, H. J. Trodahl, N. Setter, A. W. Rushforth, K. W. Edmonds, R. P. Campion, C. T. Foxon, B. L. Gallagher, and T. Jungwirth, Nat. Mater. **7**, 464 (2008).

[83] H. J. A. Molegraaf, J. Hoffman, C. A. F. Vaz, S. Gariglio, D. van der Marel, C. H. Ahn, and J.-M. Triscone, Adv. Mater. **21**, 3470 (2009).

[84] C. A. F. Vaz, J. Hoffman, Y. Segal, J. W. Reiner, R. D. Grober, Z. Zhang, C. H. Ahn, and F. J. Walker, Phys. Rev. Lett. **104**, 127202 (2010).

[85] L. Berger, Phys. Rev. B **54**, 9353 (1996).

[86] J. C. Slonczewski, J. Magn. Magn. Mater. **159**, L1 (1996).

[87] M. Tsoi, A. G. M. Jansen, J. Bass, W.-C. Chiang, M. Seck, V. Tsoi, and P. Wyder, Phys. Rev. Lett. **80**, 4281 (1998).

[88] J. Z. Sun, J. Magn. Magn. Mater. **202**, 157 (1999).

[89] E. B. Myers, D. C. Ralph, J. A. Katine, R. N. Louie, and R. A. Buhrman, Science **285**, 867 (1999).

[90] J. A. Katine, F. J. Albert, R. A. Buhrman, E. B. Myers, and D. C. Ralph, Phys. Rev. Lett. **84**, 3149 (2000).

[91] J. Fassbender, D. Ravelosona, and Y. Samson, J. Phys. D: Appl. Phys. **37**, R179 (2004).

[92] J. Fassbender and J. McCord, J. Magn. Magn. Mater. **320**, 579 (2008).

[93] J. McCord, I. Mönch, J. Fassbender, A. Gerber, and E. Quandt, J. Phys. D: Appl. Phys. **42**, 055006 (2009).

[94] J. Wenisch, C. Gould, L. Ebel, J. Storz, K. Pappert, M. J. Schmidt, C. Kumpf, G. Schmidt, K. Brunner, and L. W. Molenkamp, Phys. Rev. Lett. **99**, 077201 (2007).

[95] E. D. Ranieri, A. W. Rushforth, K. Výborný, U. Rana, E. Ahmad, R. P. Campion, C. T. Foxon, B. L. Gallagher, A. C. Irvine, J. Wunderlich, and T. Jungwirth, New J. Phys. **10**, 065003 (2008).

[96] C. S. King, J. Zemen, K. Olejník, L. Horák, J. A. Haigh, V. Novák, A. Irvine, J. Kučera, V. Holý, R. P. Campion, B. L. Gallagher, and T. Jungwirth, Phys. Rev. B **83**, 115312 (2011).

[97] E. C. Stoner and E. P. Wohlfarth, Philos. Trans. R. Soc. London, Ser. A **240**, 599 (1948).

[98] J. M. Florczak and E. D. Dahlberg, Phys. Rev. B **44**, 9338 (1991).

[99] S. Blundell, *Magnetism in Condensed Matter* (Oxford University Press, 2001).

[100] R. C. O'Handley, *Modern Magnetic Materials: Principles and Applications* (Wiley-Interscience, 2000).

[101] A. H. Morrish, *The Physical Principles of Magnetism* (IEEE Press, 2001).

[102] N. A. Spaldin, *Magnetic Materials* (Cambridge University Press, 2003).

[103] E. Olive and P. Molho, Phys. Rev. B **58**, 9238 (1998).

[104] S. Chikazumi, *Physics of Ferromagnetism*, 2nd ed. (Oxford University Press, New York, 1997).

[105] C. Bihler, M. Kraus, H. Huebl, M. S. Brandt, S. T. B. Goennenwein, M. Opel, M. A. Scarpulla, P. R. Stone, R. Farshchi, and O. D. Dubon, Phys. Rev. B **75**, 214419 (2007).

[106] R. R. Birss, *Symmetry and Magnetism*, edited by E. P. Wohlfarth (North-Holland Publishing Company, 1964).

[107] W. J. M. de Jonge, P. J. H. Bloemen, and F. J. A. den Broeder, *Ultrathin Magnetic Structures I*, edited by J. Bland and B. Heinrich (Springer Verlag, 2005).

[108] S. V. Vonsovskii, *Magnetism*, Vol. 2 (John Wiley & Sons, 1974).

[109] J. Lindner, *Ferromagnetische Resonanz an ultradünnen magnetischen Einfach- und Mehrfachlagen der 3d-Übergangsmetalle – Statik und Dynamik*, Ph.D. thesis, Freie Universität Berlin (2002).

[110] W. Limmer, M. Glunk, J. Daeubler, T. Hummel, W. Schoch, R. Sauer, C. Bihler, H. Huebl, M. S. Brandt, and S. T. B. Goennenwein, Phys. Rev. B **74**, 205205 (2006).

[111] C. Bihler, *Magnetic Semiconductors*, Ph.D. thesis, Technische Universität München (2009).

[112] E. Tatsumoto and T. Okamoto, J. Phys. Soc. Jpn. **14**, 1588 (1959).

[113] L. R. Bickford, J. Pappis, and J. L. Stull, Phys. Rev. **99**, 1210 (1955).

[114] A. Clark and H. Belson, IEEE Trans. Magn. **8**, 477 (1972).

[115] E. W. Lee, Rep. Prog. Phys. **18**, 184 (1955).

[116] C. Kittel, Rev. Mod. Phys. **21**, 541 (1949).

[117] J. F. Nye, *Physical Properties of Crystals* (Oxford University Press, 1985).

[118] R. R. Birss, Adv. Phy. **8**, 252 (1959).

[119] N. W. Ashcroft and N. D. Mermin, *Festkörperphysik* (Oldenbourg Verlag, 2001).

[120] A. E. H. Love, *A treatise on the mathematical theory of elasticity* (Cambridge University Press, 1906).

[121] C. Kittel, *Introduction to Solid State Physics* (John Wiley & Sons, 1996).

[122] L. D. Landau and E. M. Lifschitz, *Elastizitätstheorie*, edited by H. G. Schöpf, Lehrbuch der theoretischen Physik, Vol. 7 (Akademie-Verlag Berlin, 1989).

[123] D. Damjanovic, *The Science of Hysteresis*, edited by I. Mayergoyz and G. Bertotti (Academic Press, 2006).

[124] K. Bhattacharya and G. Ravichandran, Acta Mater. **51**, 5941 (2003).

[125] Part No. PSt 150/2×3/5, Piezomechanik GmbH, Germany.

[126] "M-Bond 600", Vishay Intertechnology, Inc., USA.

[127] Part No. 45600 "UHU plus endfest 300", UHU GmbH & Co. KG, Germany.

[128] "General Purpose strain gages", Vishay Intertechnology, Inc., USA.

[129] D. Damjanovic, Rep. Prog. Phys. **61**, 1267 (1998).

[130] Q. M. Zhang, H. Wang, N. Kim, and L. E. Cross, J. Appl. Phys. **75**, 454 (1994).

[131] D. Damjanovic, J. Appl. Phys. **82**, 1788 (1997).

[132] D. Damjanovic and M. Demartin, J. Phys.: Condens. Matter **9**, 4943 (1997).

[133] "Low voltage co-fired multilayer stacks, rings and chips for actuation," Piezomechanik GmbH, Germany (2010).

[134] D. Damjanovic and M. Demartin, J. Phys. D: Appl. Phys. **29**, 2057 (1996).

[135] D. V. Taylor and D. Damjanovic, J. Appl. Phys. **82**, 1973 (1997).

[136] D. V. Taylor and D. Damjanovic, Appl. Phys. Lett. **73**, 2045 (1998).

[137] D. Bolten, U. Böttger, and R. Waser, J. Appl. Phys. **93**, 1735 (2003).

[138] D. Bolten, O. Lohse, M. Grossmann, and R. Waser, Ferroelectrics **221**, 251 (1999).

[139] D. Bolten, *Reversible and Irreversible Polarization Processes in Ferroelectric Ceramics and Thin Films*, Ph.D. thesis, Rheinisch-Westfälische Technische Hochschule Aachen (2002).

[140] O. Boser, J. Appl. Phys. **62**, 1344 (1987).

[141] D. Sander, Rep. Prog. Phys. **62**, 809 (1999).

[142] P. Pedersen, Commun. Numer. Methods Eng. **11**, 821 (1995).

[143] M. T. Johnson, P. J. H. Bloemen, F. J. A. den Broeder, and J. J. de Vries, Rep. Prog. Phys. **59**, 1409 (1996).

[144] D. Sander, J. Phys.: Condens. Matter **16**, R603 (2004).

[145] M. Farle, Rep. Prog. Phys. **61**, 755 (1998).

[146] W. Kleemann, Rev. Sci. Instrum. **78**, 120901 (2007).

[147] B. Heinrich, *Ultrathin Magnetic Structures II*, edited by B. Heinrich and J. Bland (Springer Verlag, 2005).

[148] A. Hubert and R. Schäfer, *Magnetic Domains* (Springer Verlag, 1998).

[149] B. D. Cullity and S. R. Stock, *Elements of X-Ray Diffraction* (Prentice Hall, 2001).

[150] C. P. Poole, *Electron Spin Resonance*, 2nd ed. (Dover Publications, 1996).

[151] R. Meckenstock, *Untersuchung der magnetischen Eigenschaften von Fe/Ag-Schichtsystemen mit der konventionellen und der ortsaufgelösten ferromagnetischen Resonanz*, Ph.D. thesis, Ruhr-Universität Bochum (1997).

[152] K. Lenz, *Magnetische Anisotropie und Dämpfungsmechanismen in ultradünnen 3d-Ferromagneten: eine FMR-Studie*, Ph.D. thesis, Freie Universität Berlin (2005).

[153] J. Lindner and K. Baberschke, J. Phys.: Condens. Matter **15**, R193 (2003).

[154] G. A. Prinz, *Ultrathin Magnetic Structures II*, edited by B. Heinrich and J. Bland (Springer Verlag, 2005).

[155] T. Gilbert, IEEE Trans. Magn. **40**, 3443 (2004).

[156] T. Graf, *Spin-spin interactions of localized electronic states in semiconductors*, Ph.D. thesis, Technische Universität München (2003).

[157] S. T. B. Goennenwein, *Two-Dimensional Electron Gases and Ferromagnetic Semiconductors: Materials for Spintronics*, Ph.D. thesis, Technische Universität München (2003).

[158] B. Heinrich and J. F. Cochran, Adv. Phy. **42**, 523 (1993).

[159] Z. Celinski, K. B. Urquhart, and B. Heinrich, J. Magn. Magn. Mater. **166**, 6 (1997).

[160] C. Kittel, Phys. Rev. **73**, 155 (1948).

[161] J. Smit and H. G. Beljers, Philips Res. Rep. **10**, 113 (1955).

[162] H. Suhl, Phys. Rev. **97**, 555 (1955).

[163] J. O. Artman, Phys. Rev. **105**, 74 (1957).

[164] L. Baselgia, M. Warden, F. Waldner, S. L. Hutton, J. E. Drumheller, Y. Q. He, P. E. Wigen, and M. Maryško, Phys. Rev. B **38**, 2237 (1988).

[165] S. D. Bader and J. L. Erskine, *Ultrathin Magnetic Structures II*, edited by B. Heinrich and J. Bland (Springer Verlag, 2005).

[166] P. M. Oppeneer, *Handbook of Magnetic Materials*, edited by K. H. J. Buschow, Vol. 13 (Elsevier Science, 2001).

[167] P. Bruno, Y. Suzuki, and C. Chappert, Phys. Rev. B **53**, 9214 (1996).

[168] P. N. Argyres, Phys. Rev. **97**, 334 (1955).

[169] P. S. Pershan, J. Appl. Phys. **38**, 1482 (1967).

[170] M. Schlenker and Y. Souche, *Magnetism Fundamentals*, edited by E. du Trémolet de LaCheisserie, D. Gignoux, and M. Schlenker (Springer Verlag, 2004).

[171] M. Freiser, IEEE Trans. Magn. **4**, 152 (1968).

[172] W. Wettling, J. Magn. Magn. Mater. **3**, 147 (1976).

[173] J. Zak, E. R. Moog, C. Liu, and S. D. Bader, Phys. Rev. B **43**, 6423 (1991).

[174] E. Hecht, *Optik* (Oldenbourg Verlag, 2005).

[175] R. P. Hunt, J. Appl. Phys. **38**, 1652 (1967).

[176] C.-Y. You and S.-C. Shin, Appl. Phys. Lett. **69**, 1315 (1996).

[177] Z. J. Yang and M. R. Scheinfein, J. Appl. Phys. **74**, 6810 (1993).

[178] C. C. Robinson, J. Opt. Soc. Am. **53**, 681 (1963).

[179] C.-Y. You and S.-C. Shin, J. Appl. Phys. **84**, 541 (1998).

[180] J. M. Florczak and E. D. Dahlberg, J. Appl. Phys. **67**, 7520 (1990).

[181] N. Morley, M. Gibbs, E. Ahmad, I. Will, and Y. Xu, J. Magn. Magn. Mater. **300**, 436 (2006).

[182] S. Polisetty, J. Scheffler, S. Sahoo, Y. Wang, T. Mukherjee, X. He, and C. Binek, Rev. Sci. Instrum. **79**, 055107 (2008).

[183] C. A. Ballentine, R. L. Fink, J. Araya-Pochet, and J. L. Erskine, Appl. Phys. A **49**, 459 (1989).

[184] J. A. C. Bland, M. J. Padgett, R. J. Butcher, and N. Bett, J. Phys. E: Sci. Instrum. **22**, 308 (1989).

[185] Z. Q. Qiu and S. D. Bader, J. Magn. Magn. Mater. **200**, 664 (1999).

[186] D. A. Allwood, G. Xiong, M. D. Cooke, and R. P. Cowburn, J. Phys. D: Appl. Phys. **36**, 2175 (2003).

[187] N. Mikuszeit, S. Putter, R. Fromter, and H. P. Oepen, J. Appl. Phys. **97**, 103107 (2005).

[188] U. J. Gibson, L. F. Holiday, D. A. Allwood, S. Basu, and P. W. Fry, IEEE Trans. Magn. **43**, 2740 (2007).

[189] M. Pelkner, *Aufbau und Charakterisierung eines Spektrometers für magnetooptischen Kerr-Effekt*, Diploma thesis, Technische Universität München (2008).

[190] M. Brasse, *Magneto-Optical Investigations of Multiferroic Hybrid Structures*, Diploma thesis, Technische Universität München (2009).

[191] C. A. Fowler and E. M. Fryer, Phys. Rev. **94**, 52 (1954).

[192] M. Lambeck, IEEE Trans. Magn. **4**, 51 (1968).

[193] N. Bardou, B. Bartenlian, C. Chappert, R. Megy, P. Veillet, J. P. Renard, F. Rousseaux, M. F. Ravet, J. P. Jamet, and P. Meyer, J. Appl. Phys. **79**, 5848 (1996).

[194] D. Treves, J. Appl. Phys. **32**, 358 (1961).

[195] A. Honda and K. Shirae, IEEE Trans. Magn. **17**, 3096 (1981).

[196] K. Shirae and K. Sugiyama, J. Appl. Phys. **53**, 8380 (1982).

[197] F. Schmidt, W. Rave, and A. Hubert, IEEE Trans. Magn. **21**, 1596 (1985).

[198] W. Rave, R. Schäfer, and A. Hubert, J. Magn. Magn. Mater. **65**, 7 (1987).

[199] T. McGuire and R. Potter, IEEE Trans. Magn. **11**, 1018 (1975).

[200] D. Thompson, L. Romankiw, and A. Mayadas, IEEE Trans. Magn. **11**, 1039 (1975).

[201] J. Smit, Physica **17**, 612 (1951).

[202] J. Kondo, Prog. Theor. Phys. **27**, 772 (1962).

[203] R. I. Potter, Phys. Rev. B **10**, 4626 (1974).

[204] F. Y. Ogrin, S. L. Lee, and Y. F. Ogrin, J. Magn. Magn. Mater. **219**, 331 (2000).

[205] E. Post, Found. Phys. **8**, 277 (1978).

[206] P. K. Muduli, K.-J. Friedland, J. Herfort, H.-P. Schönherr, and K. H. Ploog, Phys. Rev. B **72**, 104430 (2005).

[207] W. Limmer, J. Daeubler, L. Dreher, M. Glunk, W. Schoch, S. Schwaiger, and R. Sauer, Phys. Rev. B **77**, 205210 (2008).

[208] M. Weiler, A. Brandlmaier, S. Geprägs, M. Althammer, M. Opel, C. Bihler, H. Huebl, M. S. Brandt, R. Gross, and S. T. B. Goennenwein, New J. Phys. **11**, 013021 (2009).

[209] A. Brandlmaier, S. Geprägs, G. Woltersdorf, R. Gross, and S. T. B. Goennenwein, J. Appl. Phys. **110**, 043913 (2011).

[210] A. Brandlmaier, M. Brasse, S. Geprägs, M. Weiler, R. Gross, and S. T. B. Goennenwein, *Magneto-optical imaging of voltage-controlled magnetization reorientation*, submitted for publication (2011).

[211] J. M. Leger, C. Loriers-Susse, and B. Vodar, Phys. Rev. B **6**, 4250 (1972).

[212] G. Celotti, I. Vecchi, G. Martinelli, and A. Cecchetti, J. Mater. Sci. **12**, 2537 (1977).

[213] R. Pauthenet, J. Appl. Phys. **53**, 2029 (1982).

[214] A. J. P. Meyer and G. Asch, J. Appl. Phys. **32**, S330 (1961).

[215] D. K. Smith and H. R. Leider, J. Appl. Crystallogr. **1**, 246 (1968).

[216] Y. Sumino, O. L. Anderson, and I. Suzuki, Phys. Chem. Minerals **9**, 38 (1983).

[217] M. Weiler, *Magnetization control in multiferroic heterostructures*, Diploma thesis, Technische Universität München (2007).

[218] M. Wagner, *Winkelaufgelöster Magnetotransport an ferromagnetischen dünnen Filmen*, Diploma thesis, Technische Universität München (2009).

[219] "Piezo-mechanics: An introduction," Piezomechanik GmbH, Germany (2003).

[220] M. Overby, A. Chernyshov, L. P. Rokhinson, X. Liu, and J. K. Furdyna, Appl. Phys. Lett. **92**, 192501 (2008).

[221] M. M. Hall Jnr, V. G. Veeraraghavan, H. Rubin, and P. G. Winchell, J. Appl. Crystallogr. **10**, 66 (1977).

[222] G. C. Kuczynski, Phys. Rev. **94**, 61 (1954).

[223] R. L. Parker and A. Krinsky, J. Appl. Phys. **34**, 2700 (1963).

[224] D. K. Bagchi and B. D. Cullity, J. Appl. Phys. **38**, 999 (1967).

[225] E. Klokholm, J. Vac. Sci. Technol. **10**, 235 (1973).

[226] C. Tannous and J. Gieraltowski, Physica B **403**, 3563 (2008).

[227] C. Tannous and J. Gieraltowski, Eur. J. Phys. **29**, 475 (2008).

[228] R. A. Hyman, A. Zangwill, and M. D. Stiles, Phys. Rev. B **58**, 9276 (1998).

[229] C. Daboo, R. J. Hicken, E. Gu, M. Gester, S. J. Gray, D. E. P. Eley, E. Ahmad, J. A. C. Bland, R. Ploessl, and J. N. Chapman, Phys. Rev. B **51**, 15964 (1995).

[230] F. Y. Yang, C. H. Shang, C. L. Chien, T. Ambrose, J. J. Krebs, G. A. Prinz, V. I. Nikitenko, V. S. Gornakov, A. J. Shapiro, and R. D. Shull, Phys. Rev. B **65**, 174410 (2002).

[231] X. Liu, W. L. Lim, L. V. Titova, M. Dobrowolska, J. K. Furdyna, M. Kutrowski, and T. Wojtowicz, J. Appl. Phys. **98**, 063904 (2005).

[232] E. Carpene, E. Mancini, C. Dallera, E. Puppin, and S. D. Silvestri, J. Appl. Phys. **108**, 063919 (2010).

[233] R. P. Cowburn, S. J. Gray, J. Ferré, J. A. C. Bland, and J. Miltat, J. Appl. Phys. **78**, 7210 (1995).

[234] P. R. Stone, C. Bihler, M. Kraus, M. A. Scarpulla, J. W. Beeman, K. M. Yu, M. S. Brandt, and O. D. Dubon, Phys. Rev. B **78**, 214421 (2008).

[235] P. R. Stone, L. Dreher, J. W. Beeman, K. M. Yu, M. S. Brandt, and O. D. Dubon, Phys. Rev. B **81**, 205210 (2010).

[236] S.-s. Yan, W. J. Liu, J. L. Weston, G. Zangari, and J. A. Barnard, Phys. Rev. B **63**, 174415 (2001).

[237] S. s. Yan, R. Schreiber, P. Grünberg, and R. Schäfer, J. Magn. Magn. Mater. **210**, 309 (2000).

[238] J. Kim, D. Y. Shin, S. Lee, X. Liu, and J. K. Furdyna, Phys. Rev. B **78**, 075309 (2008).

[239] N. Moutis, D. Suarez-Sandoval, and D. Niarchos, J. Magn. Magn. Mater. **320**, 1050 (2008).

[240] J. Wang, J. Hu, H. Wang, H. Jiang, Z. Wu, J. Ma, X. Wang, Y. Lin, and C. W. Nan, J. Appl. Phys. **107**, 083901 (2010).

[241] Z. Li, J. Wang, Y. Lin, and C. W. Nan, Appl. Phys. Lett. **96**, 162505 (2010).

[242] Y. Chen, T. Fitchorov, Z. Cai, K. S. Ziemer, C. Vittoria, and V. G. Harris, J. Phys. D: Appl. Phys. **43**, 155001 (2010).

[243] C. Cavaco, M. van Kampen, L. Lagae, and G. Borghs, J. Mater. Res. **22**, 2111 (2007).

[244] Y. Chen, A. L. Geiler, T. Fitchorov, C. Vittoria, and V. G. Harris, Appl. Phys. Lett. **95**, 182501 (2009).

[245] J. J. Yang, Y. G. Zhao, H. F. Tian, L. B. Luo, H. Y. Zhang, Y. J. He, and H. S. Luo, Appl. Phys. Lett. **94**, 212504 (2009).

[246] Y. Chen, T. Fitchorov, A. Geiler, J. Gao, C. Vittoria, and V. Harris, Appl. Phys. A **100**, 1149 (2010).

[247] J. Ma, Y. Lin, and C. W. Nan, J. Phys. D: Appl. Phys. **43**, 012001 (2010).

[248] Y. Zhang, J. Liu, X. H. Xiao, T. C. Peng, C. Z. Jiang, Y. H. Lin, and C. W. Nan, J. Phys. D: Appl. Phys. **43**, 082002 (2010).

[249] S. Geprägs, A. Brandlmaier, M. Opel, R. Gross, and S. T. B. Goennenwein, Appl. Phys. Lett. **96**, 142509 (2010).

[250] J. Wang, H. Wang, H. Jiang, X. Wang, Y. Lin, and C. W. Nan, J. Nanomater. **2010**, 142750 (2010).

[251] T. Wu, A. Bur, P. Zhao, K. P. Mohanchandra, K. Wong, K. L. Wang, C. S. Lynch, and G. P. Carman, Appl. Phys. Lett. **98**, 012504 (2011).

[252] T. Taniyama, K. Akasaka, D. Fu, M. Itoh, H. Takashima, and B. Prijamboedi, J. Appl. Phys. **101**, 09F512 (2007).

[253] T.-K. Chung, G. P. Carman, and K. P. Mohanchandra, Appl. Phys. Lett. **92**, 112509 (2008).

[254] T.-K. Chung, K. Wong, S. Keller, K. L. Wang, and G. P. Carman, J. Appl. Phys. **106**, 103914 (2009).

[255] H. Ohkita, K. Ishibashi, D. Tsurumoto, A. Tagaya, and Y. Koike, Appl. Phys. A **81**, 617 (2005).

[256] S. T. B. Goennenwein, M. Althammer, C. Bihler, A. Brandlmaier, S. Geprägs, M. Opel, W. Schoch, W. Limmer, R. Gross, and M. S. Brandt, Phys. Stat. Sol. (RRL) **2**, 96 (2008).

[257] C. Bihler, M. Althammer, A. Brandlmaier, S. Geprägs, M. Weiler, M. Opel, W. Schoch, W. Limmer, R. Gross, M. S. Brandt, and S. T. B. Goennenwein, Phys. Rev. B **78**, 045203 (2008).

[258] A. W. Rushforth, E. D. Ranieri, J. Zemen, J. Wunderlich, K. W. Edmonds, C. S. King, E. Ahmad, R. P. Campion, C. T. Foxon, B. L. Gallagher, K. Výborný, J. Kučera, and T. Jungwirth, Phys. Rev. B **78**, 085314 (2008).

[259] H. Ohno, Science **281**, 951 (1998).

[260] R. Shioda, K. Ando, T. Hayashi, and M. Tanaka, Phys. Rev. B **58**, 1100 (1998).

[261] V. Novák, K. Olejník, J. Wunderlich, M. Cukr, K. Výborný, A. W. Rushforth, K. W. Edmonds, R. P. Campion, B. L. Gallagher, J. Sinova, and T. Jungwirth, Phys. Rev. Lett. **101**, 077201 (2008).

[262] H. Ohno, A. Shen, F. Matsukura, A. Oiwa, A. Endo, S. Katsumoto, and Y. Iye, Appl. Phys. Lett. **69**, 363 (1996).

[263] H. Ohno, J. Magn. Magn. Mater. **200**, 110 (1999).

[264] X. Liu and J. K. Furdyna, J. Phys.: Condens. Matter **18**, R245 (2006).

[265] S. Lee, J.-H. Chung, X. Liu, J. K. Furdyna, and B. J. Kirby, Mater. Today **12**, 14 (2009).

[266] T. Dietl, Nat. Mater. **9**, 965 (2010).

[267] T. Dietl, H. Ohno, F. Matsukura, J. Cibert, and D. Ferrand, Science **287**, 1019 (2000).

[268] T. Dietl, H. Ohno, and F. Matsukura, Phys. Rev. B **63**, 195205 (2001).

[269] M. Abolfath, T. Jungwirth, J. Brum, and A. H. MacDonald, Phys. Rev. B **63**, 054418 (2001).

[270] T. Jungwirth, J. Sinova, J. Mašek, J. Kučera, and A. H. MacDonald, Rev. Mod. Phys. **78**, 809 (2006).

[271] H. Ohno and T. Dietl, J. Magn. Magn. Mater. **320**, 1293 (2008).

[272] H. F. Ding, S. Pütter, H. P. Oepen, and J. Kirschner, Phys. Rev. B **63**, 134425 (2001).

[273] M. Sawicki, F. Matsukura, A. Idziaszek, T. Dietl, G. M. Schott, C. Ruester, C. Gould, G. Karczewski, G. Schmidt, and L. W. Molenkamp, Phys. Rev. B **70**, 245325 (2004).

[274] L. V. Titova, M. Kutrowski, X. Liu, R. Chakarvorty, W. L. Lim, T. Wojtowicz, J. K. Furdyna, and M. Dobrowolska, Phys. Rev. B **72**, 165205 (2005).

[275] X. Liu, Y. Sasaki, and J. K. Furdyna, Phys. Rev. B **67**, 205204 (2003).

[276] M. Sawicki, K.-Y. Wang, K. W. Edmonds, R. P. Campion, C. R. Staddon, N. R. S. Farley, C. T. Foxon, E. Papis, E. Kamińska, A. Piotrowska, T. Dietl, and B. L. Gallagher, Phys. Rev. B **71**, 121302 (2005).

[277] V. Stanciu and P. Svedlindh, Appl. Phys. Lett. **87**, 242509 (2005).

[278] K. Hamaya, T. Taniyama, Y. Kitamoto, T. Fujii, and Y. Yamazaki, Phys. Rev. Lett. **94**, 147203 (2005).

[279] K. Hamaya, T. Watanabe, T. Taniyama, A. Oiwa, Y. Kitamoto, and Y. Yamazaki, Phys. Rev. B **74**, 045201 (2006).

[280] H. Son, S.-J. Chung, S.-Y. Yea, S. Lee, X. Liu, and J. K. Furdyna, J. Appl. Phys. **103**, 07F313 (2008).

[281] U. Welp, V. K. Vlasko-Vlasov, A. Menzel, H. D. You, X. Liu, J. K. Furdyna, and T. Wojtowicz, Appl. Phys. Lett. **85**, 260 (2004).

[282] U. Welp, V. K. Vlasko-Vlasov, X. Liu, J. K. Furdyna, and T. Wojtowicz, Phys. Rev. Lett. **90**, 167206 (2003).

[283] A. Shen, H. Ohno, F. Matsukura, Y. Sugawara, N. Akiba, T. Kuroiwa, A. Oiwa, A. Endo, S. Katsumoto, and Y. Iye, J. Cryst. Growth **175-176**, 1069 (1997).

[284] J. Zemen, J. Kučera, K. Olejník, and T. Jungwirth, Phys. Rev. B **80**, 155203 (2009).

[285] M. Glunk, J. Daeubler, L. Dreher, S. Schwaiger, W. Schoch, R. Sauer, W. Limmer, A. Brandlmaier, S. T. B. Goennenwein, C. Bihler, and M. S. Brandt, Phys. Rev. B **79**, 195206 (2009).

[286] S. Kim, H. Lee, T. Yoo, S. Lee, S. Lee, X. Liu, and J. K. Furdyna, J. Appl. Phys. **107**, 103911 (2010).

[287] T. Jungwirth, M. Abolfath, J. Sinova, J. Kučera, and A. H. MacDonald, Appl. Phys. Lett. **81**, 4029 (2002).

[288] T. Jungwirth, J. Sinova, K. Y. Wang, K. W. Edmonds, R. P. Campion, B. L. Gallagher, C. T. Foxon, Q. Niu, and A. H. MacDonald, Appl. Phys. Lett. **83**, 320 (2003).

[289] D. V. Baxter, D. Ruzmetov, J. Scherschligt, Y. Sasaki, X. Liu, J. K. Furdyna, and C. H. Mielke, Phys. Rev. B **65**, 212407 (2002).

[290] H. X. Tang, R. K. Kawakami, D. D. Awschalom, and M. L. Roukes, Phys. Rev. Lett. **90**, 107201 (2003).

[291] F. Matsukura, M. Sawicki, T. Dietl, D. Chiba, and H. Ohno, Physica E **21**, 1032 (2004).

[292] S. T. B. Goennenwein, S. Russo, A. F. Morpurgo, T. M. Klapwijk, W. Van Roy, and J. De Boeck, Phys. Rev. B **71**, 193306 (2005).

[293] K. Y. Wang, K. W. Edmonds, R. P. Campion, L. X. Zhao, C. T. Foxon, and B. L. Gallagher, Phys. Rev. B **72**, 085201 (2005).

[294] M. Althammer, *Magneto-galvanische Effekte und Verspannungen in dünnen ferromagnetischen Filmen*, Diploma thesis, Technische Universität München (2007).

[295] "First steps towards piezoaction," Piezomechanik GmbH, Germany (2010).

[296] T. Yamada, D. Chiba, F. Matsukura, S. Yakata, and H. Ohno, Phys. Status Solidi C **3**, 4086 (2006).

[297] F. Matsukura, H. Ohno, A. Shen, and Y. Sugawara, Phys. Rev. B **57**, R2037 (1998).

[298] G. P. Moore, J. Ferré, A. Mougin, M. Moreno, and L. Däweritz, J. Appl. Phys. **94**, 4530 (2003).

[299] K. Hamaya, T. Taniyama, Y. Kitamoto, R. Moriya, and H. Munekata, J. Appl. Phys. **94**, 7657 (2003).

[300] A. Winter, H. Pascher, H. Krenn, X. Liu, and J. K. Furdyna, J. Appl. Phys. **108**, 043921 (2010).

[301] S. C. Masmanidis, H. X. Tang, E. B. Myers, M. Li, K. De Greve, G. Vermeulen, W. Van Roy, and M. L. Roukes, Phys. Rev. Lett. **95**, 187206 (2005).

[302] C. Bihler, Private communication (2006).

[303] J. S. Blakemore, J. Appl. Phys. **53**, R123 (1982).

[304] N. A. Pertsev, Phys. Rev. B **78**, 212102 (2008).

[305] N. A. Pertsev and H. Kohlstedt, Appl. Phys. Lett. **95**, 163503 (2009).

[306] J.-M. Hu and C. W. Nan, Phys. Rev. B **80**, 224416 (2009).

[307] J.-M. Hu, Z. Li, J. Wang, and C. W. Nan, J. Appl. Phys. **107**, 093912 (2010).

[308] Y. Iwasaki, J. Magn. Magn. Mater. **240**, 395 (2002).

[309] A. Brandlmaier, S. Geprägs, M. Weiler, A. Boger, M. Opel, H. Huebl, C. Bihler, M. S. Brandt, B. Botters, D. Grundler, R. Gross, and S. T. B. Goennenwein, Phys. Rev. B **77**, 104445 (2008).

[310] A. Brandlmaier, S. Geprägs, M. S. Brandt, R. Gross, and S. T. B. Goennenwein, *Towards voltage-controlled nonvolatile magnetization switching*, in preparation for publication.

[311] E. W. Gorter, Proc. IRE **43**, 1945 (1955).

[312] E. J. W. Verwey and E. L. Heilmann, J. Chem. Phys. **15**, 174 (1947).

[313] S. Kale, S. M. Bhagat, S. E. Lofland, T. Scabarozi, S. B. Ogale, A. Orozco, S. R. Shinde, T. Venkatesan, B. Hannoyer, B. Mercey, and W. Prellier, Phys. Rev. B **64**, 205413 (2001).

[314] C. G. Shull, E. O. Wollan, and W. C. Koehler, Phys. Rev. **84**, 912 (1951).

[315] Z. Kąkol and J. M. Honig, Phys. Rev. B **40**, 9090 (1989).

[316] Z. Zhang and S. Satpathy, Phys. Rev. B **44**, 13319 (1991).

[317] M. Fonin, Y. S. Dedkov, R. Pentcheva, U. Rüdiger, and G. Güntherodt, J. Phys.: Condens. Matter **19**, 315217 (2007).

[318] B. A. Calhoun, Phys. Rev. **94**, 1577 (1954).

[319] F. Walz, J. Phys.: Condens. Matter **14**, R285 (2002).

[320] M. Alexe, M. Ziese, D. Hesse, P. Esquinazi, K. Yamauchi, T. Fukushima, S. Picozzi, and U. Gösele, Adv. Mater. **21**, 4452 (2009).

[321] H. Schwenk, S. Bareiter, C. Hinkel, B. Lüthi, Z. Kakol, A. Koslowski, and J. M. Honig, Eur. Phys. J. B **13**, 491 (2000).

[322] L. R. Bickford, Phys. Rev. **78**, 449 (1950).

[323] D. T. Margulies, F. T. Parker, and A. E. Berkowitz, J. Appl. Phys. **75**, 6097 (1994).

[324] D. T. Margulies, F. T. Parker, F. E. Spada, R. S. Goldman, J. Li, R. Sinclair, and A. E. Berkowitz, Phys. Rev. B **53**, 9175 (1996).

[325] B. Aktaş, Thin Solid Films **307**, 250 (1997).

[326] P. A. A. van der Heijden, M. G. van Opstal, C. H. W. Swüste, P. H. J. Bloemen, J. M. Gaines, and W. J. M. de Jonge, J. Magn. Magn. Mater. **182**, 71 (1998).

[327] S. Budak, F. Yildiz, M. Özdemir, and B. Aktaş, J. Magn. Magn. Mater. **258**, 423 (2003).

[328] D. Reisinger, M. Schonecke, T. Brenninger, M. Opel, A. Erb, L. Alff, and R. Gross, J. Appl. Phys. **94**, 1857 (2003).

[329] J. Klein, C. Höfener, L. Alff, and R. Gross, Supercond. Sci. Technol. **12**, 1023 (1999).

[330] C.-H. Lai, P.-H. Huang, Y.-J. Wang, and R. T. Huang, J. Appl. Phys. **95**, 7222 (2004).

[331] C. A. Kleint, H. C. Semmelhack, M. Lorenz, and M. K. Krause, J. Magn. Magn. Mater. **140-144**, 725 (1995).

[332] M. Paramês, J. Mariano, Z. Viskadourakis, N. Popovici, M. Rogalskid, J. Giapintzakis, and O. Conde, Appl. Surf. Sci. **252**, 4610 (2006).

[333] W. Eerenstein, T. Hibma, and S. Celotto, Phys. Rev. B **70**, 184404 (2004).

[334] D. T. Margulies, F. T. Parker, M. L. Rudee, F. E. Spada, J. N. Chapman, P. R. Aitchison, and A. E. Berkowitz, Phys. Rev. Lett. **79**, 5162 (1997).

[335] J.-B. Moussy, S. Gota, A. Bataille, M.-J. Guittet, M. Gautier-Soyer, F. Delille, B. Dieny, F. Ott, T. D. Doan, P. Warin, P. Bayle-Guillemaud, C. Gatel, and E. Snoeck, Phys. Rev. B **70**, 174448 (2004).

[336] J. B. Nelson and D. P. Riley, Proc. Phys. Soc. **57**, 160 (1945).

[337] M. S. Doraiswami, Proc. Indian Acad. Sci., Sect. A **25**, 413 (1947).

[338] S. W. Sun and R. C. O'Handley, Phys. Rev. Lett. **66**, 2798 (1991).

[339] R. Koch, M. Weber, K. Thürmer, and K. H. Rieder, J. Magn. Magn. Mater. **159**, L11 (1996).

[340] D. Sander, A. Enders, and J. Kirschner, J. Magn. Magn. Mater. **200**, 439 (1999).

[341] Z. Tian, D. Sander, and J. Kirschner, Phys. Rev. B **79**, 024432 (2009).

[342] I. L. Prejbeanu, M. Kerekes, R. C. Sousa, H. Sibuet, O. Redon, B. Dieny, and J. P. Nozières, J. Phys.: Condens. Matter **19**, 165218 (2007).

[343] J.-M. Hu, Z. Li, J. Wang, J. Ma, Y. H. Lin, and C. W. Nan, J. Appl. Phys. **108**, 043909 (2010).

[344] M. Weiler, L. Dreher, C. Heeg, H. Huebl, R. Gross, M. S. Brandt, and S. T. B. Goennenwein, Phys. Rev. Lett. **106**, 117601 (2011).

[345] C.-W. Nan, G. Liu, Y. Lin, and H. Chen, Phys. Rev. Lett. **94**, 197203 (2005).

[346] T. Morita, Y. Wagatsuma, Y. Cho, H. Morioka, H. Funakubo, and N. Setter, Appl. Phys. Lett. **84**, 5094 (2004).

[347] T. Furukawa, Phase Transitions **18**, 143 (1989).

[348] K. Uchida, S. Takahashi, K. Harii, J. Ieda, W. Koshibae, K. Ando, S. Maekawa, and E. Saitoh, Nature **455**, 778 (2008).

[349] K. Uchida, J. Xiao, H. Adachi, J. Ohe, S. Takahashi, J. Ieda, T. Ota, Y. Kajiwara, H. Umezawa, H. Kawai, G. E. W. Bauer, S. Maekawa, and E. Saitoh, Nat. Mater. **9**, 894 (2010).

[350] C. M. Jaworski, J. Yang, S. Mack, D. D. Awschalom, J. P. Heremans, and R. C. Myers, Nat. Mater. **9**, 898 (2010).

[351] K. Uchida, H. Adachi, T. An, T. Ota, M. Toda, B. Hillebrands, S. Maekawa, and E. Saitoh, arXiv:1103.6120 (2011).